Structural mechanisms of class B GPCR signaling: the case of the parathyroid hormone receptor

by

Lisa Jean Clark

B.A., Truman State University, 2014

Submitted to the Graduate Faculty of the

School of Medicine in partial fulfillment

of the requirements for the degree of

Doctor of Philosophy

University of Pittsburgh

2020

UNIVERSITY OF PITTSBURGH

SCHOOL OF MEDICINE

This dissertation was presented

by

Lisa Jean Clark

It was defended on

October 2, 2020

and approved by

James Conway, Professor, Department of Structural Biology

Guillermo Romero, Associate Professor, Department of Pharmacology and Chemical Biology

Cheng Zhang, Assistant Professor, Department of Pharmacology and Chemical Biology

Dissertation Director: Jean-Pierre Vilardaga, Professor, Department of Pharmacology and Chemical Biology

Structural mechanisms of class B GPCR signaling: the case of the parathyroid hormone receptor

Lisa Jean Clark, PhD

University of Pittsburgh, 2020

The parathyroid hormone (PTH) type 1 receptor (PTHR), a class B G protein-coupled receptor (GPCR), is the key regulator of bone turnover and mineral ion homeostasis. A thorough understanding of the structural mechanisms of PTHR function is necessary to develop therapeutics for bone and mineral disorders (e.g., osteoporosis). To further this aim, we used an interdisciplinary approach, including cryo-EM, NMR spectroscopy, and MD simulations to investigate several steps in the PTHR signaling pathway: ligand binding, receptor activation, coupling to effector proteins, and termination of signaling.

We solved high-resolution cryo-EM structures of PTHR in complex with the stimulatory G protein (G_s) for adenylyl cyclases and a long-acting PTH analog (LA-PTH). These structures provide insights into the mechanism of PTHR activation. We also sought determine how LA-PTH triggers prolonged sustained cAMP signaling in endosomes compared to PTH. In MD simulations, the N-terminal part of LA-PTH makes more contacts with PTHR in comparison to PTH. Therefore, LA-PTH remains bound to active receptor despite endosomal acidification, which destabilizes interactions between PTHR and the C-terminal part of the ligand. Next, we probed the mechanism of PTH binding to PTHR. Our results show that initial binding of the PTH C-terminal part to $PTHR^{ECD}$ during the first step reduces the mobility of the PTH N-terminal part, which primes the N-terminal part to interact with the receptor transmembrane domain during the second step.

An allosteric link between PTHR interactions with the PTH N-terminal part and receptor coupling to intracellular effectors was demonstrated through the investigation of two PTH mutations, His9→Ala9 (PTH^{H9A}) Leu7 L→D (PTH^{7d}), which inhibit β-arrestin coupling through distinct mechanisms, leading to transient and sustained cAMP production at the plasma membrane, respectively. PTH^{H9A} promotes an inward conformation of receptor intracellular loop 3 to prevent interactions with β-arrestin's finger loop. PTH^{7d} enhances a receptor polar network stabilizing an outward kink of the intracellular part of transmembrane helix 6 (TM6), which prevents the inward TM6 movement necessary for β-arrestin coupling. In total, our results likely extend to other class B GPCRs and provide a structural framework for drug design targeting bone and mineral disorders.

Table of Contents

List of Tables

List of Figures

Acknowledgements

I am incredibly grateful for the countless individuals who have supported me during graduate school. I thank Jean-Pierre Vilardaga for the excellent mentorship during my time in his laboratory. Many thanks to Ieva Sutkeviciute, from whom I received most of my training in membrane protein purification. Ieva and I are co-first authors on a *Trends in Endocrinology and Metabolism* review article, and some of this content is shown in Section 2.1.3. It has been a joy to work with past and present members of the Vilardaga lab: JP, Ieva, Alex White, Karina Peña, Frederic Jean-Alphonse, and Saifei Lei. I thank my dissertation committee for their invaluable insight: James Conway, Guillermo Romero, Jean-Pierre Vilardaga, and Cheng Zhang. I have immense gratitude for Molecular Biophysics and Structural Biology (MBSB) program Co-Directors James Conway, Gordon Rule, and Andy Hinck as well as Pharmacology and Chemical Biology Department Chair Bruce Freeman, especially during my transition into the Vilardaga lab. Many thanks to others involved in the MBSB program, including all my course instructors, Lauren Zielinski, and fellow MBSB students and graduates, especially Emily Beckwitt and Chino Cabalteja, who also joined the program in 2014, my MB II mentees (Manish Aryal, Kirill Lavrenyuk, Stephen White, Sara Whitlock), and my good friends Jennifer Boatz and Abhishek Mandal.

I have had the pleasure of working with numerous collaborators including fellow GPCR labs of Peter Friedman, Cheng Zhang, and Kevin Xiao. Thanks also to the Cheng Zhang lab for allowing me to use their equipment and to the Kevin Xiao group for performing mass spectrometry experiments (shown in Chapter 4.0). Much of the research presented in this dissertation is the result of amazing collaborations with the labs of Pei Tang and Ivet Bahar. Thanks to Vasyl Bonkarenko

for training me to perform NMR experiments. I am also incredibly grateful for the MD simulation training from James Krieger, who is a co-first author of our recent publication in *Nature Chemical Biology*.

I appreciate the financial support from the National Institutes of Health, including the Ruth L. Kirschstein National Research Service Award Institutional Research Training Grant (T32) and Individual Predoctoral Fellowship (F31), which I was awarded during graduate school.

Finally, I have received overwhelming support and love from my wonderful family, especially parents Lisa E. Clark and Richard Clark, significant other Harold Gosney, and adorable cat Sunflower.

To all those who have supported me during my PhD journey, those listed above and those not mentioned here, I dedicate this dissertation.

1.0 Background

1.1 Introduction to G protein-coupled receptors (GPCRs)

G protein-coupled receptors (GPCRs) constitute the largest family of cell membrane proteins, with approximately 800 receptors in the human genome[1]. GPCRs mediate cell signaling by interacting with a variety of extracellular stimuli, such as small molecules, peptides, larger proteins, and light. Binding of an agonist activates the receptor, triggering conformational changes that permit binding of intracellular proteins (G proteins and arrestins), which then propagate the signal (Figure 1.1). Approximately 34% of all FDA approved drugs target GPCRs, including drugs to treat depression, type 2 diabetes, and osteoporosis[1].

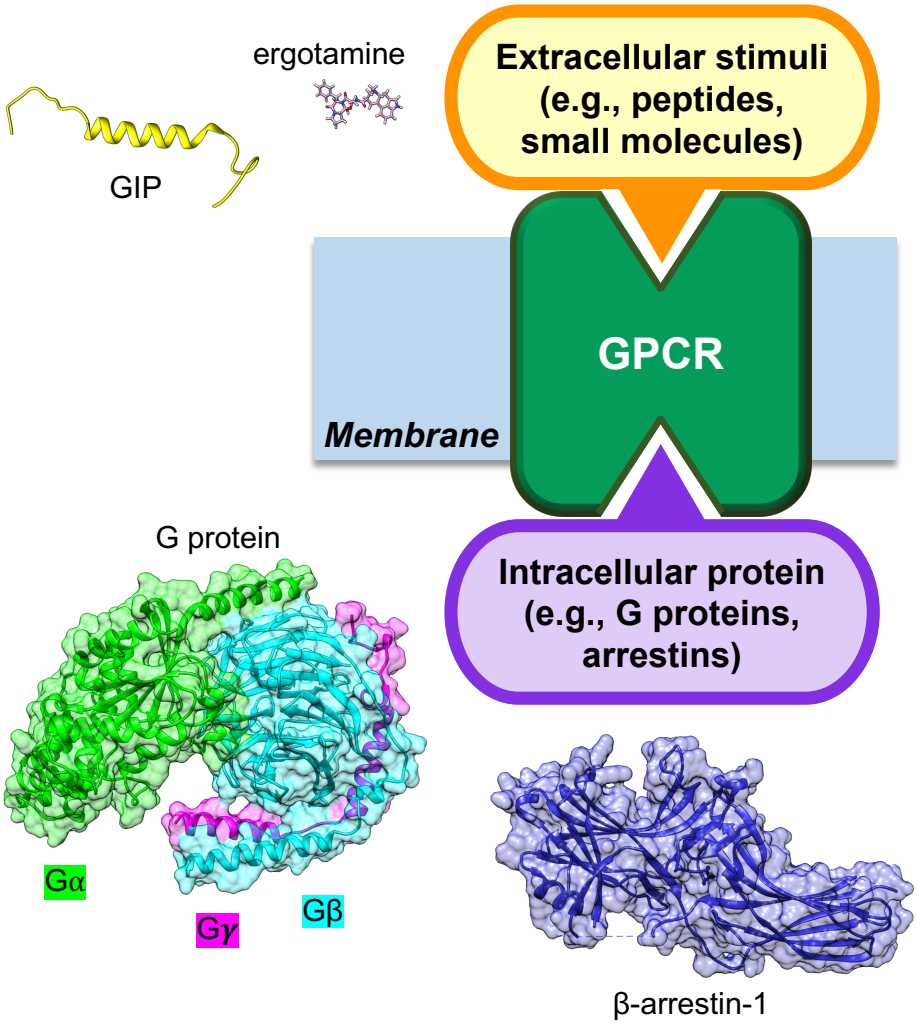

Figure 1.1. Schematic overview of GPCRs.

Examples of extracellular stimuli are the small molecule ergotamine and the gastric inhibitory peptide (GIP, PDB 2B4N[2]). Structures of a heterotrimeric G protein (PDB 1GOT[3]) and bovine β-arrestin-1 (PDB 1G4M[4]) are also displayed.

1.1.1 GPCR Classification

All GPCRs have a transmembrane domain (TMD) consisting of seven α-helices connected by three extracellular loops and three intracellular loops. GPCRs also have N-terminal

(extracellular) and C-terminal portions that differ between GPCR families. Based on sequence and functional analysis, human GPCRs were classified into five families: rhodopsin, secretin, adhesion, glutamate, and frizzled (IUPHAR "GRAFS" classification)[5,6]. The rhodopsin family (class A GPCRs) has the greatest number of members, which typically exhibit small N-terminal regions[7,8]. The vast majority of GPCR structures solved to-date have been of class A GPCRs via X-ray crystallography. The secretin family (class B GPCRs) is characterized by a large extracellular domain (ECD) that, along with the TMD, participates in peptide ligand binding[9]. Adhesion GPCRs have a large extracellular region containing several adhesion domains and a conserved GPCR Autoproteolysis INducing (GAIN) domain[10,11]. In addition to the TMD, the glutamate family (class C GPCRs) has an extracellular bilobed venus fly trap domain that binds orthosteric ligands[12]. Apart from GABA subunits, class C GPCRs have a cysteine-rich domain connecting the TMD and venus fly trap domain[13]. Class C GPCRs are obligate dimers[12]. The frizzled family (class F GPCRs) consists of frizzled receptors, which mediate the Wnt/β-catenin signaling pathway, and the smoothened receptor, which mediates the Hedgehog signaling pathway[6,14]. Class F receptors have an extracellular cysteine-rich domain[14].

1.1.2 GPCR Signaling

Agonist binding to its receptor triggers conformational changes that permit coupling and activation of a heterotrimeric G protein, consisting of subunits α, β, and γ[15]. G protein activation involves release of the guanosine-5'-diphosphate (GDP) molecule bound to Gα and the binding of a guanosine-5'-triphosphate (GTP) molecule; in this way, the activated GPCR acts as a guanine

exchange factor (GEF). GTP binding triggers dissociation of Gα from the Gβγ heterodimer, and dissociated Gα-GTP and Gβγ can then regulate other intracellular effectors.

There are four subfamilies of G proteins expressed in humans, distinguished by the Gα subunit[15]. Each Gα subfamily activates different intracellular proteins, leading to unique cellular effects. The G_s subfamily ($G\alpha_s$, $G\alpha_{olf}$) activates transmembrane adenylyl cyclases, which increase the production of intracellular cyclic adenosine monophosphate (cAMP), and cAMP activates protein kinase A (PKA)[15,16]. The $G_{i/o}$ subfamily consists of $G\alpha_{i1\text{-}3}$, $G\alpha_o$, $G\alpha_z$, and $G\alpha_{t1\text{-}3}$, all except the latter inhibiting adenylyl cyclases, thus decreasing cAMP. $G\alpha_{t1\text{-}3}$ activates cyclic guanosine monophosphate (cGMP) phosphodiesterase, which decreases cGMP. The $G_{q/11}$ subfamily ($G\alpha_q$, $G\alpha_{11}$, $G\alpha_{14}$, $G\alpha_{15}$) activates phospholipase Cβ (PLCβ)[2], which cleaves phosphatidylinositol (4,5)-bisphosphate (PIP2) to generate diacylglycerol (DAG) and inositol (1,4,5)-trisphosphate (IP3)[3]. IP3 activates calcium channels at the endoplasmic reticulum, releasing Ca^{2+} into the cytosol[3]. DAG activates protein kinase C (PKC). The $G_{12/13}$ subfamily ($G\alpha_{12}$, $G\alpha_{13}$) activates the Rho GTPase GEF (Rho-GEF)[15,16]. Gα proteins exhibit GTPase activity, which can be accelerated by GTPase activating proteins (GAPs)[17]. Once the GTP is hydrolyzed to GDP, Gα can recouple to Gβγ and bind to a GPCR for a new cycle of activation.

Humans express five subtypes of Gβ and twelve subtypes of Gγ[18]. While the specific actions of each subtype are under investigation, Gβγ heterodimers regulate many effectors, including multiple adenylyl cyclase subtypes, ion channels, and phosphoinositide 3-kinase gamma (PI3Kγ)[3,18,19]. Humans also express four arrestin subtypes: visual arrestins (arrestin-1 and arrestin-4) and non-visual arrestins (β-arrestin-1 and β-arrestin-2).

Receptor phosphorylation by G protein receptor kinases (GRKs) promotes arrestin coupling and engages internalization of the receptor into endosomes[20]. In the classic mechanism of GPCR signaling, the agonist dissociates from the receptor, and the receptor can be either degraded in lysosomes or recycled to the plasma membrane[21,22]. The parathyroid hormone type 1 receptor (PTHR) was the first receptor discovered to exhibit a new mode of signaling via G_s in which production of cAMP is maintained after receptor internalization into early endosomes (see Section 1.7 for additional description)[23].

1.2 Structures of class B GPCRs

The PTHR, which is the focus of this dissertation, is a class B GPCR that plays a crucial role in blood mineral ion (Ca^{2+} and Pi) homeostasis via the actions of PTH in bone and kidney (see Section 1.6 for a more detailed description of PTHR's impact on human health). To understand the structural basis of PTHR signaling and function, it is essential to address the known structural qualities of class B GPCRs.

Prior to the publication of the PTHR–G_s cryo-EM structures (described in Section 2.1)[24], several types of class B GPCR structures were obtained (Appendix Table 1). Figure 1.2 presents the ligand-bound structures from Appendix Table 1.

The extracellular domains of many GPCRs were crystallized in the absence or presence of ligands: calcitonin receptor (CTR; PDB 5II0[25]), calcitonin gene-related peptide receptor (CGRPR; PDB 3N7P, 3N7R, 3N7S[26], 5V6Y[27], 6D1U[28], 4RWG[29]), adrenomedullin 1 receptor (AM1R; PDB 3AQF[30], 4RWF[29]), corticotropin-releasing factor 1 receptor (CRF1F; PDB 3EHU[31]), corticotropin-releasing factor 2 receptor (CRF2F; PDB 3N96, 3N95, 3N93[32]), glucagon receptor

(GCGR; PDB 4ERS[33]), growth hormone–releasing hormone (GHRHR; PDB 2XDG[34]), gastric inhibitory polypeptide receptor (GIPR; PDB 2QKH[35], 4HJ0[36]), glucagon-like peptide 1 receptor (GLP1R; PDB 3IOL[37], 4ZGM[38], 3C5T[39], 5E94[40]), parathyroid hormone 1 receptor (PTHR; PDB 3L2J[41], 3C4M[42], 3H3G[43]), pituitary adenylate cyclase-activating polypeptide type I receptor (PAC1R; PDB 3N94[44]), vasoactive intestinal peptide receptor 2 (VPAC2R; PDB 2X57[45]). NMR ensemble structures of CRF1R (PDB 2L27[46]), CRF2R (PDB 1U34[47], 2JND[48]), and VPAC2R (PDB 2JOD[49]) ECDs were also published. These structures demonstrate direct interaction between the C-terminal portion of peptide ligands and the ECD and provide snapshots of the first step in class B GPCR peptide ligand binding to its receptor (described in-depth in Chapter 3.0). For crystal structures also displaying an N-terminal part of the ligand[35,37-39], the N-terminal part participates in crystal packing.

Several structures containing class B GPCR TMDs were solved via X-ray crystallography. Inactive state structures were solved in the presence of small molecule antagonists or negative allosteric modulators: CRF1R with antagonist CP-376395 (PDB 4K5Y[50]), GCGR with antagonists NNC0460 or MK-0893 (PDB 4L67[51], 5XEZ[52], 5EE7[53]), GLP1R with negative allosteric modulators (NAMs) PF-06372222 or NNC0460 (PDB 5VEW, 5VEX[54]). PTHR was crystallized with a mimetic PTH agonist (ePTH) but displayed an inactive conformation (PDB 6FJ3[55]). GCGR was also crystallized in the presence of partial agonist NNC1702 (PDB 5YQZ[56]). A structure of GLP1R in complex with truncated agonist peptide 5 was also published (PDB 5NX2[57]). For all structures except the GLP1R–peptide 5 complex, the receptor constructs include fusion proteins, such as T4 lysozyme, to facilitate crystallization. Improvements in cryo-EM technologies, including the direct electron detector, have increased structure resolution[58]. Prior to the publication of our PTHR–G_s structure, four structures of class B GPCRs in complex with G_s and stabilizing

nanobody 35 (Nb35) were solved: CTR (PDB 6NIY[59]), CGRPR (PDB 6E3Y[60]), GLP1R (PDB 6B3J[61], 5VAI[62]). These structures highlight differences between class A and B GPCRs, including the more extended kink of transmembrane helix (TM6) upon class B receptor activation and coupling to G_s. Our new PTHR–G_s structures confirm these observations, as described in Section 2.1.

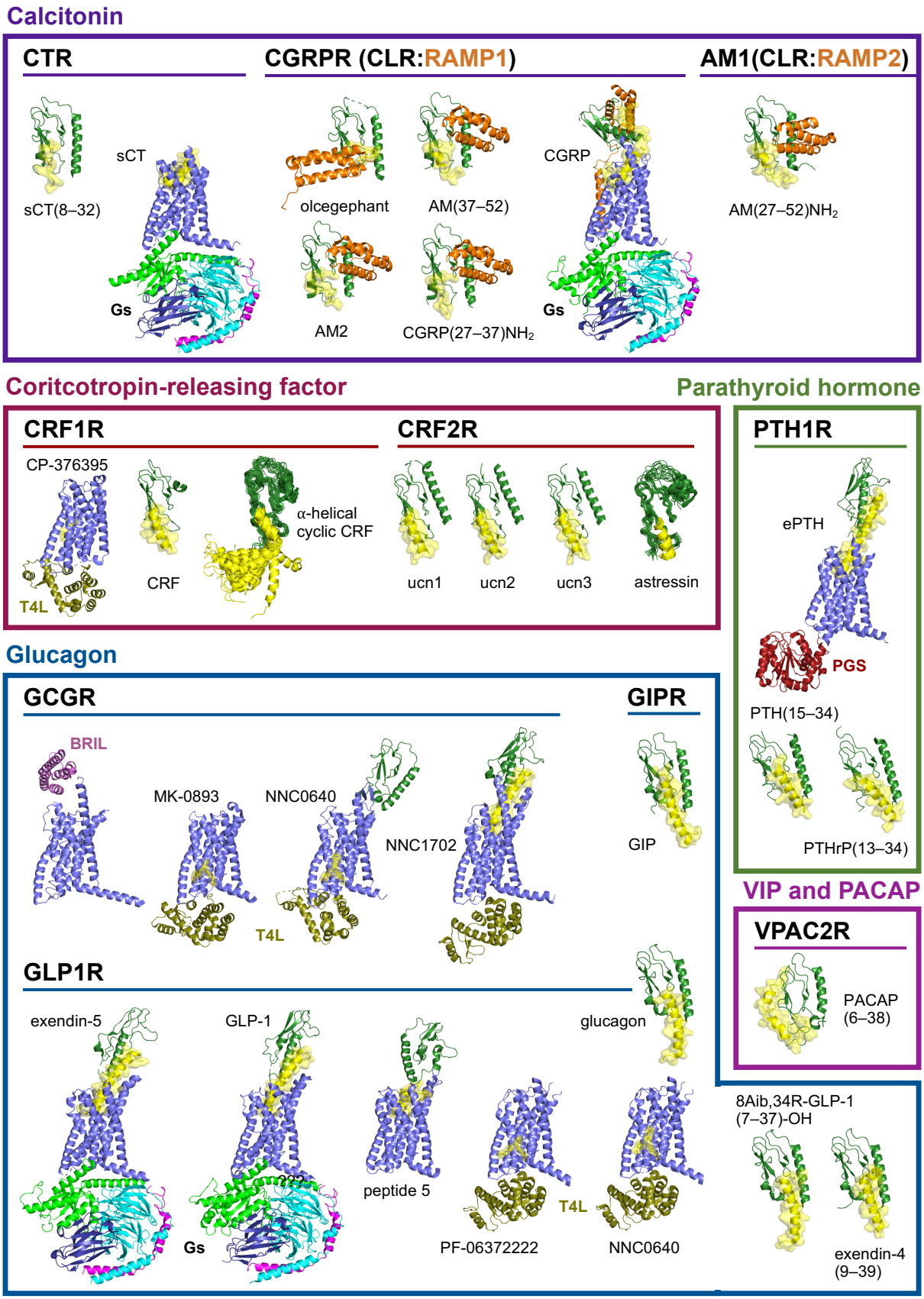
Calcitonin
CTR
CGRPR (CLR:RAMP1)
AM1(CLR:RAMP2)
sCT(8–32)
sCT
Gs
olcegephant
AM(37–52)
AM2
CGRP(27–37)NH2
CGRP
Gs
AM(27–52)NH2
Coritcotropin-releasing factor
Parathyroid hormone
CRF1R
CRF2R
CP-376395
T4L
CRF
α-helical cyclic CRF
ucn1
ucn2
ucn3
astressin
PTH1R
ePTH
PGS
PTH(15–34)
PTHrP(13–34)
Glucagon
GCGR
GIPR
BRIL
MK-0893
NNC0640
T4L
NNC1702
GIP
VIP and PACAP
VPAC2R
PACAP (6–38)
GLP1R
exendin-5
GLP-1
Gs
peptide 5
glucagon
T4L
PF-06372222
NNC0640
8Aib,34R-GLP-1 (7–37)-OH
exendin-4 (9–39)

Figure 1.2. Previously published structures of ligand-bound class B GPCRs.

Receptor ECDs are dark green. TMDs are slate blue. RAMP proteins are orange. Ligands are yellow and, apart from PDBs 2L27[46] and 2JND[48], are also displayed with transparent surface representation. Ligands, fusion proteins, and G proteins are labeled. The following structures are displayed: calcitonin receptor (CTR) – PDB 5II0[25], 6NIY[59]; calcitonin gene-related peptide receptor (CGRPR) – PDB 3N7S[26], 5V6Y[27], 6D1U[28], 4RWG[29], 6E3Y[60]; adrenomedullin 1 receptor (AM1R) – PDB 4RWF[29]; corticotropin-releasing factor 1 receptor (CRF1F) – PDB 3EHU[31], 2L27[46], 4K5Y[50]; corticotropin-releasing factor 2 receptor (CRF2F) – PDB 1U34[47], 3N96, 3N95, 3N93[32], 2JND[48]; glucagon receptor (GCGR) – PDB 4L6R[51], 5EE7[53], 5XEZ [mAb1 hidden for clarity][52], 5YQZ[56]; gastric inhibitory polypeptide receptor (GIPR) – PDB 2QKH[35]; glucagon-like peptide 1 receptor (GLP1R) – PDB 5VAI[62], 6B3J[61], 5NX2[57], 5VEW, 5VEX[54], 3IOL[37], 4ZGM[38], 3C5T[39]; parathyroid hormone 1 receptor (PTHR) – PDB 3C4M[42], 3H3G[43]; vasoactive intestinal peptide receptor 2 (VPAC2R) – PDB 2JOD[49]. Fusion proteins displayed are apocytochrome b_{562} (BRIL), T4 lysozyme (T4L), and catalytic domain of *Pyrococcus abysii* glycogen synthase (PGS). This figure was influenced by Figure 1 of de Graaf, *et al* (2017)[9].

1.3 Structural mechanism of class B GPCR activation

Previously published structures reveal that class B GPCR activation is characterized by an outward kink of the intracellular portion of TM6[54,62,63], which opens the receptor cytosolic interface for coupling to G proteins or β-arrestins (Figure 1.3). Specifically, a portion of TM6 above (C-terminal to) the conserved PxxG motif partially unwinds, and the N-terminal part of TM6 to the PxxG motif moves outward[54,62,63]. The extracellular portions of TM1 and TM7 move toward TM6 in the active state receptor. The other TM helices also exhibit shifts, mostly outward from the receptor core. These structural arrangements may contribute to the outward TM6 kink[63]. Section 2.1.3.2 describes details of PTHR activation.

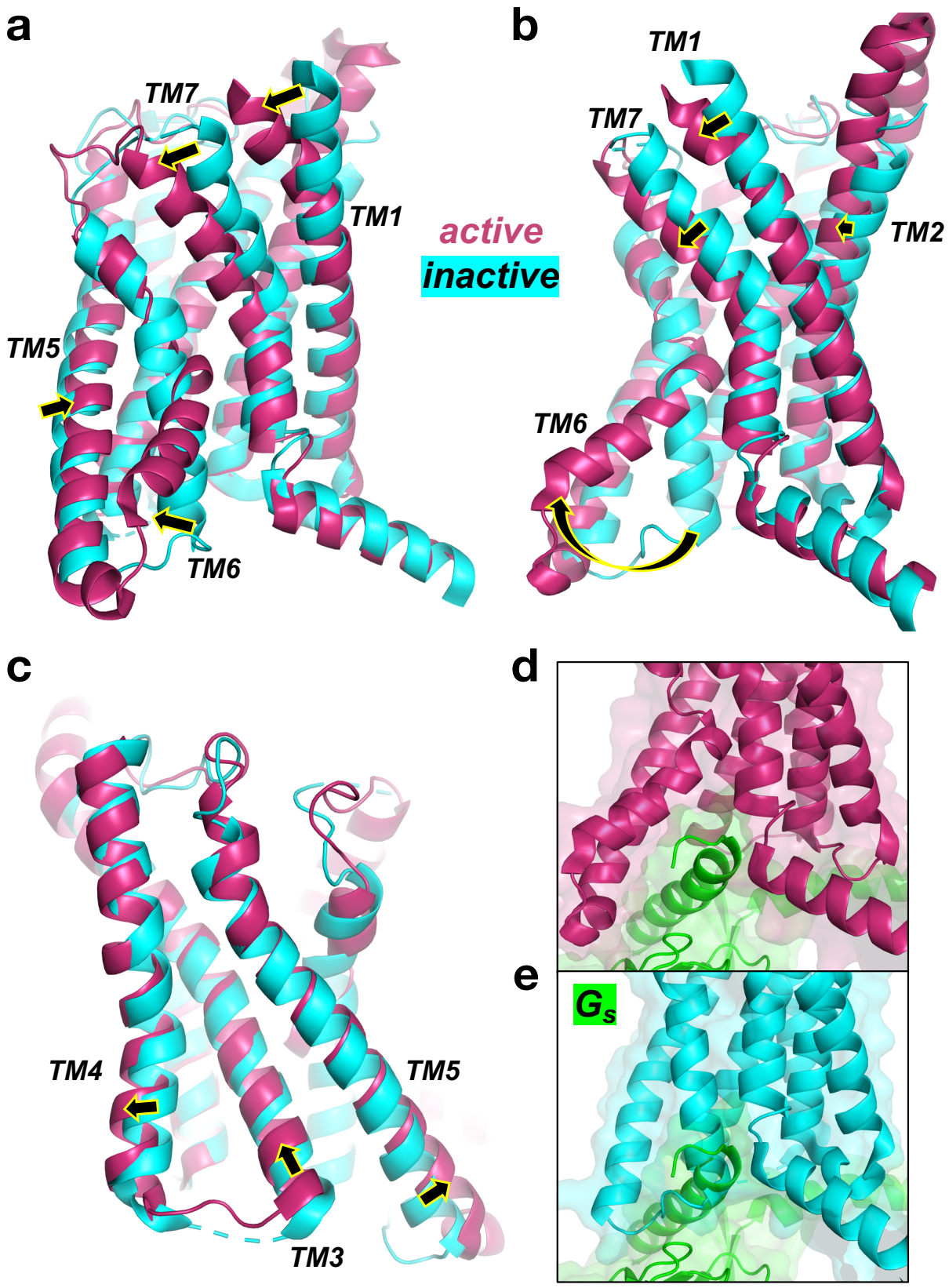
a
TM7
TM1
TM5
TM6
active
inactive
b
TM1
TM7
TM2
TM6
c
TM4
TM5
TM3
d
e
Gs

Figure 1.3. Structural signatures of class B GPCR activation.

GLP1R structures in active (warm pink, GLP1 and G_s-bound, PDB 5VAI[62]) and inactive (cyan, NAM bound, PDB 5VEW[54]) states, aligned by TMD residues 138–403. TM movement from inactive to active is shown with arrows. Ligands and the active state ECD are hidden for clarity. **a–c,** Perspectives of aligned active and inactive GLP1R structures highlighting shifts in TM helices. **d,** Stabilization of the TM6 kink by G_s (green). **e,** Overlay of inactive GLP1R and G_s structures, showing clashes between TM6 and G_s helix α5.

1.4 Structural basis of G protein activation

Structures of heterotrimeric G proteins and conformational changes during the G protein signaling cycle were determined in seminal studies published more than twenty years ago[3,64,65]. The Gα subunit consists of GTPase and helical domains (Figure 1.4a)[66]. The GTPase domain binds nucleotides and hydrolyses GTP. The helical domain forms a lid over the nucleotide binding site in the presence of nucleotides[64]. In the absence of nucleotides, the helical domain is quite flexible[67], and strong electron density for this domain has not been observed for published class B GPCR–G_s structures[59-62]. Gβ has a β-propeller structure with seven blades along with a long helical N-terminus[66]. Gγ consists of two α-helical segments, which bind to the N-terminal helix and blades 1, 4–7 of Gβ (Figure 1.4b).

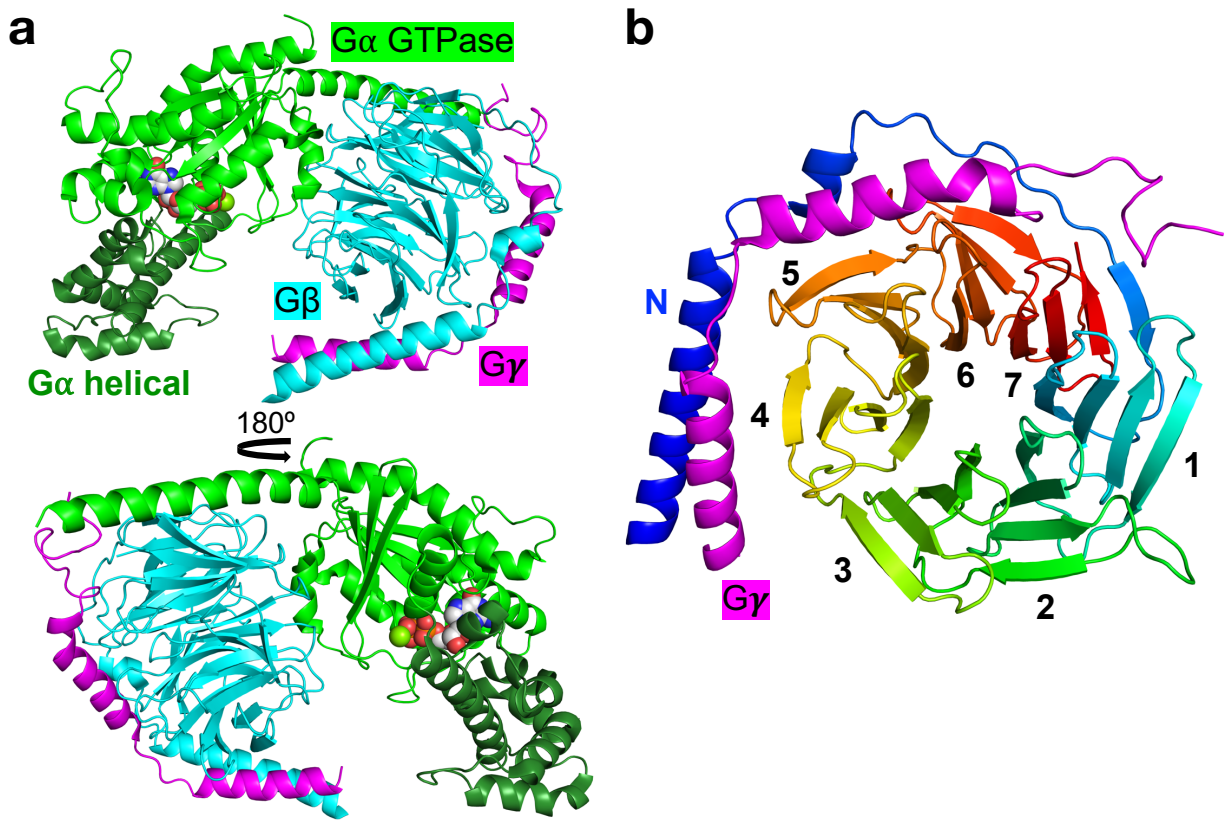

Figure 1.4. Overall architecture of heterotrimeric G proteins.

a, Structure of G_s in the GDP-bound state (PDB 6E67[68]). Gα is green, with GTPase and helical domains colored light and dark green, respectively. Gβ is cyan, and Gγ is magenta. Bound GDP and Mg^{2+} are shown as spheres.

b, Gβγ heterodimer. Gβ is colored in a rainbow spectrum, from blue (N-terminal) to red (C-terminal). Gβ β-propeller blades are numbered.

The Gα GTPase domain contains three flexible loops (termed Switches I, II, III) surrounding the nucleotide binding site[3,64]. In the heterotrimer, the Gα GTPase domain binds to Gβ primarily through its long N-terminal helix and Switch II. The binding of GTP induces conformational changes in the Switches that disrupt interactions between Gα and Gβ (Figure 1.5a, Appendix Figure 1), leading to dissociation. Current structures of GPCR–G protein complexes are solved in the nucleotide-free state and therefore represent an intermediate during GDP/GTP

exchange. A crystal structure of a β_2AR–G_s complex shows an inward movement of the nucleotide phosphate binding loop (P loop) into the binding site (Figure 1.5b). Also, the helical domain is oriented away from the nucleotide binding site, and the Switches exhibit conformations distinct from GDP- or GTP-bound states (Figure 1.5c). In the cryo-EM structures of class B GPCRs CTR and GLP1R in complex with G_s, the Gα switches, when visible, have similar conformations to those in the structure of β_2AR–G_s (Appendix Figure 2). Recent research into the β_2AR–G_s complex proposed that interactions between the receptor and the $G\alpha_s$ α5 helix propagate conformational changes to the P loop and the β6α5 loop, which interact directly with bound nucleotide, leading to GDP dissociation[68]. This study also suggested that substantial conformational changes occur during the transition from the GDP-bound state to the nucleotide-free state, including a large rotation of the $G\alpha_s$ α5 helix within the receptor core. Since the concentration of GTP is several-fold higher than GDP in cells, GTP readily binds to nucleotide-free Gα[64]. How GTP binding promotes dissociation of Gα from the receptor is not clear. It is possible that GTP binding promotes a GPCR–G protein conformation similar to the proposed GDP-bound state but the unique positions of the Switches, α5 helix, and/or other regions of Gα destabilize the complex with the receptor[66,68]. A structural dynamics study determined that the GTP-bound state is more rigid than the GDP-bound and nucleotide-free states, which may contribute to complex destabilization[69]. Crystal structures have shown effector proteins (e.g., adenylyl cyclase[70,71], GRK2[72], RGS proteins[73,74]) binding to active Gα at a concave formed by GTPase and helical domains or at the GTPase domain α3 helix and Switch II.

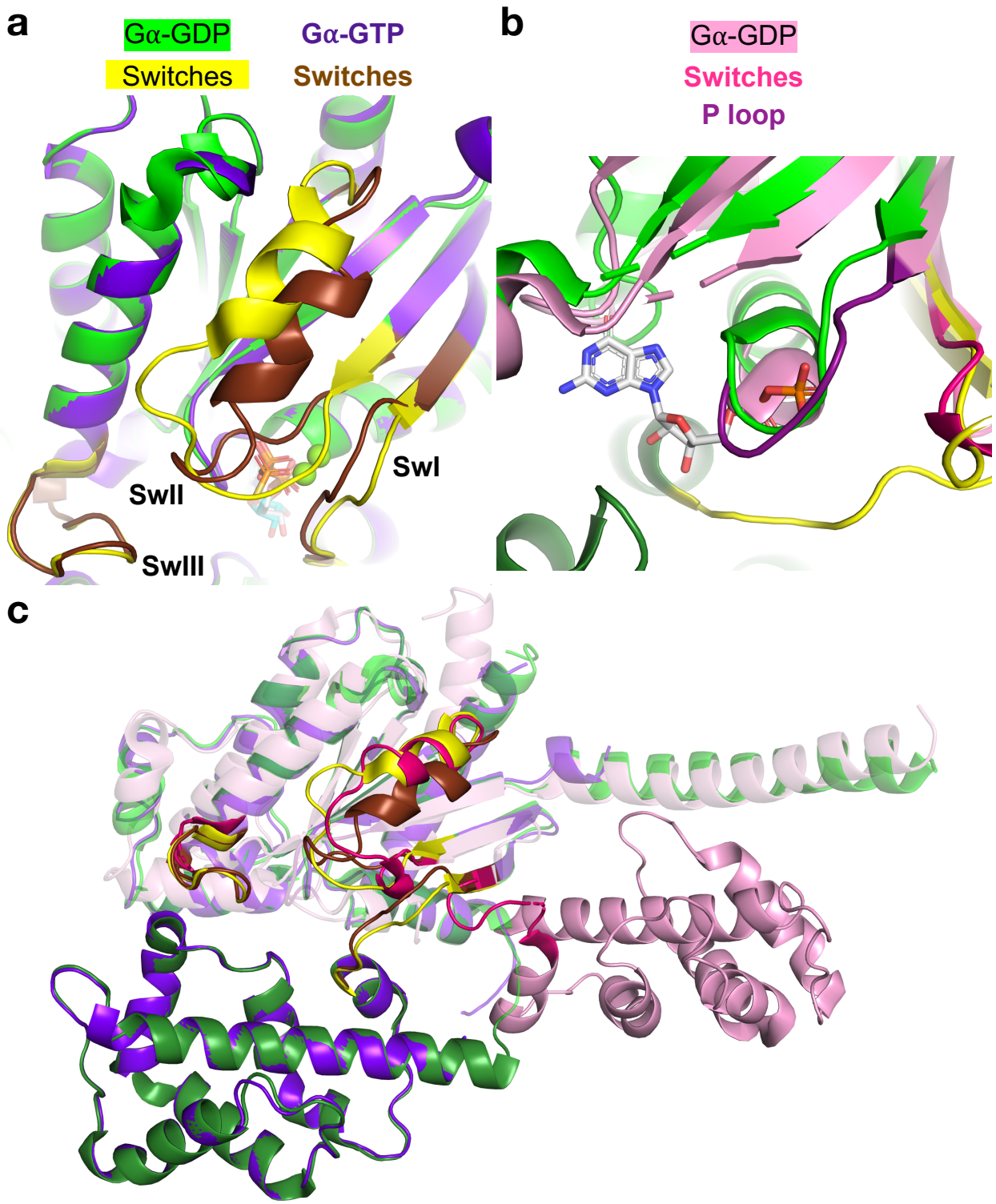

Figure 1.5. Structural differences between G protein states.

$G\alpha_s$-GDP (PDB 6E67[68]) is green, with yellow Switch loops. $G\alpha_s$-GTPγS (PDB 1AZT[65]) is purple blue, with brown Switches. Apo $G\alpha_s$ is pink (PDB 3SN6[67]), with hot pink switches. **a,** Distinct conformations of Switches I, II, and III

in $G\alpha_s$-GDP and $G\alpha_s$-GTPγS. **b,** Comparison of nucleotide binding sites in $G\alpha_s$-GDP and apo $G\alpha_s$, highlighting inward P loop (purple) movement in the absence of nucleotide. Residues 249–253 are hidden for clarity. **c,** Unique Switch conformations and helical domain position in apo $G\alpha_s$. GTPase residues, except for Switch residues, are transparent cartoon.

1.5 Structural basis of β-arrestin activation

Arrestins engage with activated GPCR at two main sites: 1) a positively charged groove located in the N-terminal domain of arrestin binds to the phosphorylated C-terminal tail (C-tail) of the receptor, 2) several regions, including a finger loop, interact with the receptor core (Figure 1.6a)[75,76]. Binding of phosphorylated receptor C-tail to arrestin displaces the arrestin C-tail (Figure 1.6b–d), disrupting a three-element interaction and a polar core that stabilize the inactive arrestin conformation (Figure 1.6e, f, PDB 1G4M[4])[70]. These changes promote an active conformation in which the N- and C-terminal domains are rotated 20° (Figure 1.6b)[69]. The arrestin finger loop adopts a helical conformation upon engagement with the receptor core (Figure 1.7a, b)[77]. Residues in the finger loop, lariat loop, and elsewhere on arrestin form hydrophobic and polar interactions with the receptor core (Figure 1.7b). In comparison with an arrestin structure bound to synthetic receptor phosphopeptide (PDB 4JQI[69]), the structure of rhodopsin-bound arrestin (PDB 5W0P[77]) exhibits unique loop conformations and a small change in the interdomain twist (Figure 1.7a).

While binding to the receptor C-tail was previously considered a prerequisite for engagement with the receptor core[75], recent research suggests that arrestin can also engage with the receptor core independently of receptor C-tail engagement[78,79]. Extensive MD simulations of rhodopsin–arrestin-1 complex determined that interactions between arrestin loops, not including

the finger loop, with receptor intracellular loops (ICL) 2 and 3 are the main mediators of arrestin activation via the receptor core (Figure 1.7c, d)[73]. Furthermore, both receptor core and phosphorylated C-tail binding trigger arrestin activation by promoting distinct conformations of arrestin C-loop and lariat loop (Figure 1.7e, f). While the molecular mechanism of arrestin C-tail displacement is not clear, the displaced C-tail binds clathrin and clathrin adaptor AP2, permitting receptor internalization[70,79-81].

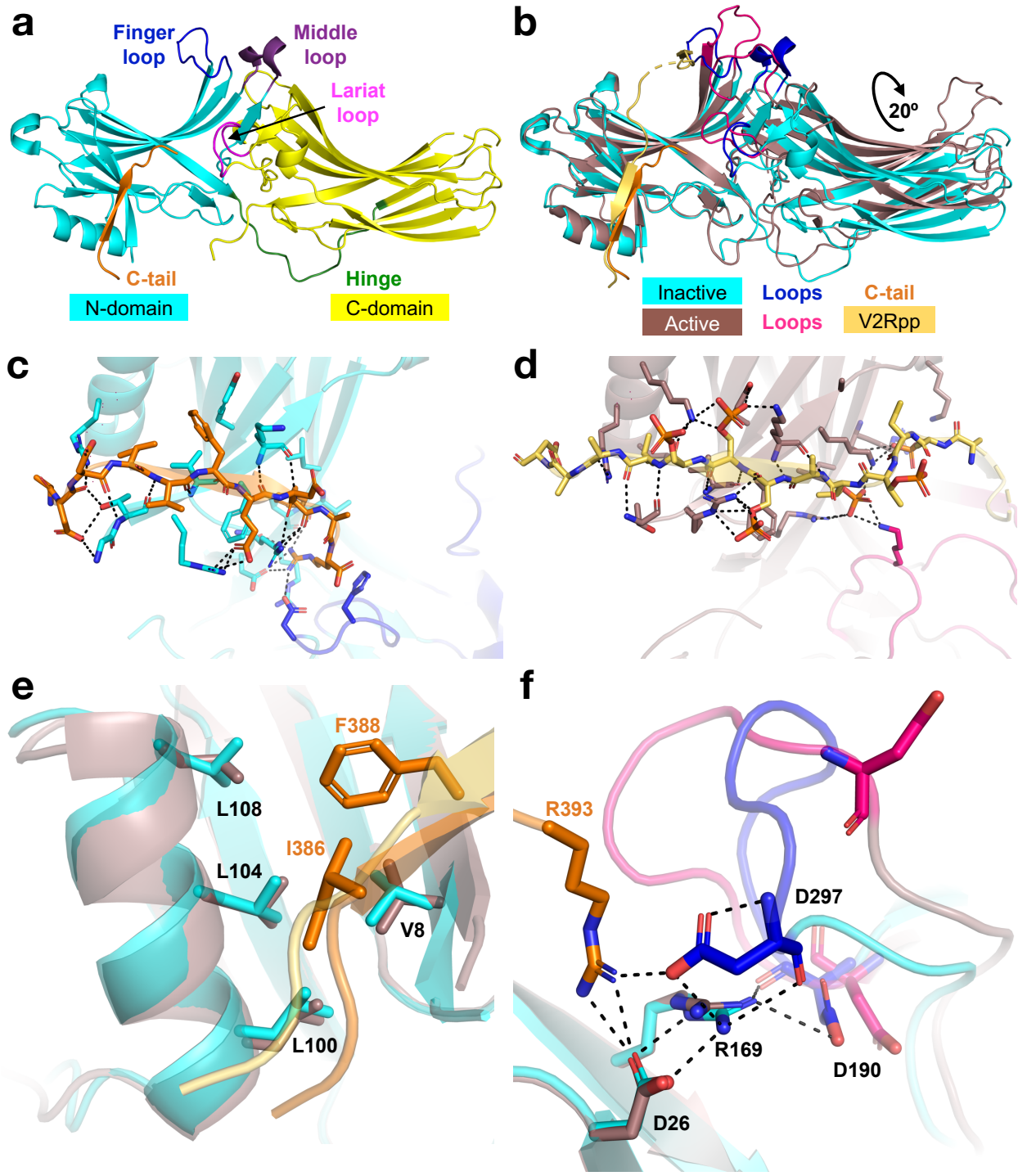

Figure 1.6. Arrestin activation by phosphorylated receptor C-tail.

a, Inactive bovine β-arrestin-1 (PDB 1G4M[4]), with major structural features labeled. **b,** Global conformational changes upon arrestin activation by V2R phosphopeptide (V2Rpp, yellow orange) (PDB 4JQI[69]), including a ~20° interdomain twist. Loops (finger, middle, lariat) of inactive and active arrestin are blue and pink, respectively. **c,** Polar

interactions (black dashes) between β-arrestin-1 C-tail (orange) and other β-arrestin-1 regions in the inactive state. **d,** Polar interactions (black dashes) between V2Rpp and active β-arrestin-1. **e,** Three-element interaction, which is disrupted in the absence of bound arrestin C-tail. **f,** Polar core in the inactive β-arrestin-1 structure, with polar interactions shown as black dashes. Conformational changes in the lariat loop upon activation disrupt the polar core.

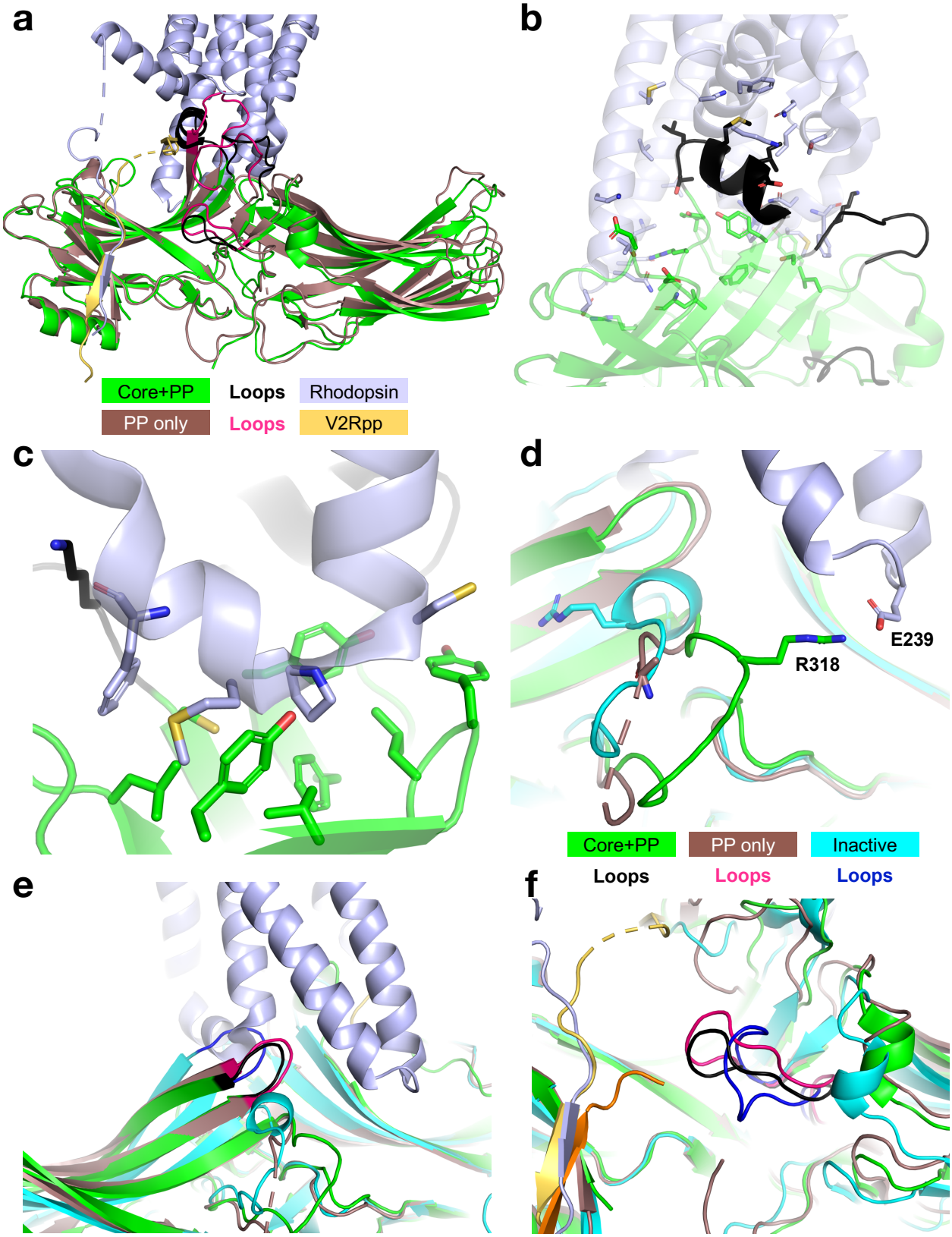

Figure 1.7. Arrestin activation by the receptor core.

a, Comparison of active arrestin structures. Rat β-arrestin-1 (brown) bound to V2Rpp (yellow orange), with loops (finger, middle, lariat) in pink (PDB 4JQI[69]). Mouse visual arrestin (green) bound to rhodopsin (light blue), with loops in black (PDB 5W0P[77]). **b,** All interactions between visual arrestin and the rhodopsin core. **c,** Interactions between arrestin and rhodopsin ICL2, which are mostly hydrophobic. **d,** Salt bridge between visual arrestin Arg318 and rhodopsin Glu239, located in ICL3. For comparison, the positions of Arg318 in inactive (cyan) and active β-arrestin-1 are also shown. **e,** C-loop conformations. **f,** Lariat loop conformations. Inactive β-arrestin-1 loops are blue.

1.6 Role of PTHR in human health

PTHR is expressed in many tissues, primarily in bone and kidney, and has two endogenous ligands: parathyroid hormone (PTH) and parathyroid hormone related peptide (PTHrP)[82-84]. PTH is secreted by the parathyroid glands upon low serum Ca^{2+} and acts on bone and kidney cells to regulate calcium, phosphate, and active vitamin D levels as well as participate in bone remodeling[22,85,86]. PTHrP mostly acts in a paracrine manner on numerous tissues, including bone, growth plate, and mammary gland during development[83,87]. While full-length PTH and PTHrP are 84 and 141 residues, respectively, synthetic N-terminal fragments (i.e., PTH(1–34) and PTHrP(1–34)) maintain full activity and are primarily used in our research[88-91]. As such, PTH and PTHrP will refer to PTH(1–34) and PTHrP(1–34), respectively unless otherwise stated.

Abnormalities in PTHR signaling cause a variety of diseases[92]. The lack of functional PTHR, such as through expression of homozygous inactivating PTHR mutants, causes fetal mortality (Blomstrand Chondrodysplasia)[93,94]. Heterozygous expression of inactive PTHR can cause enchondromatosis/Ollier disease, in which patients develop benign cartilaginous tumors[95], or primary failure of tooth eruption[96,97]. Conversely, in Jansen's metaphyseal chondrodysplasia, heterozygous constitutively active PTHR mutants are expressed, causing short-limbed dwarfism

and hypercalcemia (see Section 2.1.3.3 and Appendix E for analysis of these mutants)[98-100]. Over and under secretion of PTH causes hyper- and hypoparathyroidism, respectively[92]. Hyperparathyroidism treatment typically involves surgical removal of the parathyroid gland(s)[101]. Current treatment of hypoparathyroidism includes oral calcium, active vitamin D, and daily subcutaneous administration of recombinant human PTH(1–34) (i.e., teriparatide) or PTH(1–84)[102]. Importantly, humoral hypercalcemia of malignancy, in which malignant tumors secrete PTHrP, affects an estimated 25% of cancer patients[103].

Continuous infusion of PTH was found to promote net bone catabolism[85,104]. In contrast, intermittent PTH injections promotes net bone anabolism and has been used to treat osteoporosis and rheumatoid arthritis[84,105,106]. A synthetic analog of PTHrP, abaloparatide (ABL), was recently developed to treat postmenopausal women with osteoporosis[107]. Recent studies have demonstrated that abaloparatide is more effective than teriparatide at promoting bone formation while reducing hypercalceimic effect[107-110]. The ability of PTHR ligands to build bone versus break down bone may be related to the modes of signaling that each ligand triggers (described in Section 1.7). To better treat medical conditions related to PTHR function, a comprehensive understanding of PTHR signaling through PTH, PTHrP, and other ligands is necessary.

1.7 Non-canonical mechanism of PTHR signaling through G_s

In the classical model of GPCR signaling, G_s activation only occurs at the plasma membrane. Receptor internalization into endosomes after interaction with arrestin causes receptor desensitization[21]. PTHrP and ABL follow this signaling mode and trigger transient cAMP production at the plasma membrane (Figure 1.8)[111]. In contrast, previous work pioneered by our

lab has determined that PTH-activated receptor continues to signal through G_s after internalization into endosomes, which results in sustained cAMP production[23,111]. An endosomal complex of PTHR, β-arrestin, and Gβγ is required for endosomal cAMP production[112]. The β-arrestin stabilizes PTHR–Gβγ interactions, which permits multiple rounds of $G\alpha_s$ binding and activation. Recently, our lab demonstrated that Gβγ released upon G_q activation promotes phosphoinositide 3-kinase β conversion of $PI(4,5)P_2$ to $PI(3,4,5)P_3$, which in turn promotes β-arrestin recruitment to PTHR and formation of the ternary receptor–Gβγ–β-arrestin complex[113]. Endosomal cAMP production is blocked by a negative feedback loop in which activated PKA increases the proton pump activity of endosomal membrane-bound v-ATPase[114]. Increased endosomal acidification leads to PTH and β-arrestin dissociation from PTHR and formation of an inactive PTHR–retromer complex that traffics to the Golgi apparatus[114,115]. A synthetic, long-acting variant of PTH (LA-PTH) maintains sustained cAMP production at time points by which PTH has dissociated from the receptor[24,114]. Sustained cAMP production has important physiological consequences, as injection of LA-PTH into mice and monkeys increased serum calcium and decreased serum phosphate more dramatically and prolonged than did PTH[116,117]. Furthermore, transient cAMP production has been suggested to promote bone anabolism, which could explain the different effects of ABL and PTH on bone[118,119].

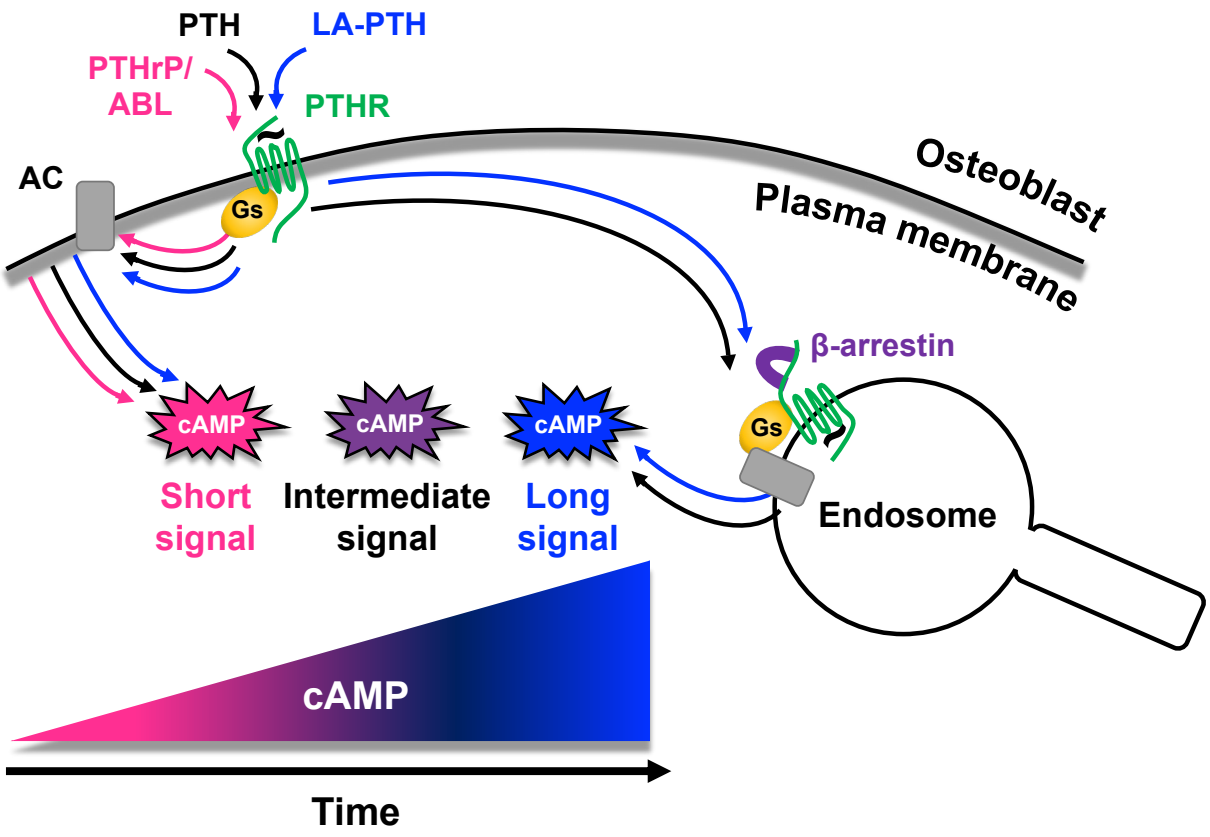

Figure 1.8. Non-canonical cAMP signaling by PTHR.

PTHrP and ABL trigger transient cAMP production from the plasma membrane. PTH and LA-PTH trigger sustained cAMP production from endosomes, with LA-PTH triggering even more prolonged cAMP production than does PTH. *Adapted from Figure 4a in Vilardaga, Jean-Alphonse, and Gardella (2014)*[111].

We hypothesize that PTHrP and PTH stabilize distinct receptor conformations to trigger these different signaling modes. The C-terminal portion of these ligands (i.e., residues 15–34) play a critical role in receptor affinity by binding to the PTHR ECD[42,43,111] (Figure 1.9). The N-terminal portion, especially the most N-terminal residues, is critical for PTHR signaling[111], as deletion of PTH Ser1 and Val2 significantly reduced cAMP production[120]. Also, PTH(7–34) was discovered to be a potent antagonist[121]. From sequence analysis, PTH and LA-PTH share multiple residues/chemical moieties that are not present in PTHrP or ABL, which may be critical for

sustained cAMP signaling in endosomes: Ile5, Met8, and the amide group on residue 10 (Figure 1.9). Indeed, using PTH[Arg^{11}](1–11) tethered to PTHR ECD, alanine substitution of Ile5 and Met8 significantly reduced cAMP production[122]. Given the potency of LA-PTH[117,119,123], this ligand was used to stabilize PTHR complex for cryo-EM (see Section 2.1)[86]. Also, the molecular basis of sustained cAMP production by LA-PTH is explored in Section 2.2.3.

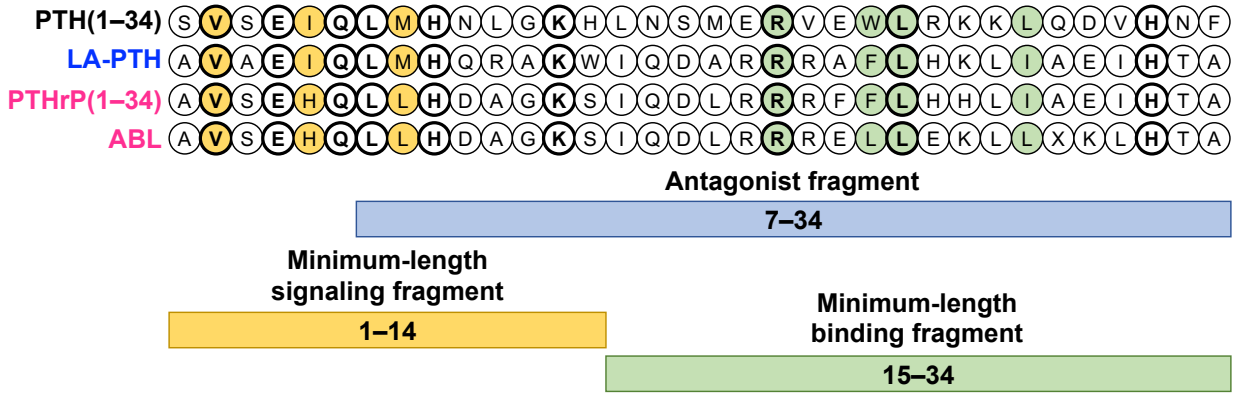

Figure 1.9. Sequence alignment of PTHR peptide ligands.

Residues conserved amongst all the listed PTHR peptide ligands are in bold. Residues critical for signaling are yellow orange, and residues critical for receptor binding are green. *Adapted from Figures 2 and 3 of Gardella and Vilardaga (2015)*[22].

1.8 Questions addressed in this dissertation

Despite our increased understanding of PTHR signaling at molecular and cellular levels, many important questions remain regarding the structural basis of steps in the signaling pathway, which we aim to address in this dissertation. How do PTHR peptide ligands recognize and bind to the receptor (Chapter 3.0)? Once bound, how do these ligands activate the receptor (Chapter 2.0, especially Section 2.1.3)? How do ligands interact with PTHR

differently to promote receptor coupling to G proteins vs β-arrestins (i.e., biased signaling, Chapter 4.0)? Finally, how is endosomal signaling terminated for PTH-bound receptor, and what causes the more prolonged cAMP production from LA-PTH-bound receptor (Section 2.2)?

2.0 LA-PTH-induced PTHR activation and G_s signaling

The following chapter describes the determination and analysis of high resolution cryo-EM structures of PTHR/G_s complex (Section 2.1). These structures were used to investigate the structural mechanism of sustained G_s signaling by LA-PTH (Section 2.2). The cryo-EM structures also provide the foundation for the research described in subsequent chapters.

2.1 Structure of PTHR/G_s complex

Section 2.1.1 describes the optimization of PTHR expression and purification as well as complex formation with stimulatory G protein (G_s), which was necessary to solve high-resolution cryo-EM structures of PTHR in complex with G_s, stabilizing nanobody (Nb35), and long-acting PTH (LA-PTH). Section 2.1.2 displays cryo-EM data, including the three published structures. Sections 2.1.1 and 2.1.2 include information from the following publication[24], of which I am an author: Li-Hua Zhao*, Shanshan Ma*, Ieva Sutkeviciute*, Dan-Dan Shen*, X. Edward Zhou, Parker W. de Waal, Chen-Yao Li, Yanyong Kang, **Lisa J. Clark**, Frederic G. Jean-Alphonse, Alex D. White, Dehua Yang, Antao Dai, Xiaoqing Cai, Jian Chen, Cong Li, Yi Jiang, Tomoyuki Watanabe, Thomas J. Gardella, Karsten Melcher, Ming-Wei Wang†, Jean-Pierre Vilardaga†, H. Eric Xu†, Yan Zhang†. Structure and dynamics of the active human parathyroid hormone receptor-1. *Science* **364,** 148-153 (2019). doi:10.1126/science.aav7942 *Contributed equally to this work. †Corresponding authors.

I contributed to preparation of the isolated PTHR–G_s complex.

Section 2.1.3 analyzes the solved structures[24], along with a previously published structure of PTHR in an inactive state[55], and was adapted from the following review article[118], of which I am co-first author: Ieva Sutkeviciute*, **Lisa J. Clark***, Alex D. White, Thomas J. Gardella, and Jean-Pierre Vilardaga. Parathyroid Hormone Receptor: Structure, Allostery, and Signaling. *Trends in Endocrinol & Metab.* **30,** 860-874 (2019). Special issue: Advancing topics in Endocrinology. doi:10.1016/j.tem.2019.07.011 *Contributed equally to this work.

I contributed to structural analysis and writing. I also generated the final figures.

2.1.1 PTHR/G_s complex optimization

The structural determinants of PTHR responsible for ligand selectivity and function are not known. This is an obstacle for the development of clinically relevant PTH analogs for bone and mineral diseases. As a first step towards understanding the structural basis for molecular recognition and receptor activation, we pursued cryo-electron microscopy of PTHR bound to LA-PTH and in complex with a stimulatory G protein G_s. For approximately 3 years, my PhD research focused on optimizing PTHR expression and purification for structural studies, including the formation of stable PTHR–G_s complex. This process required optimization of protein construct, expression through the baculovirus expression system, purification conditions, and complex formation conditions, as outlined in Figure 2.1. Section 2.1.1.1 describes the purification procedure for monomeric LA-PTH-bound PTHR. Section 2.1.1.2 details the procedure used to isolate LA-PTH-bound PTHR–G_s–Nb35 for cryo-EM structure determination[24].

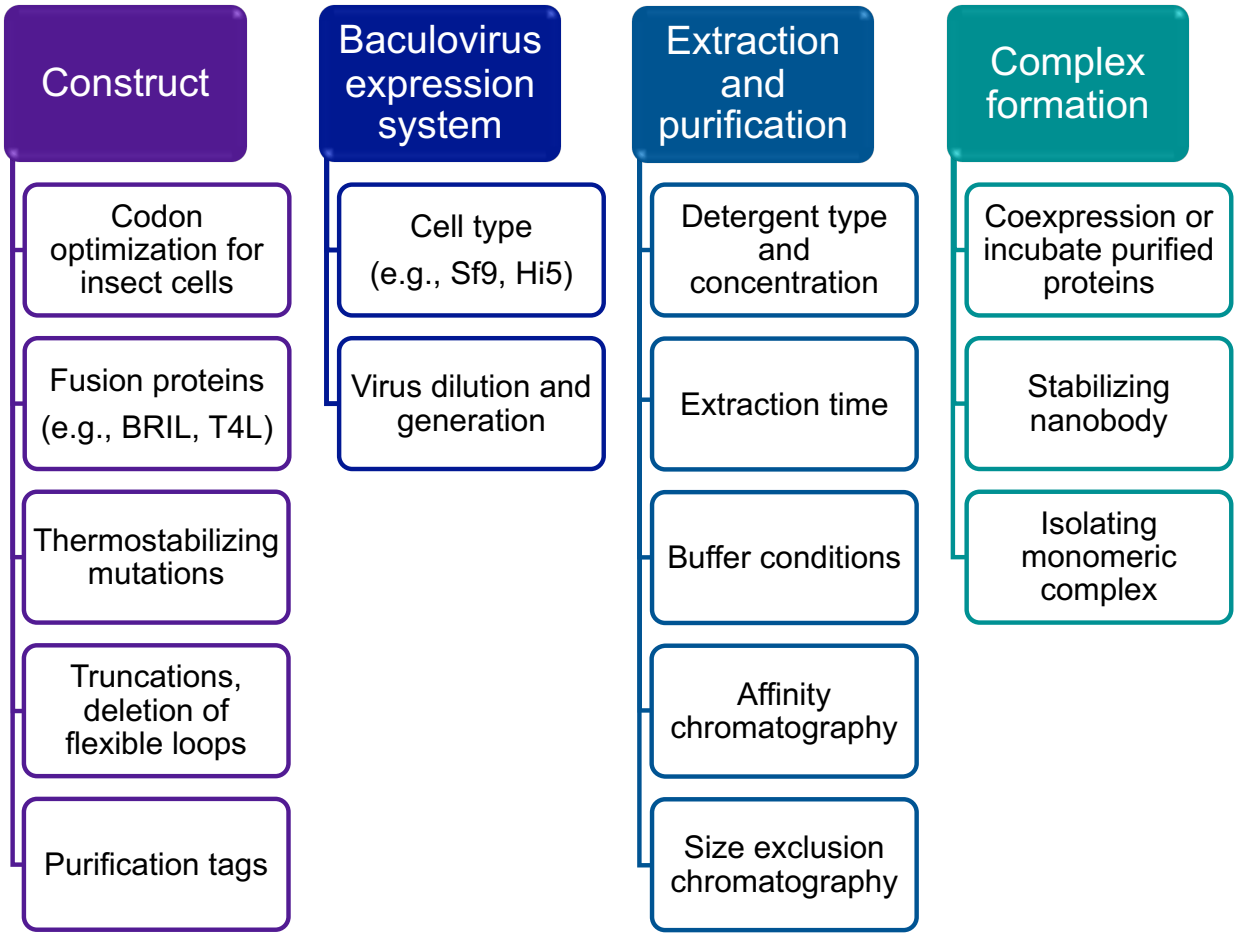

Figure 2.1. Optimization of PTHR/G_s complex purification.

For each category, factors that must be considered are listed below.

2.1.1.1 Expression and purification of cbpk-PTHR

2.1.1.1.1 Construct of cbpk-PTHR

The cbpk-PTHR construct consisted of human PTHR residues 27–483, with the highly flexible loop in receptor ECD (residues 56–105[42]) replaced with ASGSGSAS linker. To the N-terminus, the following sequences were added (starting with the most N-terminal): haemagglutinin signal peptide, Flag tag, GSGS, calmodulin binding peptide (cbp), GG, TEV

cleavage site, GG. C-terminal to the PTHR sequence, a proline then an 8xHis tag was added. The construct was cloned into pFastBac.

2.1.1.1.2 Receptor expression in insect cells

Recombinant bacmid DNA containing the cbpk-PTHR construct was isolated and used to transfect *Spodoptera frugiperda* Sf9 for P0 baculovirus generation, according to Bac-to-Bac® Baculovirus Expression System protocols (Life Technologies). P1 and P2 generations of baculovirus were subsequently produced. To express cbpk-PTHR, Sf9 culture at cell density 5-6 x 10^6 cells/mL was infected with 50X dilution cbpk-PTHR P2 baculovirus. Infected cells were cultured at 27°C, 135 rpm and harvested 72 hours post infection. Isolated cell pellets were stored at -80°C until purification.

2.1.1.1.3 Purification of cbpk-PTHR

Cell pellets were resuspended in 50 mM Tris pH 8, 100 μM TCEP, 2X protease inhibitor cocktail (PI: 10 μg/mL benzamidine, 0.69 mg/mL pepstatin A, 0.2 mg/mL leupeptin), 1 μM LA-PTH (20 mL buffer per 10 mL cell pellet) via dounce homogenization. Per 10 mL cell pellet, the following extraction mixture was added: 1 mL detergent mix (10% DMNG/10% DDM/1.2% CHS dissolved in 0.1 M Tris pH 8), 2.6 mL glycerol, 2.07 mL 5 M NaCl, 0.216 mL 5 M imidazole, 0.1 mL 1 M $CaCl_2$. Receptor was extracted by stirring for 1.5 h at 4°C. Supernatant was isolated via centrifugation and added to Ni Sepharose 6 Fast Flow resin (GE Healthcare Life Sciences) equilibrated in 25 mM HEPES pH 7.5, 400 mM NaCl, 30 mM imidazole, 1 mM $CaCl_2$, 1% glycerol, 0.007% DMNG/0.0007% CHS, 100 μM TCEP, 1X PI, 25 nM LA-PTH. After 3 h batch binding at 4°C, the Ni resin was washed, and sample was eluted in 25 mM HEPES pH 7.5, 150 mM NaCl, 0.4 M imidazole, 4 mM $CaCl_2$, 0.007% DMNG/0.0007% CHS, 25 nM LA-PTH. Ni eluate was added to αFLAG resin equilibrated in 25 mM HEPES pH 7.5, 150 mM NaCl, 4

mM $CaCl_2$, 0.007% DMNG/0.0007% CHS, 25 nM LA-PTH. After 1 h batch binding at room temperature, the αFLAG resin was washed, and cbpk-PTHR was eluted in 25 mM HEPES pH 7.5, 150 mM NaCl, 10 mM EDTA, 0.1 mg/mL flag peptide, 0.007% DMNG/0.0007% CHS, 25 nM LA-PTH. The αFLAG eluate was concentrated to < 1 mL using 50 kDa MWCO Amicon Ultra centrifugal filter (EMD Millipore) and injected to Superose 6 10/300 (Figure 2.2a, b). Superose 6 10/300 was equilibrated in 25 mM HEPES pH 7.5, 150 mM NaCl, 0.007% DMNG/0.0007% CHS, 100 μM TCEP.

2.1.1.1.4 Expression and purification of LA-PTH

We expressed LA-PTH in *E. coli* as a construct containing an N-terminal maltose binding protein (MBP). A lanthanoid binding site flanked by glycine linkers was added C-terminal to the LA-PTH sequence, followed by a Strep-tag, to enhance protein stability and purification. Culture was grown in Luria Broth at 37°C, 220 rpm, until OD_{600} ~ 0.7. Temperature was reduced to 18° C, and protein expression was induced with 0.8 mM IPTG 30 min later. Culture was grown overnight at 18°C, 220 rpm.

Harvested cells were resuspended in buffer consisting of 20 mM Tris pH 8.0, 200 mM NaCl, 1 mM EDTA, and 1X PI. Cells were lysed via sonication, and supernatant was isolated via ultracentrifugation. Supernatant was subjected to multiple rounds of amylose resin purification using a wash buffer of 20 mM Tris pH 8.0, 200 mM NaCl, 1 mM EDTA, and 1X PI. MBP-LA-PTH was eluted in 50 mM Tris pH 8, 50 mM NaCl, 2 mM $CaCl_2$, and 10 mM maltose. Amylose eluate was concentrated to > 1 mg/mL, and Tween 20 was added to 0.1%. To cleave MBP from LA-PTH, 0.4 μg enterokinase (BioVision) per mg protein was added to the sample, and sample was rotated at room temperature for 20 hr. To separate cleaved MBP from LA-PTH, sample was purified via 5 mL StrepTrap HP (GE), using a wash buffer of 25 mM Tris pH 8, 150 mM NaCl.

LA-PTH was eluted using wash buffer plus 2.5 mM D-desthiobiotin (Sigma Aldrich). Pooled eluate was then subjected to size exclusion chromatography (Superose 6 10/300, GE) and/or amylose purification (collecting cleaved LA-PTH in flow through). After SDS-PAGE analysis (Figure 2.2c), pure fractions were pooled, concentrated to > 100 μM, and aliquoted. Aliquots were flash frozen in liquid nitrogen and stored at -80°C.

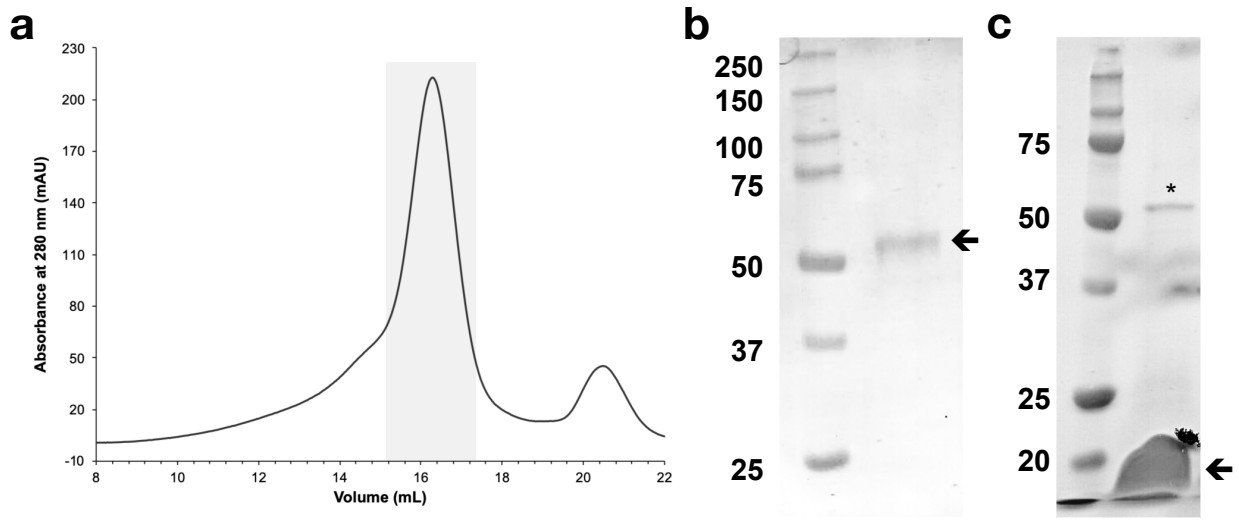

Figure 2.2. Purification of cbpk-PTHR (a, b) and LA-PTH (c).

a, Size exclusion chromatogram of cbpk-PTHR using Superose 6 10/300. Fractions highlighted in the gray box were pooled. **b,** SDS-PAGE of pooled cbpk-PTHR sample (indicated by arrow). **c,** SDS-PAGE of 30 μL 126 μM purified LA-PTH. Cleaved LA-PTH is indicated by an arrow. The proportionally small band of uncleaved MBP-LA-PTH is indicated by an asterisk.

2.1.1.2 Expression and purification of LA-PTH–PTHR–G_s–Nb35

This section contains methods from Zhao, *et al.* (2019)[24].

2.1.1.2.1 Constructs of PTHR and G_s heterotrimer

The human PTHR (residues 27–502) was cloned into pFastBac vector with two mutations (G188A and K484R), which did not affect the receptor ligand binding or activation. The native signal peptide was replaced with the haemagglutinin signal peptide (HA) to enhance receptor expression. To facilitate expression and purification, a TEV protease site and a double MBP tag followed by an 8xHis tag were inserted after the receptor C-terminus. A dominant-negative bovine $G\alpha_s$ ($DNG\alpha_s$) construct was generated by site-directed mutagenesis to incorporate mutations G226A and A366S[124]. The G226A precludes conformational changes necessary for guanine nucleotide-induced dissociation between $G\alpha_s$ subunit and $G\beta\gamma$ subunits; A366S decreases affinity for GDP. Both were reported to improve the dominant-negative effect by stabilizing interactions within the $G\alpha\beta\gamma$ complex. Rat $G\beta1$ and bovine $G\gamma2$ were cloned into a pFastBac vector. To assist G protein folding, $DNG\alpha_s$ was coexpressed with GST-Ric-8A (gift from Dr. B. Kobilka).

2.1.1.2.2 Complex expression in insect cells

The PTHR and G_s heterotrimer were coexpressed in Sf9 insect cells (Invitrogen). We prepared the viruses using the Bac-to-Bac system. Cell cultures were grown in protein-free insect cell culture medium (Expression Systems ESF 921) to a density of 2 x 10^6 cells per mL and then infected with five separate virus preparations for PTHR, $DNG\alpha_s$, $G\beta1$, $G\gamma2$, and GST-Ric-8A at equal MOIs. The infected cells were cultured at 27°C for 48 h before collection by centrifugation and the cell pellets were stored at -80°C.

2.1.1.2.3 Expression and purification of Nb35

Nanobody-35 (Nb35) was expressed in *E. coli* BL21 cells, extracted, and purified by nickel affinity chromatography as previously described[67], followed by size-exclusion chromatography using a HiLoad 16/600 Superdex 75 column.

2.1.1.2.4 LA-PTH–PTHR–G_s complex formation and purification

Cell pellets corresponding to 4 L of PTHR-G_s coexpression culture were thawed and lysed in 20 mM HEPES, pH 7.4, 100 mM NaCl, 10% glycerol, 10 mM $MgCl_2$, and 1 mM $MnCl_2$ supplemented with Protease Inhibitor Cocktail, EDTA-Free (Roche). The PTHR–G_s complex was formed in membranes by addition of 10 μM LA-PTH (Synpeptide), 10 mg Nb35–His, and 2 units of apyrase (NEB). The lysate was incubated for 2 h at room temperature, and complex from membranes was solubilized by 0.5% (w/v) lauryl maltose neopentylglycol (LMNG, Anatrace) supplemented with 0.1% (w/v) cholesteryl hemisuccinate TRIS salt (CHS, Anatrace) for 2 h at 4° C. The supernatant was isolated by centrifugation at 65,000 x g for 40 min, and the solubilized complex was incubated with Amylose resin (NEB) for 2 h at 4°C. The resin was loaded into a plastic gravity flow column and washed with 15 column volumes of 20 mM HEPES, pH 7.4, 100 mM NaCl, 10% glycerol, 10 mM $MgCl_2$, 1 mM $MnCl_2$, 0.01% LMNG, 0.01% glyco-diosgenin (GDN, Anatrace), 0.004% CHS, 1 μM LA-PTH, and 25 μM TCEP. After washing, the protein was treated overnight with His-tagged TEV protease on column. Next day, the flowthrough was collected, concentrated, and injected onto a Superdex 200 10/300 GL column (GE Healthcare) equilibrated in 20 mM HEPES, pH 7.4, 100 mM NaCl, 2 mM $MgCl_2$, 0.00075% LMNG, 0.00025% GDN, 0.0002% CHS, 1 μM LA-PTH, and 100 μM TCEP. The complex fractions were collected and concentrated individually for electron microscopy experiments. The final yield of the purified complex was ~0.5 mg/L culture (Figure 2.3, Appendix Figure 3).

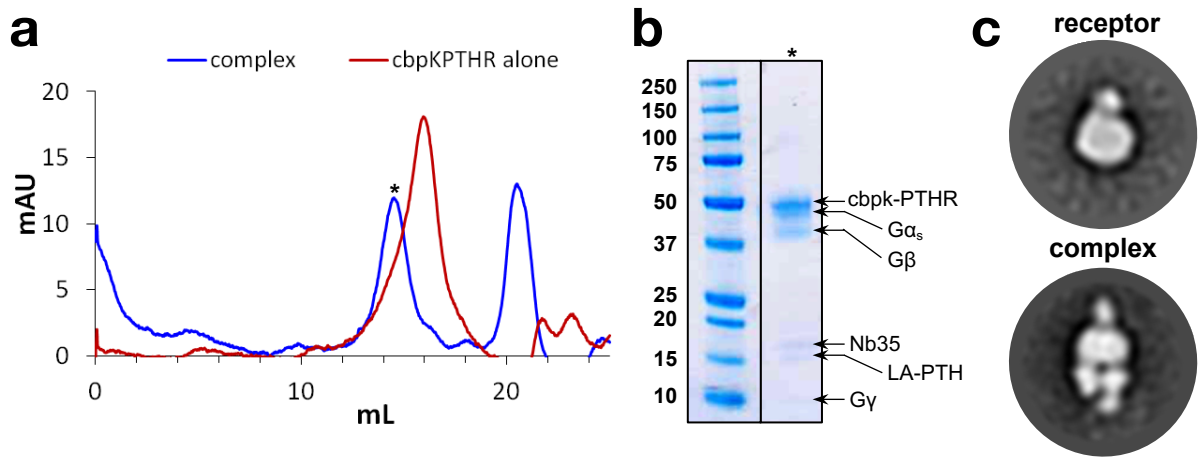

Figure 2.3. Purification and characterization of the LA-PTH–PTHR–G_s–Nb35 complex.

a, Size-exclusion chromatography elution profile of the purified complex. **b,** SDS-PAGE of the complex after size-exclusion. **c,** Two-dimensional negative stain classes of purified receptor alone (*top*) and purified complex (*bottom*).

2.1.2 Cryo-electron microscopy of PTHR–G_s complex

This section contains methods and data from Zhao, *et al.* (2019)[24].

2.1.2.1 Cryo-EM data acquisition

The purified LA-PTH–PTHR–G_s complex (3.5 to 4.0 µL at 5 mg/mL) was applied onto a glow-discharged holey carbon grid (Quantifoil R1.2/1.3) and subsequently vitrified using a Vitrobot Mark IV (ThermoFisher Scientific). Cryo-EM imaging was performed on a Titan Krios equipped with a Gatan K2 Summit direct electron detector in the Center of Cryo-Electron Microscopy, Zhejiang University (Hangzhou, China). The microscope was operated at 300 kV accelerating voltage at a nominal magnification of 29,000X in counting mode, corresponding to a pixel size of 1.014 Å. In total, 1,828 movies were obtained at a dose rate of about 7.5 e-/Å^2/s with a defocus range of -0.5 to -3.0 µm. The total exposure time was set to 8 s, with intermediate frames recorded every 0.2 s, resulting in an accumulated dose of 60 e-/Å^2.

2.1.2.2 Image processing and 3D reconstruction

Dose-fractionated image stacks were subjected to beam-induced motion correction using MotionCor2.1[125]. A sum of all frames, filtered according to the exposure dose, in each image stack was used for further processing. Contrast transfer function (CTF) parameters for each non-dose weighted micrograph were determined by Gctf[126]. Particle selection, 2D and 3D classifications were performed on a binned dataset with a pixel size of 2.028 Å using RELION-3.0-beta2[127]. Semi-automated selection yielded 1,410,056 particle projections that were subjected to reference-free 2D classification to discard false positive particles or particles categorized in poorly defined classes, producing 1,343,128 projections for further processing. An *ab initio* map generated with cryoSPARC v2 was used as initial reference model for max-likelihood-based 3D classification[128]. One stable class accounting for 538,936 particles showed detailed features for all subunits and was subsequently subjected to 3D refinement, producing a map at a global 3.0 Å resolution (Appendix Figure 4). Further 3D classification with the alignment focusing on PTHR and LA-PTH yielded three distinct conformations of the receptor extracellular layer: 211,618 particles (state 1), 134,774 particles (state 2), and 73,189 particles (state 3). The micrographs with the measured resolution worse than 3.7 Å and the total motion determined by MotionCor2.1 greater than 40 pixels were excluded from the dataset. Subsequently, all three conformations were refined individually to high resolution: 3.0 Å (state 1), 3.5 Å (state 2), and 4.0 Å (state 3). Local resolution was determined using Bsoft package with half maps as input maps[129].

2.1.2.3 Model building and refinement

The cryo-EM structure of GLP-1R–G_s–Nb35 complex (PDB 6B3J) was used as the start for model rebuilding and refinement against the electron microscopy map of the TMD and G protein regions. For the state 1 model, the ECD was built by docking the crystal structure of

PTHR ECD (PDB 3H3G) in the density map. The model was docked into the EM density map using Chimera[130], followed by iterative manual adjustment and rebuilding in COOT[131]. Real space and Rosetta refinements were performed using Phenix[132]. The model statistics were validated using MolProbity[133]. Structural figures were prepared in Chimera and PyMOL (https://pymol.org/2/). The final refinement statistics are provided in Appendix Table 2. The extent of any model overfitting during refinement was measured by refining the final model against one of the half-maps and by comparing the resulting map versus model FSC curves with the two half-maps and the full model.

The state 2 model was built by docking the first model into the second map. The receptor TMD and all the G protein subunits nicely fit in the second map, except the ECD, which was fit in the density by performing rigid body refinement with other parts of the complex fixed. The whole model was refined using phenix.real_space_refine. All residues were checked for density fitting, Ramachandran angles, and rotamers. The refined state 2 model has good density fitting and model geometry.

The state 3 model was built by the same way as the state 2, using the state 1 model as the initial model to be docked in the density map. The state 1 model fit in the map of conformation 3 well, apart from the ECD domain, which was re-oriented by rigid-body shifting. The whole model was refined using phenix.real_space_refine. All residues were check for density fitting, Ramachandran angles, and rotamers. Note that alternative models are possible for the map of state 3, with its relatively low resolution. The current model represents the most likely model based on the density map and the orientation of the LA-PTH helix.

2.1.2.4 Final models of PTHR–G_s

Figure 2.4 displays the three final refined models of PTHR–G_s complex, along with their corresponding electron density maps. Each model exhibits a unique orientation of the receptor ECD with respect to the TMD (Figure 2.5, Figure 2.6).

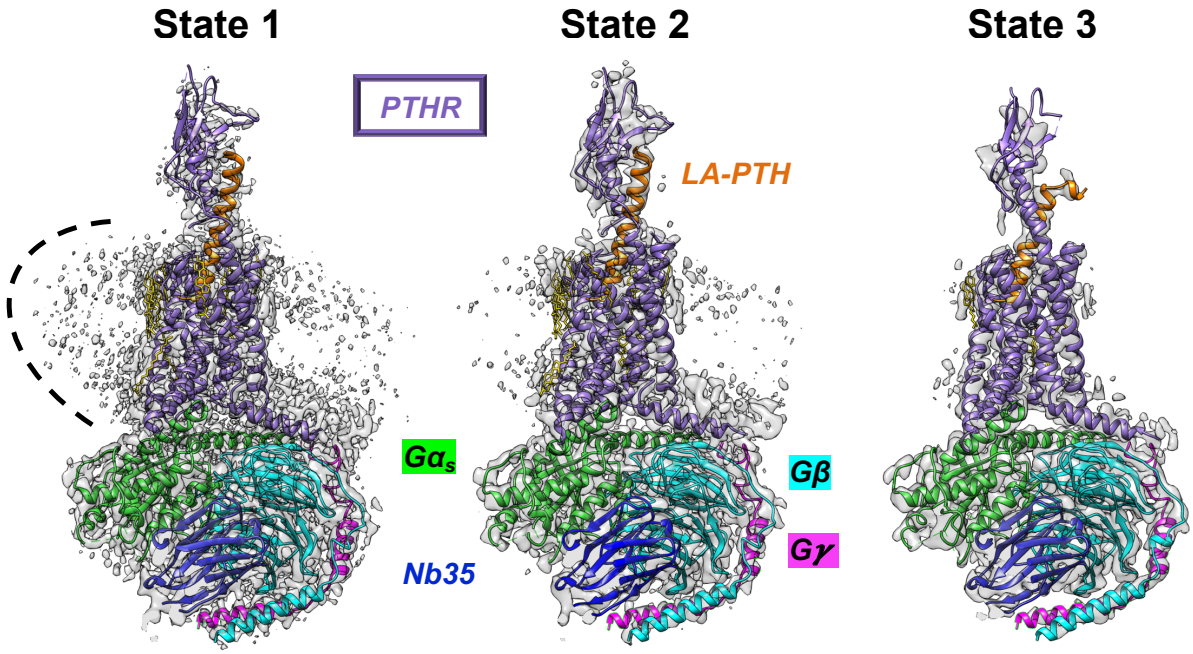

Figure 2.4. High-resolution cryo-EM structures of LA-PTH–PTHR–G_s–Nb35.

Electron density maps for each state are also shown, with contour levels set to 0.02. Structural lipids are shown as yellow sticks. Images were generated in Chimera[130].

2.1.3 Analysis of PTHR structures

2.1.3.1 Near atomic structures of the PTH receptor signaling complex

The highest resolution structure of the PTHR complex (state 1) revealed an extensive binding interface of the LA-PTH with the PTHR as well as the contacts of the receptor's cytosolic core with the G_s protein (Figure 2.5). The LA-PTH is bound to the PTHR as a continuous α-helix,

with the C-terminal fragment of the peptide (residues 16–34, ^{C}LA-PTH) interacting with the N-terminal domain of PTHR (PTHR^{ECD}) in a "hot-dog in a bun" mode, closely resembling the crystal structure of PTHrP-bound PTHR^{ECD} [42]. The N-terminal fragment of LA-PTH (residues 1–15, ^{N}LA-PTH) is inserted deep into the core of the receptor transmembrane domain (PTHR^{TMD}) and serves as a trigger for the receptor activation. Such binding mode of LA-PTH superposes the PTHR^{ECD} perpendicularly to the cell membrane plane in a structurally dynamic manner, as indicated by extensive cryo-EM data analysis (Figure 2.6a). G_s primarily interacts with PTHR through C-terminal α5 helix of the Gα subunit, and the Gβ subunit makes additional contacts with ICL1 and helix 8 (H8) of the receptor (Figure 2.5b).

While the 15–34 segment of PTH is responsible for an initial high affinity receptor binding via a rapid interaction with PTHR^{ECD} that only depends on hormone concentration, the N- terminal peptide portion contains the signaling moieties and binds the PTHR^{TMD} with slower kinetics[22]. Thus, PTHR activation has been described by a two-step model: first, the C-terminal peptide fragment associates with the PTHR^{ECD}, and second, the low affinity N-terminal peptide fragment binds to PTHR^{TMD}, which triggers receptor activation and intracellular signaling events. The three structures of the LA-PTH–PTHR–G_s complex, differing mostly by the positioning of LA-PTH on PTHR^{ECD}, indicate that this domain is more dynamic than initially thought and permits us to revise the two-state model of PTHR activation (Figure 2.6a). The description of the PTHR complex state 1 structure is consistent with those seen for structures of other family B GPCR structures, where the ligand peptide adopts an α-helical conformation[62,134,135]. The other two LA-PTH–PTHR–G_s states show a release of the C-terminal portion of the ligand interacting with PTHR^{ECD}, while the position of the N-terminal portion remains unchanged (Figure 2.6a).

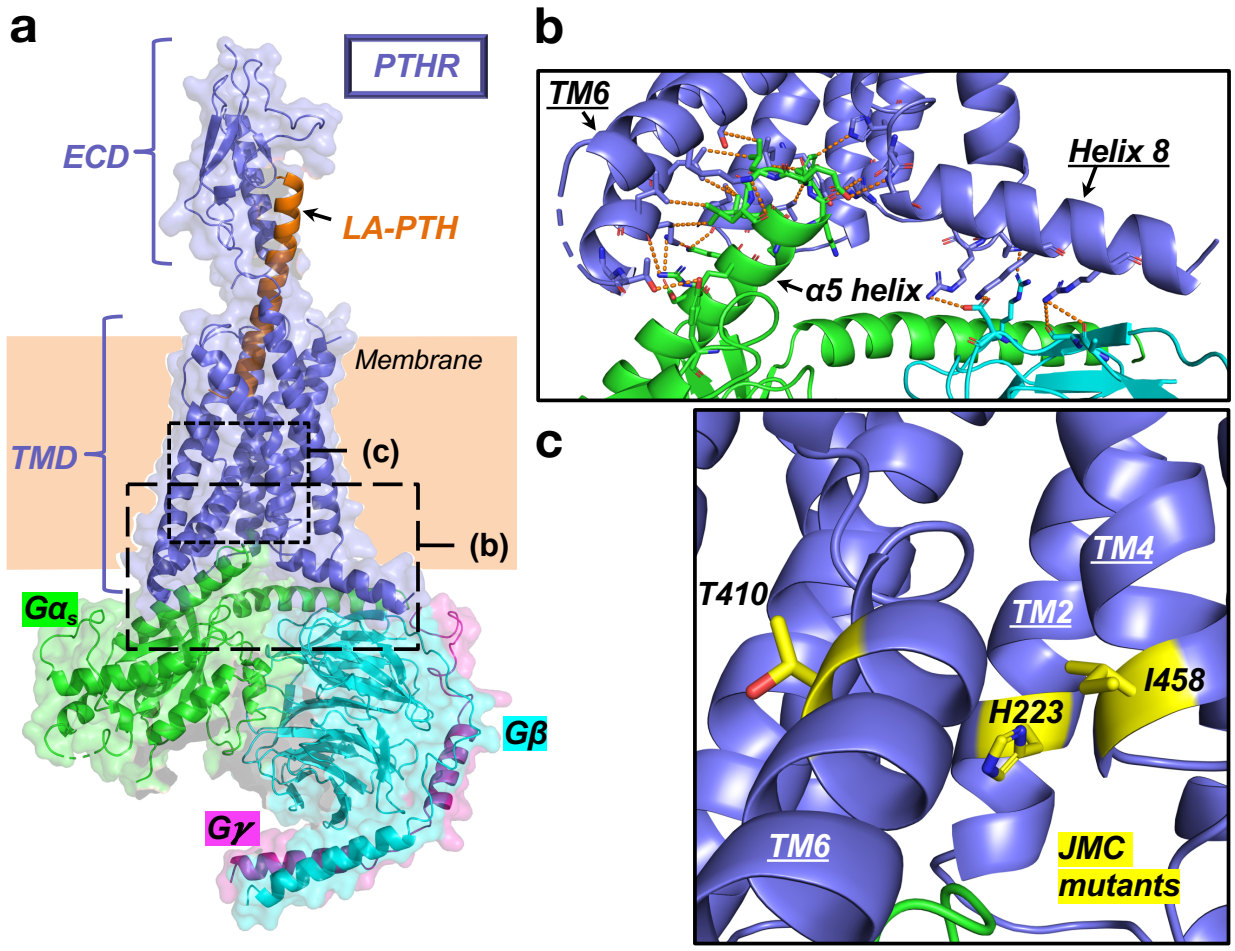

Figure 2.5. Cryo-EM structure of active state PTHR bound to LA-PTH and in complex with G_s heterotrimer.

a, Overall structure of the complex in cartoon and transparent surface representation; PTHR, LA-PTH, $G\alpha_s$, Gβ, and Gγ are shown in purple, orange, green, cyan, and magenta, respectively. Light orange rectangle represents the putative membrane bilayer boundaries. **b,** Close-up view of G_s heterotrimer–PTHR interaction interface. The interacting residues are shown as sticks, and contacts are represented by orange dashed lines (polar interactions ≤ 4 Å, hydrophobic interactions ≤ 5 Å). **c,** PTHR mutations causing Jansen's metaphyseal chondroplasia (JMC). The receptor, $G\alpha_s$, Gβ, and Gγ are shown in slate blue, green, cyan, and magenta, respectively. Wild-type residues His223, Thr410, and Ile458 are shown as yellow sticks. Single point mutation to Arg223, Pro410, or Arg458 causes the disease.

Structurally, the closer proximity of Asp137 and Glu177 to LA-PTH residue Asp17 in state 3 may induce dissociation via negative charge repulsion (Figure 2.6b). This observation coupled to early kinetics studies of the PTHR activation suggest that the C-terminal portion of the peptide can repeatedly and rapidly bind and unbind from the $PTHR^{ECD}$ before its N-terminal portion can be fully released from the $PTHR^{TMD}$, thus enabling persistent activation. This extended view of the two-state model for PTHR could be relevant to other class B GPCRs to explain how prolonged signaling via G_s occurs. Prolonged signaling via G_s triggered by LA-PTH is further explored in Section 2.2.3.

2.1.3.2 Structural mechanism of PTH receptor activation

The structural signature of GPCR activation is the relative separation of the cytoplasmic parts of transmembrane helices 3 and 6 (i.e., TM3 and TM6), which involves induction of a sharp kink in the middle of TM6 (Figure 2.7a). The outward movement of TM3 and TM6 is a prerequisite for G protein coupling and activation, as it opens the cytosolic cavity of the receptor to permit the insertion of the C-terminal α5 helix of $G\alpha_s$. This interhelical movement has been verified for both class A (rhodopsin-like) and class B (secretin receptor-like) GPCRs via multiple approaches, including electron paramagnetic resonance and mutagenesis[136-138]. In the case of PTHR, constraining the movements between TM3 and TM6 using engineered inter-transmembrane zinc ion (Zn^{2+}) bridges blocked G protein activation in response to PTH[137,139]. The cryo-EM structures of active PTHR–G_s complex reveal two major triggers of ligand-mediated PTHR activation: 1) interaction of peptide hormone residues 1–3 with receptor TM6, and 2) expansion of TMD polar network by hormone residue Glu4 (Figure 2.7b). Previous research has demonstrated that N-terminal truncations of PTH as short as two amino acids

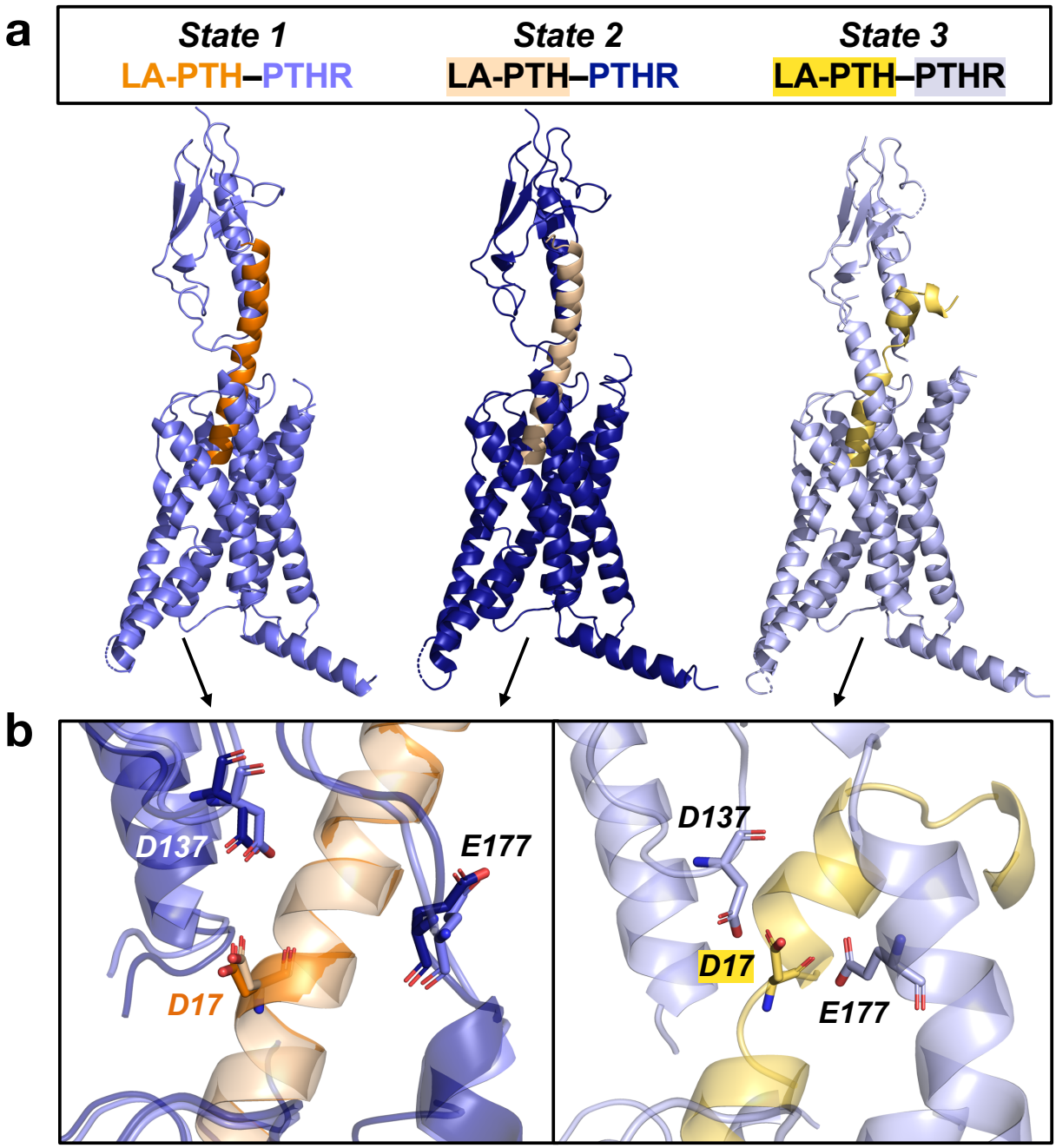

Figure 2.6. Structural dynamics of LA-PTH–PTHR complex.

a, Three distinct conformational states of LA-PTH–PTHR complex obtained from cryo-EM data analysis. PTHR and LA-PTH are shown as different shades of blue and orange, respectively. The oscillation of the N-terminal domain of PTHR ($PTHR^{ECD}$) is evident, while the TMD core shows higher degree of stability, likely due to tight binding of ^{N}LA-PTH. Notably, state 3 captures the event of partial dissociation of ^{C}LA-PTH from $PTHR^{ECD}$ (yellow helix). **b,** Potential mechanism of ^{C}LA-PTH dissociation, with LA-PTH Asp17 and PTHR Asp137 and Glu177 shown as sticks. *Left,* states 1 and 2. *Right,* state 3.

significantly reduce or eliminate biological activity of the hormone, making truncated variants potent antagonists[140,141]. Indeed, the cryo-EM structure revealed that LA-PTH residues 1–3 push against TM6 (Figure 2.7c), stabilizing the kink and outward movement of TM6. In a recent crystal structure of thermostabilized, inactive-like PTHR with modified PTH (ePTH), the N-terminal tip of ePTH faces TM5 (Figure 2.7d–f)[55]. Given that the amino acid sequence of ePTH(1–3) is structurally similar to that of LA-PTH(1–3) (Figure 2.7g), the different binding position of ePTH may reflect an intermediate pose prior to receptor activation. The "inactive" receptor conformation is likely forced by protein modifications used to favor receptor crystallization: 1) thermostabilizing PTHR mutations such as Y191C in TM1, K240M in TM2, and Q440R in TM6, and 2) fusion of 196-residue domain of *Pyrococcus abysii* glycogen synthase (PGS) to PTHR ICL3, which connects TM5 and TM6. The PGS may have promoted a straighter conformation of TM6 to favor crystal packing.

Appendix Table 3 lists the interactions between LA-PTH and PTHR in all three cryo-EM structures. The LA-PTH–PTHR–G_s structure reveals that LA-PTH residue Glu4, a conserved residue among peptide hormone ligands of PTHR (Figure 1.9, Figure 2.7g), forms two key polar interactions with Tyr195 and Arg233 (Figure 2.7b). These interactions lead to the formation of a more extensive hydrogen bond network within the $PTHR^{TMD}$ that opens the receptor's cytosolic cavity. The same polar interactions of Glu4 with Tyr195 and Arg233 are also observed in the structure of thermostabilized ePTH–PTHR complex (Figure 2.7d, e). However, these interactions lead to the formation of a sparser polar network that fails to switch the receptor to its active state, possibly due to thermostabilizing mutations and PGS domain insert in ICL3. In the inactive structure, the positions of the peptide and the $PTHR^{ECD}$ are both altered relative to those of the

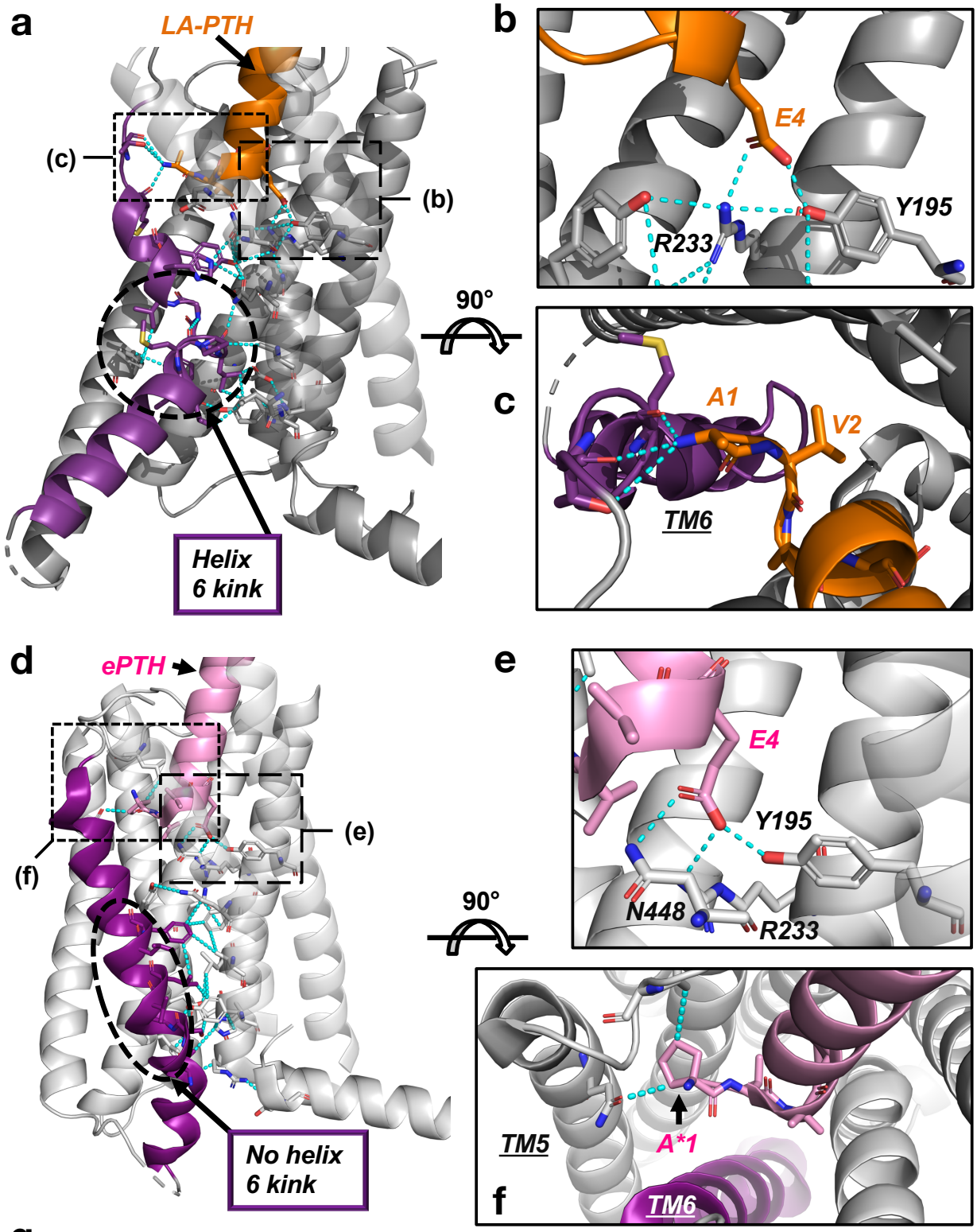

g

PTH	S V S EIQLMHNL GKH	LNSM ERVEWLRKKLQDVHNF
ePTH	***A****VA§ EIQLMHQ***R***§AKW	LNS***L***^{n} ERVEWLRKKLQDVHNY
LA-PTH	A V A EIQLMHQR AKW	I QDA RRRAF LHKL I AE I HTA

Figure 2.7. Structures of PTHR in active (A–C) and inactive (D–F) states.

a, Residue interaction network within the $PTHR^{TMD}$ core of the active structure. Interacting residues (with interaction distances ≤ 4 Å) are shown as sticks, and contacts are represented by cyan dashed lines. LA-PTH and TM6 of the receptor are shown in orange and purple, respectively. TM1 and TM7 are transparent cartoons for clarity. **b,** Close-up view demonstrating the key activating polar interactions of Glu4 of LA-PTH with Tyr195 and Arg233 of the receptor. **c,** Close-up top view showing the position and interaction of the N-terminal tip of LA-PTH with receptor TM6. **d,** Amino acid interaction network within the $PTHR^{TMD}$ core of the inactive structure. Interacting residues (with interaction distances ≤ 4 Å) are shown as sticks, and contacts are represented by cyan dashed lines. LA-PTH and TM6 of the receptor are shown in pink and purple, respectively. TM1 and TM7 are transparent cartoons for clarity. **e,** Close-up view demonstrating the key activating polar interactions of Glu4 of ePTH with Tyr195 and Arg233 of the receptor. The failure to switch the receptor to its active state is likely due to multiple thermostabilizing mutations in the receptor. Glu4 makes an additional contact with Asn448 in the ePTH–PTHR structure. **f,** Close-up top view showing the position and interaction of the N-terminal tip of ePTH with the TM5 of the receptor. **g,** Sequence alignment of PTH, ePTH, and LA-PTH. Residues interacting with the $PTHR^{TMD}$ are highlighted in lilac. Unnatural amino acids of ePTH: A^{*} – aminocyclopentane-1-carboxylic acid, $A^{\S}$ – α-aminoisobutyric acid, $R^{\S}$ – homoarginine, L^{n} – norleucine.

active structure (Figure 2.8a). However, the overall conformations of the $PTHR^{ECD}$ are identical in the two structures (Figure 2.8b), indicating that the linker (residues 171–179) connecting the $PTHR^{ECD}$ and the $PTHR^{TMD}$ play a key role in the flexibility of the $PTHR^{ECD}$.

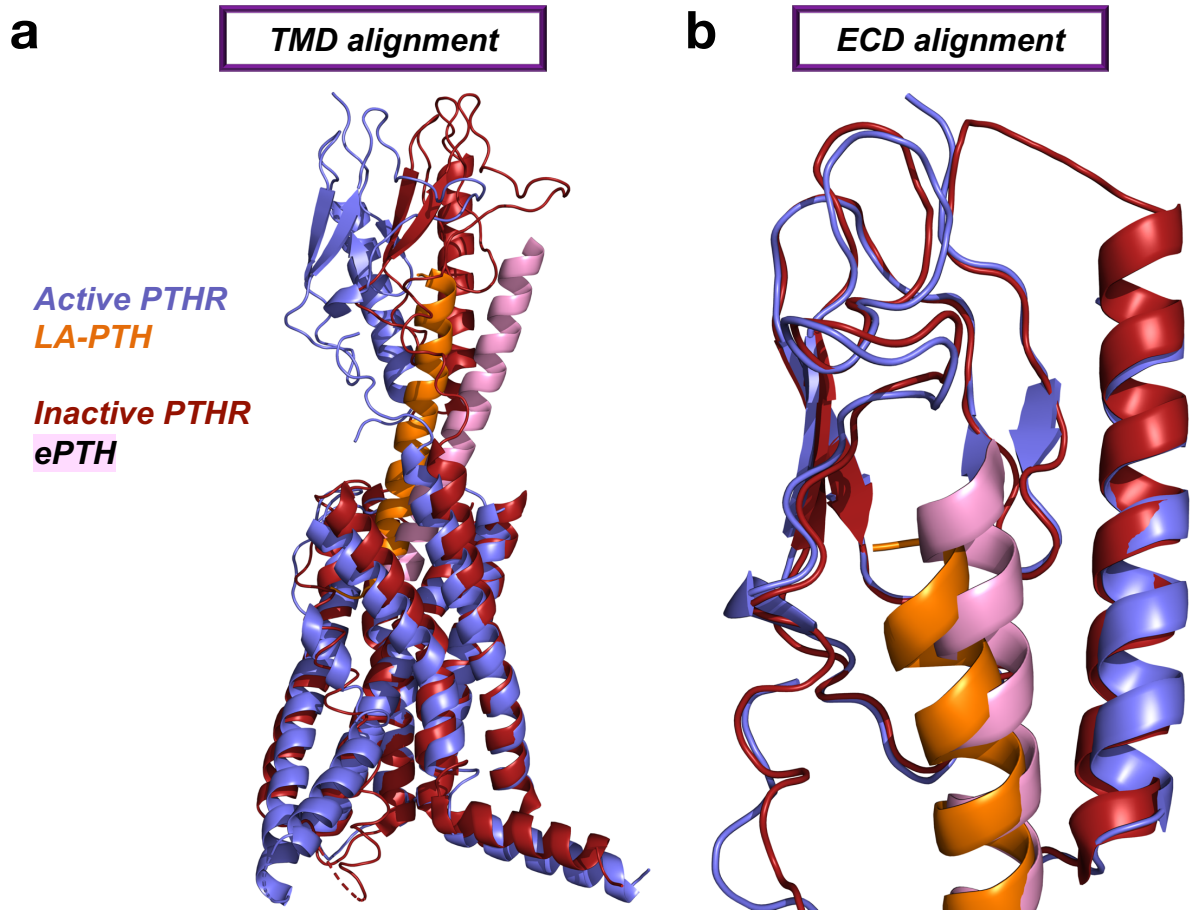

Figure 2.8. Overlay of inactive and active PTHR structures.

The receptor and ePTH of the inactive structure are colored dark red and pink, respectively. The receptor and LA-PTH of the active structure are colored slate blue and orange, respectively. **a,** Alignment of the two structures by $PTHR^{TMD}$ residues 180–460. **b,** Structural alignment by $PTHR^{ECD}$ residues (27–168), showcasing similar $PTHR^{ECD}$ conformations between the two structures.

2.1.3.3 Structural basis for bone/mineral metabolism diseases caused by mutations in PTHR and G_s

Recently published structures of PTHR give insight into the molecular basis for altered PTHR signaling in bone/mineral diseases. Numerous heterozygous loss-of-function mutations have been identified in patients with primary failure of tooth eruption, consistent with a prominent

role for the PTHR/PTHrP signaling system in tooth bud development[142,143], while in a compound heterozygous state, such PTHR loss-of-function alleles result in a rare neonatal-lethal condition called Blomstrand's chondrodysplasia[144]. Such loss-of function mutations, for example, P132L, which impacts a highly conserved proline in the $PTHR^{ECD}$, presumably disrupt proper receptor folding and/or function.

A previous study found that chronic hypocalcemia occurring in patients with idiopathic hypoparathyroidism can be caused by a single point mutation in residue 25 of PTH (PTH-R25C) that cannot engage endosomal PTHR signaling as well as blood Ca^{2+} elevation in animals[145]. Our group determined that PTH-R25C eliminated positive allosteric effects of Ca^{2+} on PTHR signaling[89]. Ligand residue 25 in the LA-PTH–PTHR active structures and in the ePTH–PTHR inactive structure, faces the flexible linker connecting the $PTHR^{ECD}$ and the $PTHR^{TMD}$ (Appendix Figure 5a, b). The ePTH Arg25 side chain forms a polar interaction with the main chain carbonyl of PTHR Leu174 (Appendix Figure 5b). Based on the active PTHR structures, substitution of LA-PTH His25 to Arg25 would not permit interaction with Leu174, and no other interactions are visible. Mass-spectrometry analysis determined that acidic residues in PTHR ECL1 coordinate Ca^{2+} [89]. Although the ECL1 did not display clear electron density in near-atomic structures of PTHR, ECL1 is long and flexible and could reach Arg25. In our current model, PTH Arg25 interacts with glutamate residues in the ECL1 to promote coordination of Ca^{2+} (Appendix Figure 5c, d). Later, MD simulations of PTH–PTHR (in absence of Ca^{2+}, see Section 2.2.5.5 for methodology) display Arg25 primarily facing the extracellular solvent (Appendix Figure 6). However, some polar interactions are captured (Appendix Table 4), including between Arg25 and ECL1 residues Glu259 and Glu260 in one simulation. Coordination of Ca^{2+} by ECL1 could move the acidic residues closer to Arg25,

which then stabilize the coordination. Alternatively, Ca2+ coordination could influence PTH peptide binding, promoting a unique position of PTH within the $PTHR^{TMD}$ to enhance signaling.

Jansen's metaphyseal chondrodysplasia, characterized by short-limbed dwarfism and hypercalcemia, is caused by constitutively active PTHR mutants: H223R, T410P, or I458R located on TM2, TM6, and TM7, respectively (Figure 2.5c)[98-100]. Based on the active state PTHR structure, the H223R and I458R mutations would generate clashes with residues in TM6. We propose these clashes would promote the opening of the receptor cytosolic core in the absence of agonist. Similarly, we anticipate that the T410P mutation triggers a kink in TM6 that is independent from the agonist-induced polar interactions (Figure 2.5c, Figure 2.7a). The mechanism of constitutive PTHR activation by H223R mutation is further investigated using MD simulations in Appendix E.

Lastly, a single point mutation in $G\alpha_s$, F376V, was recently identified in two young patients presenting with skeletal abnormalities and gonadotrophin-independent precocious puberty[146]. This mutation increases signaling independently of PTHR ligands. In the crystal structure of GTPγS-bound $G\alpha_s$, Phe376 engages in extensive contacts with nonpolar residues in α1, α5 helices and β1, β2, β3 strands (Appendix Figure 7a, c). In the structure of the PTHR–G_s complex, the α5 helix has straightened out and rotated to engage with the cytosolic core of the receptor. Now, Phe376 engages in a sparser network of hydrophobic contacts with residues in β2 and β3 strand (Appendix Figure 7b). Mutation from bulky nonpolar phenylalanine to smaller nonpolar valine would disrupt these interactions in both $G\alpha_s$ states and is anticipated to also indirectly disrupt the GDP/GTP binding site, as supported by previous modeling studies[146].

Disruption of the $G\alpha_s$ catalytic site could enhance GDP/GTP exchange independently of ligand-mediated PTHR activation, although this remains to be tested experimentally.

2.2 Molecular insights into sustained endosomal PTHR/G_s signaling by LA-PTH

Both PTH and LA-PTH trigger sustained PTHR/G_s signaling from endosomes[111]. For PTH, cAMP production decreases over time as PTH dissociates from the receptor due to endosomal acidification[114]. Specifically, PTH dissociation begins approximately 15 minutes post-ligand washout, corresponding to pH ~6.5. PTH release from PTHR promotes uncoupling of β-arrestins and G_s and coupling of the retromer complex[114], which mediates PTHR trafficking to the Golgi apparatus[115]. In contrast, LA-PTH does not dissociate from PTHR, thus maintaining G_s signaling, at timepoints in which endosomal pH ranges from 6.5 to below 6.0[24,114], suggesting reduced pH sensitivity of LA-PTH binding to receptor.

To investigate how LA-PTH prolongs endosomal signaling in comparison to PTH, we first assessed the effects of decreasing pH on PTH secondary structure when not bound to PTHR. Next, we investigated the role of PTH His protonation state on PTHR/G_s signaling. Finally, we utilized MD simulations to compare receptor interactions between PTH and LA-PTH.

2.2.1 pH effects on ^{15}N-PTH secondary structure

To determine the effects of pH on PTH conformation, we first collected two-dimensional ^{1}H-^{15}N heteronuclear single quantum coherence (HSQC) nuclear magnetic resonance (NMR) spectra of purified and fully functional ^{15}N-labeled PTH at three pH values: 5.9, 6.5, 7.2 (Figure

2.9, Appendix Figure 9a, c, Appendix Figure 10). We collected three-dimensional ^{15}N-edited NOESY-HSQC (NOESY) NMR spectra to assign the HSQC peaks (Appendix Figure 11). Dramatic chemical shift perturbations upon pH change were observed for histidine residues in PTH (i.e., His9, His14, His32) as well as in the attached Strep-Tag (i.e., His39). The chemical shift of Leu15 also greatly changed upon pH decrease.

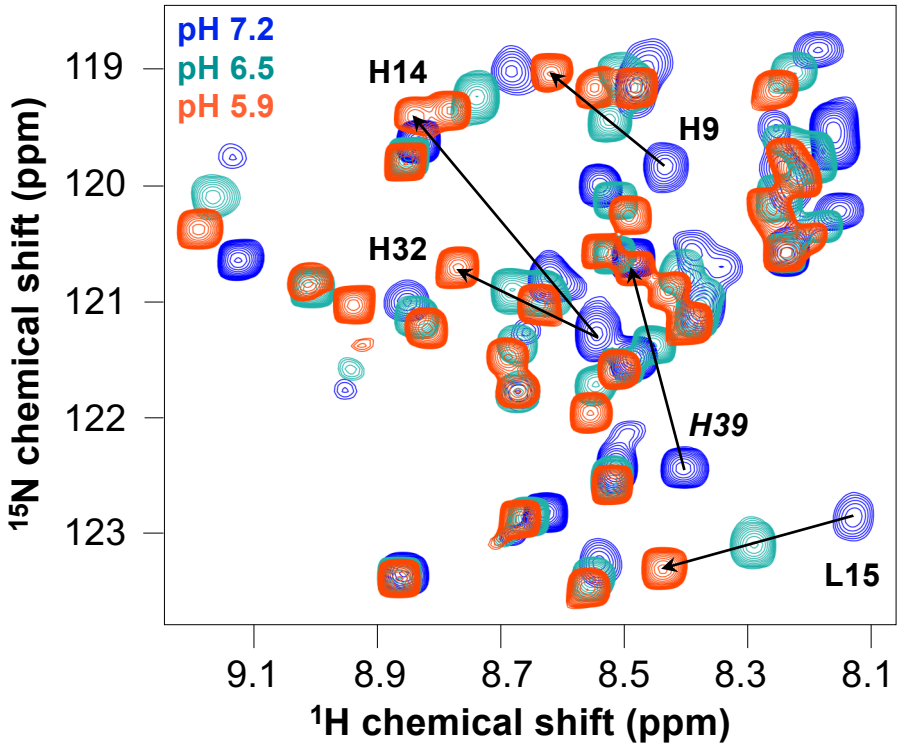

Figure 2.9. HSQC spectra of ^{15}N-PTH at multiple pH values.

The peaks of residues experiencing large chemical shift perturbations upon decreasing pH are labeled with bold text. The label of Strep-tag residue His39 is italicized. Spectra at pH 7.2, 6.5, and 5.9 are colored blue, teal, and orange, respectively.

To assess the effects of pH on PTH secondary structure, we acquired NOESY spectra of ^{15}N-PTH at pH 5.9 and 7.2. From these spectra, we determined the Hα chemical shift (δHα) of each PTH residue at each pH value and calculated a chemical shift index (CSI) (Figure 2.10, Appendix Table 5). The CSI of -1 occurs when an experimental δHα is smaller than the random coil value for that residue minus 0.10 ppm[147]. The CSI of +1 occurs when an experimental δHα is greater than the random coil value plus 0.10 ppm. A residue's CSI is zero when its δHα is within the random coil value ± 0.10 ppm. A region of a peptide or protein with four or more consecutive -1 CSIs is considered α-helical[147]. Our data are consistent with previously determined NMR structures of PTH, where the C-terminal portion (residues 16–34) is α-helical and the N-terminal portion (residues 1–15) is more flexible and less α-helical (see Chapter 3.0 for more in-depth discussion of PTH secondary structure). Furthermore, the CSI values at pH 7.2 and 5.9 are identical for each residue, which the exception of Val21 (Figure 2.10b, Appendix Table 5). While CSI of Val21 changes from -1 to 0 upon pH decrease from 7.2 to 5.9, the δHα only increases by 0.02 ppm (Appendix Table 5).

From these data, we can conclude that pH changes encountered by PTH during receptor signaling and trafficking do not dramatically affect peptide secondary structure. Therefore, the large chemical shift perturbations of the histidine residues are likely due to population changes of histidine side chain protonation states, as the histidine side chain pKa of ≈ 6.0 is within the pH range tested[148]. While protein histidine side chain pKa is dependent on its chemical environment, an analysis of experimentally determined pKa values of surface-exposed histidine residues (defined as having percent solvent assessable surface area > 40%) gave an average value of 6.4[148]. In addition, the large chemical shift change of Leu15 may be caused by its proximity to His14.

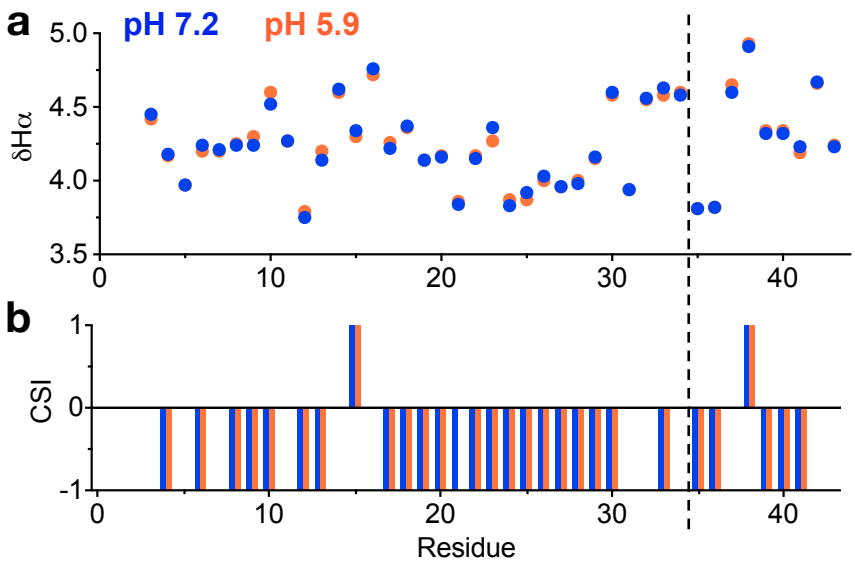

Figure 2.10. Effects of pH on PTH-Strep secondary structure.

NMR data acquired at pH 7.2 and 5.9 are colored blue and orange, respectively. The dashed line separates PTH from the attached glycine linker and Strep-tag (i.e., residues 35–44). **a,** Hα chemical shift values for each PTH residue. **b,** Calculated chemical shift indices (CSI) for each residue, based on comparison with random coil δHα values.

2.2.2 Effects of ligand protonation state on PTHR signaling

Given that we did not detect significant differences in PTH secondary structure upon decrease in pH, we next sought to determine if the protonation state of PTH while bound to the receptor affects the extent of sustained signaling in endosomes. We synthesized three PTH mutants in which each histidine is mutated to an alanine (i.e., PTH^{H9A}, PTH^{H14A}, PTH^{H32A}). We supposed that if protonation of a PTH histidine contributes to PTH dissociation from receptor in endosomes, the lack of protonation at this residue would increase sustained cAMP signaling from endosomes. The PTH^{H32A} mutant displayed a modest but significant increase in cAMP production (Figure 2.11a), while no significant differences between wild-type PTH (PTH^{WT}) and PTH^{H14A} were seen (Figure 2.11b). Interestingly, PTH^{H9A} eliminated sustained endosomal

signaling and slightly decreased transient cAMP production (Figure 2.11c); PTH^{H9A} is further characterized in Chapter 4.0. These results suggest that protonation of PTH His32 could destabilize peptide interactions with PTHR.

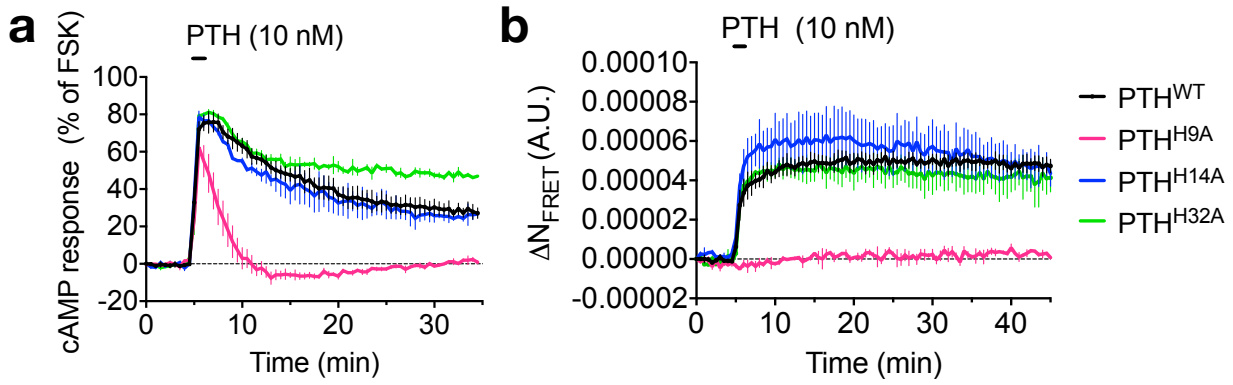

Figure 2.11. Signaling properties of PTH histidine mutants.

a, Averaged cAMP responses (percentage cAMP responses relative to response in the presence of forskolin, FSK) in HEK-293 cells stably expressing PTHR after 30 s stimulation with 10 nM ligand. Data represent the mean ± s.e.m. of N = 2–3 experiments with n ≥ 12 cells per experiment. **b,** Averaged time courses of β-arrestin-2^{YFP} recruitment to $PTHR^{CFP}$ after 30 s stimulation with 10 nM ligand, measured by FRET in HEK-293 cells. Data represent the mean ± s.e.m. of n ≥ 27 cells carried out in duplicate. *Data were acquired by Alex White.*

To further explore the consequences of PTH His32 protonation, we performed 1 ns MD simulations of PTH–PTHR with and without His32 side chain protonation at both nitrogens (i.e., PTH^{H32}, PTH^{H32+}). With PTH^{H32}, the His32 side chain makes polar and aromatic interactions with Tyr167 (Figure 2.12a). Positively charged His32 moves away from Tyr167 at the start of the simulation (Figure 2.12a). From 12 ps to 34 ps of simulation, the helix of PTH^{H32+} increases in curvature (Figure 2.12b), and this curvature is maintained for the rest of the simulation (Appendix Figure 8). In contrast, the PTH^{H32} helix does not exhibit such dramatic curvature. We hypothesize

that the PTH helix curvature induced by PTH His32 protonation in endosomes destabilizes peptide-receptor interactions to promote dissociation.

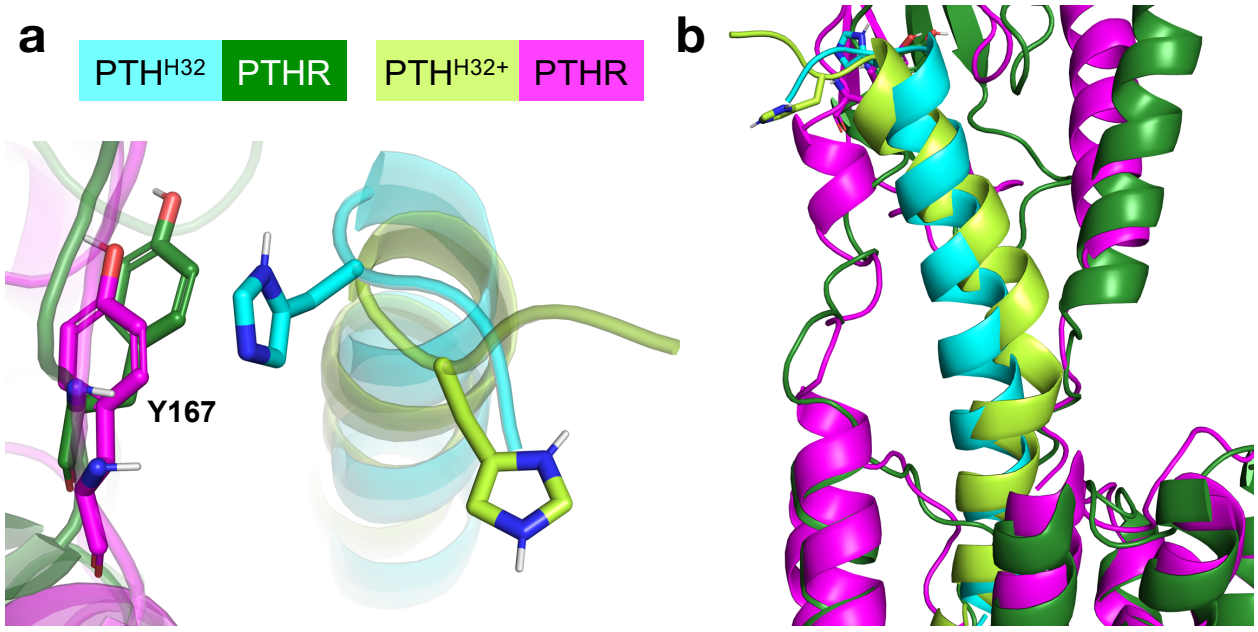

Figure 2.12. Snapshots of the PTH–PTHR complex after 34 ps MD simulation reveal effects of PTH His32 protonation on peptide-receptor interactions.

Neutral and positively-charged PTH His (H32 and H32+, respectively) and PTHR Tyr167 are shown as sticks. **a,** PTH His32 interacts with PTHR Tyr167, whereas additional protonation of His32 eliminates this interaction. **b,** Induced curvature of PTH^{H32+} helix in comparison to PTH^{H32}. PTHR residues 248–275 are hidden for clarity.

2.2.3 Interactions of PTH and LA-PTH with PTHR

His32 is conserved amongst all PTHR ligands (Figure 1.9). Furthermore, a cryo-EM structure of LA-PTH bound to PTHR exhibited dissociation of LA-PTH(18–34) from the $PTHR^{ECD}$ (Figure 2.6a, state 3). These results suggest that peptide C-terminal residues undergo many dissociation-rebinding cycles while in complex with PTHR, and potentially His32 protonation in endosomes prevents rebinding. We then hypothesized that LA-PTH permits more contacts between the receptor and the first 14 peptide residues than does PTH, decreasing the

likelihood of peptide dissociation at endosomal pH. To test this hypothesis, we performed a 200 ns MD simulation of LA-PTH bound to membrane-embedded PTHR for comparison with PTH–PTHR simulations. For each simulation, we determined the number of interactions between ligand residues 1–14 and receptor in the last frame of simulation. LA-PTH(1–14) formed 62 interactions with PTHR, in contrast with PTH(1–14), which formed an average of 45 interactions from three simulations (Appendix Table 6). We also analyzed simulations of LA-PTH-bound (100 ns) and PTH-bound (200 ns) PTHR–G_s complexes. In the presence of G_s, PTH(1–14) increased the number of interactions with receptor to 50. At the end of the 100 ns simulation, LA-PTH(1–14) formed 57 interactions with PTHR–G_s, although it is possible that more interactions would form during an additional 100 ns simulation. The increased number of contacts by LA-PTH primarily occur through nonpolar interactions (Appendix Table 6). In the presence of G_s, these additional interactions mainly occur through Val2, Glu4, and Ala12 (Figure 2.13, Appendix Table 6). In simulations without G_s, where the difference in number of nonpolar interactions is more pronounced, Ala1, Ala12, and Trp14 are primary contributors (Figure 2.14, Appendix Table 6).

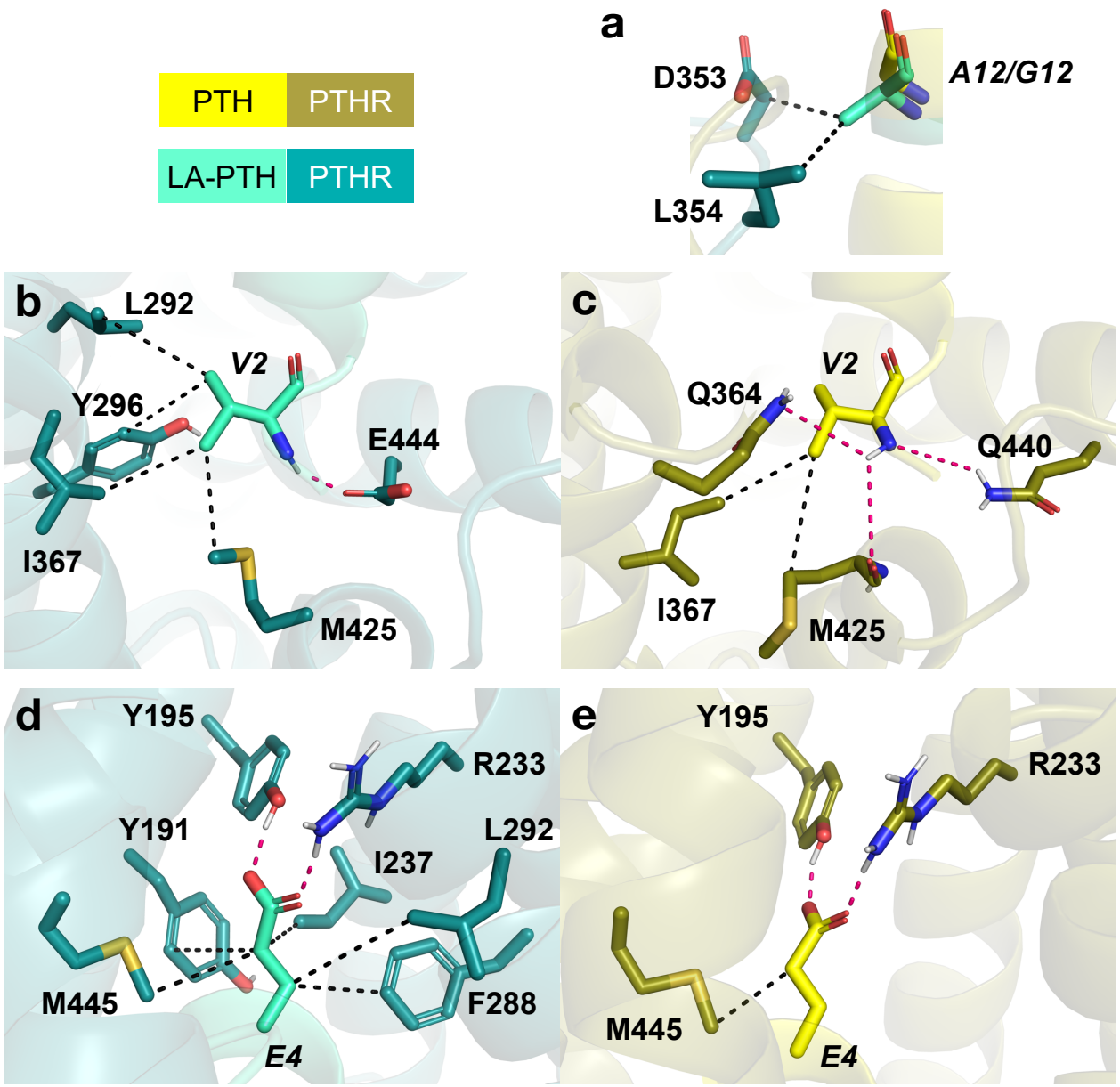

Figure 2.13. Primary contributors of nonpolar interactions in LA-PTH–PTHR–G_s simulation.

Final simulation snapshots of LA-PTH (green cyan) bound to PTHR–G_s (deep teal) and PTH (yellow) bound to PTHR–G_s (deep olive). Polar interactions are hot pink dashes. Nonpolar interactions are black dashes. **a,** LA-PTH Ala12 interactions. PTH Gly12 is also shown. **b,** LA-PTH Val2. **c,** PTH Val2. **d,** LA-PTH Glu4. **e,** PTH Glu4.

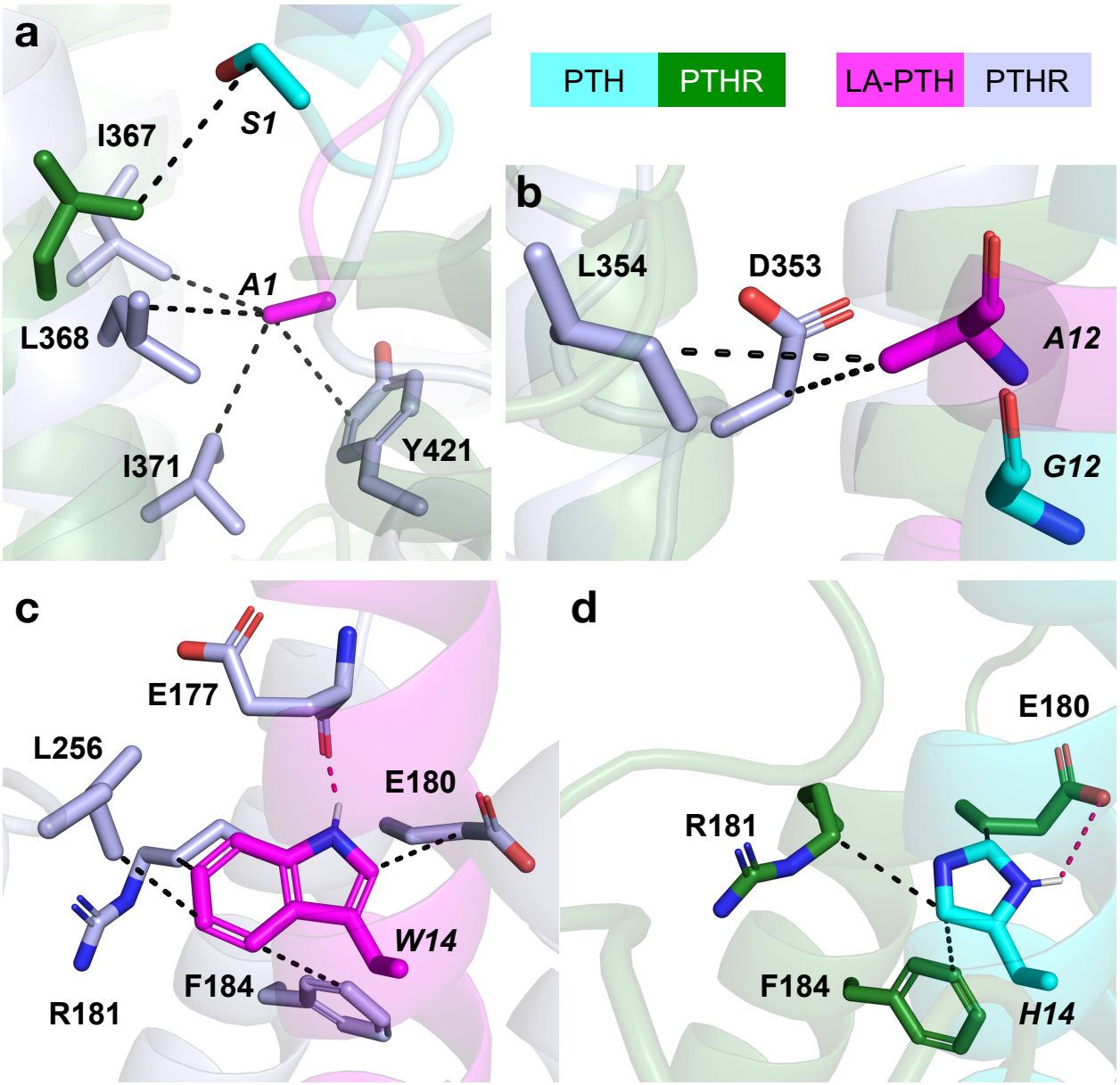

Figure 2.14. Primary contributors of nonpolar interactions in LA-PTH–PTHR simulation.

Final simulation snapshots of LA-PTH (magenta) bound to PTHR (light blue) and PTH (cyan) bound to PTHR (dark green). Polar interactions are hot pink dashes. Nonpolar interactions are black dashes. **a,** LA-PTH Ala1 and PTH Ser1. **b,** LA-PTH Ala12 interactions. PTH Gly12 is also shown. **c,** LA-PTH Trp14. **d,** PTH His14.

2.2.4 Summary, Final Model, and Future Directions

Using NMR experiments, we determined that the secondary structure of PTH unbound to receptor is not dramatically altered by a decrease in pH that occurs in endosomes (Figure 2.10). These results remove the possibility of PTH being unable to rebind to PTHR in endosomes solely because of pH-dependent PTH conformational change in the endosomal lumen. Instead, the pH decrease affects receptor conformation and/or destabilizes PTH–PTHR interactions, the latter of which is supported by our studies of PTH His32. Mutation of His32 to Ala increased sustained cAMP production in endosomes (Figure 2.11). Furthermore, protonation of His32 in 1 ns MD simulations promoted curvature of the peptide helix (Figure 2.12), suggesting that the protonation of solvent-exposed His32 destabilizes PTH–PTHR interactions. Although not directly tested, it is possible that protonation of His32 in LA-PTH also destabilizes peptide–receptor interactions. In addition, a cryo-EM structure of LA-PTH in complex with PTHR and G_s reveals dissociation of LA-PTH residues 18–34 from the $PTHR^{ECD}$ (Figure 2.6, state 3). We then hypothesized that contacts between peptide residues 1–14 and the $PTHR^{TMD}$ are critical for maintaining active peptide–receptor complex during dissociation and, potentially, re-association events of the C-terminal peptide part. Analyzing final structure snapshots from MD simulations, we determined that LA-PTH(1–14) forms more contacts with PTHR than does PTH(1–14) in the absence and presence of G_s (Appendix Table 6). The additional contacts of LA-PTH are primarily nonpolar. In the absence of G_s, LA-PTH Ala1, Ala12, and Trp14 are primary contributors of nonpolar interactions, all of which are unique to LA-PTH.

From these data, we propose a model for sustained endosomal signaling by LA-PTH in which the increased contacts between LA-PTH and $PTHR^{TMD}$ reduce ligand dissociation at endosomal pH, despite dissociation of the ligand C-terminal part (Figure 2.15). In contrast, the

destabilization of PTH–PTHR at endosomal pH, in part due to protonation of His32, leads to release of PTH from the receptor and termination of signaling.

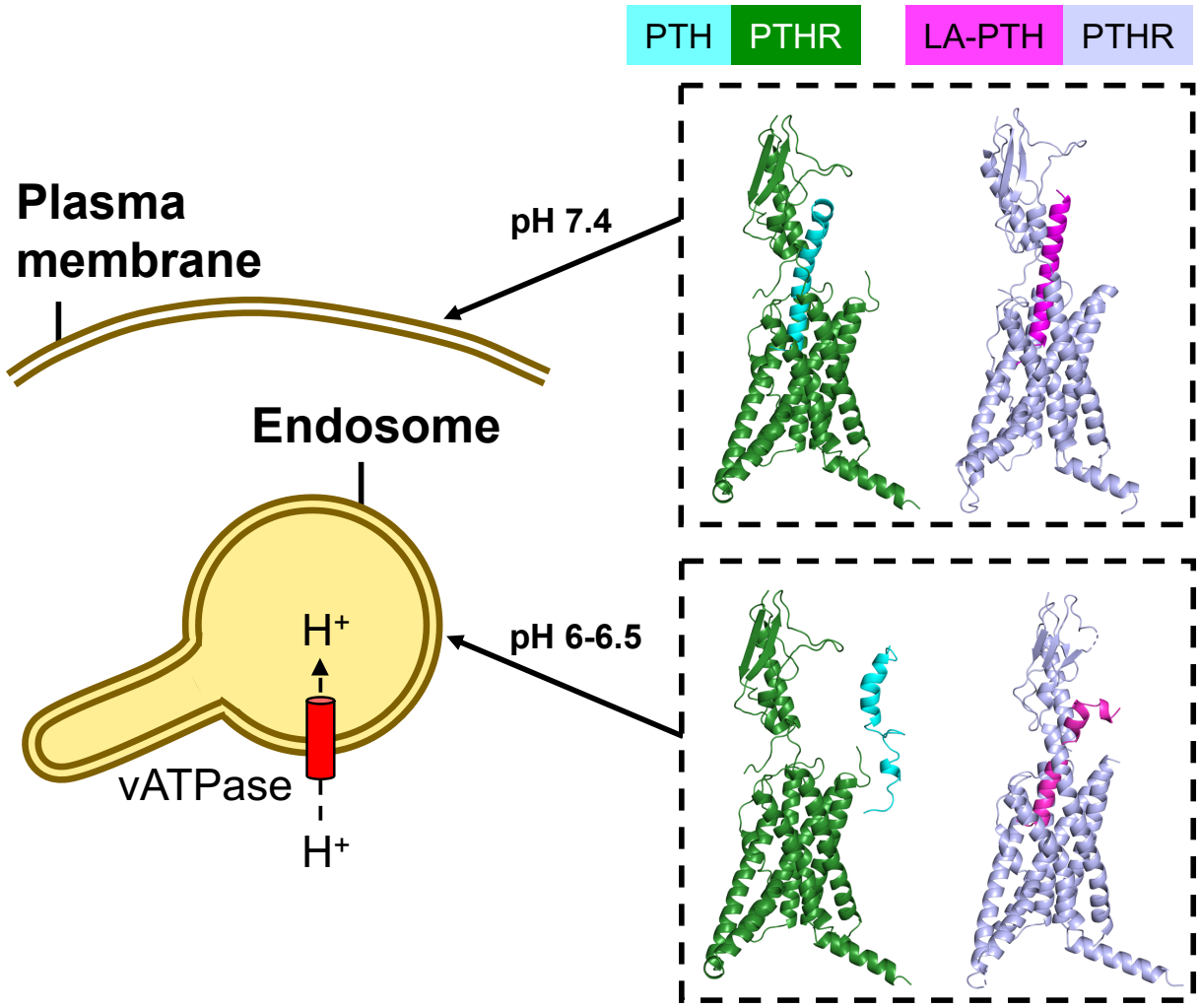

Figure 2.15. Model of sustained endosomal signaling by LA-PTH.

Interactions between peptide ligand and receptor are stable at plasma membrane pH. Upon internalization into endosomes, cAMP signaling by PTHR complexes activates vATPase, which acidifies the endosomal lumen. The decrease in pH destabilizes PTH interactions with the receptor, including through the protonation of PTH His32. PTH dissociates, thus rendering the receptor inactive. While protonation of LA-PTH His32 may also contribute to C-terminal peptide dissociation from the receptor ECD, increased contacts between LA-PTH residues 1–14 and $PTHR^{TMD}$ maintain binding and continued cAMP signaling from endosomes.

Additional structural and computational methods can be pursued to investigate PTHR complexes in endosomes. Cryo-EM data of PTHR isolated in liposomes can be collected under different ligand (e.g., PTH and LA-PTH) and pH conditions. For liposomes in which the $PTHR^{ECD}$ is oriented outward, we can model PTHR in endosomes by collecting data at acidic pH (e.g., pH 6.0 and 6.5). Higher resolution structures of LA-PTH–PTHR at plasma membrane and endosomal pH, by comparing to PTH–PTHR liposome structure at plasma membrane pH, may further reveal the mechanism by which LA-PTH uniquely remains bound to PTHR upon endosomal acidification. Two-dimensional class averages of PTH–PTHR liposome at acidic pH values may also capture PTH dissociation. Starting with PTH- and LA-PTH-bound models stabilized by MD simulations, constant-pH MD simulations in NAMD can monitor the protonation states of ligand and receptor histidines at plasma membrane and endosomal pH values[149]. Thus, the effects of histidine protonation on protein conformation and dynamics can also be explored.

2.2.5 Methods

2.2.5.1 ^{15}N-PTH expression and purification

We expressed ^{15}N-PTH in *E. coli* as a construct containing an N-terminal maltose binding protein (MBP) and a C-terminal Strep-tag plus glycine linker (GGWSHPQFEK) to enhance protein stability and purification. Culture was grown in Luria Broth at 37°C, 220 rpm, until OD_{600} ~ 0.6 and then was centrifuged at 900 x g, 15 min. Pellets were gently washed with M9 media without glucose or $(^{15}NH_4)_2SO_4$ and centrifuged at 900 x g, 15 min. Cell pellets were resuspended in M9 media (500 mL M9 media per 2 L LB culture) and incubated for 30 min at 37°C. Temperature was reduced to 18°C, and expression of ^{15}N-MBP-PTH was induced with 0.8 mM IPTG 30 min later. Culture was grown overnight at 18°C, 220 rpm. M9 media consists of 7 g/L

Na_2HPO_4, 3 g/L KH_2PO_4, 0.5 g/L NaCl, 1 g/L $(^{15}NH_4)_2SO_4$, 10 g/L glucose, 1 mM $MgSO_4$, 0.1 mM $CaCl_2$, 50 mg/L thiamine, and ~4 mg/L $FeCl_3$.

Harvested cells were resuspended in buffer consisting of 20 mM Tris pH 8.0, 200 mM NaCl, 1 mM EDTA, and 1X PI. Cells were lysed via sonication, and supernatant was isolated via ultracentrifugation. Supernatant was subjected to multiple rounds of amylose resin purification using a wash buffer of 20 mM Tris pH 8.0, 200 mM NaCl, 1 mM EDTA, and 1X PI. MBP-PTH was eluted in 25 mM HEPES pH 7.5, 50 mM NaCl, 2 mM $CaCl_2$, and 10 mM maltose. Amylose eluate was concentrated to > 1 mg/mL, and Tween 20 was added to 0.1%. To cleave MBP from PTH, 0.4 μg enterokinase (BioVision) per mg protein was added to the sample, and sample was rotated at room temperature for 20 hr. To separate cleaved MBP from PTH, sample was purified via 5 mL StrepTrap HP (GE), using a wash buffer of 25 mM HEPES pH 7.5, 150 mM NaCl, 1 mM $CaCl_2$. PTH was eluted using wash buffer plus 2.5 mM D-desthiobiotin (Sigma Aldrich). Eluate was pooled and concentrated using 3 kDa MWCO Amicon Ultra centrifugal filter (EMD Millipore) prior to size exclusion chromatography with a buffer of 25 mM HEPES pH 7.5, 150 mM NaCl (Superdex Peptide 10/300, GE, Appendix Figure 9a). After SDS-PAGE analysis, pure fractions were pooled, concentrated to 135 μM, and aliquoted. Aliquots were flash frozen in liquid nitrogen and stored at -80°C. Prior to NMR experiments, an aliquot was thawed and centrifuged to demonstrate the absence of sample precipitation. The pH of the sample was adjusted to 6.5 and then to 5.9 by adding 3.5 and then 1.5 μL of 10X diluted HCl, respectively.

2.2.5.2 NMR data acquisition, processing, and analysis

All NMR samples also contained 6% D2O for deuterium lock and 16 μM DSS (sodium trimethylsilylpropanesulfonate) for chemical shift calibration. NMR experiments were carried out at 10°C using Bruker Avance 700, 800, and 900 NMR spectrometers equipped with a triple-resonance inverse-detection cryoprobe, TCI (Bruker Instruments, Billerica, MA). For assignment of PTH ^{15}N and ^{1}H chemical shifts, two-dimensional (2D) ^{1}H-^{15}N HSQC, ^{1}H homonuclear NOESY and TOCSY, and three-dimensional (3D) ^{15}N-edited NOESY-HSQC were collected (Appendix Figure 11). The previously published ^{1}H chemical shifts of PTH at pH 6.8 and 5°C were also used as a guide for assignments[150]. The ^{1}H-^{15}N HSQC spectra were acquired with a spectral width of 12 and 25 ppm in the ^{1}H and ^{15}N dimension, respectively and 2048 (^{1}H) × 256 (^{15}N) total data points. 3D ^{15}N-edited NOESY was collected at 700.13 MHz with a spectral width of 12 (^{1}H) × 25 (^{15}N) × 12 (^{1}H) ppm and 2048 (^{1}H) × 48 (^{15}N) × 128 (^{1}H) data points. A mixing time was set at 200 ms in the 3D NOESY experiments. A relaxation delay of 1 s was set in all NMR experiments.

The HSQC spectra were acquired at pH 7.2, 6.5, and 5.9. The NOESY spectra were acquired at pH 7.2 and 5.9. CcpNmr Analysis (v2 or v3) was used to prepare NMR spectra for figures[151]. The alpha hydrogen chemical shift (δHα) of each PTH residue at pH 7.2 and 5.9 was determined using the NOESY spectra. These values were then used to calculate the chemical shift index (CSI) of each PTH residue at pH 7.2 and 5.9.

$$\mathrm{CSI} = \begin{cases} -1, \text{ if } \delta H\alpha_{exp} < (\delta H\alpha_{rand} - 0.10) \\ 0, \text{ if } (\delta H\alpha_{rand} - 0.10) < \delta H\alpha_{exp} < (\delta H\alpha_{rand} + 0.10) \\ +1, \text{ if } \delta H\alpha_{exp} > (\delta H\alpha_{rand} + 0.10) \end{cases},$$

where $\delta H\alpha_{exp}$ and $\delta H\alpha_{rand}$ are experimental and random coil chemical shifts, respectively. Chemical shift and CSI data were plotted in GraphPad Prism[152].

2.2.5.3 Chemicals and peptides

Forskolin (#344270) was purchased from EMD-Millipore. PTH was synthesized and characterized as previously described[114]. Histidine mutants PTH^{H9A}, PTH^{H14A}, PTH^{H32A} were synthesized by LifeTein and received in lyophilized form. Histidine mutants were resuspended in 10 mM acetic acid to make 1 mM peptide aliquots.

2.2.5.4 Time-course measurements of cAMP production

Cyclic AMP was assessed using FRET-based assays. Cells were transiently transfected with the FRET-based biosensor Epac1-CFP/YFP for measuring cAMP[153]. Measurements were performed and analyzed as previously described[114]. In brief, cells plated on poly-D-lysine coated glass coverslips were mounted in Attofluor cell chambers (Life Technologies), maintained in HEPES buffer containing 150 mM NaCl, 20 mM HEPES, 2.5 mM KCl and 0.1–10 mM $CaCl_2$, 0.1% BSA, pH 7.4, and transferred on the Nikon Ti-E equipped with an oil immersion 40X N.A 1.30 Plan Apo objective and a moving stage (Nikon Corporation). CFP and YFP were excited using a mercury lamp. Fluorescence emissions were filtered using a 480 ± 20 nm (CFP) and 535 ± 15 nm (YFP) filter set and collected simultaneously with a LUCAS EMCCD camera (Andor Technology) using a DualView 2 (Photometrics) with a beam splitter dichroic long pass of 505 nm. Fluorescence data were extracted from single cell using Nikon Element Software (Nikon Corporation). The FRET ratio for single cells was calculated and corrected as previously described[114]. Individual cells were perfused with buffer or with the ligand for the time indicated by the horizontal bar.

2.2.5.5 MD simulations

2.2.5.5.1 System preparation

The 3.0 Å cryo-EM structure of LA-PTH–PTHR–Gs–Nb35 complex (PDB 6NBF)24 was used to generate initial PTHR models. I-TASSER was then used to model flexible loops absent in the cryo-EM structure: ECD residues 56–104, ECL1 residues 247–275, and ICL3 residues 394–398[154-156]. In PyMOL[157], structures of Nb35, palmitic acid, and cholesterol were removed. Thestructure of G_s was also removed for G protein-free models. For the PTH-bound model, LA-PTH residues were mutated to the corresponding PTH residues, as necessary, using the PyMOL Mutagenesis Wizard. For the PTH^{H32+}-bound model, the protonation state of His32 was specified in CHARMM-GUI[158]. Each initial model was oriented in a model membrane using the Orientations of Proteins in Membranes (OPM) PPM Server[159]. Using oriented models, inputs for Nanoscale Molecular Dynamics (NAMD) were generated using CHARMM-GUI Membrane Builder[158,160-165]. Disulfide bonds Cys48-Cys117, Cys108-Cys148, Cys131-Cys170, and Cys281-Cys351 were specified to ensure correct formation. A heterogeneous lipid bilayer consisting of 75% POPC and 25% cholesterol was assembled around the receptor model using the Replacement Method. The system was solvated in a box of TIP3P waters, and ions were added to a concentration of 150 mM NaCl using Monte Carlo sampling.

2.2.5.5.2 Unbiased MD simulations

All-atom simulations were performed using NAMD with the CHARMM36m force field[166,167]. Prior to production simulations, 10,000 steps of conjugate gradient energy minimization were performed followed by 0.675 ns equilibration in which restraints were

applied and then slowly released over six steps following the protocol established by the CHARMM-GUI group[158]. Next, production simulations with 2 fs timestep were performed for the models and lengths of time shown in Table 1.

Table 1. Chapter 2 MD simulation systems.

Model	Production simulation length (ns)	Number of simulations
PTH–PTHR (PTH^{H32}–PTHR)	200	3
LAPTH–PTHR	200	1
PTH–PTHR–G_s	200	1
LAPTH–PTHR–G_s	100	1
PTH^{H32+}–PTHR	1	1

Non-bonded interactions were cut off at 12.0 Å, and van der Waals force switching was applied between 10.0 Å and 12.0 Å. Langevin dynamics and Langevin piston were used to maintain temperature at 303.15 K and pressure at 1 atm.

2.2.5.5.3 MD trajectory analysis

MD trajectories were analyzed in Visual Molecular Dynamics (VMD) and PyMOL[157,168]. PTHR snapshots were aligned using receptor TM helices ($PTHR^{TMD}$ without ECLs or ICLs: residues 180–211, 218–246, 280–311, 317–343, 359–392, 399–425, 435–460).

3.0 Mechanism of PTH binding to PTHR

The binding of a PTHR ligand to its receptor is the first step of the PTHR signaling mechanism. Understanding the molecular details of peptide ligand binding will give insight into the structural basis of PTHR signaling and may indicate how different PTHR ligands, including biased ligands, affect PTHR conformation. Previous research supports a two-step binding mechanism for PTH. In the first, fast step, the C-terminal part of the ligand (residues 16–34) binds to the receptor extracellular domain ($PTHR^{ECD}$). In the second, slow step, the N-terminal part of the ligand (residues 1–15) binds to the receptor transmembrane domain ($PTHR^{TMD}$). Through NMR experiments titrating unlabeled purified $PTHR^{ECD}$ into a sample of ^{15}N-labeled PTH, we demonstrate that binding of the PTH C-terminal part to $PTHR^{ECD}$ reduces the mobility of the PTH N-terminal part independently of the $PTHR^{TMD}$. From these results, along with MD simulations and structural modeling, we propose an extended mechanism of PTH binding to PTHR in which the reduced mobility of the PTH N-terminal part during the first step primes this region for interaction with $PTHR^{TMD}$ during the second step.

This chapter was adapted from the following publication:

Lisa J. Clark*, James Krieger*, Alex D. White, Vasyl Bondarenko, Saifei Lei, Fei Fang, Ji Young Lee, Pemra Doruker, Thore Böttke, Frederic Jean-Alphonse, Pei Tang, Thomas J. Gardella, Kunhong Xiao, Ieva Sutkeviciute, Irene Coin, Ivet Bahar†, Jean-Pierre Vilardaga†. Allosteric interactions in the parathyroid hormone GPCR–arrestin complex formation *Nat. Chem. Biol.* doi: 10.1038/s41589-020-0567-0 (2020). *Contributed equally to this study. †Corresponding authors.

3.1 Introduction

The PTHR is a prototypical member of GPCR class B, which includes receptors for many medically important peptide hormones (e.g., secretin, vasoactive intestinal peptide, glucagon, glucagon-like peptide, calcitonin, corticotropin-releasing factor, gastric inhibitory peptide, growth hormone-releasing hormone, pituitary adenylate cyclase-activating peptide) regulating vital functions in human body systems (e.g., skeletal, endocrine, gastrointestinal, cardiovascular). Class B GPCR peptide ligands consist of two common structural components, each with a distinct role: the more structured (α-helical) C-terminal part is critical for binding to the large N-terminal extracellular domain (ECD) of the receptor, and the more flexible N-terminal part of the ligand inserts into the receptor's transmembrane (TM) domain (TMD) and is critical for engaging signaling via G proteins and β-arrestins[9,169]. The kinetics of this two-step binding process were initially analyzed for PTH(1–34)[170], the fully functional N-terminal fragment of PTH that is currently used to treat osteoporosis[171,172]. Fluorescence resonance energy transfer (FRET) experiments indicated that in the first step, the C-terminal part of PTH (i.e., residues 16–34) binds to the ECD with fast kinetics (time constant ≈ 140 ms); in the second step, the PTH N-terminal part (residues 1–15) binds to the TMD with slower kinetics (time constant ≈ 1 s)[170]. This two-step mechanism has been extended to other class B GPCRs, supported structurally through the crystal structures of class B GPCR ECDs in complex with peptide C-terminal helices as well as full-length receptor structures in which each peptide is a continuous α-helix (Figure 1.2, Appendix Table 1)[9,173]. However, once the binding to the receptor N-terminal domain takes place during the first step, how the information is transmitted to trigger the second binding event at the TMD, which, in turn, leads to the intracellular interaction with G proteins and β-arrestins, is largely unknown. Here,

we describe how the receptor ECD works to favor the formation of the peptide α-helical structure, which permits optimal insertion of the peptide signaling domain into the receptor's TMD. This mechanism is changing the view of the classical two-state binding model for class B GPCRs and how PTHR signaling and its coupling to G proteins and β-arrestins occur.

3.2 Methods

3.2.1 Protein expression and purification

3.2.1.1 ^{15}N-PTH

We expressed ^{15}N-PTH in *E. coli* as a construct containing an N-terminal maltose binding protein (MBP) and a C-terminal Strep-tag plus glycine linker (GGWSHPQFEK) to enhance protein stability and purification. Culture was grown in Luria Broth at 37°C, 220 rpm, until OD_{600} ~ 0.6 and then was centrifuged at 900 x g, 15 min. Pellets were gently washed with M9 media without glucose or $(^{15}NH_4)_2SO_4$ and centrifuged at 900 x g, 15 min. Cell pellets were resuspended in M9 media (500 mL M9 media per 2 L LB culture) and incubated for 30 min at 37°C. Temperature was reduced to 18°C, and expression of ^{15}N-MBP-PTH was induced with 0.8 mM IPTG 30 min later. Culture was grown overnight at 18°C, 220 rpm. M9 media consists of 7 g/L Na_2HPO_4, 3 g/L KH_2PO_4, 0.5 g/L NaCl, 1 g/L $(^{15}NH_4)_2SO_4$, 10 g/L glucose, 1 mM $MgSO_4$, 0.1 mM $CaCl_2$, 50 mg/L thiamine, and ~4 mg/L $FeCl_3$.

Harvested cells were resuspended in buffer consisting of 20 mM Tris pH 8.0, 200 mM NaCl, 1 mM EDTA, and 1X PI. Cells were lysed via sonication, and supernatant was isolated via ultracentrifugation. Supernatant was subjected to multiple rounds of amylose resin purification

using a wash buffer of 20 mM Tris pH 8.0, 200 mM NaCl, 1 mM EDTA, and 1X PI. MBP-PTH was eluted in 25 mM HEPES pH 7.5, 50 mM NaCl, 2 mM $CaCl_2$, and 10 mM maltose. Amylose eluate was concentrated to > 1 mg/mL, and Tween 20 was added to 0.1%. To cleave MBP from PTH, 0.4 μg enterokinase (BioVision) per mg protein was added to the sample, and sample was rotated at room temperature for 20 hr. To separate cleaved MBP from PTH, sample was purified via 5 mL StrepTrap HP (GE), using a wash buffer of 25 mM HEPES pH 7.5, 150 mM NaCl, 1 mM $CaCl_2$. PTH was eluted using wash buffer plus 2.5 mM D-desthiobiotin (Sigma Aldrich). Eluate was pooled and concentrated using 3 kDa MWCO Amicon Ultra centrifugal filter (EMD Millipore) prior to size exclusion chromatography with a buffer of 25 mM HEPES pH 7.5, 150 mM NaCl (Superdex Peptide 10/300, GE, Appendix Figure 9a). After SDS-PAGE analysis, pure fractions were pooled, concentrated, and aliquoted. Aliquots were flash frozen in liquid nitrogen and stored at -80°C. Prior to NMR experiments, some aliquots were thawed, and size exclusion chromatography was performed. Pooled fractions were concentrated to 166 μM.

3.2.1.2 $PTHR^{ECD}$

We purified PTHR(29–187) (i.e., $PTHR^{ECD}$) N-terminally fused to maltose binding protein (MBP) to enhance protein stability and solubility in detergent-free buffer. This strategy was previously used to determine a crystal structure of PTH(15–34) bound to $PTHR^{ECD}$ [42]. In brief, MBP-$PTHR^{ECD}$ was expressed in *E. coli* Shuffle cells via induction by 0.4 mM IPTG. Harvested cells were resuspended in buffer consisting of 50 mM Tris pH 8.0, 150 mM NaCl, 5 mM reduced glutathione (GSH), 1 mM glutathione disulfide (GSSG), 10% glycerol, and 2X PI. Cells were lysed via sonication, and supernatant was isolated via ultracentrifugation. MBP-$PTHR^{ECD}$ was purified using Ni Sepharose 6 Fast Flow resin, followed by amylose resin, and finishing with size exclusion chromatography with a buffer of 25 mM

HEPES pH 7.5, 150 mM NaCl (Superose 6 10/300 GL, Appendix Figure 9b). Prior to NMR experiments, pure fractions were combined and concentrated to 526 μM using 15 kDa MWCO Amicon Ultra centrifugal filter (EMD Millipore).

3.2.2 NMR data acquisition, processing, and analysis

All NMR samples also contained 6% D_2O for deuterium lock and 16 μM DSS (sodium trimethylsilylpropanesulfonate) for chemical shift calibration. NMR experiments were carried out at 10°C using Bruker Avance 700, 800 and 900 NMR spectrometers equipped with a triple-resonance inverse-detection cryoprobe, TCI (Bruker Instruments, Billerica, MA). For assignment of PTH ^{15}N and ^{1}H chemical shifts, two-dimensional (2D) ^{1}H-^{15}N HSQC, ^{1}H homonuclear NOESY and TOCSY, and three-dimensional (3D) ^{15}N-edited NOESY-HSQC were collected (Appendix Figure 11). The previously published ^{1}H chemical shifts of PTH at pH 6.8 and 5°C were also used as a guide for assignments[150]. The ^{1}H-^{15}N HSQC spectra were acquired with a spectral width of 12 and 25 ppm in the ^{1}H and ^{15}N dimension, respectively and 2048 (^{1}H) × 256 (^{15}N) total data points. The 2D NOESY and TOCSY spectra were recorded at the ^{1}H resonance frequency of 800.3 MHz using 2048 × 400 data points and a spectral window of 11 ppm in both ^{1}H direct and indirect dimensions. 3D ^{15}N-edited NOESY was collected at 700.13 MHz with a spectral width of 12 (^{1}H) × 25 (^{15}N) × 12 (^{1}H) ppm and 2048 (^{1}H) × 48 (^{15}N) × 128 (^{1}H) data points. A mixing time was set at 200 ms in the 2D and 3D NOESY experiments. For the $PTHR^{ECD}$/^{15}N-PTH titration experiment (Appendix Table 7), 2D ^{1}H-^{15}N TROSY-HSQC spectra were acquired at 900 MHz with a spectral window of 12 ppm for ^{1}H and 25 ppm for ^{15}N and 2048 (^{1}H) × 256 (^{15}N) data points. The receptor-to-peptide molar ratios of 0, 0.1, 0.25, 0.5,

and 0.75 were used with increased numbers of scans 12, 12, 24, 36, and 72, respectively, to compensate the loss of peak intensities. A relaxation delay of 1 s was set in all NMR experiments. Titration TROSY spectra with 0.5 and 0.75 of $PTHR^{ECD}$/^{15}N-PTH molar ratios generated observable changes in peak intensity (peak height) and chemical shift. The peak intensities in these spectra were normalized by Ser3 intensity prior to calculation of I_{bound}/ I_{free} for each residue. Chemical shift perturbation (Δδ) for each residue was calculated via the equation:

$$\Delta\delta = \sqrt{(\delta_{bound}^{^1H} - \delta_{free}^{^1H})^2 + \frac{(\delta_{bound}^{^{15}N} - \delta_{free}^{^{15}N})^2}{25}},$$

where δ_{bound} and δ_{free} are chemical shifts in the presence and absence of $PTHR^{ECD}$, respectively.

These data were analyzed and plotted in GraphPad Prism[152]. PTH structures were colored according to I_{bound}/I_{free} and chemical shift perturbation values in PyMOL[157] (Figure 3.2c, d, Appendix Figure 14a, b). CcpNmr Analysis (v2 or v3) was used to prepare NMR spectra for figures[151].

3.2.3 MD simulations

3.2.3.1 System preparation

The 3.0 Å cryo-EM structure of LA-PTH–PTHR–G_s–Nb35 complex (PDB 6NBF)[24] was used to generate initial PTHR models. I-TASSER was then used to model flexible loops absent in the cryo-EM structure: ECD residues 56–104, ECL1 residues 247–275, and ICL3 residues 394–398[154-156]. In PyMOL[157], structures of G_s, Nb35, palmitic acid, and cholesterol were removed.

The LA-PTH was also removed to generate an initial apo PTHR model. For the PTH-bound model, LA-PTH residues were mutated to the corresponding PTH residues, as necessary, using the PyMOL Mutagenesis Wizard. Each initial model was oriented in a model membrane using theOrientations of Proteins in Membranes (OPM) PPM Server[159]. Using oriented models, inputs for Nanoscale Molecular Dynamics (NAMD) were generated using CHARMM-GUI Membrane Builder[158,160-165]. Disulfide bonds Cys48-Cys117, Cys108-Cys148, Cys131-Cys170, and Cys281-Cys351 were specified to ensure correct formation. A heterogeneous lipid bilayer consisting of 75% POPC and 25% cholesterol was assembled around the receptor model using the Replacement Method. The system was solvated in a box of TIP3P waters, and ions were added to a concentration of 150 mM NaCl using Monte Carlo sampling.

3.2.3.2 Unbiased MD simulations

All-atom simulations were performed in triplicate for apo and PTH-bound models using NAMD with the CHARMM36m force field[166,167]. Prior to production simulations, 10,000 steps of conjugate gradient energy minimization were performed followed by 0.675 ns equilibration in which restraints were applied and then slowly released over six steps following the protocol established by the CHARMM-GUI group[158]. Next, 200 ns production simulation with 2 fs timestep was performed. Non-bonded interactions were cut off at 12.0 Å, and van der Waals force switching was applied between 10.0 Å and 12.0 Å. Langevin dynamics and Langevin piston were used to maintain temperature at 303.15 K and pressure at 1 atm.

3.2.3.3 MD trajectory analysis

MD trajectories were analyzed in Visual Molecular Dynamics (VMD) and PyMOL[157,168]. PTHR snapshots were aligned using receptor TM helices ($PTHR^{TMD}$ without ECLs or ICLs:

residues 180–211, 218–246, 280–311, 317–343, 359–392, 399–425, 435–460). RMSD of $PTHR^{ECD}$ (residues 27–179) and PTHR TM helices were acquired for each trajectory. RMSD and distance data were analyzed and plotted in GraphPad Prism[152].

3.2.4 Structural modeling

To investigate the position of $PTHR^{ECD}$ required for PTH binding, we first acquired snapshots every 10 ns from the apo PTHR 200 ns simulation. In PyMOL[157], the PTH(15–34)–$PTHR^{ECD}$ crystal structure (PDB 3C4M)[42] was aligned with the $PTHR^{ECD}$ of an apo snapshot. Next, residues 19–29 of the PTH NMR structural ensemble (PDB 1ZWA)[150] were aligned with PTH(19–29) from the crystal structure. The process was repeated for all snapshots. The extent of steric clashes between PTH and the receptor was assessed for each snapshot. The apo receptor snapshot and PTH NMR structure that generated the least steric clashes between PTH and PTHR were selected to represent initial binding of PTH C-terminal helix to $PTHR^{ECD}$ (Step 1a). For Step 1b, the same apo receptor snapshot was used. To model the increased rigidity of PTH residues 19–34, PTH(19–34) from the NMR structure was replaced by PTH(19–34) helix from the crystal structure. Also, the secondary structure of PTH(6–15) was changed to α-helix in PyMOL. To show engagement of PTH N-terminal part with $PTHR^{TMD}$ (Step 2a), we selected an apo receptor snapshot in which $PTHR^{ECD}$ is bent down toward $PTHR^{TMD}$. The PTH model from Step 2a was docked to $PTHR^{ECD}$ as described above. For Steps 1b and 2a, the PTH models were minimized using the *clean* command in PyMOL. The PTH–PTHR models were additionally optimized using sculpting in PyMOL. The Step 2b model (i.e., continuous PTH helix formation) is the snapshot of PTH^{WT}–PTHR after 200 ns simulation.

3.3 Results

3.3.1 Effects of $PTHR^{ECD}$ on PTH conformation

We tested the hypothesis that the initial binding of the parathyroid hormone (PTH) C-terminal part (residues 16–34) to the receptor ECD ($PTHR^{ECD}$) induces a conformational change within its N-terminal part (residues 1–15), which facilitates its engagement with the receptor TMD ($PTHR^{TMD}$) during the second step[170]. To this end, we collected two-dimensional ^{1}H-^{15}N transverse relaxation optimized spectroscopy (TROSY) nuclear magnetic resonance (NMR) spectra of purified and fully functional ^{15}N-labeled PTH in the absence and presence of a submolar ratio of unlabeled $PTHR^{ECD}$ (Figure 3.1, Appendix Figure 9, Appendix Figure 12). To promote folding and facilitate purification, $PTHR^{ECD}$ was expressed and purified as PTHR(29–187) with an N-terminal maltose-binding protein fusion, as previously described[42].

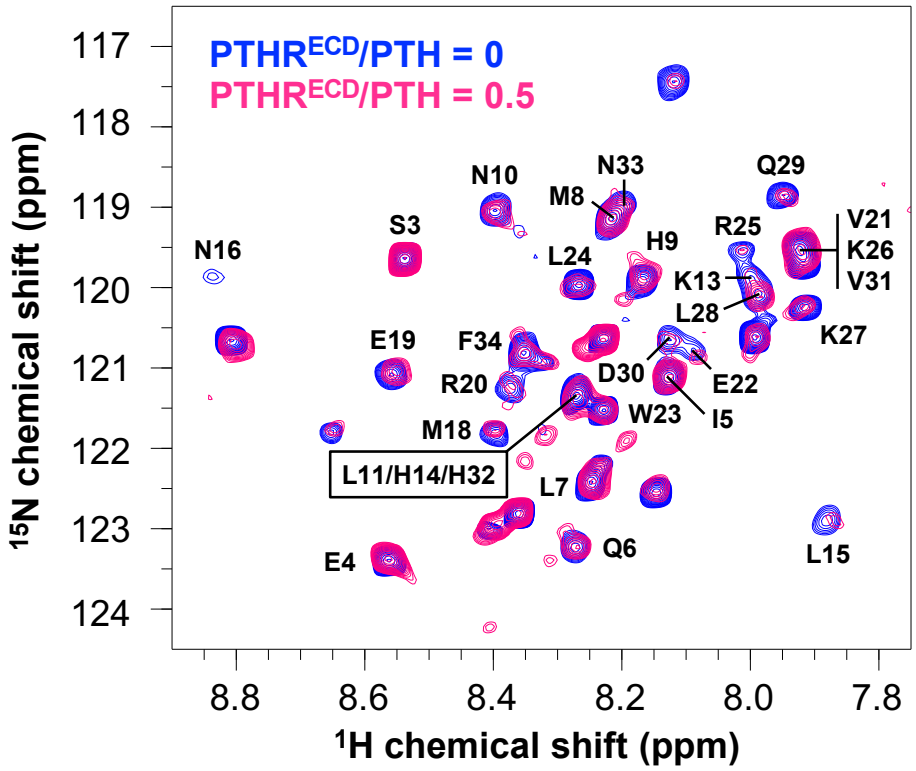

Figure 3.1. Two-dimensional ^{1}H-^{15}N transverse relaxation optimized spectroscopy (TROSY) spectra of ^{15}N-PTH in the absence (blue) and presence (pink) of 0.5 molar ratio PTHR^{ECD}.

PTH peaks are labeled with bold text.

Binding of ^{15}N-PTH to PTHR^{ECD} significantly reduces the peptide's molecular tumbling, thus decreasing NMR peak intensity as measured by peak height (Appendix Figure 13a). To quantitatively account for these changes, the peak intensity for each PTH residue was normalized with respect to that of PTH Ser3, which did not change significantly in the presence of PTHR^{ECD} (Figure 3.1). In these experiments, PTH residues that experience reduced mobility upon binding to PTHR^{ECD}, either through direct interactions with PTHR^{ECD} or through induced conformational changes, show a larger reduction in peak intensities. The extent of reduced mobility for a residue is estimated by calculating the ratio of peak intensities in the presence and absence of PTHR^{ECD} (I_{bound}/I_{free}, Figure 3.2a, c). In addition, the change in chemical shift upon addition of PTHR^{ECD}

(i.e., chemical shift perturbation, Δδ) estimates the relative modification of that residue's chemical environment upon binding to $PTHR^{ECD}$ (Figure 3.2b, d) (see Section 3.2.2). The overall trends of I_{bound}/I_{free} and chemical shift perturbation with 0.5 molar ratio $PTHR^{ECD}$ (Figure 3.2) were mirrored in NMR data collected in the presence of 0.75 molar ratio $PTHR^{ECD}$, thus indicating that an increased concentration of PTH–$PTHR^{ECD}$ complex did not alter how PTH interacts with $PTHR^{ECD}$ (Appendix Figure 13b, c). Note that residues 15–17 at 0.75 $PTHR^{ECD}$/PTH molar ratio were not included in the quantitative data analysis because of their extremely weak NMR signal (Appendix Figure 12, Appendix Figure 13).

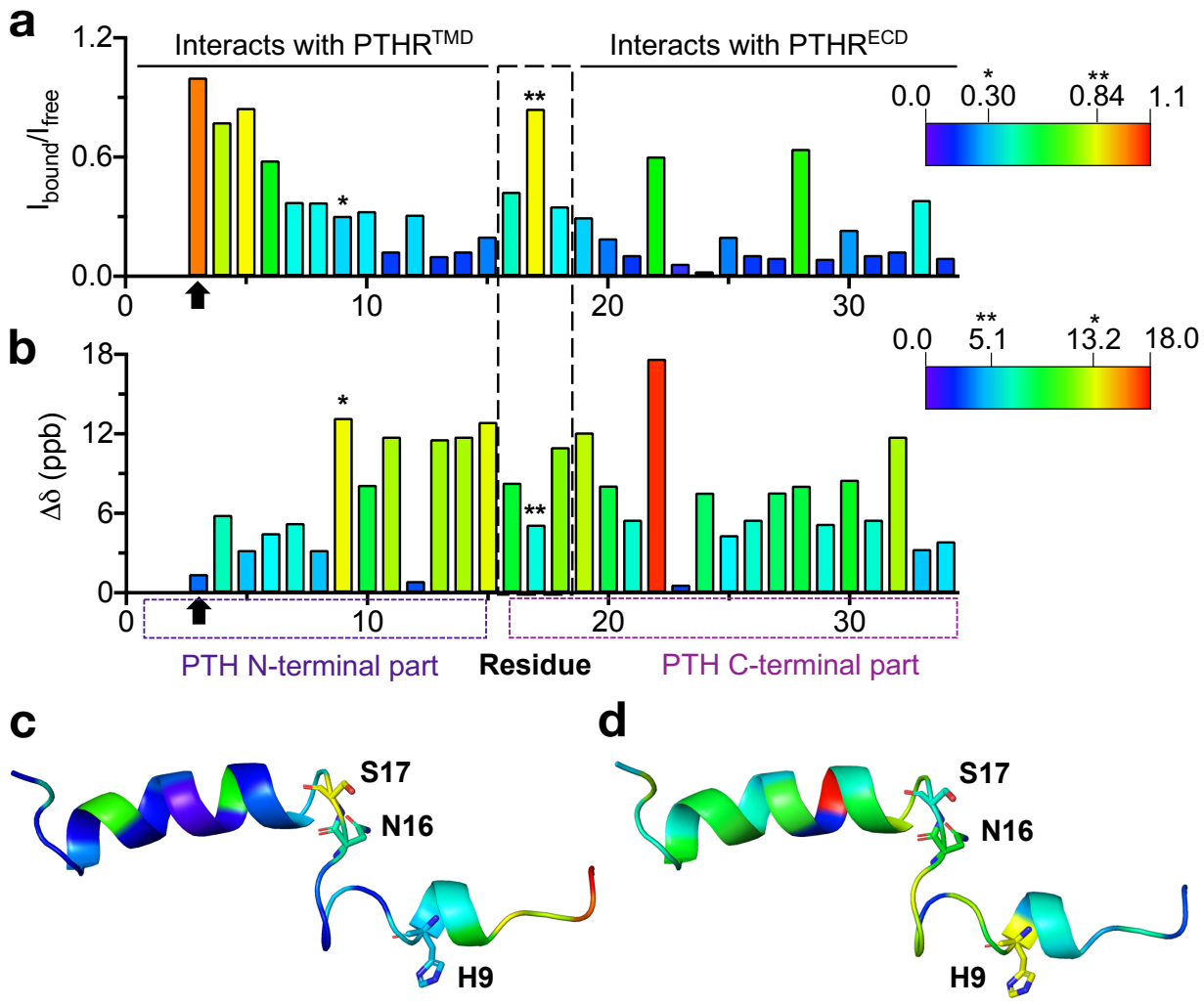

Figure 3.2. NMR analysis uncovers new molecular aspects of the PTH–PTHR binding mechanism.

a, For each residue, TROSY peak intensity (height) in the presence of 0.5 molar ratio PTHR^{ECD} relative to intensity in the absence of PTHR^{ECD} (I_{bound}/I_{free}) indicates the extent of reduced mobility upon PTH binding to PTHR^{ECD}. Peak intensity for each residue was normalized with respect to that of residue Ser3 prior to the calculations of I_{bound}/I_{free}. Bars are colored according to I_{bound}/I_{free} values, from most restricted (small I_{bound}/I_{free}, indigo) to most retained mobility (large I_{bound}/I_{free}, red). **b,** For each residue, TROSY peak chemical shift perturbation (Δδ) in the presence of 0.5 molar ratio PTHR^{ECD} indicates the extent of chemical environment change upon PTH binding to PTHR^{ECD}. Bars are colored from small (indigo) to large (red) chemical shift perturbations. For **a** and **b**, Ser3 is indicated by an arrow. His9 is indicated by a single asterisk, and Ser17 is indicated by a double asterisk. PTH residues 1–15 interact with PTHR^{TMD}. The central flexible region of the peptide, residues 16–18, is indicated by a large-dashed box. Residues 19–34 interact

with $PTHR^{ECD}$. PTH N- (residues 1–15) and C-terminal (residues 16–34) parts are indicated by small-dashed boxes. **c, d,** Structure of free PTH (PDB 1ZWA) colored according to I_{bound}/I_{free} values (**c**) and to chemical shift perturbation (**d**). His9, Asn16, and Ser17 are shown as sticks.

In the previously reported NMR structural ensemble of free PTH (PDB 1ZWA)[150], residues Glu19–Asp30 form an α-helix and a stable helical turn is detected at Gln6–His9, while the other peptide regions are highly flexible. The C-terminal residues Glu19–Asp30 generally exhibit small I_{bound}/I_{free} values and modest changes in chemical shifts, suggesting that this region interacts with $PTHR^{ECD}$ and maintains its helical structure (Figure 3.2a, b, Appendix Figure 13b, c) as seen in the crystal structure of $PTHR^{ECD}$ bound to PTH(15–34) (PDB 3C4M)[42]. Glu22 (Figure 3.2b, red bar) exhibits a large shift, suggesting a change in chemical environment. Based on the structures of PTH in free (PDB 1ZWA) and bound (PDB 3C4M) states, this shift may be caused by breaking an ionic interaction between Glu22 and Arg25 upon $PTHR^{ECD}$ binding[42,150], as Arg25 interacts with the main chain carbonyl of PTHR stalk residue Leu174[42]. Changes in position/orientation of nearby Met18, Val21, and Trp23 side chains may also account for the large chemical shift perturbation. However, the chemical environment of Glu22 does not result in a significant change in its mobility (Figure 3.2a, green bar), as the Glu22 sidechain remains facing solvent after PTH binding[42,150]. Leu28 retains its mobility after PTH binding to $PTHR^{ECD}$ (Figure 3.2a, green bar). Hydrophobic Leu28 faces the $PTHR^{ECD}$ in the PTH–$PTHR^{ECD}$ structure, but these interactions may not significantly change Leu28 mobility, as Leu28 is α-helical in both free and bound forms[42,150].

PTH Ser17 stands out as having an I_{bound}/I_{free} ratio close to 1 (Figure 3.2a, Appendix Figure 12a, Appendix Figure 13b), indicating that its mobility is minimally affected by binding. In the aforementioned NMR ensemble[150], Asn16–Met18 participate in the central flexible region that

connects the N- and C-terminal portions of the peptide, and the conformational flexibility at this site is largely maintained after binding to $PTHR^{ECD}$, as supported by our NMR data. The mobility of residues His9–Leu15, on the other hand, is dramatically decreased in the presence of $PTHR^{ECD}$. Larger chemical shift perturbations in the same region (except Gly12) are also induced, with His9 experiencing the largest change. These data demonstrate that PTH binding to $PTHR^{ECD}$ triggers a distinct and more structured conformation in the N-terminal region of PTH, independently of the interaction with $PTHR^{TMD}$.

3.3.2 Expanded mechanism of PTH binding to PTHR

We further investigated the PTH binding mechanism using MD simulations and modeling. Using the 3.0 Å cryo-EM structure of active full-length PTHR bound to the stimulatory G protein (G_s) and a long-acting PTH analog (LA-PTH) (PDB 6NBF)[24], we generated models of ligand-free (apo) and PTH-bound PTHR, embedded in a lipid bilayer composed of 75% POPC and 25% cholesterol. POPC is a standard lipid for MD simulations of GPCRs[174-176]. We included high percentage of cholesterol to mimic the plasma membrane composition[177,178]. Furthermore, cholesterol is required to stabilize purified GPCRs, including PTHR[24]. For each model, we performed 200 ns atomistic MD simulations in triplicate. Simulations showed that the $PTHR^{ECD}$ flexibility was significantly high in the absence of ligand but suppressed upon peptide binding (Figure 3.3).

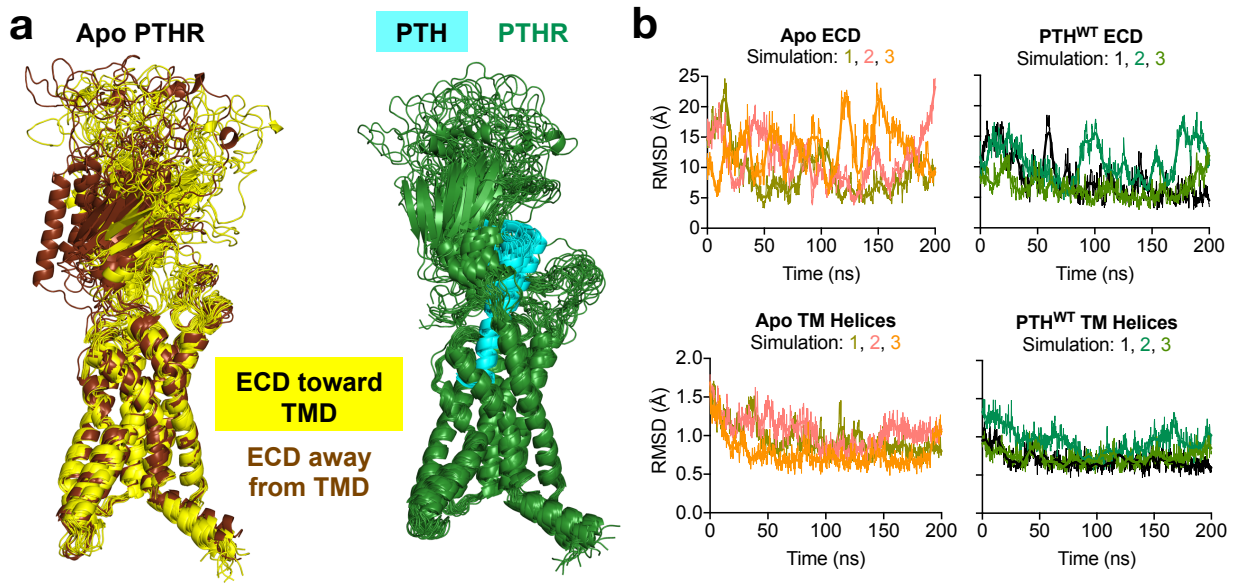

Figure 3.3. MD simulations of apo and PTH-bound receptor.

a, Snapshots of apo and PTH^{WT}-bound receptor collected every 10 ns during simulations (50 ns to 200 ns), aligned using PTHR TM helices. In the *left panel*, apo PTHR snapshots where $PTHR^{ECD}$ moved away from $PTHR^{TMD}$ are colored brown, and those snapshots with $PTHR^{ECD}$ oriented toward $PTHR^{TMD}$ are colored yellow. In the *right panel*, the receptor is dark green, and PTH is cyan. **b,** Root-mean-square deviation (RMSD) in residue coordinates with respect to their average positions, observed during the course of three sets of 200 ns simulations for $PTHR^{ECD}$ (residues 27–179; upper panels) and the PTHR TM helices (lower panels; see Section 3.2.3.3 for methods) for each 200 ns simulation. Note the lower RMSDs in the presence of PTH. Raw data are shown as thin lines. Second-order smoothed data (over 30 neighbors) are shown as thick lines.

Also, the interactions observed between the PTH C-terminal helix and the $PTHR^{ECD}$ during the course of simulations mirrored closely those in the PTH(15–34)-bound $PTHR^{ECD}$ crystal structure (Appendix Figure 14)[42]. We docked the free PTH conformers observed in the NMR structural ensemble onto $PTHR^{ECD}$ based on the position of the C-terminal helix in the PTH(15–34)–$PTHR^{ECD}$ crystal structure and determined that $PTHR^{ECD}$ must be oriented away from $PTHR^{TMD}$ to permit PTH(16–34) binding while minimizing clashes between PTH(1–15) and extracellular loops 1 and 2 (ECL1, ECL2) of the $PTHR^{TMD}$ (Figure 3.4).

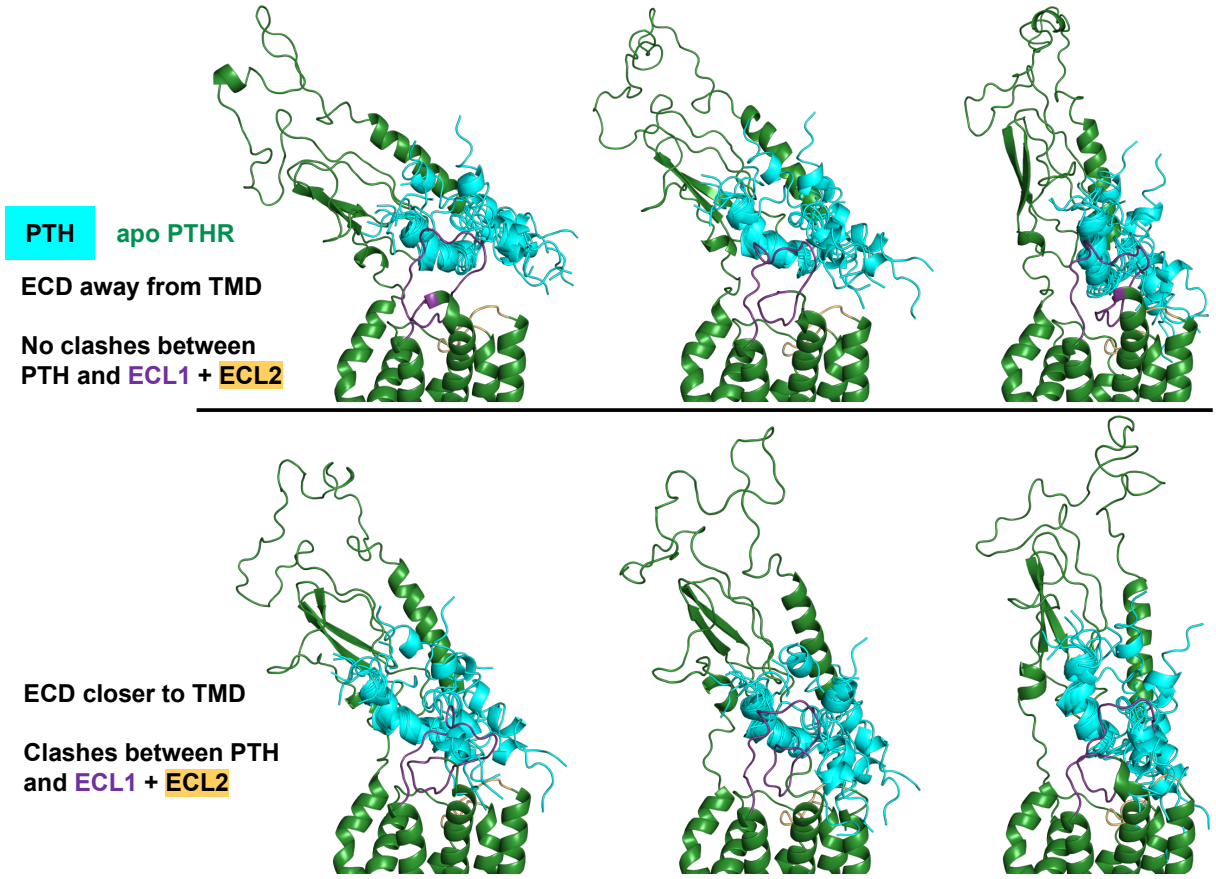

Figure 3.4. Docking of PTH onto PTHR^{ECD} in the apo state using conformers from MD.

The NMR structural ensemble of free PTH (cyan, PDB 1ZWA) was docked onto MD snapshots of apo PTHR (dark green, see Section 3.2.4 for docking protocol). When the PTH ensemble is docked onto PTHR^{ECD} oriented toward PTHR^{TMD}, the N-terminal portion of PTH clashes significantly with extracellular loops 1 and 2 (ECL1 and ECL2, colored purple and light orange, respectively). These clashes are reduced when the PTH ensemble is docked onto PTHR^{ECD} oriented away from PTHR^{TMD}.

3.4 Discussion

From these data, along with the NMR results, we propose an expanded two-step model of PTH binding to PTHR (Figure 3.5). First, initial contacts take place between the C-terminal part of PTH and $PTHR^{ECD}$ (Figure 3.5, Step 1a). Residues Glu19–Asp30, which preferentially form an α-helix even in isolation, maintain their α-helical state, now further stabilized by interfacial contacts with the $PTHR^{ECD}$ and likely extending up to Phe34 (Figure 3.5, Step 1b; see also Appendix Figure 14), as evidenced by the small I_{bound}/I_{free} values of these residues (Figure 3.2a, c). Our NMR data further showed that the flexibilities of residues Gln6–Leu15 decreased in the presence of $PTHR^{ECD}$ (Figure 3.2a). Since residues Gln6–His9 already form a helical turn in the free peptide (Figure 3.2c, d), the helix may propagate to adjacent residues Asn10–Leu15 in the presence of $PTHR^{ECD}$ (Figure 3.5, Step 1b). The helix-forming capability of Asn10–Leu15 has been previously demonstrated in the crystal structure of PTH (PDB 1ET1)[179]. Residues Asn10–Lys13 are also α-helical in the NMR structure of PTH in the presence of helix-stabilizing 20% trifluoroethanol (PDB 1HPY)[150]. Although Gly12 experiences small chemical shift perturbation in the presence of $PTHR^{ECD}$ (Figure 3.2b), it does encounter a significant reduction in peak intensity (Figure 3.2a). The small I_{bound}/I_{free} values and large chemical shift perturbations of flanking residues (i.e., His9–Leu11, Lys13–Leu15) suggest that the Gln6–His9 α-helix propagates continuously to Leu15.

The conformational change near His9 could explain the new NMR peak observed in the presence of $PTHR^{ECD}$ (Appendix Figure 12c). Also, the conformational change in Leu15 could explain the new peak observed at the adjacent residue Asn16 in the presence of $PTHR^{ECD}$ (Appendix Figure 12d). Next, the relatively loose packing at the interface between the $PTHR^{ECD}$

and the $PTHR^{TMD}$, along with the conformational flexibility of the PTH central residues Asn16–Met18, especially Ser17, permits the insertion of the N-terminal helix into the $PTHR^{TMD}$ (Figure 3.5, Step 2a). Ultimately, this step results in a continuous PTH helix that connects $PTHR^{ECD}$ and $PTHR^{TMD}$ and can account for the slow kinetics observed in live-cell FRET experiments measuring PTH binding during the second step (Figure 3.5, Step 2b)[170].

This study proposes an updated two-step mechanism of PTH binding to PTHR that could serve as a model for class B GPCRs. We utilized a combination of NMR experiments and MD simulations to describe how the initial binding of the PTH C-terminal part to $PTHR^{ECD}$ increases structural rigidity to the PTH N-terminal part independently from interactions with $PTHR^{TMD}$. We predict that these changes prime the interactions between the PTH N-terminal portion and $PTHR^{TMD}$ to promote the formation (or propagation) of an α-helical peptide structure. Such placement of the PTH N-terminal part, especially of residues 1–4, stabilizes the active receptor conformation, given that N-terminal PTH residues 1–4 are essential to trigger receptor coupling to G proteins and cAMP production[24,118,141]. Furthermore, we demonstrate that the mobility of $PTHR^{ECD}$ is critical for PTH binding. A recently published MD simulation of apo GLP-1R also observed a mobile ECD oriented away from the TMD[180], suggesting that the importance of a mobile ECD in ligand binding is applicable to all class B GPCRs. Finally, we hypothesize that interactions between PTH residues 5–14 and $PTHR^{TMD}$ during ligand binding affect the position of the PTH helix within the $PTHR^{TMD}$ and stabilize receptor conformations critical for specific G protein and/or β-arrestin coupling. We explore this hypothesis further in Chapter 4.0, where we study the structural mechanisms of two PTH mutants that impair β-arrestin recruitment.

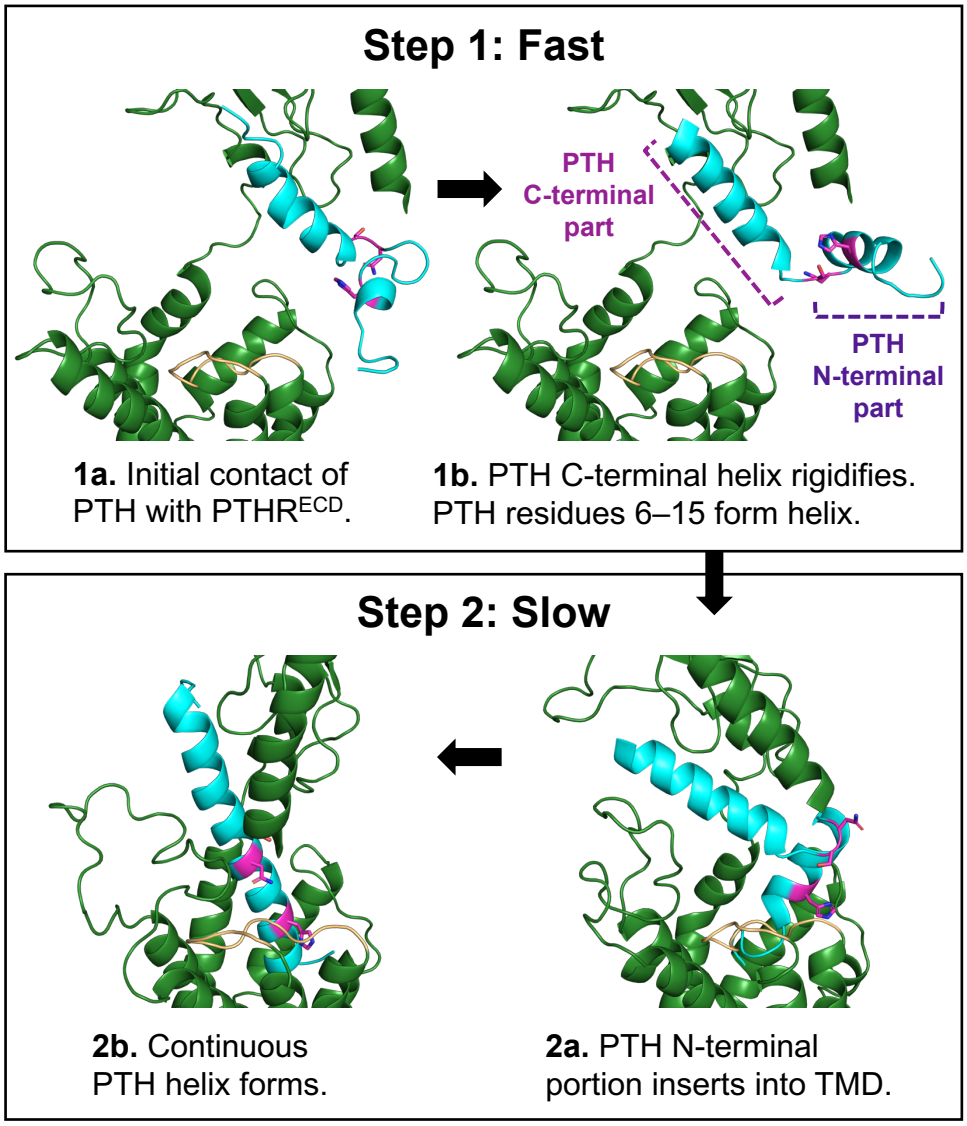

Figure 3.5. Expanded two-step model of PTH binding to PTHR.

PTHR is colored dark green, with ECL2 highlighted in light orange. PTH is colored cyan, with residues His9, Asn16, and Ser17 displayed as magenta sticks. In the fast first step (Step 1), binding of the C-terminal part of PTH to $PTHR^{ECD}$ (Step 1a) rigidifies the C-terminal helix as well as residues 6–15 within the N-terminal part of PTH (Step 1b). These conformational changes may expand the small N-terminal helix from residues 6–9 to 6–15. In the slow second step (Step 2), the N-terminal part of PTH is inserted into $PTHR^{TMD}$ (Step 2a). Interactions between the N-terminal portion of PTH and the $PTHR^{TMD}$, including ECL2, promote the formation of a continuous PTH helix (Step 2b).

3.5 Acknowledgements

Research reported in this chapter was supported by the National Institute of Diabetes and Digestive and Kidney Disease (NIDDK), the National Institute of General Medical Sciences (NIGMS), the National Institute of Arthritis and Musculoskeletal and Skin Diseases (NIAMS), and the National Institute on Drug Abuse (NIDA) of the US National Institutes of Health (NIH) under grant Awards Number R01-DK111427, R01-DK116780, and R01-DK122259 (to Jean-Pierre Vilardaga), P41-GM103712 and P30-DA035778 (to Ivet Bahar), R01-DA046939 (Pei Tang), and F31-AR074843 (to Lisa Jean Clark).

3.6 Author contributions

Lisa Jean Clark performed and analyzed NMR studies with Vasyl Bondarenko and Pei Tang, and MD simulations with James Krieger, Pemra Doruker, and Ivet Bahar. Ieva Sutkeviciute. designed and optimized purification for the PTH construct. The original manuscript from which this chapter was adapted was written by Lisa Jean Clark, Ieva Sutkeviciute, Ivet Bahar, and Jean-Pierre Vilardaga.

4.0 Allosteric interactions in PTHR–β-arrestin complex formation

The structural mechanisms that link interactions between class B G-protein-coupled receptors (GPCR) and their peptide ligands to the intracellular receptor–arrestin interactions are not fully understood. Using signaling experiments and computational approaches, we discovered that the PTH peptide carries signal-selective residues that are essential for the coupling of PTHR with β-arrestins but not G proteins. Individual mutation of these two 'hot-spot' PTH residues, His9→Ala9 (PTH^{H9A}) or Leu7 L→D (PTH^{7d}), inhibits β-arrestin coupling through distinct mechanisms, leading to transient (PTH^{H9A}) and sustained (PTH^{7d}) cAMP production at the plasma membrane. PTH^{H9A} promotes an inward conformation of PTHR intracellular loop 3 that prevents interactions with β-arrestin's finger loop. In contrast, PTH^{7d} enhances a receptor polar network that stabilizes an outward kink of the intracellular part of transmembrane helix 6 (TM6), preventing the inward TM6 movement necessary for β-arrestin coupling. These results unveil structural determinants for PTHR–β-arrestin complex formation, demonstrate that the position of PTH peptides within the transmembrane domain effect the intracellular receptor conformation and bias PTHR signaling, and likely extend to other class B G-protein-coupled receptors.

This chapter was adapted from the following manuscripts:

Lisa J. Clark*, James Krieger*, Alex D. White, Vasyl Bondarenko, Saifei Lei, Fei Fang, Ji Young Lee, Pemra Doruker, Thore Böttke, Frederic Jean-Alphonse, Pei Tang, Thomas J. Gardella, Kunhong Xiao, Ieva Sutkeviciute, Irene Coin, Ivet Bahar†, Jean-Pierre Vilardaga†. Allosteric

interactions in the parathyroid hormone GPCR–arrestin complex formation *Nat. Chem. Biol.* doi: 10.1038/s41589-020-0567-0 (2020). *Contributed equally to this study. †Corresponding authors.

Alex D. White*, Karina A. Peña*, Lisa J. Clark*, Zhiqiang Cheng, Shi Liu, Fei Fang, Frédéric G. Jean-Alphonse, Chia-Ling Tu, Nicholas Szeto, Asuka Inoue, Thomas J. Gardella, Samuel H. Gellman, Kunhong Xiao, Wenhang Chang, and Jean-Pierre Vilardaga†. Regulation of parathyroid hormone receptor biological effectiveness via location bias in cAMP signaling. (2020). *In revision in Science Signaling.* *Contributed equally to this study. †Corresponding author.

4.1 Introduction

GPCR biased ligands promote selectively one signaling pathway over another (e.g., G_s vs. β-arrestin) relative to wild-type ligands. However, the molecular mechanisms of class B GPCR biased agonists and other peptides with altered signaling are not well understood[16]. In this chapter, we utilize MD simulations, structural modeling, signaling experiments, and photo-crosslinking coupling to mass spectrometry to investigate two such peptides of PTHR: PTH^{H9A} and PTH^{7d}.

During our investigation of PTHR ligand protonation and its effects on signaling, we mutated each PTH histidine residue to alanine, under the assumption that a mutation would increase sustained cAMP signaling if protonation of that residue in endosomes promoted ligand dissociation (see Section 2.2.2). Unexpectedly, alanine substitution of PTH His9 (PTH^{H9A}) eliminated sustained cAMP signaling through lack of β-arrestin recruitment to PTHR (Figure 2.11). PTH His9 also experienced the largest NMR chemical shift perturbation among the PTH

residues that are interacting with the $PTHR^{TMD}$ (Figure 3.2b, d). In our binding model, His9 comes into proximity of PTHR ECL2 (Ala347–Gly357, colored light orange in Figure 3.5) and could assist in positioning the PTH helix within the $PTHR^{TMD}$ to permit receptor activation. We sought to further elucidate the functional importance of His9 by studying PTH^{H9A}.

Backbone modifications of PTH peptides, such α→β amino acid replacements, have altered peptide selectivity to PTHR versus PTH2R, improved peptide stability in the presence of proteases, and triggered biased agonism[181-183]. For example, replacing L-α-Leu7 with (R*)-β^2- or (S*)-β^3-Leu7 caused PTHR-selective agonism, while the (S*)-β^2-Leu7 substitution maintained agonism of both PTHR and PTH2R[182]. Also, the (R*)-β^2-Leu7 substitution caused G_s bias[183]. In an earlier study, substitution of Leu7 with natural and unnatural amino acids changed EC_{50} values of cAMP production and β-arrestin recruitment, and multiple peptides demonstrated G_s bias[184]. Overall, these results suggested that Leu7 is amenable to substitutions, and binding of mutant peptides to PTHR may trigger distinct responses. To this end, we synthesized a PTH variant in which L-Leu7 is replaced with D-Leu7 (i.e., PTH^{7d}) for comparison with wild-type PTH.

4.2 Methods

4.2.1 Cell culture and transfection

Cell culture reagents were obtained from Corning (CellGro). Human embryonic kidney (HEK-293; ATCC, Georgetown, DC) cells stably expressing the recombinant human PTHR were grown in selection medium (DMEM, 5% FBS, penicillin/streptomycin 5%, 500 μg/mL neomycin) at 37°C in a humidified atmosphere containing 5% CO_2. For transient expression, cells were

seeded on glass coverslips coated with poly-D-lysine in six-well plates and cultured for 24 hours prior to transfection with the appropriate cDNAs using Fugene-6 (Promega) or Lipofectamine 3000 (Life Technologies) for 48-72 h before experiments. We optimized expression conditions to ensure the expression of fluorescently labeled proteins was similar in examined cells by performing experiments in cells displaying comparable fluorescence levels.

4.2.2 Chemicals and peptides

Forskolin (#344270) was purchased from EMD-Millipore. PTH, PTH^{TMR}, LA-PTH were synthesized and characterized as previously described[114]. PTH^{H9A} was synthesized by LifeTein and received in lyophilized form. PTH^{H9A} was resuspended in 10 mM acetic acid to make 1 mM peptide aliquots.

(*D*)-Leu(7)-PTH-NH_2 (PTH^{7d}) was synthesized by microwave-assisted reactions on NovaPEG Rink amide resin. For each coupling step, the resin was treated with 4 equivalents of protected amino acid, 4 equivalents of HATU, and 8 equivalents of *N,N*-diisopropylethylamine (DIEA) in DMF. Fmoc deprotection was carried out by using 20% (v/v) piperidine with 0.1 M HOBT in DMF. Upon completion of the synthesis, the peptide was cleaved from the resin using a solution of 94% trifluoroacetic acid (TFA), 2.5 % H_2O, 2.5% 1,2-ethanedithiol (EDT), and 1% triisopropylsilane (TIS). After the cleavage, the crude peptide was precipitated by addition of cold diethyl ether. The precipitated material was purified by preparative HPLC. Peptide purity was assessed by UPLC (BEH C18 stationary phase, 2.1 mm x 100 mm, the solvent gradient was 10-60% acetonitrile over 5 min), and peptide mass was checked by MALDI-TOF MS. The peptide reported here was > 95% pure as determined by UPLC. Since PTH^{7d} contains one tryptophan in its sequence, the peptide concentration was determined by UV spectroscopy using the absorbance

at 280 nm (the molecular extinction coefficient of tryptophan at 280 nm is 5690 $M^{-1}cm^{-1}$). After concentration determination, the peptide was aliquoted, lyophilized to dry powder, and stored at -20 ºC.

4.2.3 MD simulations

4.2.3.1 System preparation

The 3.0 Å cryo-EM structure of LA-PTH–PTHR–G_s–Nb35 complex (PDB 6NBF)[24] was used to generate initial PTHR models. I-TASSER was then used to model flexible loops absent in the cryo-EM structure: ECD residues 56–104, ECL1 residues 247–275, and ICL3 residues 394–398[154-156]. In PyMOL[157], structures of G_s, Nb35, palmitic acid, and cholesterol were removed. The LA-PTH was also removed to generate an initial apo PTHR model. For the PTH-bound model, LA-PTH residues were mutated to the corresponding PTH residues, as necessary, using the PyMOL Mutagenesis Wizard. His9 on PTH was then mutated to alanine using the PyMOL Mutagenesis Wizard to generate the PTH^{H9A}–PTHR model. The chirality of Leu7 in the PTH^{WT} model was changed in PyMOL to generate the PTH^{7d}–PTHR model. Each initial model was oriented in a model membrane using the Orientations of Proteins in Membranes (OPM) PPM Server[159]. Using oriented models, inputs for Nanoscale Molecular Dynamics (NAMD) were generated using CHARMM-GUI Membrane Builder[158,160-165]. Disulfide bonds Cys48-Cys117, Cys108-Cys148, Cys131-Cys170, and Cys281-Cys351 were specified to ensure correct formation. A heterogeneous lipid bilayer consisting of 75% POPC and 25% cholesterol was assembled around the receptor model using the Replacement Method. The system was solvated in a box of TIP3P waters, and ions were added to a concentration of 150 mM NaCl using Monte Carlo sampling.

4.2.3.2 Unbiased MD simulations

All-atom simulations were performed in triplicate for apo, PTH-bound, PTH^{H9A}-bound, and PTH^{7d}-bound models using NAMD with the CHARMM36m force field[166,167]. Prior to production simulations, 10,000 steps of conjugate gradient energy minimization were performed followed by 0.675 ns equilibration in which restraints were applied and then slowly released over six steps following the protocol established by the CHARMM-GUI group[158]. Next, 200 ns production simulation with 2 fs timestep was performed. Non-bonded interactions were cut off at 12.0 Å, and van der Waals force switching was applied between 10.0 Å and 12.0 Å. Langevin dynamics and Langevin piston were used to maintain temperature at 303.15 K and pressure at 1 atm.

4.2.3.3 Accelerated MD simulations

Accelerated MD (aMD) simulations was performed using NAMD for apo PTHR[166,185,186], starting with the receptor system after equilibration (see above). In NAMD[166], aMD was performed in dual boost mode, meaning independent boost potentials were applied to dihedral potential and (Total – dihedral) potential. The threshold energy E_d and acceleration factor α_d for the dihedral potential were calculated using the relations $E_d = 1.3V_d$ and $\alpha_d = 0.06V_d$ where V_d is dihedral energy. The threshold energy E_{T-d} and acceleration factor α_{T-d} for (Total – dihedral) were calculated using $E_{T-d} = V_T + 0.2\ N_a$ and $\alpha_{T-d} = 0.2N_a$ where V_T is total potential energy, and N_a is total number of atoms in the system. All other simulation parameters were the same as in unbiased MD.

4.2.3.4 MD trajectory analysis

MD trajectories were analyzed in Visual Molecular Dynamics (VMD) and PyMOL[157,168]. PTHR snapshots were aligned using receptor TM helices ($PTHR^{TMD}$ without ECLs or ICLs: residues 180–211, 218–246, 280–311, 317–343, 359–392, 399–425, 435–460). RMSD of $PTHR^{ECD}$ (residues 27–179) and PTHR TM helices were acquired for each trajectory. Distances between PTHR Thr392 Cα (in kink 5) and Val455 Cα (in TM7) were calculated using the VMD distance.tcl script. Val455 Cα was chosen as a reference atom because it experienced little movement throughout the 200 ns simulations (RMSD = 0.55 Å, Figure 4.5). RMSD and distance data were analyzed and plotted in GraphPad Prism[152]. PTH Glu4 hydrogen bond analysis was performed using HBonds Plugin in VMD. Number of hydrogen bonds throughout the trajectories was plotted in GraphPad Prism (Figure 4.12d).

4.2.4 Structural modeling

The models of PTHR bound to β-arrestin-1 were generated using snapshots of PTH^{WT}–PTHR after triplicate 200 ns simulation. Three structures of GPCR–arrestin complexes were used to generate these models: rhodopsin–visual-arrestin-1 (PDB 5W0P, Model 1)[77], M2R–β-arrestin-1 (PDB 6U1N, Model 2)[187], and NTSR1–β-arrestin-1 (PDB 6UP7, Model 3)[188]. PyMOL was used to perform structural, sequence-independent alignment of the TMD of the GPCR–β-arrestin-1 template structure to the $PTHR^{TMD}$ (residues 180–460) from each snapshot (Table 2). The PTHR snapshot with the lowest RMSD was used for the final model, and the template GPCR was subsequently removed.

Table 2. Structural alignment of GPCR–arrestin template structures with PTH^{WT}–PTHR snapshots.

RMSD (Å) from each alignment is displayed. The PTH^{WT}–PTHR snapshot with the lowest RMSD (bold) would be used for that PTHR–β-arrestin-1 complex model.

	PTH^{WT}–PTHR Run 1	PTH^{WT}–PTHR Run 2	PTH^{WT}–PTHR Run 3
Rhodopsin–arrestin (PDB 5W0P) TMD residues 34–307	6.615	**4.650**	7.266
M2R–β-arrestin-1 (PDB 6U1N) TMD residues 20–441	5.169	11.136	**5.033**
NTS1R–β-arrestin-1 (PDB 6UP7) TMD residues 59–365	**7.082**	7.176	8.673

For Model 1, a homology model of human β-arrestin-1 in the receptor core conformation was generated in SWISS-MODEL using the structure of visual arrestin-1 as a template[189,190]. The β-arrestin-1 model was aligned with visual arrestin-1 in PyMOL. Minor side chain clashes between PTHR and β-arrestin-1 were eliminated using sculpting in PyMOL. To assess the structural effects of PTH^{H9A} and PTH^{7d} on β-arrestin coupling, PTH^{H9A}–PTHR and PTH^{7d}–PTHR snapshots after 200 ns simulation were then aligned with PTH^{WT}–PTHR.

Models of PTH^{7d}–PTHR and PTH^{H9A}–PTHR bound to G_s were generated by aligning receptor TM helices from MD snapshots after 200 ns with the structure of PTHR–G_s complex (PDB 6NBF)[24]. Minor side chain clashes between PTH^{7d}–PTHR and G_s were eliminated using sculpting in PyMOL.

4.2.5 Anisotropic network model (ANM) analysis

In the ANM, the protein is represented as a network where residues serve as the nodes, the positions of which are identified by those of the α-carbons. We used the 3.0 Å cryo-EM structure of LA-PTH–PTHR–G_s–Nb35 complex (PDB 6NBF)[24] to generate an initial PTH–PTHR model composed of a total of 455 residues for receptor and 34 residues for PTH (the same as the initial structure in our MD simulations). We built a membrane using an SC lattice with an edge length of

6.2 Å between nearest neighbors with 5 layers and a circular shape with 100 Å radius from the center of the protein (a total of 3,953 nodes for membrane). The protein was positioned into the membrane using the OPM database[159]. Our network model (receptor, ligand, and membrane) had a total of N = 4,442 nodes and $3N$-6 (13,320) normal modes that form a complete basis set for all possible motions of the $3N$-dimensional structure. The overall potential is represented as the sum of harmonic potentials between pairs of nodes within an interaction range (C^{α}-C^{α} distance < 15 Å). The spring constants for the $3N \times 3N$ interactions (N nodes in $3D$) are given by the elements of the Hessian matrix **H**. The inverse $\mathbf{H}^{-1}$ is proportional to the covariance matrix **C**. i.e. the cross-correlations between residue fluctuations away from their mean position. **C** can be written as a sum of correlations contributed by normal modes which are calculated by eigenvalue decomposition of **H**. Figure 4.1a displays the normalized correlation matrix corresponding to mode 14, evaluated by dividing the off-diagonal elements of **C** by the corresponding diagonal elements. Individual rows or columns corresponding to PTH residue His9 or PTHR residue Thr392 were extracted from this matrix and equivalent ones for other modes to produce the colored structures in Figure 4.1a and plots in Appendix Figure 15. To generate a conformation along a given ANM mode k, we use the following equation: $\mathbf{R}^{(k)} = \mathbf{R}^{(0)} \pm s\lambda_k^{-1/2} \boldsymbol{u}_k$, where $\mathbf{R}^0$ is a $3N$-dimensional vector representing initial coordinates, λ_k is the eigenvalue for mode k, and $\boldsymbol{u_k}$ is the corresponding eigenvector. All computations were performed using the ProDy API[191,192].

4.2.6 Immunoprecipitation and Western blots

HEK-293 cells stably expressing hemagglutinin (HA)-tagged PTHR and cultured on a 10-cm dish were stimulated with PTH-NH2 or analogues at 100 nM for 5 min. Cells were then washed with ice-cold PBS prior to crosslinking for 2 h with dithiobis(succinimidyl propionate) (DSP,

Covachem, #13301) in PBS at 4°C. The reaction was stopped by addition of 10 mM Tris–HCl for 10 min and cell lysates were prepared using lysis buffer (1% Triton X-100, 50 mM Tris–HCl pH 7.4, 140 mM NaCl, 0.5 mM EDTA) containing protease and phosphatase inhibitors (Roche, #11873580001). Protein concentration was determined using BCA protein assay kit (ThermoFisher, #23225), and lysates were incubated with anti-HA agarose antibody beads (Sigma-Aldrich; #A2095 clone HA-7) overnight at 4°C. Elution was done using LDS loading buffer (Life Technologies), and samples were loaded on 10% SDS-PAGE and transferred to nitrocellulose membrane. We used primary antibodies against HA (Covance, clone 16B12, Mouse IgG1) and β-arrestin1/2 (Cell Signaling; #4674, clone D24H9, Rabbit IgG); anti-Mouse HRP and anti-Rabbit HRP (Dako, Goat polyclonal) secondary antibodies were then used. Immunoreactive bands were visualized with Luminata Forte (EMD Millipore) and autoradiography film.

4.2.7 Radioligand binding

Data are the average of n = 4 to 5 independent assays. Each assay consists of 11 analog concentrations per analog, with duplicate wells for each concentration point. Binding to the R^G and R^0 conformations of the human PTHR was assessed by competition reactions performed in 96-well plates by using transiently transfected COS-7 cell membranes as previously described[88,119]. In brief, binding to R^0 was assessed by using ^{125}I-PTH as tracer radioligand and including GTPγS in the reaction (1 x 10^{-5} M). Binding to R^G was assessed by using membranes containing a high-affinity, negative-dominant $G\alpha_s$ subunit ($G\alpha_s$ ND)[61], and ^{125}I-M-PTH(1–15) as tracer radioligand.

4.2.8 Time-course measurements of cAMP production, and PTHR recruitment of β-arrestin in live cells.

Cyclic AMP was assessed using FRET-based assays. Cells were transiently transfected with the FRET-based biosensors, Epac1-CFP/YFP[153] for measuring cAMP and PTHR-CFP with βarr2-YFP for measuring arrestin recruitment. Measurements were performed and analyzed as previously described[114]. In brief, cells plated on poly-D-lysine coated glass coverslips were mounted in Attofluor cell chambers (Life Technologies), maintained in HEPES buffer containing 150 mM NaCl, 20 mM HEPES, 2.5 mM KCl and 0.1–10 mM $CaCl_2$, 0.1% BSA, pH 7.4, and transferred on the Nikon Ti-E equipped with an oil immersion 40X N.A 1.30 Plan Apo objective and a moving stage (Nikon Corporation). CFP and YFP were excited using a mercury lamp. Fluorescence emissions were filtered using a 480 ± 20 nm (CFP) and 535 ± 15 nm (YFP) filter set and collected simultaneously with a LUCAS EMCCD camera (Andor Technology) using a DualView 2 (Photometrics) with a beam splitter dichroic long pass of 505 nm. Fluorescence data were extracted from single cell using Nikon Element Software (Nikon Corporation). The FRET ratio for single cells was calculated and corrected as previously described[114]. Individual cells were perfused with buffer or with the ligand for the time indicated by the horizontal bar.

4.2.9 Receptor internalization/recycling

Live-imaging trafficking of SEP-PTHR was done using a Nikon A1 confocal microscope as previously described[193]. Briefly, HEK-293 cells stably expressing a pH-sensitive GFP variant, pHluorin, inserted in the N-terminal domain of the human PTHR (SEP-PTHR) were seeded on glass coverslips coated with Poly-Lysine D (Sigma #P7280) for 24 hours. Experiments were

carried out at 37°C in FRET buffer used for cAMP experiments. Cells were stimulated by the ligand for 10 min then washed out to allow recycling. Images were acquired every 30 s.

4.2.10 Photometric FRET recordings of receptor activation kinetics

FRET experiments were performed as previously described[114]. In brief, cells grown on glass coverslips were maintained in buffer A (137 mM NaCl, 5 mM KCl, 1 mM $MgCl_2$, 20 mM HEPES, pH 7.4) at room temperature and placed on a Zeiss inverted microscope (Axiovert 200) equipped with an oil immersion X100 objective and a dual emission photometric system (Till Photonics, Germany). Cells were excited with light from a polychrome V (Till Photonics). To minimize photobleaching, the illumination time was set to 5–15 ms applied with a frequency between 1 and 75 Hz.

For receptor activation, individual cells were perfused with buffer or with the ligand for the time indicated by the horizontal bar. The emission fluorescence intensities were determined at 535 ± 15 and 480 ± 20 nm (beam splitter dichroic long-pass (DCLP) 505 nm) upon excitation at 436 ± 10 nm (DCLP 460 nm) and were corrected for the spillover of CFP into the 535-nm channel, the spillover of YFP into the 480-nm channel, and the direct YFP excitation to give a corrected FRET emission ratio F^{CFP}/F^{YFP}. Changes in fluorescence emissions due to photobleaching were systematically subtracted.

4.2.11 Statistical analysis

Data were processed using Excel 2013 (Microsoft Corp., Redmond, WA) and Prism 7.0 or 8.0[152]. Data are expressed as mean ± s.e.m. Curves were fit to the data using a four-parameter,

non-linear regression function. Statistical analyses were performed using unpaired, 2-tailed Student's *t* tests for comparisons between 2 groups. Data from binding dose–response assays were analyzed by using a sigmoidal dose–response model with variable slope. Paired data sets were statistically compared by using Student's *t* test (two-tailed) assuming unequal variances for the two sets.

4.2.12 Photo-crosslinking in cells

4.2.12.1 Cell culture

The photo-activatable amino acid p-Benzoyl-*L*-phenylalanine (Bpa) was incorporated into position 75 of β-arrestin-1 in response to the amber stop codon according to the expanded genetic code technology[194-196]. For each photo-crosslinking experiment, nine 10 cm dishes of HEK-293 cells were needed. One day before transfection, the exponentially growing cells were collected and plated at a density of 2 x 10^6 cells/dish to each poly-D-lysine pretreated plate with the appropriate complete medium. HEK-293 cells for transfection were cultured at 37°C in a humidified incubator with an atmosphere of 5% CO_2, in DMEM high glucose medium (pH 7.4, Gibco) supplemented with 5% inactivated fetal bovine serum (5% FBS, Invitrogen), and 100 U/mL penicillin and 100 μg/mL streptomycin (1% Pen-Strep, Invitrogen). Before transfection, the medium was changed to fresh medium containing 250 μM of the unnatural, UV-crosslinkable amino acid Bpa and cultured for another 1 h. Cells were transfected using the lipofectamine 3000 transfection kit (Invitrogen) with expression plasmids at 80–90% confluence with three plasmids: one carried the gene of the PTHR (3.2 μg); another contained the β-arrestin-1 gene bearing a TAG codon instead of the triplet encoding for Phe75 under the control of the CMV promoter (pcDNA3.1 vector, 3.2

ug); the third plasmid, pIRE4-Bpa, contained the humanized gene of the BpaRS derived from the *E.coli* TyrRS[194] under control of the PGK promoter and 4 tandem repeats of the amber suppressor tRNA derived from the *B. stearothermophilus* $tRNA^{Tyr}$ under control of the U6 promoter, similar as previously described (4 μg)[197]. Twenty-four hours after transfection, cells were stimulated with the desired agonists for the desired time, washed twice and irradiated with UV light (365 nm) for 15 min in cold PBS using UVP crosslinker (Analytik Jena) with 2000X 100 microjoules per cm^2 energy exposure at a 2.5 cm distance.

4.2.12.2 Calcium phosphate-mediated transient transfection

The calcium phosphate-DNA co-precipitate transient transfection method was used. The following solutions were prepared for transfection experiments, including sterilized $CaCl_2$ (2 M) and 2X HBS-buffered saline (280 mM NaCl, 1.5 mM Na_2HPO_4, 50 mM HEPES, 10 mM KCl, 12 mM Dextrose, pH 7.05). For each 15-cm dish, 960 μL of ddH_2O, 140 μL of 2 M $CaCl_2$, and 45 μL of plasmid DNA (PTHR, β-$arrestin^{Phe75Bpa}$, and pIRE4-Bpa, 1 mg/mL for each) were mixed, followed by the drop-wise addition of 1.125 mL of HBS buffered saline (at a ratio of 1:1). Mixture was incubated at room temperature for 30 min, and the total of 2.25 mL of calcium phosphate-DNA particle complex was added to each plate. Sixteen hours after transfection, the medium was gently aspirated, and pre-warmed fresh medium containing 250 μM Bpa was added to the plates.

4.2.12.3 Co-IP and proteolytic digestion

The cells were cultured for another 36 hours and stimulated with 200 nM PTH for 10 min. After washing with PBS, the cells in PBS were irradiated by ultraviolet for 15 min. Then, the PBS was aspirated, and 1 mL of RIPA buffer containing 50 mM Tris, pH 8.0, 150 mM NaCl,

1% NP-40, 0.1% SOC, 2 mM EDTA, and 1% protease inhibitor was added to each plate and incubated at 37°C for 15 min. Using a 1 mL pipette, the cells were scraped and gently lysed by pipetting up and down 5–8 times. The total cell lysate from 9 plates was transferred to a 15-mL Eppendorf tube, and the supernatant was collected after centrifugation at 14,000 x g for 15 min, then vortexed for 3–5 s and kept on ice.

For co-IP experiments, 150 µL of anti-HA agarose was added to the supernatant and incubated with gentle end-over-end mixing overnight at 4ºC. After centrifugation at 1,000 x g for 5 min at 4ºC and aspiration of the supernatant, the beads were washed with RIPA buffer six times. The protein complex was eluted from the beads by incubating with 3 mg/mL HA peptide solution for 30 min at 25ºC. After centrifugation at 1,000 x g for 5 min at 4ºC, the supernatant was collected for subsequent in-gel digestion.

4.2.12.4 General mass spectrometric analysis

The obtained peptides were separated by C18 Columns (10.5 cm; particle size, 3 µm; pore size, 120 Å; New Objective) using a nano-LC ACQUITY high-performance liquid chromatography system (Waters). The two eluent buffers were H_2O with 2% ACN and 0.1% FA (A), and ACN with 2% H_2O and 0.1% FA (B); both were at pH 3. The gradient of the mobile phase was set as follows: 2%–35% B in 44 min, 35%–98% B in 1 min and maintained at 80% B for 3 min. The flow rate was 350 nL/min.

LC-MS/MS data were collected using an LTQ Orbitrap Velos mass spectrometer equipped with an ESI probe Ion Max Source with a microspray kit. The system was controlled by Xcalibur software version 1.4.0 from Thermo Fisher (Waltham, MA, USA) in the data-dependent acquisition mode. The capillary temperature was held at 275ºC, and the mass spectrometer was operated in positive ion mode. Full MS scans were

acquired in the Orbitrap analyzer over the m/z 350–1,600 range with a resolution of 30,000; the AGC target was 1e6. The 20 most intense ions were fragmented, and tandem mass spectra were acquired in the ion trap mass analyzer. The dynamic exclusion time was set to 30 s, and the maximum allowed ion accumulation times were 60 ms for MS scans.

4.2.12.5 Data analysis

Raw data files were first converted to mzXML files using ProteoWizard 3.0.18199 and subjected to StavroX (v3.6.6) analysis for identification of cross-linked products[198]. MS/MS spectra were matched with a Uniprot *Homo sapiens* database (entries downloaded at July 24, 2018) using the following parameters: full trypsin digest with maximum 3 missed cleavages, static modification carbamidomethylation of cysteine (+57.021 Da), as well as dynamic modification oxidation of methionine (+15.995 Da), acetylation of protein N-term (+42.010565) and phosphorylation of serine, threonine, and tyrosine (+79.966331). Precursor mass tolerance was 10 ppm, and product ions fragment ion tolerance was 0.5 Da. Peptide spectral matches were validated using percolator based on q-values at a 1% false discovery rate (FDR).

4.2.13 Stable Isotope Labeling by/with Amino acids in Cell culture (SILAC

We used a HEK-293 cell line stably expressing the human HA-tagged PTHR, previously generated in our lab[89]. Three pools of HA-PTHR/HEK-293 cells were maintained side-by-side in Stable Isotope Labeling with Amino acids in Cell (SILAC) “Light”, “Medium”, and “Heavy” media. The SILAC media were prepared from custom-ordered DMEM powder without arginine, lysine, and leucine (Gibco, formula # 03-5080EB) (Gibco/Invitrogen). [$^{2}H_{4}$]-L-lysine (50 mg/L) and [$^{13}C_{6}$]-L-arginine (25 mg/L) (Cambridge Isotope Laboratories) were added to the “Medium”

culture medium; and [13C6, 15N2]-L-lysine (50 mg/L) and [13C6,15N4]-L-arginine (25 mg/ L) (Cambridge Isotope Laboratories) were added to the "Heavy" culture medium, whereas equal concentrations of conventional (i.e., natural) lysine and arginine were added to the "Light" culture medium. All "Light", "Medium" and "Heavy" media were supplemented with L-leucine (104 mg/L), L-proline (10 mg/L), 10% dialyzed FBS (Hyclone) (Thermo Scientific), 1% penicillin/streptomycin, and G418 (150 mg/mL). The SILAC cells were cultured for more than six doublings until the isotope incorporation rates in "Medium" and "Heavy" cells were higher than 95%. The SILAC cells were then expanded. When the cells reached ~80% confluence, they were serum-starved for 4 hours. To map the phosphorylation sites on the PTHR induced by PTH^{WT} or PTH^{7d}, the "Light" labeled cells cultured in "Light" medium were treated with 30 nM PTH^{WT} for 5 min before harvesting; the "Medium" labeled cells cultured in "Medium" medium were treated with 30 nM for 5 min before harvesting; the "Heavy" labeled cells cultured in "Heavy" medium served as control without any treatment. Equal numbers of "Light", "Medium", and "Heavy" labeled cells (generally six 150-mm culture dishes for each) were mixed, flash-frozen in liquid nitrogen, and stored at -80°C. The SILAC experiments were repeated three times.

4.2.13.1 HA-PTHR isolation, digestion, and peptide desalting

HA-PTHR was isolated from SILAC cells over-expressing HA-PTHR using Pierce™ Anti-HA Agarose beads (Catalog number: 26181, Thermo Fisher Scientific). Briefly, crude membrane fractions were prepared from the equally mixed ("Light":"Medium:"Heavy" = 1:1:1) SILAC cells as previously described[199,200]. HA-PTHR was then extracted from crude membrane preparations with 1X buffer [20 mM Tris-HCl (pH 8.0), 100 mM NaCl, and 2 mM EDTA] containing 1% DDM (n-dodecyl b-D-maltoside), protease inhibitors, and phosphatase inhibitors.

HA-PTHR was isolated from the extraction solution by incubating with 200 µL Pierce™ Anti-HA Agarose beads with rotation at 4°C for 4 hours. The HA-PTHR bound anti-HA Agarose beads were washed with 1X buffer containing 0.1% DDM five times and then eluted with 100 µL 2X SDS-PAGE buffer (containing 10 mM dithiothreitol (DTT)) by incubating at 37°C for 1 hour. The receptor proteins were alkylated with 30 mM iodoacetamide (IAA) in the dark at room temperature for 30 min. The samples were then subjected to SDS-PAGE separation. The protein bands corresponding to HA-PTHR were excised from SDS-PAGE gel for in-gel protein digestion.

Tryptic digestion of HA-PTHR was performed as previously described[201,202]. In brief, the excised gel bands were chopped into small pieces and destained by destaining solution (50 mM ammonium bicarbonate in 50% acetonitrile). Sequence grade trypsin (10 ng/µL, modified, Promega) in 50 mM NH_4HCO_3 (pH 8.0) was then added to the tubes to cover the destained gel pieces. The tryptic digestion reactions were incubated at 37°C for overnight. An equal volume of 100% acetonitrile (CH_3CN) was added to the digested gel samples for peptide extraction and repeated for three times. The extracted peptides were pooled into a pre-washed protein LoBind tube (Catalog number: 13698793, Fisher) and then dried under vacuum on a SpeedVac evaporator. The peptide samples were desalted with handmade Stage Tips as previously described[201]. The desalted peptides were lyophilized with a SpeedVac evaporator, reconstituted in 0.1% trifluoroacetic acid, 2% acetonitrile, and 25 mM citrate, and subjected to LC-MS/MS analysis.

4.2.13.2 MS and data analyses

LC-MS/MS analyses were performed on a Thermo Scientific LTQ Orbitrap Velos mass spectrometer (Thermo Fisher) with a Finnigan Nanospray II electrospray ionization source. The peptide samples were loaded onto a nanoViper Compatible PicoChip Column (Catalog number:

1PCH7515-105H354-NV, New Objective) and separated with a Waters nanoACQUITY UPLC System. Instrument control and primary data processing were done with the Xcalibur software package. The LTQ Orbitrap Velos was operated in data-dependent mode using a TOP10 strategy[203]. MS/MS spectra were searched with the SEQUEST algorithm against a composite database containing the human HA-PTHR sequence or HA-PTHR with its interacting proteins, as well as their reverse sequences. Search parameters allowed for three missed tryptic cleavages, a mass tolerance of ± 80 parts per million (ppm), a static modification of 57.02146 daltons (carboxyamidomethylation) on cysteine, and up to eight total dynamic modifications: 79.96633 daltons (phosphorylation) on serine, threonine, and tyrosine; 15.99491 daltons (oxidation) on methionine; 6.02012 daltons or 10.00827 daltons on arginine; and 4.00709 daltons or 8.01420 daltons on lysine. Search results were filtered to include < 1% matches to reverse sequences by restricting the mass tolerance window and setting thresholds for Xcorr and dCn′ (defined as the normalized difference between Xcorr values of the top-ranked candidate peptide and the next candidate with a different amino acid sequence). Matches for phosphopeptides were validated manually with special consideration of intense fragment ions formed through cleavage N-terminal to proline residues and neutral losses of phosphoric acid. Peptide quantification was performed with the Vista program[204] as well as by manual calculation with Qual Browser (version 3.0.63). In brief, the theoretical mass of "Light", "Medium", and "Heavy" variants of each peptide was calculated and used to identify ion peaks in the high mass accuracy precursor scans. The intensity of the peaks was used to construct ion chromatograms. For each isotopic variant, the peak height and background-subtracted area under the curve were used to calculate the "Light"-to-"Heavy"(PTH^{WT}: nonstimulation) and "Medium"-to-"Heavy" (PTH^{7d}: nonstimulation) abundance ratios.

4.3 Results

4.3.1 Anisotropic network model analysis of PTHR

We first sought to determine whether the overall PTHR architecture intrinsically favors an allosteric coupling between the PTH binding region and the intracellular region by performing an anisotropic network model (ANM) analysis on a membrane-embedded PTH^{WT}–PTHR model[192,205,206]. In brief, the ANM provides a unique analytical solution for the spectrum of collective motions intrinsically accessible to each biomolecular system; and among the modes of motions predicted by the ANM, the lowest frequency modes, also called *global* modes, usually represent the coupled movements of the overall system, including allosteric changes in structure, while high frequency modes describe *local* fluctuations[207-209]. ANM analysis of the 20 lowest frequency modes of motion of PTH^{WT}–PTHR in the presence of membrane indeed revealed several modes (modes 3, 4, 8, 14, 16–18, 20 in Appendix Figure 15) where the PTH-binding region was coupled to the cytoplasmic ends of $PTHR^{TMD}$. Modes 3, 14, and 18 were distinguished by large opposite direction fluctuations of TM5/TM6 cytoplasmic ends (and connecting ICL3) relative to H8, in concert with $PTHR^{ECD}$ movements that engaged the PTH. The cross-correlation map from one such mode (mode 14) is illustrated in Figure 4.1a. The map shows which pairs of residues move in a correlated (coupled, same direction; red), anti-correlated (coupled, opposite direction; blue), or uncorrelated/orthogonal (green) manner. The C-terminal region Val455–Leu481 (solid blue curve in Figure 4.1b) is anticorrelated with Thr392, meaning that these two regions undergo concerted opposite direction (opening/closing) movements, which reflects a motion that occurs during receptor activation.

To help understand whether structural alterations at PTHR residues participating in PTH binding would elicit cooperative responses consistent with PTHR activation, we examined the cross-correlation between all PTH residues with Thr392 (at the cytoplasmic end of TM5) and all other residues in mode 14. The results are displayed by the color-coded PTH-bound structure in Figure 4.1b and the plot in Figure 4.1c. Notably, PTH residues 1–14 have strong positive (> 0.5) cross-correlations with the intracellular part of the receptor, which supports previous observations that this region constitutes the signaling portion of the peptide[22,111]. Our ANM analysis suggests that the opening/closure of the intracellular region is allosterically coupled to the structural changes at residues interacting with the N-terminal portion of PTH. Specifically, PTH residues 1–4 are determinant for receptor activation[24,118,141]. From our previous investigations into PTH peptides with β-amino acid substitutions and our PTH binding model (Chapter 3.0)[183], we hypothesized that residues within PTH(5–14) are determinant for signal selectivity. We decided to focus on PTH Leu7 and His9, both of which exhibited high cross-correlation values: 0.85 and 0.74, respectively. We also hypothesized that these residues would be amenable to substitutions that trigger biased signaling.

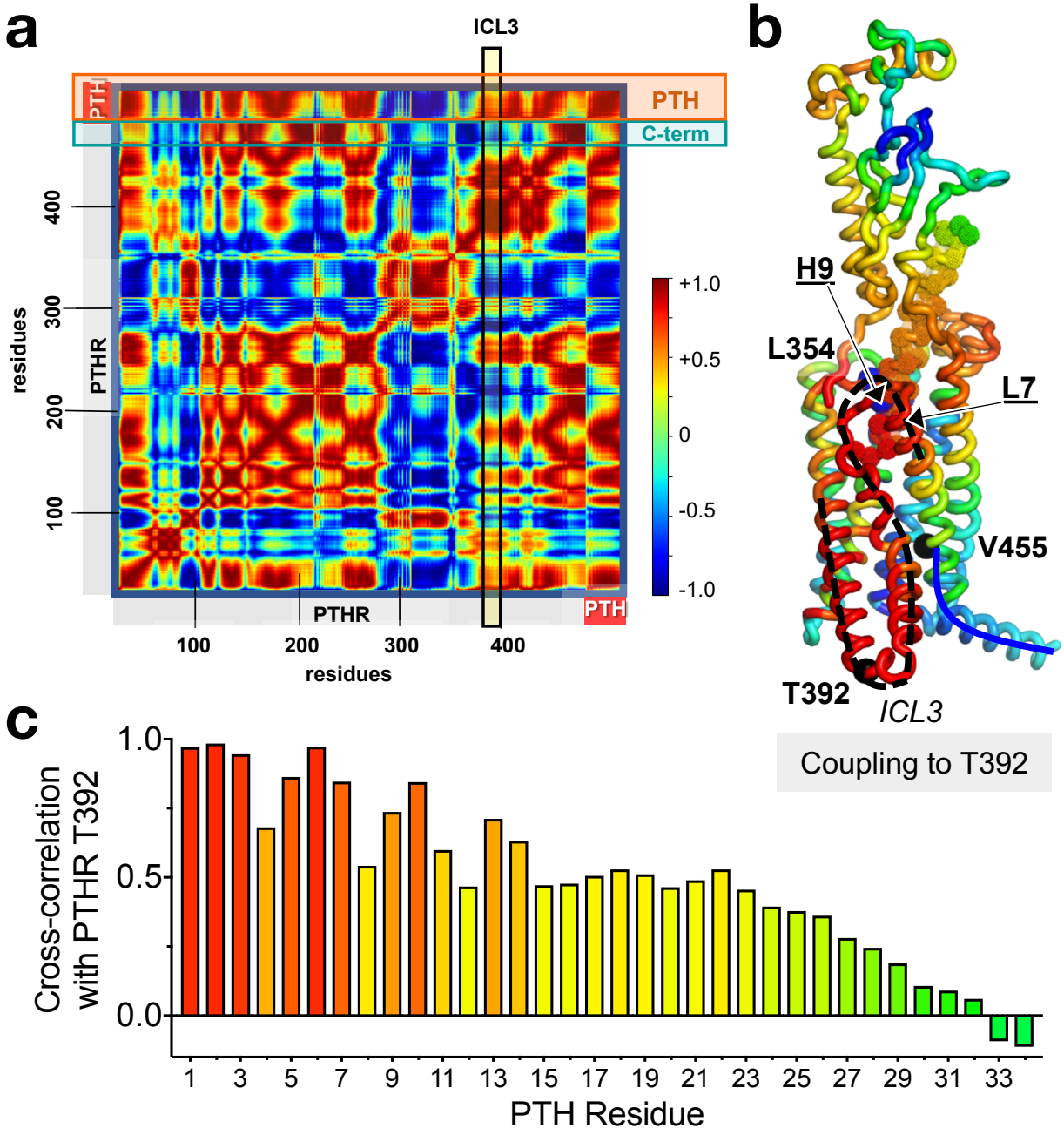

Figure 4.1. ANM results for PTH^{WT}-bound receptor reveal an allosteric coupling between N-terminal part of peptide and cytosolic end of TM5/TM6.

a, Cross-correlation map for the PTH-bound receptor. The entries in the map represent the orientational cross-correlations ($-1 \leq C_{ij} \leq 1$; see the scale on the color-coded bar) between all pairs of nodes (residues) i and j. The two horizontal boxes indicate PTH and PTHR H8, and the vertical box indicates the position of the ICL3 connecting TM5 and TM6 at the cytoplasmic face of the PTHR. Their intersections indicate the cross-correlations between those

regions, e.g. ICL3 and PTH are positively correlated (red), and ICL3 and H8 are negatively correlated (blue). This result is based on ANM soft mode 14. **b**, Cartoon representation colored by the type and strength of correlation of all residues with PTHR Thr392. Blue and red regions indicate anticorrelated and correlated movements, respectively. Thr392 (on TM5 cytoplasmic end) and Val455 (near C-terminus) are shown in black balls, and Leu354 and His9 in blue balls. Ala369–His442, which are strongly correlated with His9 and Thr392, are highlighted with a black dashed curve, and Val455–Leu481, anticorrelated with ICL3, with a solid blue curve. **c,** Plot of cross-correlation between PTH residues and PTHR Thr392, colored in the same manner as in **b**. Note the high (> 0.5) cross-correlations for PTH residues 1–14. *ANM calculations were performed by Ji Young Lee, and the figure was prepared by Ivet Bahar, Ji Young Lee, and Lisa Clark.*

4.3.2 PTH^{H9A} triggers transient cAMP signaling from the plasma membrane

We assayed the effects of the His9→Ala9 point mutation (PTH^{H9A}) for ligand binding affinity and PTHR signaling. Time course recordings of cAMP production in HEK-293 cells revealed that PTH^{H9A}, unlike wild-type PTH (PTH^{WT}), did not sustain cAMP signaling after ligand washout (Figure 4.2a), which is consistent with the failure of PTH^{H9A} to engage PTHR internalization or coupling to β-arrestin-1/2 (Figure 4.2b, c). No significant differences were detected in the capacities of PTH^{WT} and PTH^{H9A} to bind the G protein-dependent state of PTHR (R^G) (Appendix Figure 16, Appendix Table 8)[88], which is consistent with the similar transient cAMP production induced by each ligand (Figure 4.2a). A significant (P = 0.02) reduction in PTH^{H9A} binding to the G protein-independent state of PTHR (R^0)[88], a conformation thought to promote β-arrestin coupling[23], was also observed. Thus, PTH^{H9A} signals exclusively from the plasma membrane and cannot trigger the previously discovered endosomal PTHR signaling[23,118]. Our data also indicate that the PTH His9→Ala9 point mutation stabilizes a distinct receptor

conformation that selectively engages acute plasma membrane cAMP signals while preventing endosomal cAMP signaling.

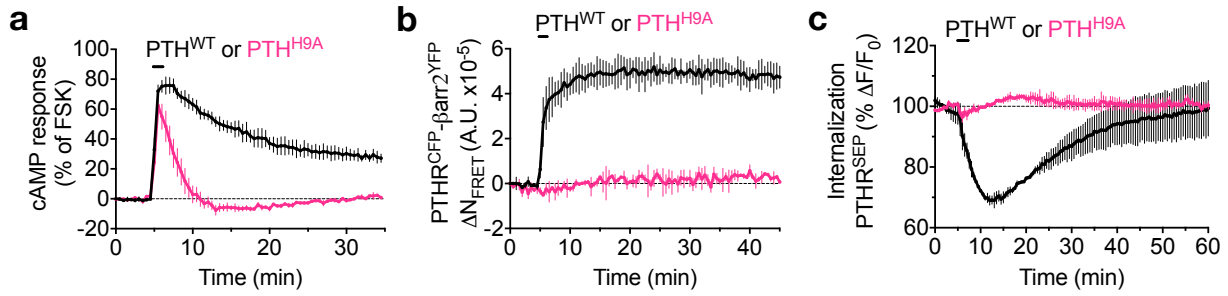

Figure 4.2. Transient cAMP signaling by PTH^{H9A}.

a, Averaged cAMP responses (percentage cAMP responses relative to response in the presence of forskolin, FSK) in HEK-293 cells stably expressing PTHR after 30 s stimulation with 10 nM PTH^{WT} or PTH^{H9A}. Data represent the mean ± s.e.m. of $n \geq 32$ cells carried out in triplicate. **b,** Averaged time courses of β-arrestin-2^{YFP} recruitment to $PTHR^{CFP}$ after 30 s stimulation with 10 nM PTH^{WT} or PTH^{H9A}, measured by FRET in HEK-293 cells. Data represent the mean ± s.e.m. of $n \geq 27$ cells carried out in duplicate. **c,** Averaged time courses of PTHR internalization after 60 s stimulation with 100 nM PTH^{WT} or PTH^{H9A} in HEK-293 cells stably expressing $PTHR^{SEP}$. Data represent the mean ± s.d. of $n \geq 27$ cells carried out in duplicate. *Data were acquired by Alex White.*

4.3.3 Molecular dynamics simulations of PTH^{H9A}-bound PTHR

In our ANM analysis, the ECL2 residues (including Leu354), which interact with PTH His9, as well as the region from Ala369 to His442 (dashed black curve on Figure 4.1b) exhibit strong correlations with Thr392. These results indicate that PTH His9 interactions with PTHR can cooperatively drive a conformational change near Thr392, which would be accompanied by accommodating movements at the adjacent loop ICL3. To discover structural signatures of PTH^{H9A}-stabilized receptor, we performed 200 ns MD simulations of PTH^{H9A}-bound PTHR in

triplicate and compared them to those of PTH^{WT}-bound PTHR. During the simulations of PTH^{WT}-bound PTHR, His9 formed polar interactions with multiple PTHR residues: Ser355 and Gly357 on ECL2, Gln364 on TM5, and Tyr429 on ECL3 (Figure 4.3a–e). His9 was also observed to form aromatic-aromatic interactions with Tyr429 on ECL3.

In contrast, Ala9 in PTH^{H9A} appears to interact with Leu354 on ECL2 (Figure 4.3f), leading to a ECL2 conformation more similar to that of the apo receptor (Figure 4.4a, b, Appendix Figure 18) and a bending of the PTH^{H9A} peptide toward TM2 (Appendix Figure 21). We therefore predict that the extensive interactions between His9 and PTHR are critical for properly positioning the PTH peptide within the $PTHR^{TMD}$. Remarkably, PTH^{H9A} stabilized an inward kink in the cytosolic extension of TM5 (residues $Val382^{5.58}$–$Thr392^{5.68}$, referred to as 'kink 5'; Figure 4.5a, Appendix Figure 18), which is correlated with a slightly inward movement of TM6 in MD trajectories (Figure 4.4c). Also present in the apo PTHR simulations, kink 5 is further predicted to be stabilized by PTH^{H9A}, as evidenced by calculating the distances between the Cα atoms of $Thr392^{5.68}$ (in kink 5) and $Val455^{7.53}$ (in TM7; serving as reference as a residue with minimal displacements between PTH^{WT}- and PTH^{H9A}-bound PTHR) throughout the simulations (Figure 4.5a, b**,** Appendix Figure 17a). Kink 5 promoted the unraveling of the helical residues 394–397 in ICL3 and an inward movement of the loop (Figure 4.4d).

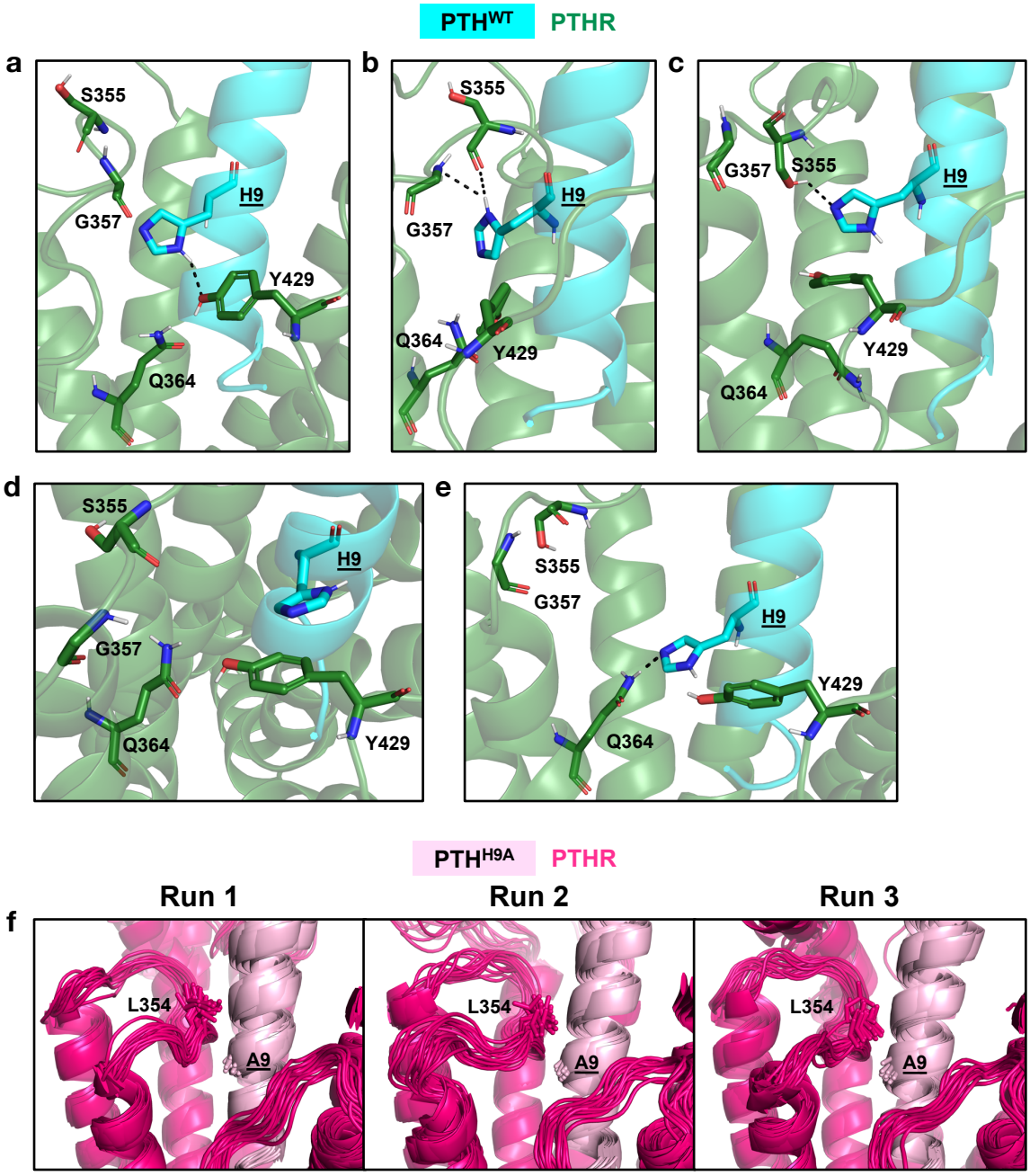

Figure 4.3. Interactions between PTH^{WT} His9 side chain and PTHR residues, and comparison with the interactions of the mutant PTH^{H9A}.

Panels **a–e** display MD snapshots of PTH^{WT}-bound receptor, and panel **f**, those for the PTH^{H9A} -bound receptor. PTH^{WT} is cyan, and PTHR is green in panels **a–e**. PTH^{H9A} is light pink, and PTHR is hot pink in panel **f**. MD snapshots of PTH^{WT}-bound receptor showing different interactions. **a,** His9 hydrogen bond with Tyr429 (ECL3). **b,** Hydrogen bonds with Ser355 and Gly357 main chain (ECL2). **c,** Hydrogen bond with Ser355 side chain (ECL2). **d,** Aromatic-

aromatic interactions between His9 and Tyr429 (ECL3). **e,** Hydrogen bond with Gln364 (TM5). **f,** Interactions between PTHR Leu354 and PTH^{H9A} Ala9 in triplicate simulations. MD snapshots were collected every 10 ns during the last 50 ns of each simulation are aligned by $PTHR^{TMD}$ (residues 180–460).

All unbiased simulations began with PTHR in an active conformation, as the LA-PTH–PTHR–G_s structure was used as a template to generate initial models[24]. This structure was a more favorable starting point than the inactive crystal structure of PTHR[55], which contained several thermostabilizing mutations and a 196-residue *Pyrococcus abysii* glycogen synthase fusion to ICL3 that promoted the crystallization of an inactive conformation[55,118]. While the inward movement of ICL3 in apo and PTH^{H9A}-bound PTHR simulations could be viewed as a first step toward transitioning to an inactive state, the outward position of TM6, a signature of class B GPCRs in the active state, was maintained in these simulations. Previous studies with specialized hardware showed that unbiased MD simulations starting from the active state would require tens of microseconds to simulate the transition to the active state[210]. To possibly observe conformational changes toward the inactive state, we carried out an additional accelerated MD (aMD) run of 100 ns. The lower energy barriers between side chain rotational isomeric states[185,186] help accelerate the sampling of conformational transitions. This additional run revealed the high mobilities of TM6 and TM5, as well as the connecting loop ICL3 (Appendix Figure 19). However, the observed TM6 conformations differed from that of the inactive PTHR structure[55]. These results confirm that the simulations of the active-to-inactive transition in GPCRs is beyond the reach of conventional MD and requires specialized hardware or adoption of adaptive/biased sampling methods, as performed in recent studies of β_2AR and apo adenosine receptor[211,212] or earlier ANM-guided simulations of rhodopsin photoactivation[213].

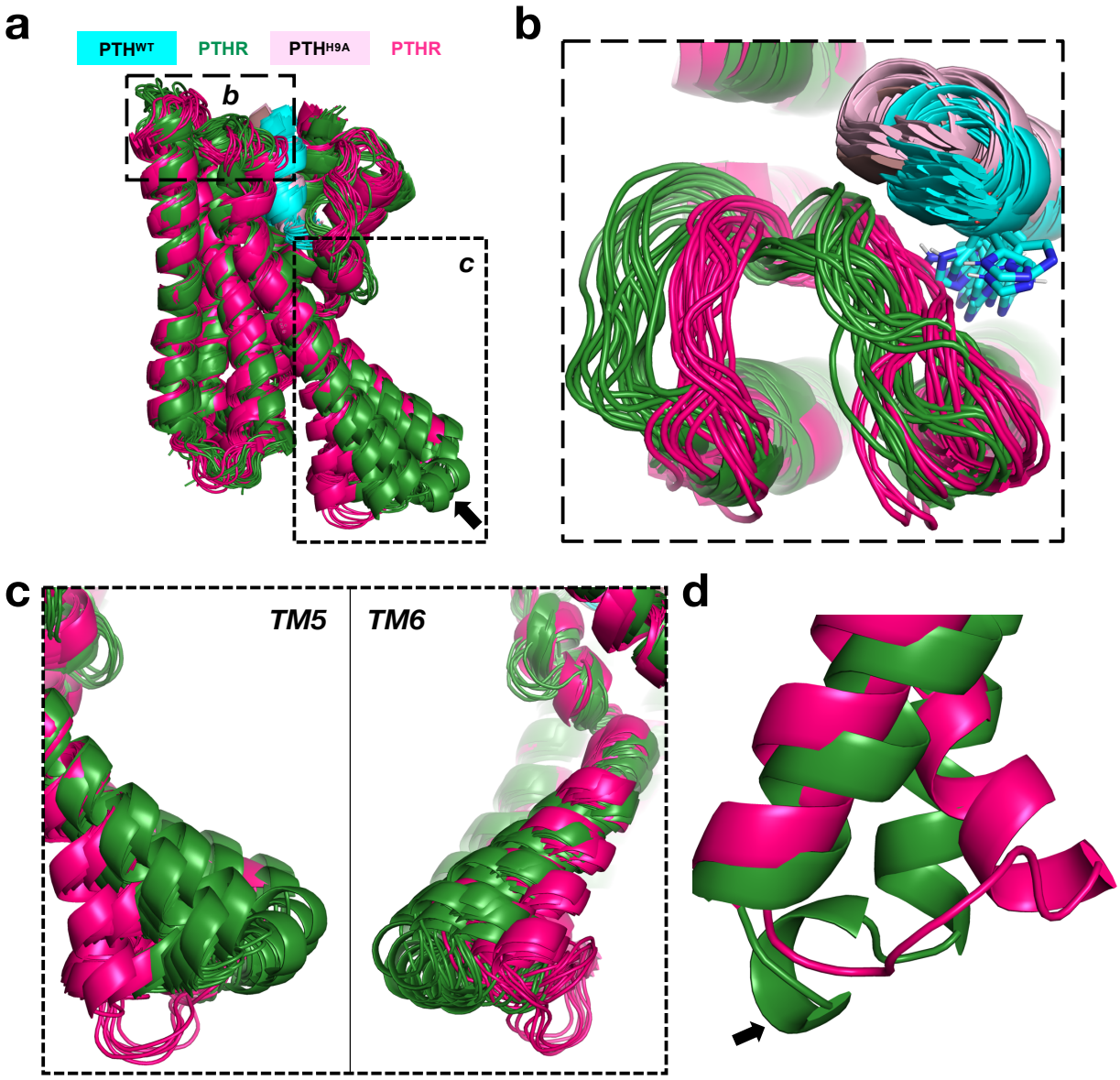

Figure 4.4. Receptor conformations stabilized by PTH^{WT} and PTH^{H9A}.

Snapshots of PTH^{WT}- and PTH^{H9A}-bound receptor collected during the last 50 ns of triplicate simulations (10 ns intervals), aligned by PTHR TM helices. **a,** Aligned receptor structures, with dashed boxes indicating areas shown in **b** and **c**. The arrow points to the helical turn (residues 394–397) in ICL3. $PTHR^{ECD}$ (residues 27–179), ECL1 (residues 247–275), TM3 residues 276–280, and peptide residues 14–34 are hidden for clarity. **b,** ECL2 conformation. **c,** *Left*, relative inward movement of PTH^{H9A}–PTHR TM5. *Right,* relative inward movement of PTH^{H9A}–PTHR TM6. **d,** ICL3 conformations in PTH^{WT}- and PTH^{H9A}-bound receptor snapshots after one 200 ns simulation. The helical turn in ICL3 stabilized by PTH^{WT} is indicated by an arrow.

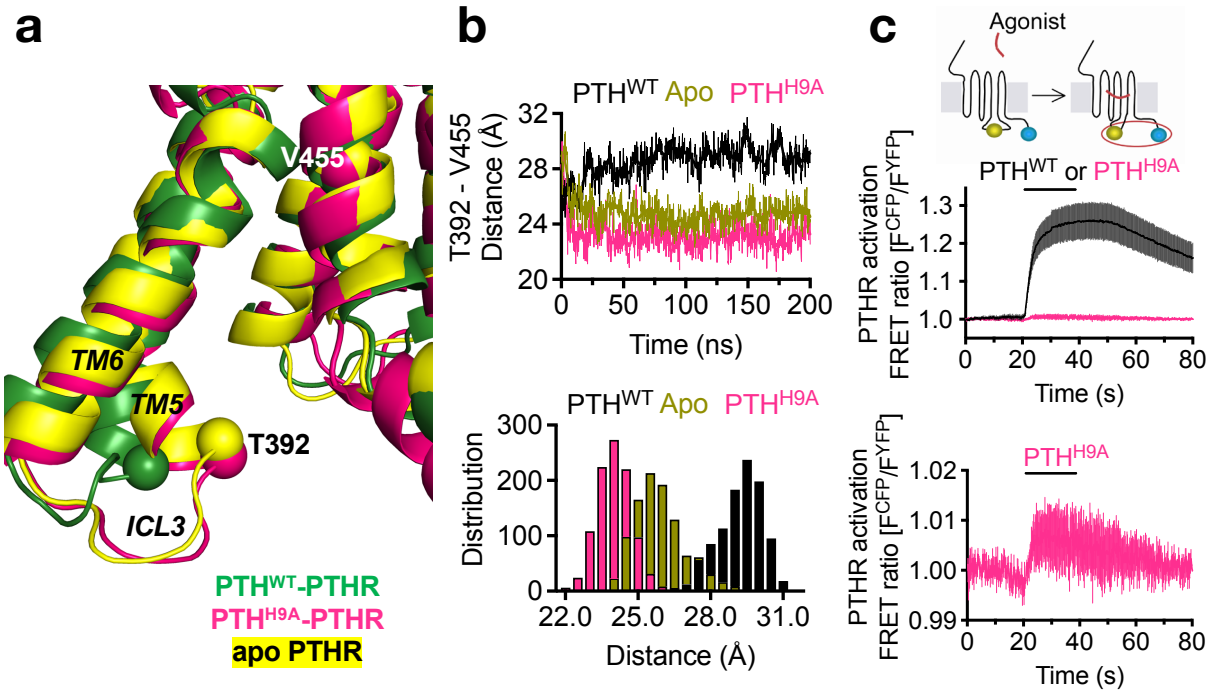

Figure 4.5. PTH^{H9A} dramatically alters PTHR signaling by stabilizing a unique receptor conformation.

a, Snapshots of apo, PTH^{WT}-bound, and PTH^{H9A}-bound receptor at 200 ns simulation, with Cα atoms of kink 5 residue Thr392 and reference residue Val455 shown as spheres. **b,** *Top*, Thr392-Val455 distance distributions over one 200 ns simulation of apo, PTH^{WT}-bound, and PTH^{H9A}-bound receptor. Raw data are shown as thin lines. Second-order smoothed data (over 30 neighbors) are shown as thick lines. *Bottom*, histogram of distance distributions deduced from triplicate MD simulations for each case. **c,** PTHR activation assay. *Top*, schematic of PTHR activation assay. YFP is attached to ICL3, and CFP is attached to receptor C-tail. When receptor is in an inactive state, CFP and YFP act as a FRET donor/acceptor pair. Upon addition of agonist (e.g., PTH^{WT}), YFP and CFP move farther apart, resulting in decreased FRET (i.e., increased F^{CFP}/F^{YFP}). *Middle*, averaged time courses of PTHR activation, measured after stimulation by 1 μM PTH^{WT} or PTH^{H9A}. *Bottom*, averaged time courses of PTHR activation, measured after stimulation by 1 μM PTH^{H9A} (zoomed in to reveal details). Data in *middle* and *bottom* panels represent the mean ± s.e.m. of n = 12–15 cells carried out in triplicate. *The data in* ***c*** *were acquired by Alex White.*

The unique PTHR conformation stabilized by PTH^{H9A} according to unbiased MD was supported experimentally using a FRET-based PTHR sensor, $PTHR^{CFP/YFP}$, which specifically reports intramolecular conformational rearrangements of ICL3 via FRET changes[214]. As previously reported[214], a short perfusion of PTH^{WT} to cells expressing $PTHR^{CFP/YFP}$ induced a rapid decline of FRET signal (corresponding to an increased FRET emission intensity ratio, F^{CFP}/F^{YFP}) that persisted even after washout of the ligand (Figure 4.5c). These data reflect the stabilization of the active PTHR conformation by PTH^{WT}, which involves an ICL3 conformation outward from the cytoplasmic receptor core. Since stabilization of kink 5 by PTH^{H9A} moved ICL3 inward, PTH^{H9A} did not induce a significant change in FRET ratio (Figure 4.5c). Given that PTH^{H9A} changed the FRET ratio slightly (Figure 4.5c, *bottom* panel) and maintained G_s signaling at the plasma membrane, we conclude that PTH^{H9A} induces a unique receptor conformation instead of merely stabilizing the apo state. When the TMD of the PTH^{H9A}–PTHR complex stabilized after 200 ns simulation was aligned with the structurally resolved TMD from the PTHR–G_s cryo-EM structure, the kink 5/ICL3 region was observed to clash with the $G\alpha_s$ α5 helix and α4-β6 loop (Appendix Figure 17b), suggesting that the interactions of the PTHR with G_s would be disrupted upon complexation with PTH^{H9A}, consistent with the small reduction of acute cAMP in response to PTH^{H9A} (Figure 4.2a).

4.3.4 Model of PTHR–β-arrestin complex

To determine the cause of deficient β-arrestin recruitment in response to PTH^{H9A}, we first sought to identify contacts between PTH^{WT}-activated receptor and β-arrestin using photo-crosslinking coupled to mass spectrometry (MS) experiments. Although we used β-arrestin-1 in these experiments, class B GPCRs have similar affinities to both β-arrestin isoforms[215]. We selected five residues located in the β-arrestin-1 finger loop that were in close proximity to bound vasopressin receptor-2 phosphopeptide (PDB 4JQI, Figure 4.6a)[75]. In the crystal structure of rhodopsin bound to mouse visual arrestin-1 (PDB 4ZWJ, Figure 4.6b)[189], the finger loop interacts with the receptor residues located in TM5 and TM6. HA-tagged β-arrestin-1 constructs in which these residues were individually substituted with UV-crosslinkable *p*-benzoyl-L-phenylalanine (Bpa) were tested for its ability to crosslink with PTHR transiently expressed in HEK-293 cells[216]. After photoactivation, the MS analysis identified crosslinks between β-arrestin-1 Leu73Bpa and PTHR residues $Lys405^{6.32}$, $Lys408^{6.35}$, and $Lys484^{8.68}$ (Appendix Figure 20a–c). PTHR $Lys405^{6.32}$ and $Lys408^{6.35}$ are located at the cytoplasmic end of TM6 (Figure 4.8). $Lys484^{8.68}$ is located within the flexible C-terminal tail and is not visible in the cryo-EM structure of PTHR[24]. Crosslinks were also identified between β-arrestin-1 Phe75Bpa and PTHR residues $Val384^{5.64}$ and $Thr392^{5.71}$ (Appendix Figure 20d, e), located at the cytoplasmic end of TM5 (at the above-mentioned kink 5 region) (Figure 4.8). These photo-crosslinks support a conformation in which the β-arrestin-1 finger loop is engaging with the receptor cytosolic core.

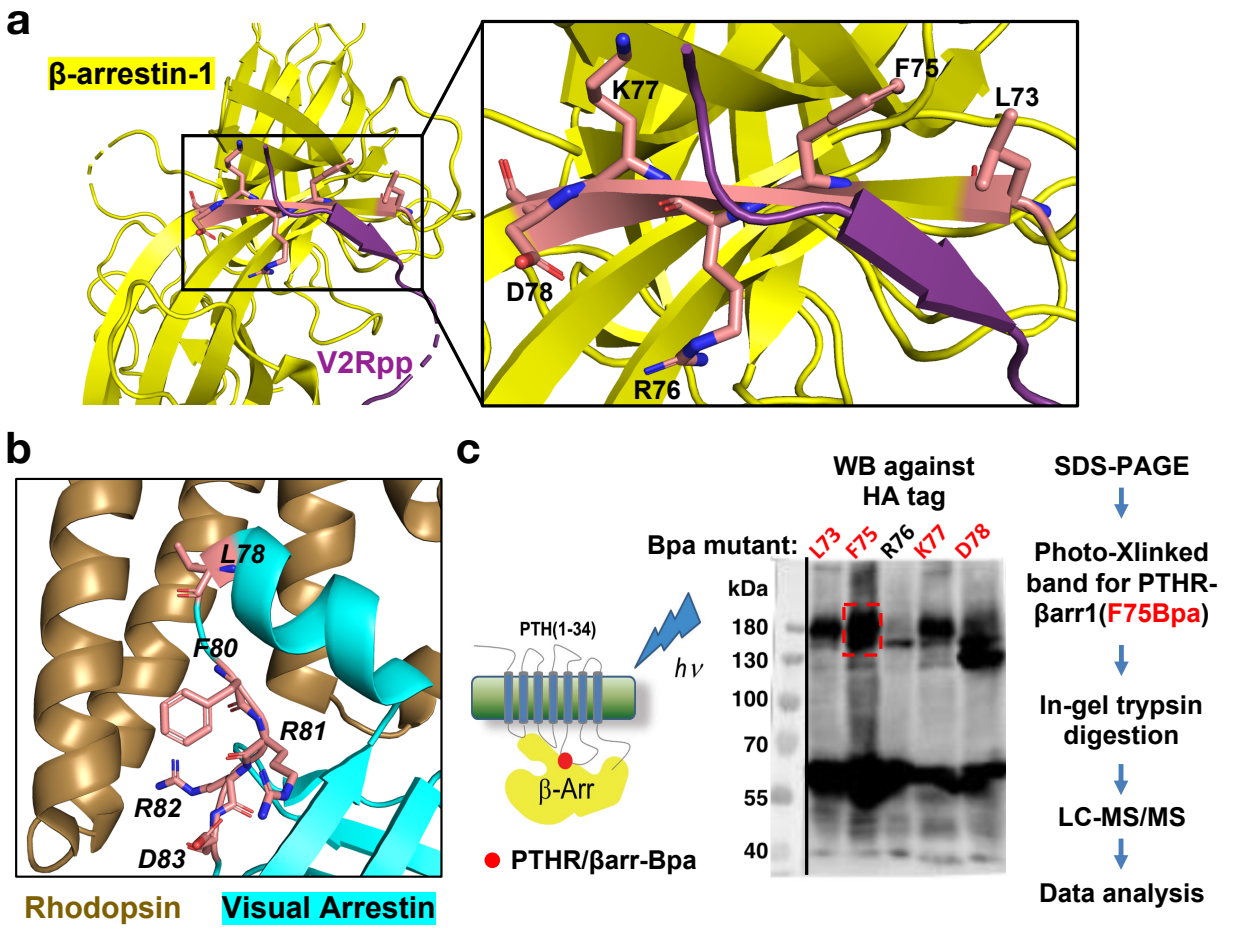

Figure 4.6. Bpa substitution at β-arrestin-1 finger loop residues.

a, Structure of rat β-arrestin-1 (yellow) bound to vasopressin 2 receptor phosphopeptide (V2Rpp, purple), PDB 4JQI[75]. β-arrestin-1 residues in peach sticks were selected for Bpa substitution. **b,** Structure of rhodopsin (brown) bound to mouse visual-arrestin-1 (cyan), PDB 4ZWJ[189]. Visual-arrestin-1 residues corresponding to the β-arrestin-1 residues selected for photo-crosslinking experiments are within the finger loop that interacts with receptor TM5/ICL3/TM6 (peach sticks). **c,** Schematic procedure for identifying: First, β-arrestin-1 p-benzoyl-L-phenylalanine (Bpa) mutants that photo-crosslink with PTHR. Second, PTHR residues that photo-crosslink with β-arrestin-1 Phe75Bpa. *These data were acquired by Ieva Sutkeviciute, Frederic Jean-Alphonse, and Kunhong Xiao.*

We investigated these identified interactions by generating models of PTHR–β-arrestin-1 complex using the most reliable structures of three unique GPCRs in complex with arrestin (as of February 2020): rhodopsin–visual-arrestin-1 (PDB 5W0P)[77], M2R–β-arrestin-1 (PDB 6U1N)[187], and NTSR1–β-arrestin-1 (PDB 6UP7)[188]. For each receptor, we structurally aligned its TMD with the TMD (residues 180–460) of triplicate PTH^{WT}–PTHR snapshots after 200 ns MD simulation and then selected the PTH^{WT}–PTHR snapshot with the lowest RMSD to use for the PTHR–β-arrestin-1 model (also see Structural modeling methods section). Minor clashes between PTHR and β-arrestin-1 were removed using the sculpting in PyMOL[157]. For the model using the rhodopsin–arrestin structure, we also generated a homology model of human β-arrestin-1 in the receptor core conformation using the visual arrestin-1 structure[77,190]; this β-arrestin-1 model was structurally aligned with visual arrestin-1 (RMSD = 0.255 Å). Each model presented unique positions of β-arrestin-1 with respect to the PTHR cytosolic core and to the plasma membrane. The PTHR–β-arrestin-1 models generated using the rhodopsin (Model 1) and M2R (Model 2) structures resulted in similar TMD RMSD values: 4.650 Å and 5.033 Å, respectively. The TMD RMSD between PTHR and NTSR1 was larger: 7.082 Å. Also, the C-edge β-arrestin-1 loops of the NTSR1-derived complex (Model 3) clashed significantly with the membrane used for PTHR MD simulations (Figure 4.7c). For Models 1 and 2, C-edge loops were slightly embedded in the membrane (Figure 4.7a, b), as observed in other GPCR–arrestin structures[77,187,188,217]. Orienting Model 3 to a model membrane using Orientation of Proteins in Membranes server eliminated H8 interactions with the membrane (Figure 4.7d, e)[159].

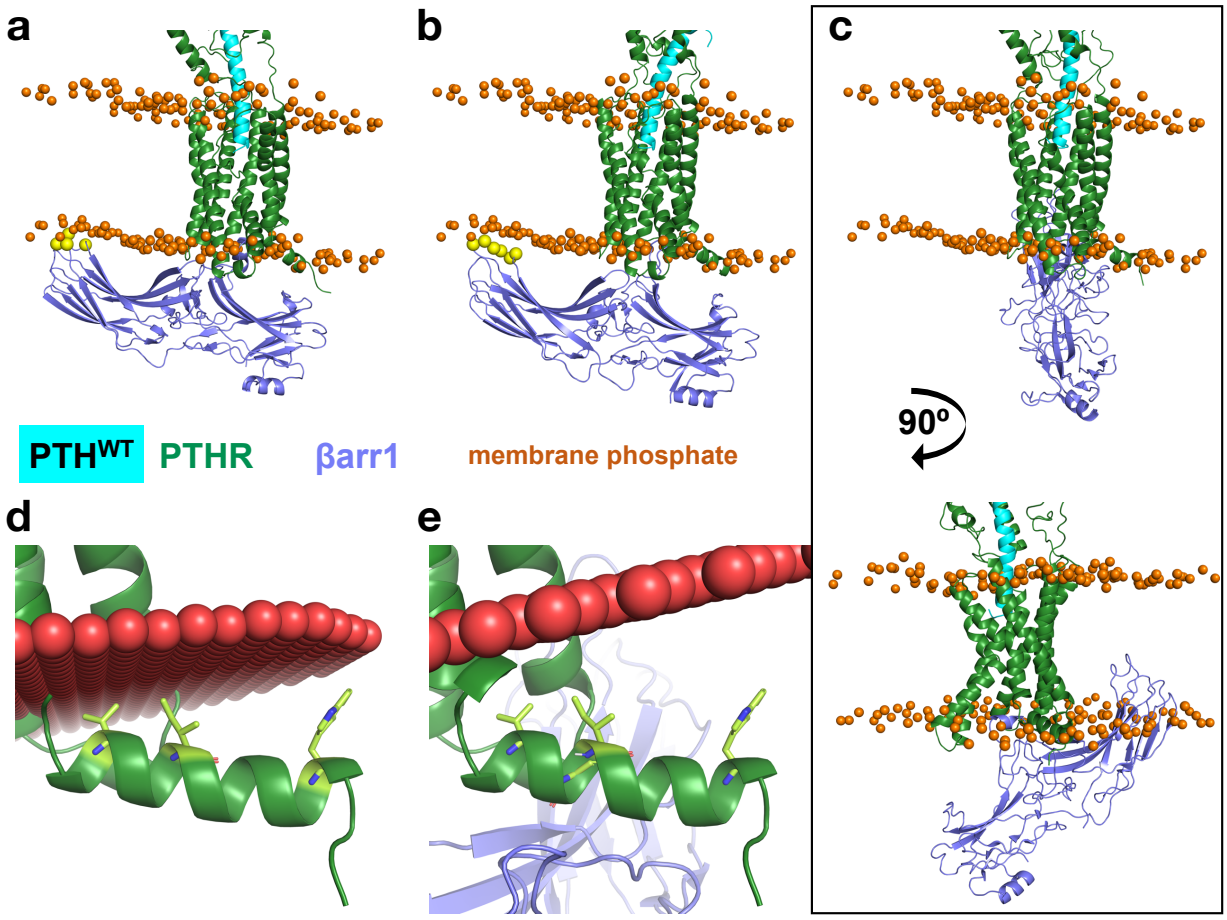

Figure 4.7. Position of β-arrestin-1 relative to the membrane in PTHR–β-arrestin-1 models.

In all panels, PTH^{WT} is cyan, PTHR is dark green, and β-arrestin-1 is slate blue. The orange spheres represent membrane phosphates after 200 ns MD simulation. In **a** and **b**, yellow spheres are β-arrestin-1 C-edge loop residues that contact the membrane. **a,** Model 1: PTHR–β-arrestin-1 model generated using the rhodopsin–arrestin structure (PDB 5W0P) as a template. **b,** Model 2: PTHR–β-arrestin-1 model with M2R–β-arrestin-1 template structure (PDB 6U1N). **c–e,** Model 3: PTHR–β-arrestin-1 model with NTSR1–β-arrestin-1 template structure (PDB 6UP7). **c,** *Top*. Model 3 with same orientation as **a** and **b**. *Bottom.* Model 3 rotated 90º to highlight significant embedment of β-arrestin-1 C-edge in the membrane. In **d** and **e**, PTHR alone and Model 3 positioned in membrane (red spheres) by the OPM server, with H8 residue interacting with the membrane in **d** represented as limon sticks.

All three models satisfied distance restraints between β-arrestin-1 Leu73 and PTHR Lys484$^{8.68}$ as well as the position of phosphorylated receptor C-terminal tail within the N-terminal domain of β-arrestin-1; these results are presented and discussed in Appendix D.3. In the rhodopsin and NTSR1-derived models, Cα-Cα distances between β-arrestin-1 Leu73 and PTHR Lys405$^{6.32}$/Lys408$^{6.35}$ as well as between β-arrestin-1 Phe75 and PTHR Val384$^{5.64}$/Thr392$^{5.71}$ were within Bpa photo-crosslinking restraints (Figure 4.8a, c, Table 3). In the M2R-derived complex, Leu73Bpa photo-crosslinking may be less feasible, with smaller Cα-Cα distances of 8.0 Å and 9.3 Å for Lys405$^{6.32}$ and Lys408$^{6.35}$, respectively (Figure 4.8b, Table 3).

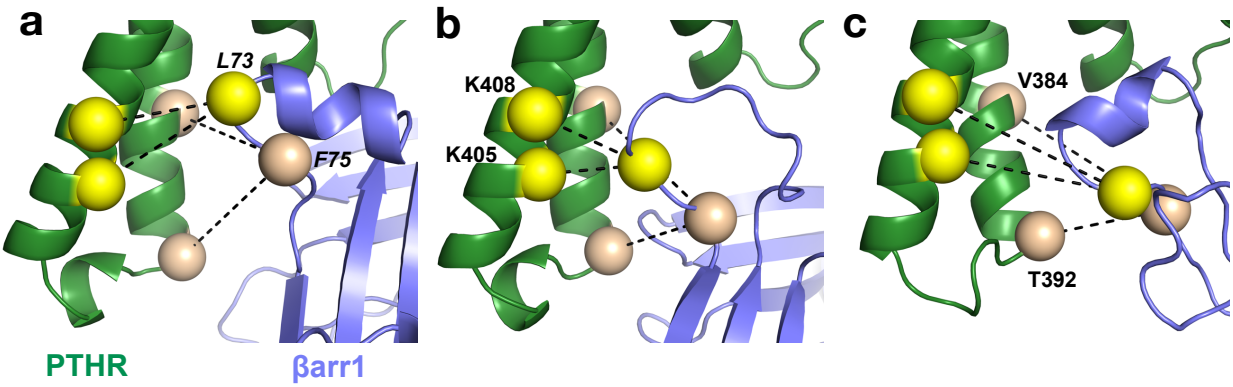

Figure 4.8. PTHR–β-arrestin-1 models in the context of Bpa photo-crosslinks.

PTHR is dark green, and β-arrestin-1 is slate blue. PTHR residues 461–481 are hidden for clarity. β-arrestin-1 Leu73, PTHR Lys405, and Lys408 are yellow spheres. β-arrestin-1 Phe73, PTHR Val384, and Thr392 are wheat spheres. Dashed black lines represent theoretical photo-crosslinks. **a,** Model 1. **b,** Model 2. **c,** Model 3. Distances in each of these models are presented in Table 3.

Table 3. Distances between photo-crosslinked β-arrestin-1 and PTHR residues in PTHR–β-arrestin-1 models.

		Distance (Å)		
β-arrestin-1	**PTHR**	**Model 1**	**Model 2**	**Model 3**
Leu73	Lys405	12.2	8.0	13.9
	Lys408	10.4	9.3	16.3
Phe75	Val384	14.2	15.7	16.8
	Thr392	15.2	11.7	10.4

The inward movement of receptor TM6 relative to the G_s-bound conformation has been reported essential for β-arrestin coupling[218]. All three PTHR–β-arrestin-1 models would permit this TM6 inward movement without clashing with β-arrestin-1 (Figure 4.9). The PTHR/β-arrestin-1 complex interface of Model 1 includes many contacts on ICL1 and ICL2 (Figure 4.9a). Complex interface contacts are sparing in Model 2 (Figure 4.9b), potentially because PTHR ICL2 is shorter than M2R ICL2, which interacts significantly with β-arrestin-1 (Figure 4.9e). In Model 3, H8 residues provide most contacts with β-arrestin-1 (Figure 4.9c). All together, these results suggest that the position of β-arrestin-1 in Model 1 (i.e., the rhodopsin structure-derived model) is most likely, given the conformation of PTHR after 200 ns MD simulation.

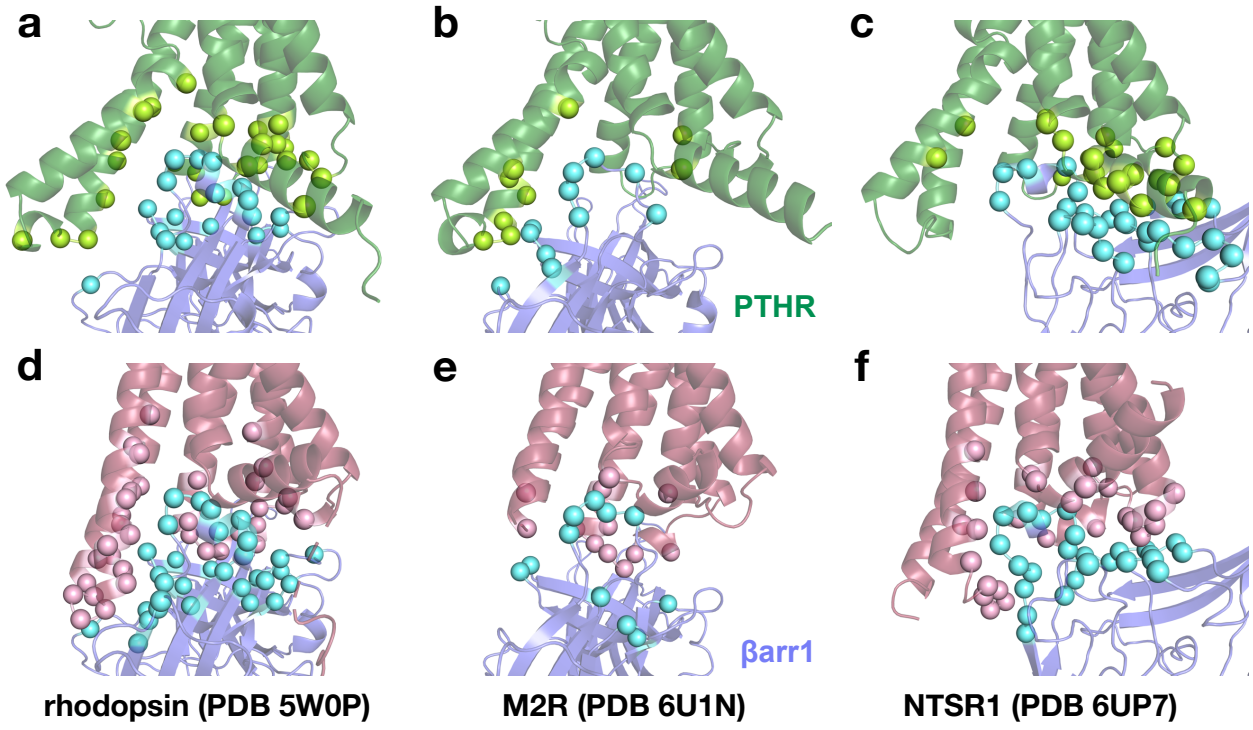

Figure 4.9. PTHR/β-arrestin-1 complex interfaces in PTHR models and and published structures. **a–c,** PTHR Models 1, 2, and 3, respectively. PTHR and β-arrestin-1 residues within 5 Å of each other are limon and cyan spheres, respectively. **d–f,** Published GPCR–arrestin structures used as templates for the above models. GPCR and β-arrestin-1 residues within 5 Å of each other are pink and aquamarine spheres, respectively. Cartoon representation is shown at 40% transparency for clarity.

4.3.5 PTH^{H9A}-triggered ICL3 inward movement prevents β-arrestin-1 coupling

To determine the structural basis for impaired β-arrestin-1 recruitment by PTH^{H9A}, we aligned the TM helices of a PTH^{H9A}–PTHR snapshot after 200 ns MD simulation to each PTH^{WT}–PTHR–β-arrestin-1 model (Figure 4.10a–c). For all three models, the inward ICL3 conformation induced by PTH^{H9A} was unfavorably close to the β-arrestin-1 finger loop

(Figure 4.10a–c). As expected, a photo-crosslinked band was not visible in the PTHR sample stimulated with PTH^{H9A} (Figure 4.10d), supporting the previously determined lack of β-arrestin recruitment (Figure 4.2b, c).

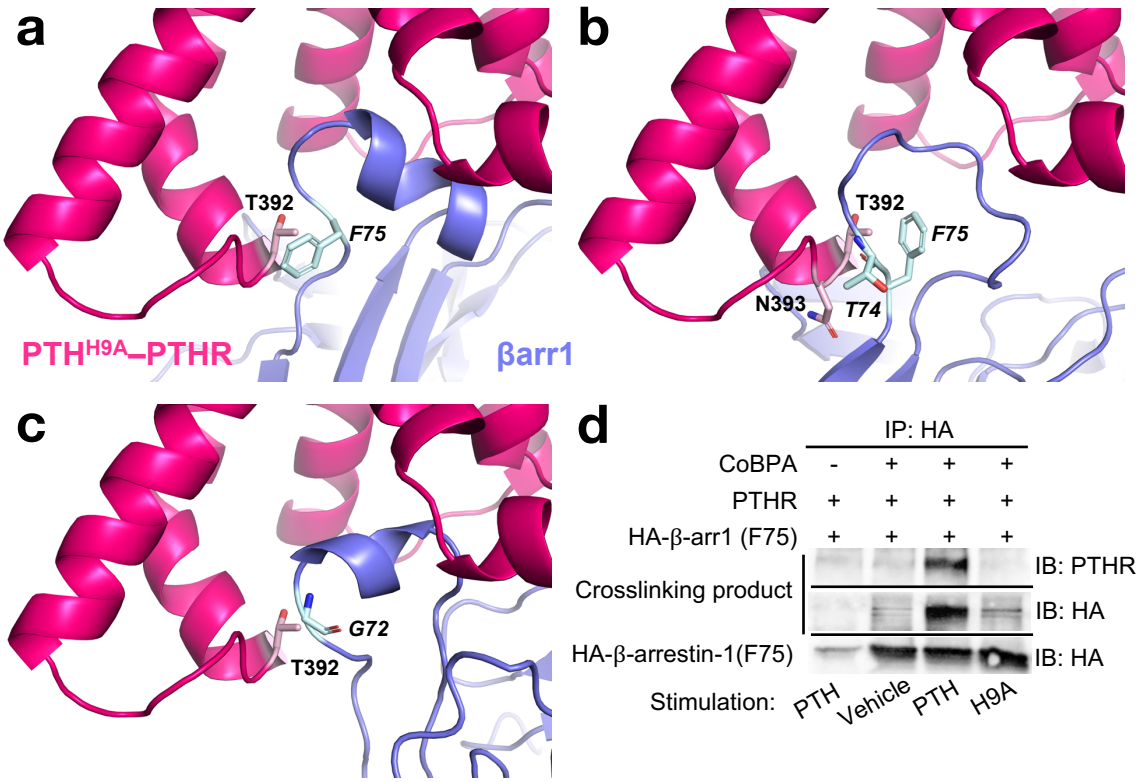

Figure 4.10. Structural mechanism of impaired β-arrestin coupling by PTH^{H9A}.

a–c, A snapshot of PTH^{H9A}–PTHR after 200 ns simulation was aligned with PTHR TM helices in Models 1, 2, and 3, respectively. PTH^{H9A}–PTHR is hot pink, and β-arrestin-1 is slate blue. Near-clashing PTH^{H9A}–PTHR and β-arrestin-1 residues are pink and pale cyan sticks, respectively. **d,** Co-immunoprecipitation of HA-tagged β-arrestin-1 Phe75Bpa and photo-crosslinked PTHR. Samples were immunoprecipitated using an anti-HA antibody and immunoblotted for β-arrestin-1 (anti-HA) and PTHR (anti-PTHR). Stimulation with PTH^{H9A} does not photo-crosslink PTHR with β-arrestin-1 Phe75Bpa. *This photo-crosslinking pull-down was performed by Saifei Lei.*

4.3.6 PTH^{7d} triggers sustained cAMP signaling from the plasma membrane

We determined that the peptide PTH^{7d} also prevented β-arrestin recruitment and PTHR internalization (Figure 4.11a, b). In contrast to PTH^{H9A}, PTH^{7d} triggered sustained cAMP from the plasma membrane (Figure 4.11c). Expression of a dominant-negative dynamin mutant (DynK44A), which blocks receptor internalization, significantly reduced cAMP responses induced by PTH^{WT} but not by PTH^{7d} (Figure 4.11c). Also, the addition of a cell-impermeable PTHR competitive antagonist (D-Trp^{12},Tyr^{34}-$bPTH_{7-34}$) eliminated sustained cAMP after washout (Figure 4.11d). The differences in signaling between PTH^{7d} and PTH^{WT} were not due to differences in binding affinity in equilibrium competition assays utilizing tetramethylrhodamine (TMR)-labeled PTH as reporter ligand (Figure 4.11e).

We sought to determine the molecular mechanisms that prevented PTH^{7d}-bound receptor from recruiting β-arrestin while maintaining cAMP signaling. Recruitment of β-arrestins to activated receptors is thought to occur by phosphorylation of ICL3 and C-terminal tail by GRKs, and recent studies have proposed that receptor phosphorylation status is determinant for GPCR–β-arrestin interactions[219-221]. We examined whether PTH^{WT} and PTH^{7d} trigger distinct PTHR phosphorylation patterns by performing Stable Isotope Labeling by Amino acids in Cell culture (SILAC)-based proteomics (Appendix Figure 22). SILAC analysis did not identify differences in sites or extent of PTHR phosphorylation between PTH^{WT} and PTH^{7d} treatments. These data suggest that PTH^{7d} induces a distinct receptor conformation that prevents β-arrestin complex formation. Furthermore, the epimerization of PTH Leu7 was predicted to affect receptor cytosolic conformation, as the ANM cross-correlations between PTH Leu7 and PTHR TM5–ICL3–TM6 region were strong (Figure 4.1).

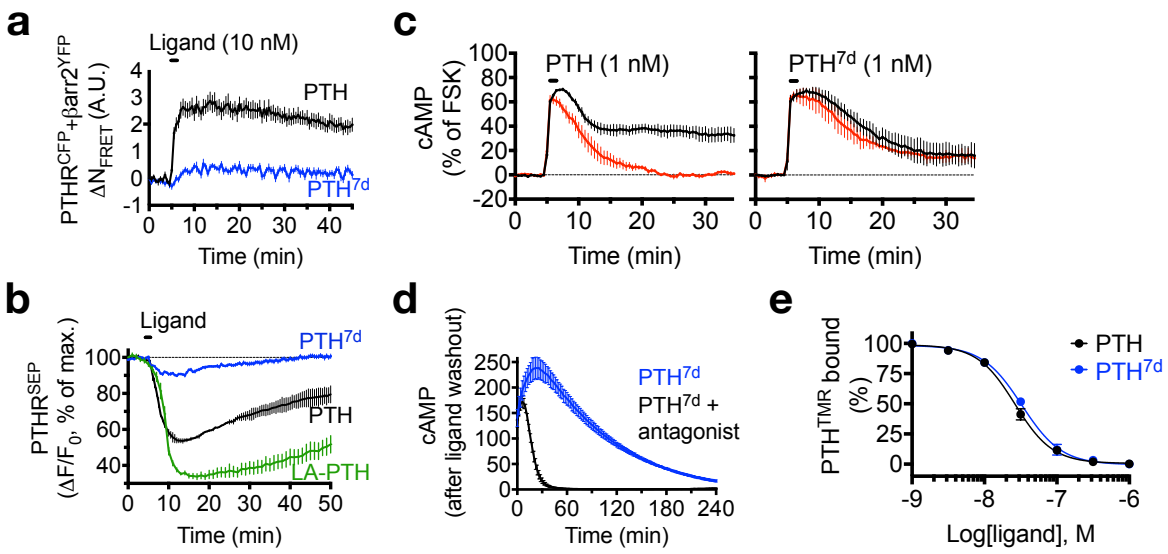

Figure 4.11. Sustained cAMP signaling by PTH^{7d}.

a, Averaged time courses of β-arrestin-2^{YFP} recruitment to PTHR^{CFP} after brief stimulation with 10 nM PTH^{WT} or PTH^{7d}, measured by FRET in HEK-293 cells. Data represent the mean ± s.e.m. of $n \geq 28$ cells carried out in triplicate. **b,** Time courses of internalization and recycling of PTHR tagged with superecliptic pHluorin (SEP) in response to ligand, measured by time-lapse confocal microscopy with images acquired every 30 s. The baseline was established for 5 min, then cells were stimulated with 100 nM PTH, PTH^{7d}, or LA-PTH for 30 s. Data are the mean ± s.e.m. of N = 3 independent experiments with n = 11–14 cells per experiment. **c,** Averaged cAMP responses (percentage cAMP responses relative to response in the presence of forskolin, FSK) in HEK-293 cells stably expressing PTHR after 30 s stimulation with 10 nM PTH^{WT} or PTH^{7d}. Red curves represent cAMP response in cells also expressing dominant-negative dynamin mutant (DynK44A). Data represent the mean ± s.e.m. of n ≥ 15 cells carried out in triplicate. **d,** cAMP time-courses after washout of 1 nM PTH^{7d} in the presence (black curve) or absence (blue curve) of cell-impermeable competitive antagonist. Data are the mean ± s.e.m. of N = 3 experiments. **e,** Competition binding at equilibrium for PTH^{WT} (black) and PTH^{7d} (blue), performed with tetramethylrhodamine (TMR)-labeled PTH as reporter ligand and HEK-293 cells stably expressing HA-tagged PTHR. Data are the mean ± s.e.m. of N = 3 independent experiments with triplicate wells for each concentration point. *Experiments presented in this figure were performed by Karina Peña and Alex White.*

4.3.7 Molecular dynamics simulations of PTH^{7d}-bound PTHR

We utilized molecular dynamics (MD) simulations and structural modeling to assess PTHR conformations stabilized upon binding of either PTH^{WT} or PTH^{7d}. As with PTH^{WT}–PTHR, the cryo-EM structure of active PTHR bound to G_s and LA-PTH (PDB 6NBF)[24] was used to generate initial models of PTH^{7d}–PTHR for triplicate 200 ns MD simulations. In the initial PTH^{7d}–PTHR model, D-Leu7 is unfavorably close to neighboring TM7 residues Trp437 and Met441 of the receptor (Figure 4.12a), and simulations revealed that the D-Leu7 side chain shifts to mirror L-Leu7 nonpolar interactions in the PTH^{WT}–PTHR model (Figure 4.12a). We found that this shift induces a kink in the PTH^{7d} helix toward the C-terminal portion TM6 (Figure 4.12b), along with a concomitant shift of the $PTHR^{ECD}$ closer to TM2 without altering interactions at the peptide-binding interface of the $PTHR^{ECD}$ (Appendix Figure 21). The PTH^{7d} helix kink also permits additional polar interactions between Glu4 of PTH^{7d} and PTHR residues that are not observed for PTH^{WT} (Figure 4.12c, d, Appendix Table 9). In the active-state cryo-EM structure of PTHR, Glu4 promotes an extensive polar interaction network that stabilizes the outward kink of TM6 that is considered prerequisite for coupling to G proteins[24,118]. The increased polar contacts by Glu4 of PTH^{7d} further extends this polar interaction network relative to PTH^{WT}–bound receptor (Figure 4.13). Also, the kink of the PTH^{7d} helix causes the peptide N-terminus to push on the C-terminal portion of TM6, resulting in a slight shift compared to PTH^{WT} simulations (Figure 4.13b). Based on previous structural analyses recently reviewed[118], this conformational change is expected to contribute to the TM6 kink.

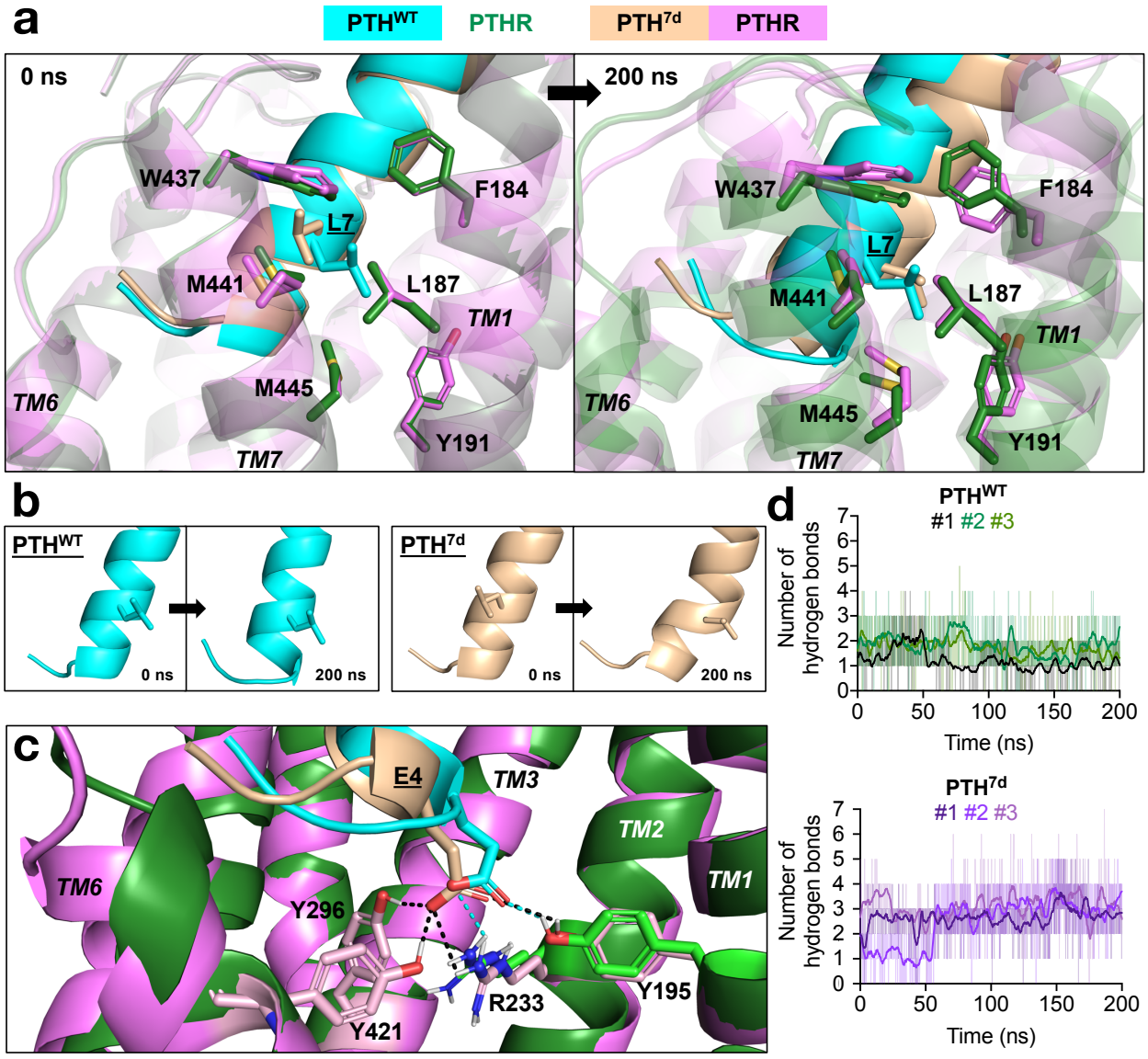

Figure 4.12. Molecular changes induced by PTH^{7d}.

a, PTH^{WT} and PTH^{7d} are colored cyan and wheat, respectively. PTH^{WT}- and PTH^{7d}-bound receptors are colored dark green and violet, respectively. PTH Leu7 and receptor residues within 4 Å of Leu7 are shown as sticks. The *left* panel shows initial MD models of PTH^{WT}–PTHR and PTH^{7d}–PTHR. In the initial model of PTH^{7d}–PTHR, D-Leu7 is unfavorably close to PTHR residues Trp437 and Met441. The *right* panel shows MD models after 200 ns, where the D-Leu7 side chain has shifted to promote more favorable interactions with nonpolar residues in TM1 and TM7. **b,** Snapshots of PTH^{WT} and PTH^{7d} peptide helices at the start (0 ns) and end (200 ns) of MD simulations. PTH Leu7 side chain is shown as sticks. At 200 ns, note the break in the PTH^{7d} helix and the resulting outward push of the peptide

N-terminus. **c,** Polar contacts between PTH Glu4 and receptor residues. Residues interacting with PTH^{WT} Glu4 are green sticks, and interactions are cyan dashes. Residues interacting with PTH^{7d} Glu4 are light pink sticks, and interactions are black dashes. **d,** Number of hydrogen bonds between Glu4 (PTH^{WT}, *top*; PTH^{7d}, *bottom*) and receptor residues over triplicate simulations. Raw data are connected by thin lines. Second-order smoothed data (over 20 neighbors) are shown as thick lines.

These observations, combined with previous reports that an inward movement of TM6 is essential for efficient β-arrestin coupling[218], led us to hypothesize that the increased stabilization of the outward TM6 kink by PTH^{7d} relative to PTH^{WT} may provide the structural basis for differences in β-arrestin recruitment. In PTHR–β-arrestin-1 Models 1 and 2, PTHR TM6 residue Val412 engaged in nonpolar interactions with β-arrestin-1 Leu73 and Leu71, respectively (Figure 4.14a, b). We aligned snapshots of PTH^{7d}–PTHR after triplicate 200 ns MD simulations with PTHR–β-arrestin-1 Models 1 and 2, which revealed that the TM6 kink induced by PTH^{7d} shifted Val412 of the away from Leu71/73 of β-arrestin-1 (Figure 4.14a–c). In the last 50 ns of MD simulations, distances between PTHR Val412 CB atom and β-arrestin-1 Leu73 CG atom in Model 1 were approximately 1 Å greater in the presence of PTH^{7d}. This increased distance could prevent or reduce PTHR Val412–β-arrestin-1 Leu71/Leu73 nonpolar interactions, thus destabilizing PTHR–β-arrestin complex formation. Accordingly, β-arrestin-1 Leu73Bpa photo-crosslinked with PTHR in PTH^{WT}-treated cells but not in PTH^{7d}-treated cells (Figure 4.14d).

We also performed 200 ns simulation of a PTH^{WT}–PTHR–G_s model. Using the final snapshot from this simulation, we generated a model of PTH^{7d}–PTHR bound to G_s and compared with the PTH^{WT}-bound model (Appendix Figure 24). In both models, $G\alpha_s$ α5 helix is inserted into the receptor core and interacts with PTHR residues located on ICL2/3, TM2, TM3, TM5, and TM6 (Appendix Figure 24a). In the PTH^{WT}–PTHR–G_s snapshot, three TM6 residues interact with three $G\alpha_s$ residues located on the flexible α5 C-tail (Appendix Figure 24b).

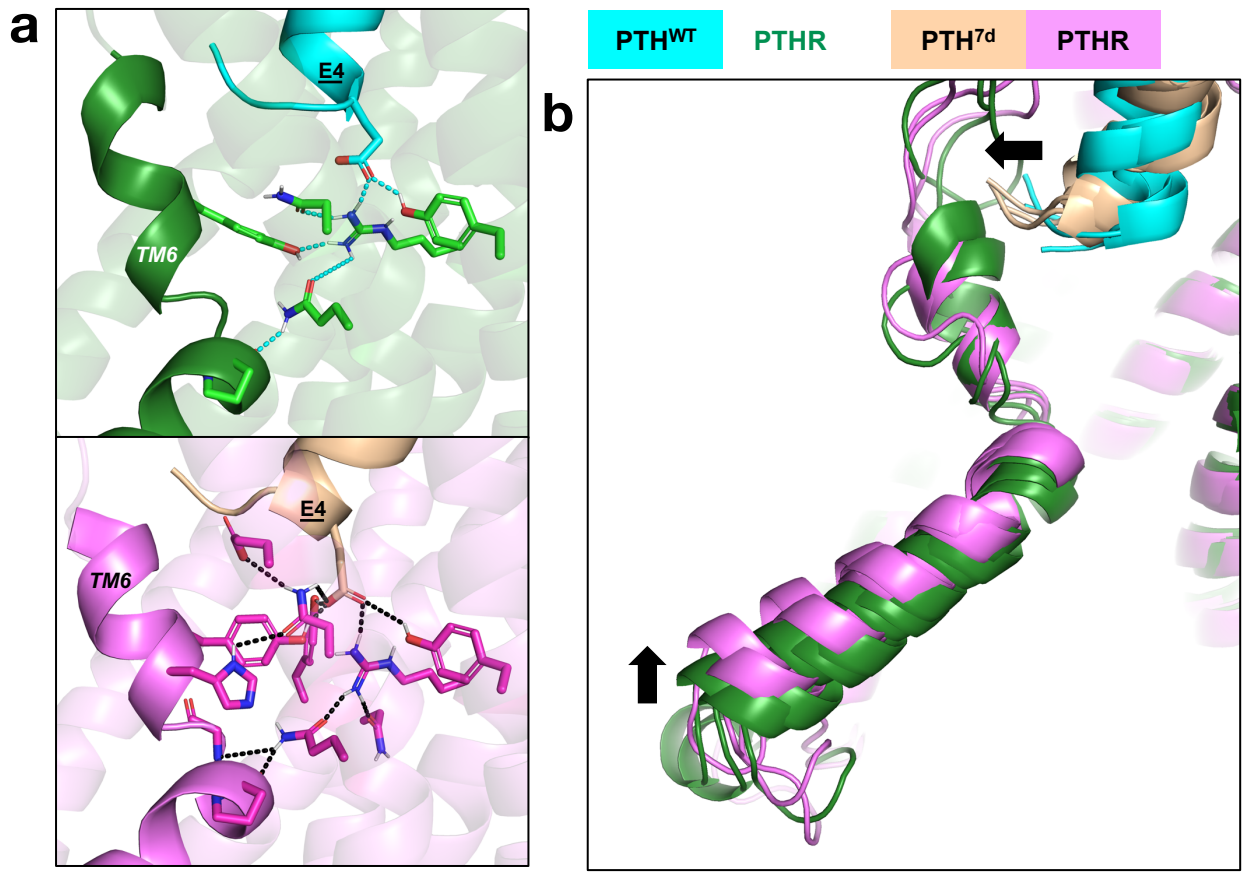

Figure 4.13. Consequences of PTH Glu4 polar network.

a, Polar network induced by PTH Glu4 interactions. PTH peptide and PTHR TM6 helices are opaque helices, whereas all other receptor helices are transparent. In the *upper* panel, receptor residues within the polar network are green sticks, and interactions are cyan dashes. In the *lower* panel, receptor residues within the polar network are magenta sticks, and interactions are black dashes. Note that PTH^{7d} Glu4 interactions induce more polar contacts with receptor TM6, which are important for stabilizing an outward kink of TM6. **b,** Snapshots of triplicate MD simulations, highlighting the push of PTH^{7d} N-terminus on the C-terminal portion of PTHR TM6 as well as the upward movement of the N-terminal portion of TM6. The relative movements of PTH^{7d} N-terminus and PTHR TM6 in PTH^{7d}–PTHR from PTH^{WT}–PTHR are indicated by arrows. All structures are snapshots after 200 ns MD simulations.

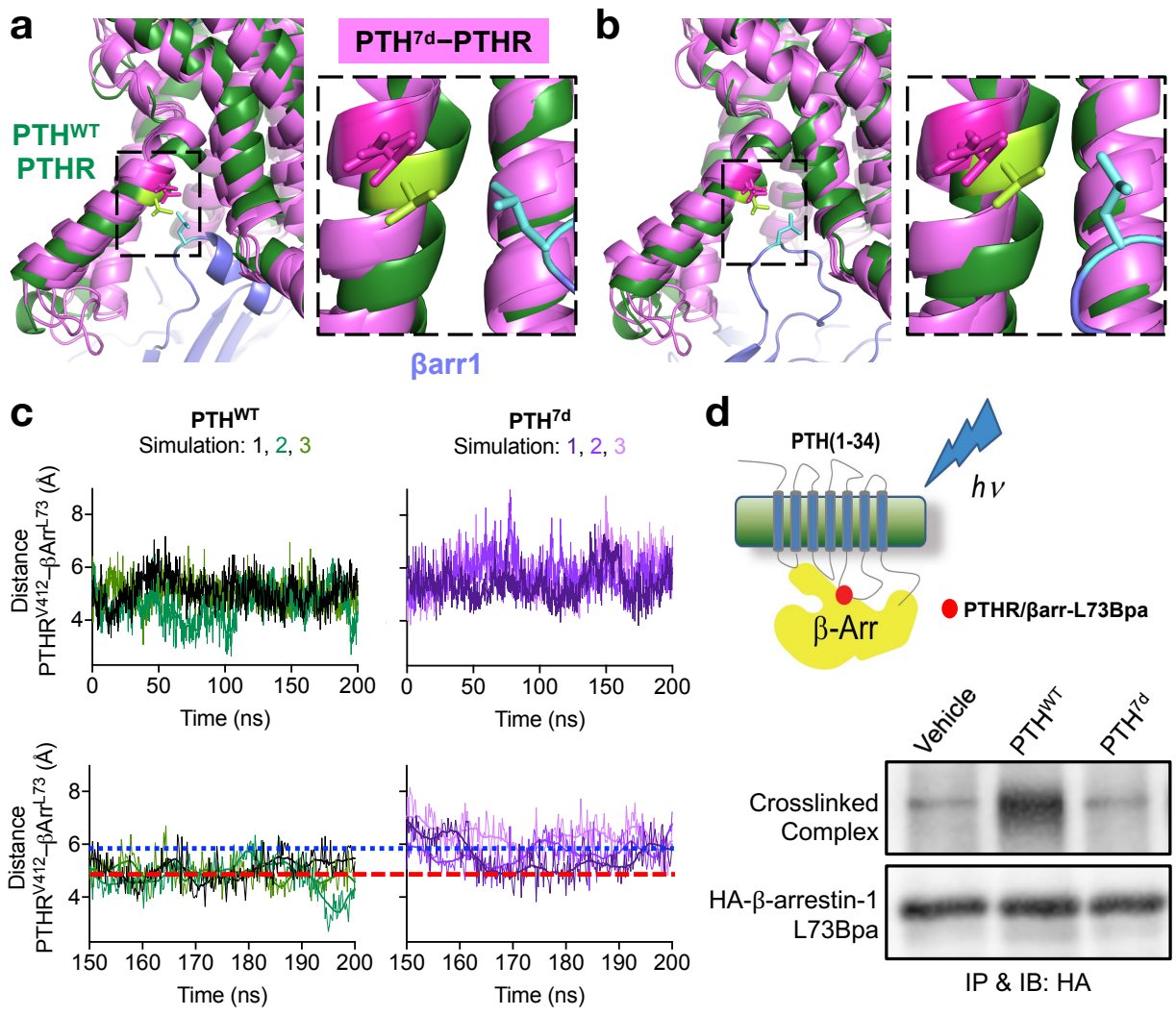

Figure 4.14. Structural basis for impaired β-arrestin coupling by PTH^{7d}.

a, b, Triplicate snapshots of PTH^{7d}–PTHR (violet) MD simulations after 200 ns were aligned by receptor TM helices to Model 1 (**a**) and Model 2 (**b**). PTH^{WT}–PTHR is dark green, and β-arrestin-1 is slate blue. The dashed boxes highlight potential interactions of PTHR TM6 residue Val412 with β-arrestin-1 Leu73. **c,** Distance distributions between PTHR Val412 CB and β-arrestin-1 Leu73 CG (Model 1) side chain atoms over triplicate MD simulations of PTH^{WT}- and PTH^{7d}-bound receptor. Raw data are shown as thin lines. Second-order smoothed data (over 20 neighbors) are shown as thick lines. *Top*, distance data over 200 ns simulations. *Bottom*, distance data over the last 50 ns of each simulation. 5.8 Å is indicated by blue dotted line. 4.8 Å is indicated by red dashed line. **d,** Photo-crosslinking between β-arrestin-1 Leu73Bpa and PTHR. *Top,* schematic procedure. *Bottom,* co-immunoprecipitation of HA-tagged β-arrestin-1 Leu73Bpa and photo-crosslinked PTHR–β-arrestin-1 complexes. Samples were immunoprecipitated and immunoblotted using an anti-HA antibody. *This photo-crosslinking pull-down was performed by Saifei Lei.*

The extended TM6 kink in the PTH^{WT}–PTHR–G_s model reduces the interactions to one TM6 residue and one $G\alpha_s$ residue (Appendix Figure 24c). However, all but one of the same α5 residues interact with PTHR TM2, TM3, ICL2, and TM5 residues in both models (Appendix Figure 24d, e).

4.4 Discussion

Here, we have presented two PTH mutants that prevent β-arrestin coupling to the receptor by distinct structural mechanisms, with each mechanism uniquely affecting the duration of cAMP production at the plasma membrane: PTH^{H9A} induces transient cAMP production, and PTH^{7d} induces sustained cAMP production.

By comparing PTH^{WT} and PTH^{H9A}, we demonstrate the existence of structure-encoded allosteric coupling between PTHR ECL2 and PTH residue His9 that determines direct interaction between PTHR's intracellular loop 3 (ICL3) and β-arrestins and duration of cAMP signaling. PTH His9 engages in a network of key contacts with PTHR residues belonging to ECL2, ECL3, and TM5, independently of binding affinity, to trigger PTHR conformational rearrangements in favor of its coupling to β-arrestin. The PTH^{H9A} peptide lacks these key contacts and is predicted by MD simulations to adopt a distinctive binding pose within $PTHR^{TMD}$, which ultimately eliminates β-arrestin coupling by stabilizing the inward movement of PTHR ICL3. It appears that the stabilization of a kink in the cytoplasmic extension of TM5 (kink 5) by PTH^{H9A} decreases the exposed area within the receptor cytosolic core for G proteins and β-arrestins to bind. Since the PTH^{H9A}-bound receptor retained transient G_s signaling but eliminated β-arrestin coupling, the exposure of a suitable binding epitope at the cytoplasmic

surface of PTHR may be particularly critical for β-arrestin recruitment. G_s could also be more amenable to conformational changes upon initial clashing with kink 5/ICL3 that permit G_s activation by PTH^{H9A}-bound receptor. This mechanism of reduced β-arrestin signaling may extend to other class B GPCRs, as chemical properties of residues $382^{5.58}$–$389^{5.65}$ in kink 5 are highly conserved amongst class B GPCRs (Appendix Figure 23). Kink 5 has not been previously observed in structurally resolved class B GPCRs[24,50,52,53,55-57,59-62,222], as these structures are either in the inactive state or in complex with G_s, which would block the TM5 movement due to inward TM6 movement or $G\alpha_s$ occupation, respectively. In the thermostabilized intermediate state structure of GLP1R[20], the cytosolic portion of TM5 is stabilized by contacts with another receptor monomer via crystal packing. Nevertheless, structures containing peptide ligands display stabilization of ECL2 by one or more ligand residues[24,55-57,59-62]. Furthermore, alanine substitutions of GLP1R ECL2 residues led to distinct effects on cAMP, Ca^{2+}, and ERK1/2 signaling by three peptide ligands (GLP1, exendin-4, oxyntomodulin), suggesting the importance of ECL2 in biased agonism of class B GPCRs[223,224]. In our study, mutating the only PTH residue that interacts with ECL2 caused remarkable structural and signaling changes in PTHR.

In the case of PTH^{7d}, L→D isomerization at position 7 of PTH enhanced the polar network between ligand and PTHR required for receptor activation and thus promoted an outward movement of PTHR TM6 helix according to MD simulation analysis. This outward movement does not cause clashing with G_s, in contrast to PTH^{H9A}-induced conformations, which may explain why PTH^{7d} permits sustained G_s signaling while PTH^{H9A} only induces transient signaling (Figure 4.15). Previous studies have reported that an inward movement of TM6 is essential for efficient β-arrestin coupling[218]. From these studies and our MD results, we hypothesize that the stabilized

outward TM6 of PTH^{7d}-bound receptor cannot move inward as necessary to form a stable PTHR–β-arrestin complex. In the presented PTHR–β-arrestin models, only one β-arrestin residue interacts with TM6 (Figure 4.9a, b), given that the outward TM6 kink in G-protein stabilized receptor remains after 200 ns of MD simulation. However, both models would permit inward movement of TM6 to increase contacts with β-arrestin (Figure 4.9a, b).

Our structural analyses suggest that stabilization of the outward TM6 kink by PTH^{7d} also reduces PTHR contacts with $G\alpha_s$ (Appendix Figure 24). Since PTH^{7d} triggers sustained cAMP signaling at the plasma membrane, we can hypothesize that TM6 interactions with the α5-helix of $G\alpha_s$ are less crucial for stabilizing PTHR–G_s complex. It is possible that $G\beta\gamma$ serves to anchor $G\alpha_s$ to the receptor despite reduced TM6–$G\alpha_s$ contacts. Alternatively, G_s could shift/rotate toward TM6 in the PTH^{7d}-bound complex to increase contacts. Since the publication of the PTHR–G_s cryo-EM structures[63], eight additional class B GPCR–G_s structures were solved[225-229]. Comparing all unique structures by structurally aligning their TMDs reveals flexibility in TM6 and position of G_s within the receptor core (Appendix Figure 25). GLP1R–G_s cryo-EM structures with bound peptide ligands GLP1 and exendin-5 (a biased agonist with enhanced cAMP signaling but retained β-arrestin recruitment) revealed a 6º rotation of $G\alpha_s$ α5 within the receptor core[61], further supporting the possibility of unique interactions between PTHR and G_s in PTH^{7d}- and PTH^{H9A}-bound complexes. Interestingly, both PTH^{7d} and exendin-5 are oriented toward TM1 and push on TM6 more than their respective wild-type ligands (Appendix Figure 21)[61], suggesting these structural features are important for G_s biased agonism in class B GPCRs. Using BRET experiments, exendin-5 was shown to increase the rate of G protein conformational change/activation[61]. PTH^{7d} may also enhance cAMP signaling via such a mechanism, although it remains to be experimentally tested.

Our results and previous studies demonstrate the crucial role of TM6 in class B GPCR structure and function, as further evidenced by the strong chemical conservation of TM6 amongst class B GPCRs (Appendix Figure 26). FRET experiments determined that the glucagon receptor maintains an active TM6 conformation minutes after G protein dissociation, suggesting a large energy barrier between open and closed TM6 conformations[63]. Since the cryo-EM structure of PTHR–G_s was used to generate our starting PTHR models for MD simulations, inward TM6 movement was unlikely to be observed in the presence of a full agonist without implementation of biased sampling methods. However, MD simulations of the glucagon receptor demonstrated that the TM6 kink is more outward in the presence of a full agonist than in the presence of a partial agonist[63].

After the completion of our PTH^{H9A} and PTH^{7d} structural studies, a structure of the beta-1-adrenoceptor (β_1AR) in complex with β-arrestin-1 was published (PDB 6TKO)[230]. This structure is similar to the rhodopsin and M2R complexes in arrestin orientation and position of the arrestin finger loop within the receptor core (Appendix Figure 27)[77,187,230]. Importantly, cryo-EM analysis of M2R and NTSR1 complexes revealed conformational heterogeneity of arrestin relative to the receptor and membrane[133,188]. Membrane curvature has been proposed to affect arrestin tilt, which may give rise to unique receptor–arrestin conformations at the plasma membrane versus endosomes, the latter of which exhibits high degrees of curvature[188].

The expanded mechanism of PTH binding to PTHR (detailed in Chapter 3.0) suggests that interactions between the N-terminal portion of PTH and the $PTHR^{TMD}$ during the binding process are important for positioning PTH within the $PTHR^{TMD}$ to permit receptor activation. The current chapter described two PTH mutants (PTH^{H9A} and PTH^{7d}) whose unique positions within the $PTHR^{TMD}$ altered PTHR signaling. Relative to PTH^{WT}, PTH^{H9A} and PTH^{7d} were shifted toward

TM2 and TM1/2, respectively (Appendix Figure 21). The receptor ECDs also shifted in the same direction, further demonstrating that the $PTHR^{ECD}$ position is flexible and dependent on peptide interactions with the $PTHR^{TMD}$.

To summarize our findings, PTH^{7d} stabilizes outward TM6 kink, which maintains G_s coupling while preventing β-arrestin recruitment, leading to sustained cAMP production at the plasma membrane (Figure 4.15). In contrast, PTH^{H9A} promotes an inward ICL3 conformation that also prevents β-arrestin recruitment. While such a conformation is not predicted to enhance G_s coupling, as in the case of PTH^{7d}, some G_s coupling is maintained to generate transient cAMP at the plasma membrane. These results give insight into the structural determinants of G protein and β-arrestin coupling to class B GPCRs.

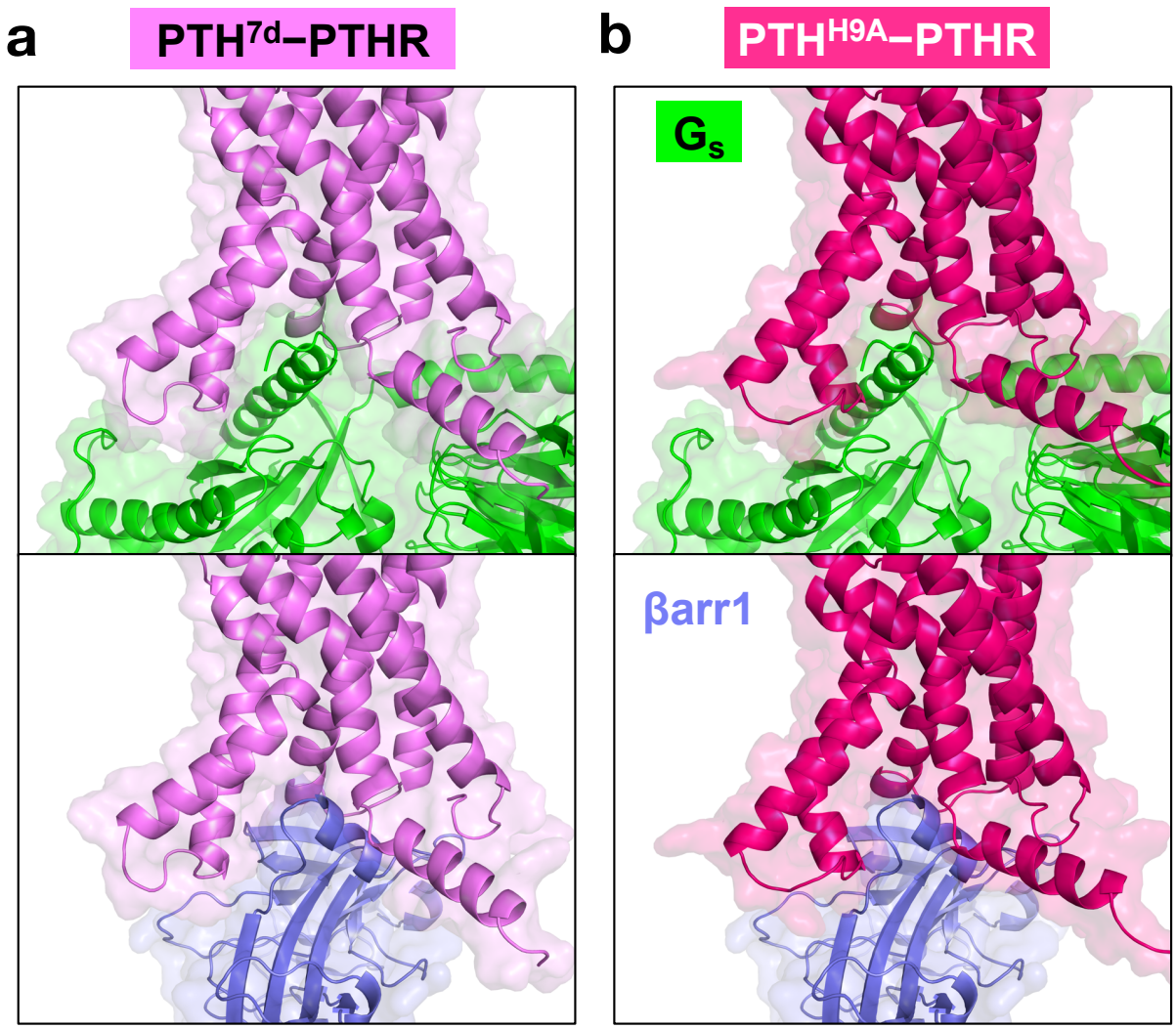

Figure 4.15. Structural basis of altered cAMP signaling by PTH^{7d} and PTH^{H9A}.

Models of PTH^{7d}–PTHR (a) and PTH^{H9A}–PTHR (b) bound to G_s or βarr1 were generated using MD snapshots after 200 ns simulation.

4.5 Acknowledgements

Research reported in this chapter was supported by the National Institute of Diabetes and Digestive and Kidney Disease (NIDDK), the National Institute of General Medical Sciences (NIGMS), the National Institute of Arthritis and Musculoskeletal and Skin Diseases (NIAMS), and the National Institute on Drug Abuse (NIDA) of the US National Institutes of Health (NIH) under grant Awards Number R01-DK111427, R01-DK116780, and R01-DK122259 (to Jean-Pierre Vilardaga), P41-GM103712 and P30-DA035778 (to Ivet Bahar), and F31-AR074843 (to Lisa Jean Clark).

4.6 Author Contributions

Lisa Jean Clark performed MD simulations with James Krieger, Pemra Doruker, and Ivet Bahar. Ji Young Lee performed ANM calculations. Alex White and Karina Peña performed signaling studies. Ieva Sutkeviciute, Frederic Jean-Alphonse, Saifei Lei, Fei Fang, and Kunhong Xiao optimized and performed photo-crosslinking coupled to MS assays. The original manuscripts from which this chapter was adapted were written by Lisa Jean Clark, Alex White, Ieva Sutkeviciute, Ivet Bahar, and Jean-Pierre Vilardaga.

5.0 Dissertation Summary

We optimized the expression and purification of PTHR–G_s complex bound to LA-PTH and stabilizing Nb35 (Section 2.1.1). With this sample, we used cryo-EM to solve three high resolution (3.0, 3.5, and 4.0 Å) structures, with each structure displaying a unique orientation of $PTHR^{ECD}$ relative to the $PTHR^{TMD}$ (Figure 2.4, Figure 2.6). The 4.0 Å structure also exhibits dissociation of the C-terminal LA-PTH residues. These structures permitted us to characterize LA-PTH interactions with PTHR, which involves a continuous α-helix connecting the $PTHR^{ECD}$ and $PTHR^{TMD}$, as seen in other published structures of class B GPCR–G_s complexes[61,62,226-229]. By comparing our active structure with a previously published inactive structure, we determined that the first three residues of LA-PTH push against TM6, and Glu4 stabilizes an extensive polar core network within the receptor, both of which promote the outward TM6 kink characteristic of receptor activation. From our structural analyses and MD simulations, PTHR point mutations in Jansen's metaphyseal chondrodyplasia render the receptor constitutively active by stabilizing the outward TM6 kink in the absence of agonist (Section 2.1.3.3 and Appendix E).

We also investigated the two-step mechanism of PTH binding to PTHR (Chapter 3.0): 1) the helical C-terminal part of PTH binds to the $PTHR^{ECD}$ (fast step), 2) the less structured N-terminal part of PTH binds to the $PTHR^{TMD}$ (slow step). Unlabeled $PTHR^{ECD}$ was titrated into ^{15}N-PTH to probe the conformational changes of the agonist during the first step of binding, and spectral analysis revealed that the mobility of the N-terminal part is reduced during the first binding step, independently of interactions with $PTHR^{TMD}$. In MD simulations, the flexibility of the $PTHR^{ECD}$ in relation to the $PTHR^{TMD}$ is significantly higher for the apo receptor than in the presence of PTH. From these data, we proposed an extended two-step binding mechanism in which

reduced mobility of the N-terminal part of PTH during the first binding step primes this part for interaction with the $PTHR^{TMD}$. We hypothesized that these interactions, especially involving ligand residues 5–14, influence the position of the peptide ligand within the receptor and contribute to specific signaling responses.

We tested this hypothesis in part by examining two PTH mutants with unique signaling responses (Chapter 4.0). While both PTH^{H9A} and PTH^{7d} prevented β-arrestin recruitment, these peptides triggered transient and sustained cAMP production at the plasma membrane, respectively, because of their unique interactions with the receptor. PTH^{H9A} promoted an inward movement of PTHR ICL3, which would block complex formation with β-arrestin but maintain some G_s coupling. PTH^{7d} enhanced the receptor polar network stabilizing the outward TM6 kink, a conformation favored for G_s coupling, while preventing the inward TM6 movement necessary for coupling to β-arrestin. These results showcase the importance of the PTHR TM5-ICL3-TM6 region for G_s and β -arrestin signaling and give insight into the mechanisms of biased agonism.

In total, this dissertation provides important insight into structural mechanisms of PTHR signaling, including ligand binding, receptor activation, and coupling to G_s and β-arrestin. Nevertheless, many questions remain. Although we made models of PTHR–β-arrestin based on available structures, conformational heterogeneity of GPCR–arrestin complexes has been observed[133,188]. Cryo-EM analysis of 2D class averages from purified PTHR–β-arrestin could reveal possible conformations of this complex. Importantly, what are the structural differences between PTHR–β-arrestin complexes at the plasma membrane versus in endosomes (i.e., supercomplex with both β-arrestin and G_s bound)[118]? While this dissertation focuses on G_s coupling, PTHR also couples to G_q and $G_{12/13}$[22]. What structural features contribute to Gα subtype specificity? Also, how does PTHrP/ABL stabilize unique conformations of PTHR that lead to

transient cAMP production at the plasma membrane? Answering this last question will help explain the differential effects of PTH and ABL on bone turnover and calcium levels.

Appendix A Supporting Information for Chapter 1

Appendix A.1 Chapter 1 Supporting Figures

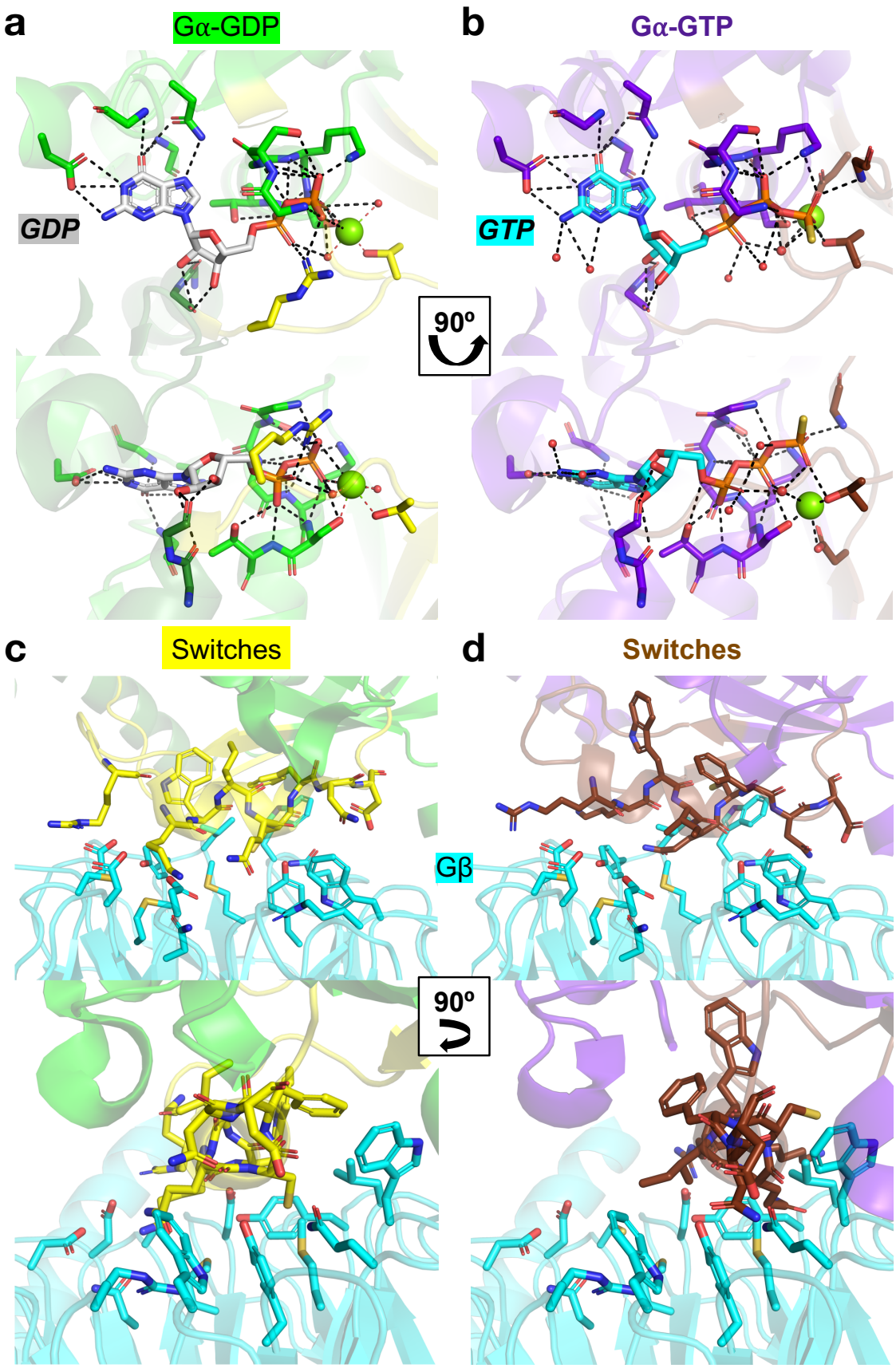
a
Gα-GDP
GDP
b
Gα-GTP
GTP
90º
c
Switches
d
Switches
Gβ
90º

Appendix Figure 1. Comparison of G_s in GDP- and GTP-bound states.

GDP-bound $G\alpha_s$ (PDB 6E67[68]) is green, with Switches in yellow. GTPγS-bound $G\alpha_s$ (PDB 1AZT[65]) is purple blue, with Switches in brown. **a, b,** Polar interactions between $G\alpha_s$ and guanine nucleotide, shown as black dashes. Water molecules are shown as small red spheres. In **b,** the GTP γ-phosphate forms two new polar contacts with Switches I and II residues. **c,** Interactions between Switch residues and Gβ (cyan) in GDP-bound G_s. **d,** Reduced interactions between $G\alpha_s$-GTP Switch residues and Gβ. The structure of $G\alpha_s$-GTP was aligned with $G\alpha_s$-GDP to model changes in the $G\alpha_s$–Gβ interface upon GTP binding. In the bottom panel, note the lack of interactions with a significant portion of the Gβ surface.

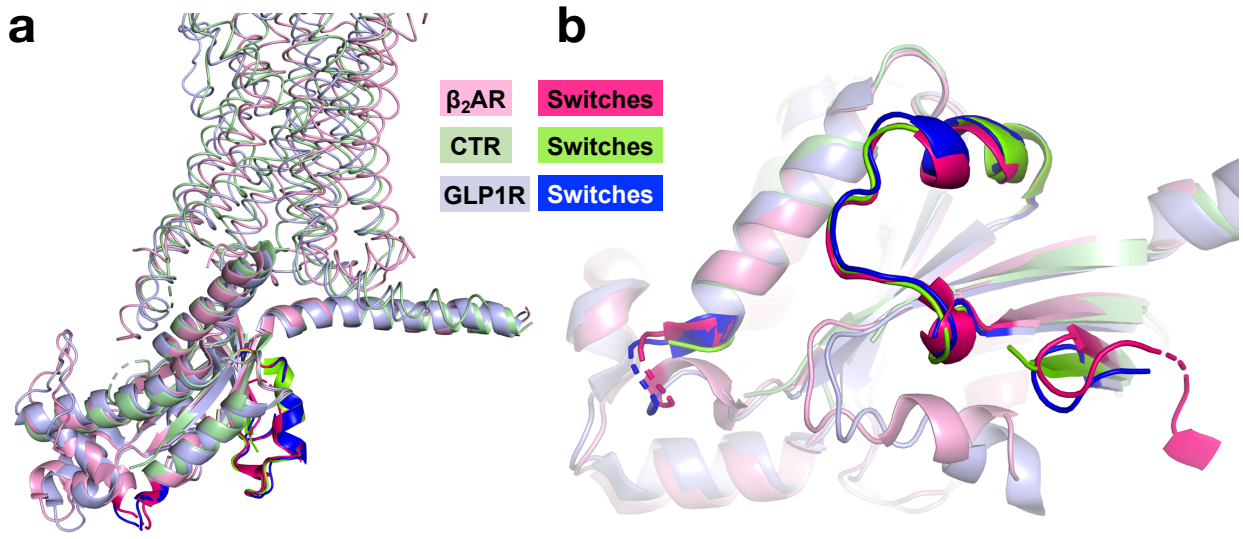

Appendix Figure 2. $G\alpha_s$ conformations in complex with class A and class B GPCRs.

Structures of GPCRs in complex with G_s: β_2AR (class A, PDB 3SN6[67]), CTR (class B, PDB 6NIY[59]), GLP1R (class B, PDB 5VAI[62]). The subunits of these structures were aligned. **a,** Overall conformations of subunits $G\alpha_s$. Receptors are displayed as loops. **b,** Zoomed-in image highlighting the three Switch loops.

Appendix A.2 Chapter 1 Supporting Tables

Appendix Table 1. Published structures of class B GPCRs.

Unique class B GPCR structures published prior to the PTHR–G_s cryo-EM structures are listed, including those of the extracellular domain alone (ECD) or the transmembrane domain (TMD) with or without clear ECD density. Structure data obtained from GPCRdb and RCSB PDB (rcsb.org)[231,232].

Receptor Family	Receptor	PDB	Method	ECD/ TMD	Res. (Å)	Ligand	Additional Proteins		Ref
Calcitonin	CALCR (CTR)	5II0	X-ray	ECD	2.10	salmon calcitonin analog [BrPhe^{22}]sCT(8–32)			25
		6NIY	cryo-EM	TMD	3.3	sCT	G_s	Nb35	59
	CGRPR (CLR: RAMP1)	3N7P 3N7R 3N7S	X-ray	ECD	2.80 2.90 2.10	telcagepant olcegepant			26
		5V6Y	X-ray	ECD	2.80	adrenomedullin variant AM(37–52)		MBP	27
		6D1U	X-ray	ECD	2.05	adrenomedullin 2		MBP	28
		4RWG	X-ray	ECD	2.44	CGRP(27–37)NH_2		MBP	29
		6E3Y	cryo-EM	TMD	3.3	CGRP	G_s	Nb35	60
	AM1R (CLR: RAMP2)	3AQF	X-ray	ECD	2.60				30
		4RWF	X-ray	ECD	1.76	AM(27–52)NH_2		MBP	29
Corticotropin-releasing factor	CRF1R	4K5Y	X-ray	TMD	2.98	antagonist CP-376395		T4L	50
		3EHU	X-ray	ECD	1.96	CRF		MBP	31
		2L27	NMR	ECD		α-helical cyclic CRF			46
	CRF2R	1U34	NMR	ECD					47
		3N96 3N95 3N93	X-ray	ECD	2.75 2.72 2.50	urocortin 1 urocortin 2 urocortin 3		MBP	32
		2JND	NMR	ECD		antagonist astressin(27–41)			48
Glucagon	GCGR	4L6R	X-ray	TMD	3.30	NNC0640 (density not observed)		BRIL	51

Appendix Table 1 continued.

		5EE7	X-ray	TMD	2.50	antagonist MK-0893		T4L	[53]
		5XEZ	X-ray	TMD	3.00	NNC0640		T4L, mAb1	[52]
		5YQZ	X-ray	TMD	3.00	partial agonist NNC1702		T4L	[56]
		4ERS	X-ray	ECD	2.64			Fab	[33]
	GHRHR	2XDG	X-ray	ECD	1.95				[34]
	GIPR	2QKH	X-ray	ECD	1.90	GIP			[35]
		4HJ0	X-ray	ECD	3.00			Gipg013 Fab	[36]
	GLP1R	6B3J	cryo-EM	TMD	3.30	exendin-5	G_s	Nb35	[61]
		5NX2	X-ray	TMD	3.70	truncated agonist peptide 5			[57]
		5VAI	cryo-EM	TMD	4.10	GLP-1	G_s	Nb35	[62]
		5VEW 5VEX	X-ray	TMD	2.70 3.00	PF-06372222 NNC0640		T4L	[54]
		3IOL	X-ray	ECD	2.10	Glucagon			[37]
		4ZGM	X-ray	ECD	1.80	8Aib,34R-GLP-1(7–37)-OH			[38]
		3C5T	X-ray	ECD	2.30	exendin-4(9–39)			[39]
		5E94	X-ray	ECD	2.00			Fab	[40]
Parathyroid hormone	PTHR	6FJ3	X-ray	TMD	2.50	ePTH		PGS	[55]
		3L2J	X-ray	ECD	3.24			MBP	[41]
		3C4M	X-ray	ECD	1.95	PTH(15–34)		MBP	[42]
		3H3G	X-ray	ECD	1.94	PTHrP(13–34)		MBP	[43]
VIP and PACAP	PAC1R	3N94	X-ray	ECD	1.80			MBP	[44]
	VPAC2R	2JOD	NMR	ECD		PACAP(6–38)			[49]
		2X57	X-ray	ECD	2.10				[45]

Appendix B Supporting Information for Chapter 2

Appendix B.1 Chapter 2 Supporting Figures

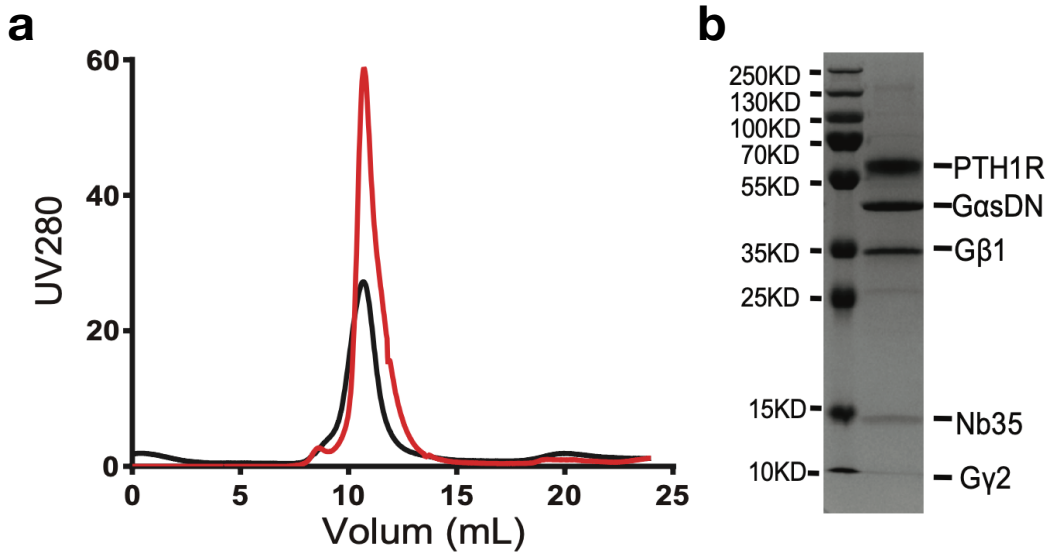

Appendix Figure 3. Purification of the LA-PTH–PTHR–G_s–Nb35 complex.

Size-exclusion chromatography elution profile of the purified complex (**a**, red line) and SDS-PAGE analysis of the complex after size-exclusion (**b**). *Adapted from Fig S1B and D in Zhao, et al. (2019)*[24].

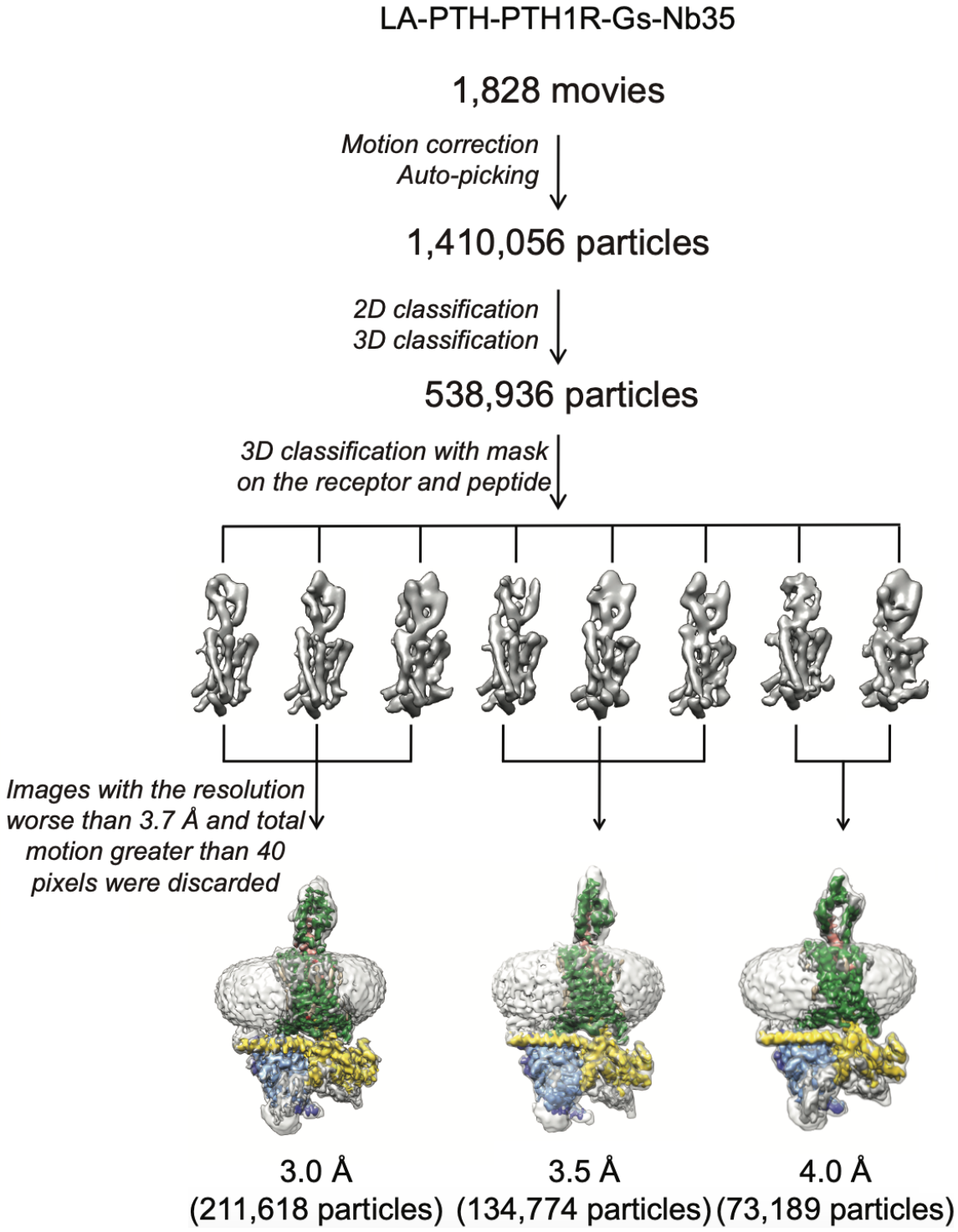

Appendix Figure 4. Flowchart of cryo-EM data analysis.

Single-particle cryo-EM of the LA-PTH−PTHR−G_s complexes, including particle projection selection, classification, and refinement. *Adapted from Fig. S4 in Zhao, et al. (2019)*[24].

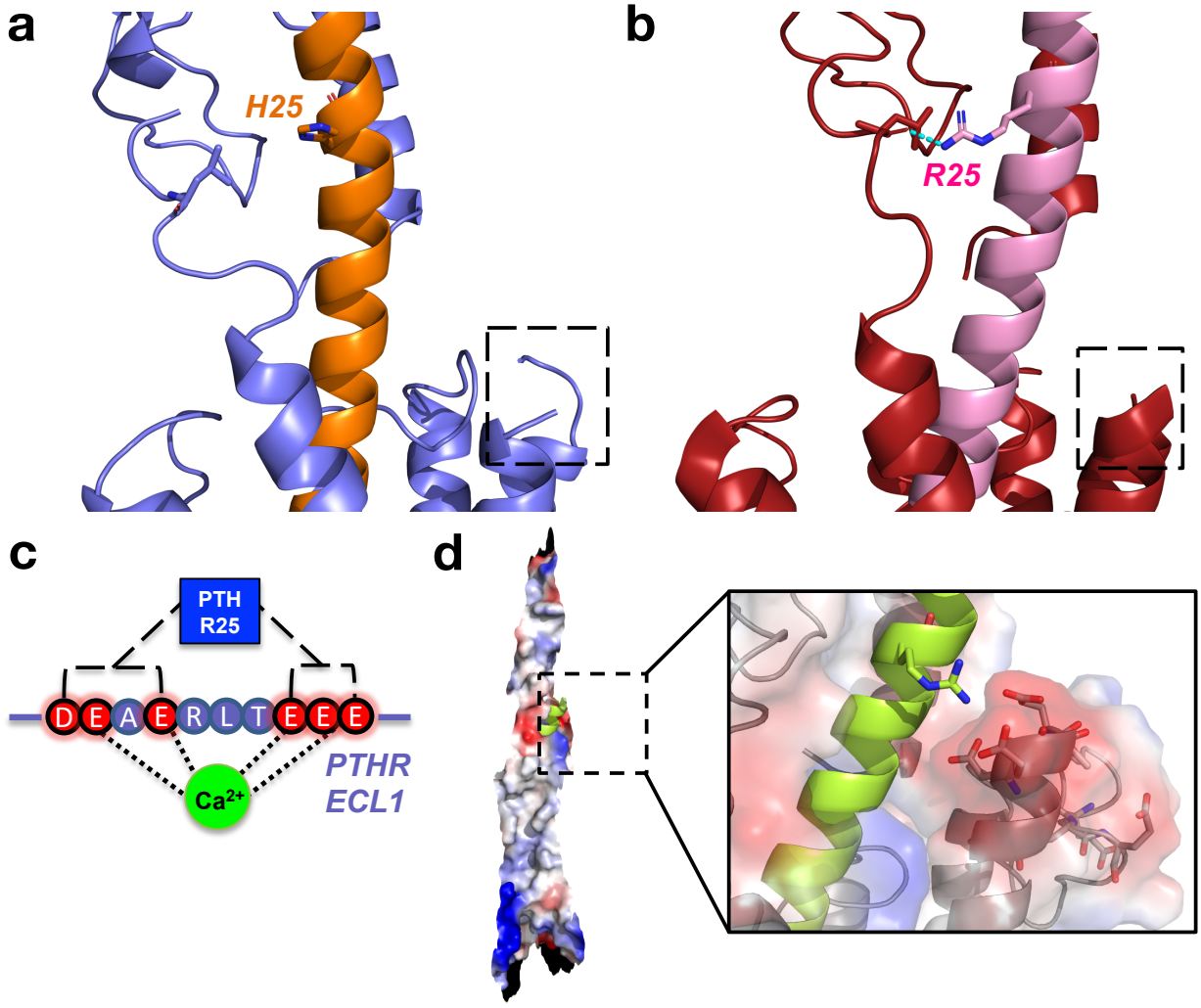

Appendix Figure 5. Structural basis of PTH-Arg25 contribution to Ca^{2+} allostery.

a, Active PTHR state 1, with LA-PTH His25 and PTHR Leu174 shown as sticks. The receptor and LA-PTH of the active structure are colored slate blue and orange, respectively. ECL1 location indicated by dashed box. **b,** Inactive PTHR structure, with ePTH Arg25 and PTHR Leu174 shown as sticks. The receptor and ePTH of the inactive structure are colored dark red and pink, respectively. ECL1 location indicated by dashed box. **c,** Schematic diagram of Ca^{2+} coordination by PTH–PTHR. PTH Arg25 interactions with two acidic clusters in ECL1, permitting these clusters to coordinate Ca^{2+}. **d,** Homology model of the PTHR generated from GPCR-I-TASSER with the modeled PTH^{233}. PTHR is shown as an electrostatic surface, and the PTH is represented as a green helix. PTH Arg25 points toward an acidic face of PTHR in ECL1[89].

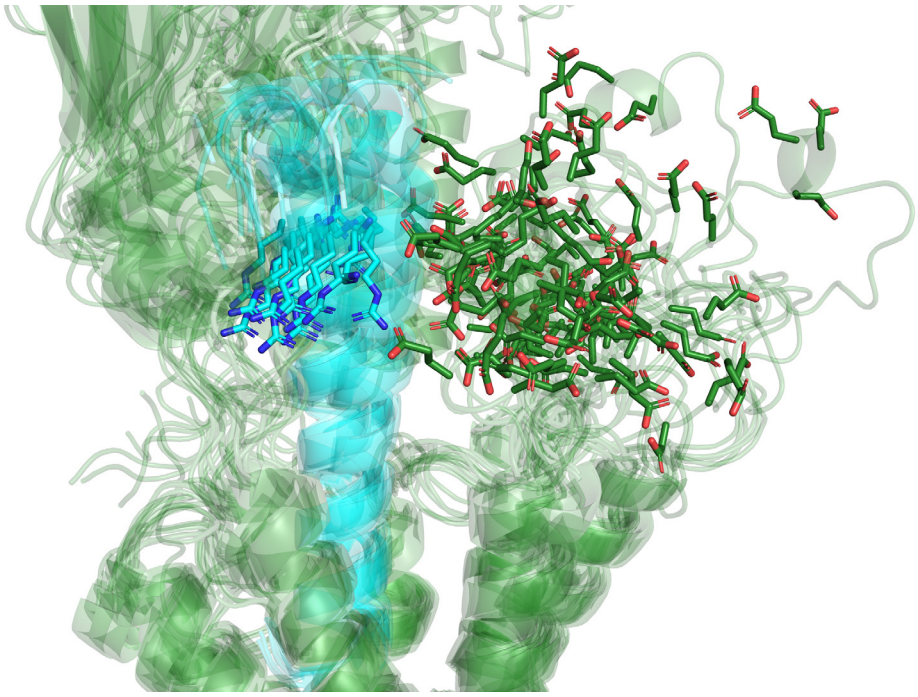

Appendix Figure 6. Position of PTH Arg25 and acidic PTHR ECL1 residues in triplicate MD simulations.

Alignment of snapshots from the last 50 ns of MD simulation. PTH is cyan, and PTHR is dark green. PTH Arg25 and PTHR ECL1 acidic residues (Asp251, Glu252, Glu254, Glu258–261) are shown as sticks.

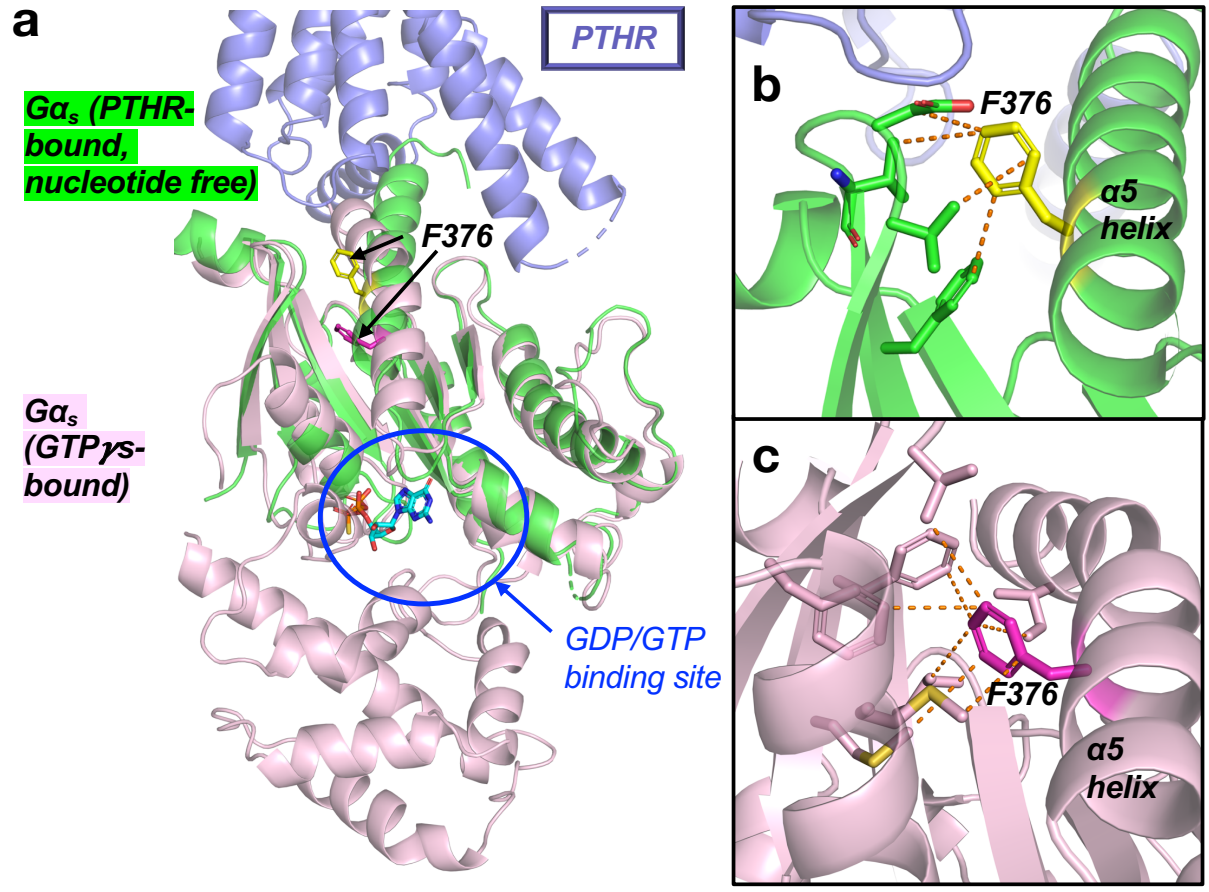

Appendix Figure 7. Effects of F376V mutation on Gαs structure.

a, Alignment of Gαs structures. The receptor-bound state is state 1 of the LA-PTH–PTHR–Gs structure. The receptor and Gαs are colored slate blue and green, respectively. The receptor-free state is the crystal structure of GTPγS-bound Gαs (PDB 1AZT), colored pink. GTPγS is shown as cyan sticks. The GDP/GTP binding site of Gαs is circled blue. **b,** Hydrophobic interactions between Phe376 (yellow) and other Gαs residues, shown as sticks, in the receptor-bound form. **c,** Hydrophobic interactions between Phe376 (magenta) and other Gαs residues, shown as sticks, in the receptor-free form.

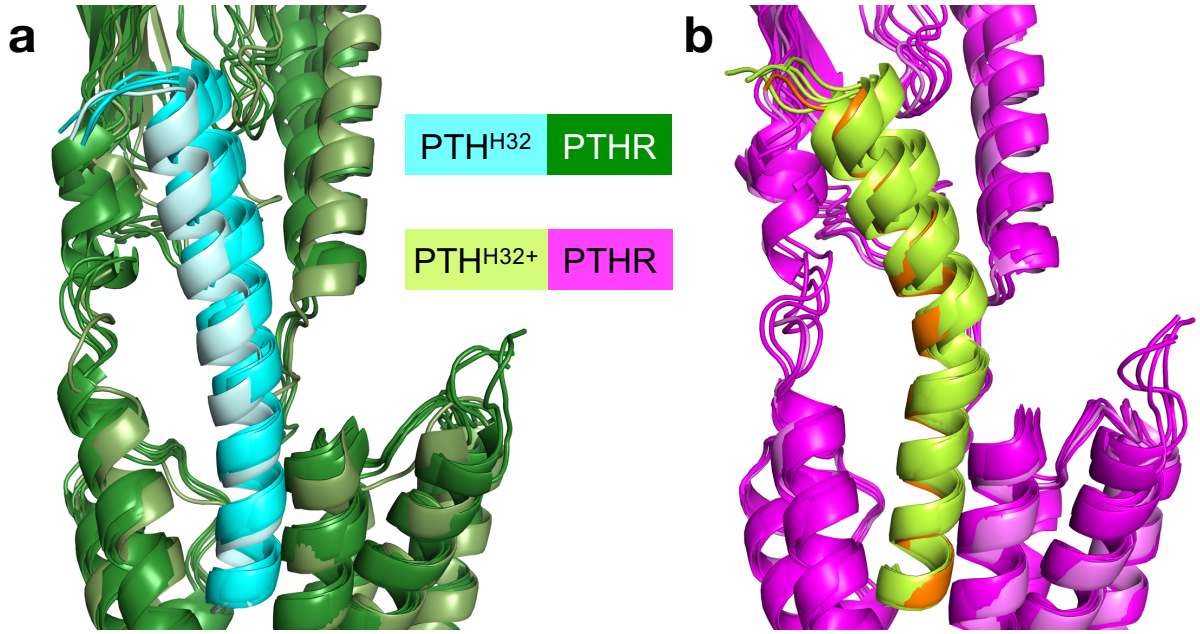

Appendix Figure 8. Curvature of PTH helix in PTH^{H32}/PTH^{H32+}–PTHR 1 ns MD simulations.

Snapshots collected every 0.3 ns simulation (starting at t = 0.1 ns) were aligned in PyMOL. Snapshots at 12 ps, where PTH^{H32+} curvature initiates, are distinctly colored: **a,** PTH^{H32} is pale cyan, and PTHR is smudge green. **b,** PTH^{H32+} is orange, and PTHR is violet.

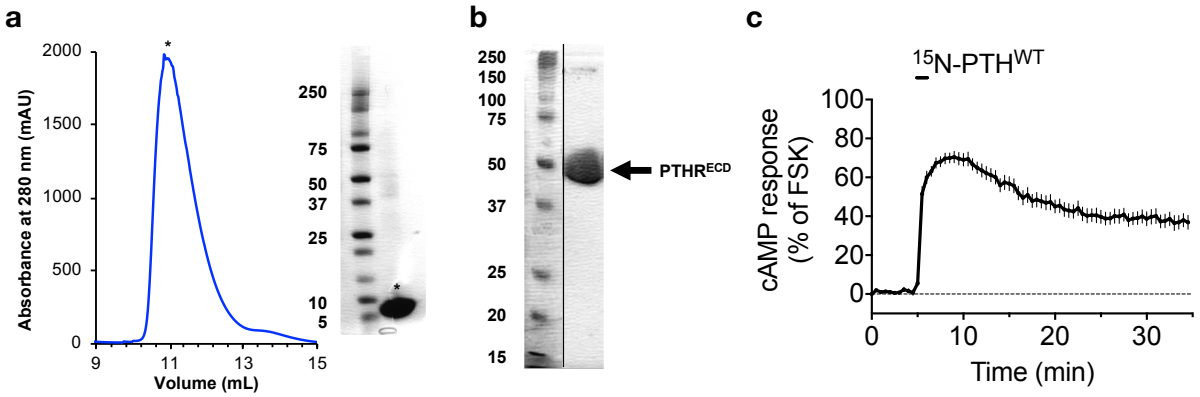

Appendix Figure 9. Purification of ^{15}N-PTH and PTHR^{ECD}.

a, Size exclusion chromatogram of ^{15}N-PTH using Superdex Peptide 10/300 (*left*), and SDS-PAGE of the fraction indicated by asterisk (*right*). **b,** SDS-PAGE of purified PTHR^{ECD}. **c,** Averaged cAMP production (relative to production in the presence of forskolin, FSK) mediated by 10 nM ^{15}N-PTH^{WT} in HEK-293 cells stably expressing PTHR. Data represent the mean ± s.e.m. of N = 2 experiments with *n* = 19 cells per experiment. *The cAMP assay was performed by Alex White.*

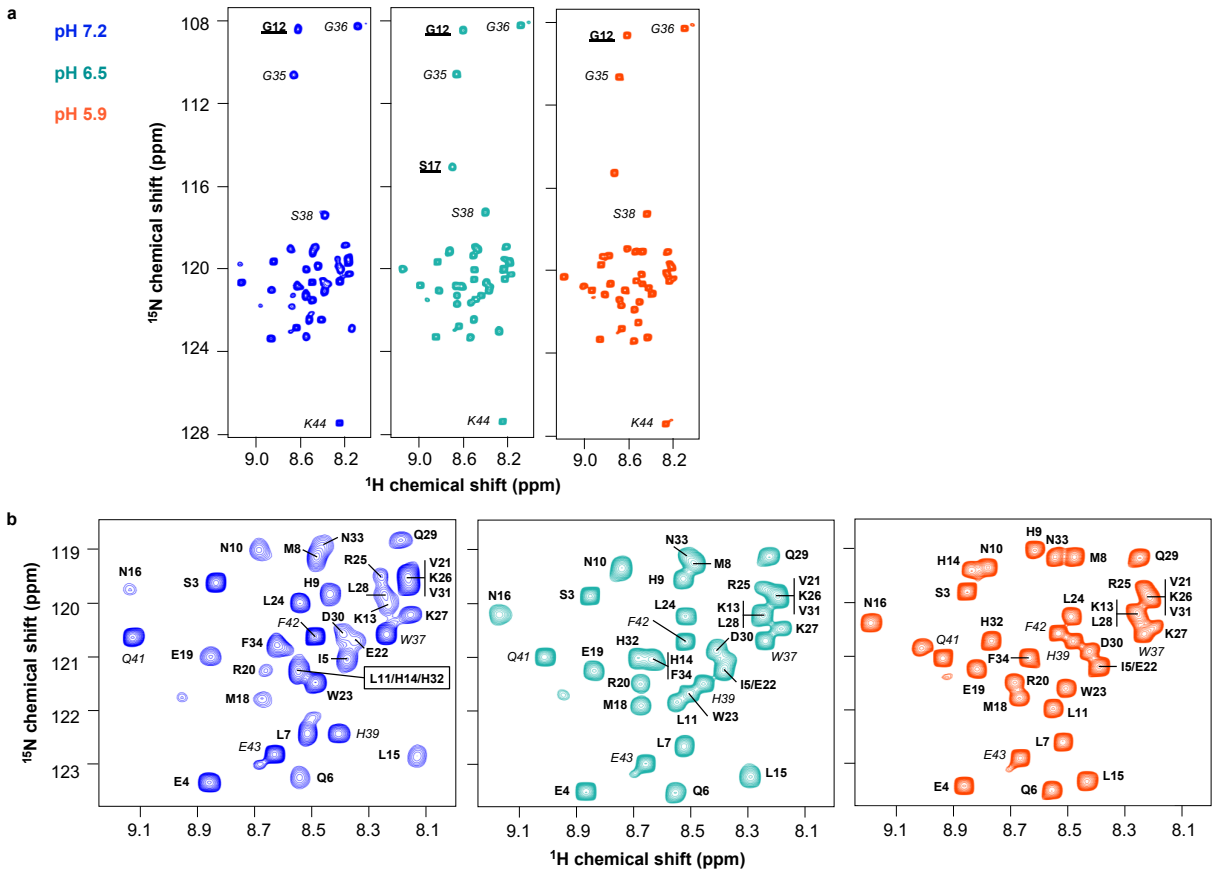

Appendix Figure 10. Two-dimensional ^{1}H-^{15}N heteronuclear single quantum coherence (HSQC) spectra of ^{15}N-PTH at multiple pH values.

Spectra were obtained at pH 7.2 (blue), 6.5 (teal), and 5.9 (orange). **a,** Full spectra showing all peaks of PTH. **b,** Zoomed-in spectra showing most peaks of PTH. PTH peaks are labeled with bold text, and peaks corresponding to attached Strep-tag are labeled with italicized text.

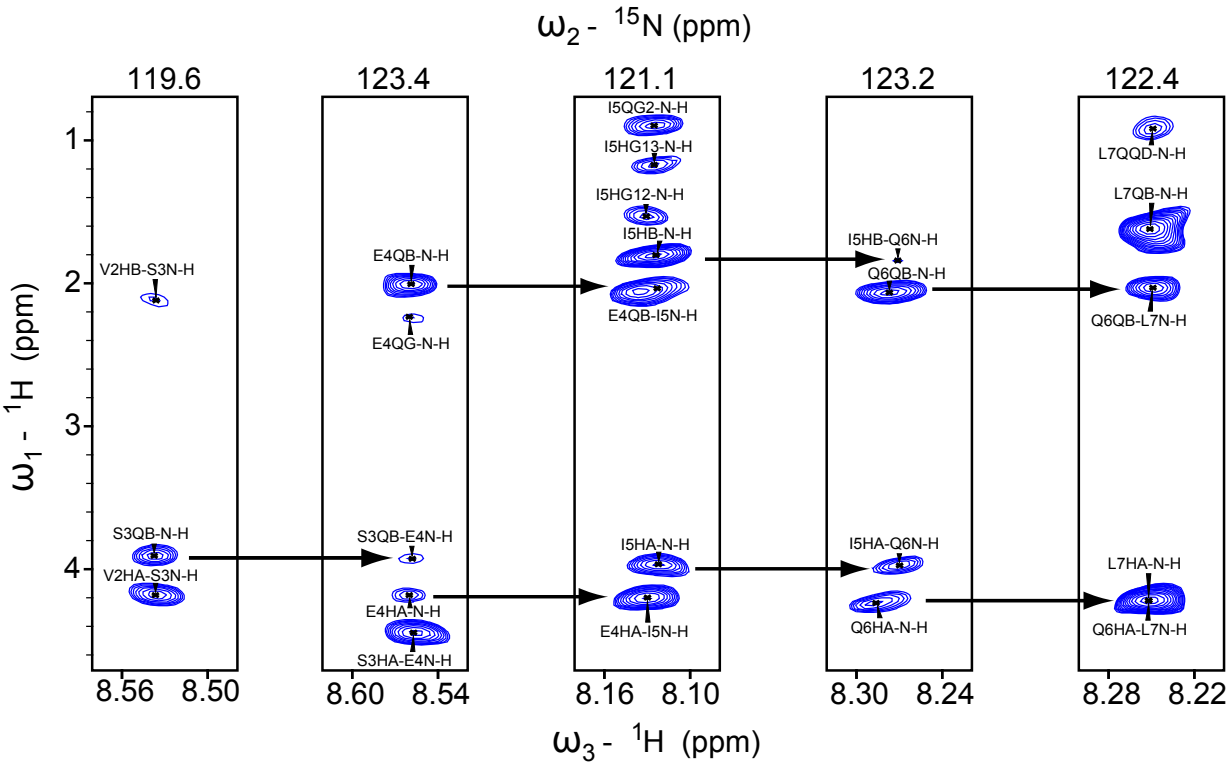

Appendix Figure 11. Representative strip plots for residues Ser3–Leu7 from the 3D ^{15}N-edited NOESY spectrum of PTH.

These plots demonstrate sequential Hα(*i*) to HN(*i*+1) and Hβ(*i*) to HN(*i*+1) connectivities, indicated by arrows. The spectrum was recorded at 10ºC and with a ^{1}H resonance frequency of 700.13 MHz. *Figure was prepared by Vasyl Bondarenko.*

Appendix B.2 Chapter 2 Supporting Tables

Appendix Table 2. Cryo-EM data collection, model refinement, and validation statistics.

Adapted from Table S2 in Zhao, et al. (2019)[24].

LA-PTH–PTHR–G_s–Nb35	State 1	State 2	State 3
Data collection and processing			
Magnification	49310	49310	49310
Voltage (kV)	300	300	300
Electron exposure ($e^-/Å^2$)	60	60	60
Defocus range (μm)	-0.5 ~ -3.0	-0.5 ~ -3.0	-0.5 ~ -3.0
Pixel size (Å)	1.014	1.014	1.014
Symmetry imposed	C1	C1	C1
Initial particle projections (no.)	1,410,056	1,410,056	1,410,056
Final particle projections (no.)	211,618	134,774	73,189
Map resolution (Å)	3.0	3.5	4.0
FSC threshold	0.143	0.143	0.143
Map resolution range (Å)	2.5-6	2.8-6	3.1-6
Refinement			
Initial model used (PDB code)	6B3J	6B3J	6B3J
Model resolution (Å)	3.0	3.5	3.8
FSC threshold	0.5	0.5	0.5
Model resolution range (Å)	50-3.0	50-3.5	50-3.8
Map sharpening *B* factor ($Å^2$)	-94	-178	-169
Model composition			
Non-hydrogen atoms	9419	9497	9190
Protein residues	1048	1159	1141
Lipids	10	10	1
B factors ($Å^2$)			
Protein	65.7	109.7	138.8
Lipids	74.6	99.0	169.1
R.m.s. deviations			
Bond lengths (Å)	0.010	0.005	0.005
Bond angles (°)	1.113	1.140	1.160
Validation			
MolProbity score	1.40	1.38	1.3
Clashscore	3.8	3.9	3.5
Poor rotamers (%)	0.1	0.1	0.2
Ramachandran plot			
Favored (%)	96.5	96.7	96.4
Allowed (%)	3.5	3.3	3.6
Disallowed (%)	0	0	0
EMD accession numbers	0410	0411	0412
PDB Codes	6NBF	6NBH	6NBI

Appendix Table 3. LA-PTH interactions with PTHR in the three cryo-EM states.

–NH and –CO represent the main chain amine and carbonyl groups of a residue, respectively. H-bond, hydrogen bond. Polar interactions are < 4 Å. Hydrophobic interactions are < 5 Å. Interactions occur in all three states unless otherwise indicated.

Residue		Interactions
1	Ala	$–NH_3^+$ H-bonds with Met425 –CO; Thr427 –CO and –NH. States 1 and 2: Additional H-bond between $–NH_3^+$ and Thr427 –OH.
2	Val	Side chain hydrophobic interactions with Leu292, Tyr296, Ile367 side chains. Main chain –NH H-bonds with Gln364 side chain.
3	Ala	Side chain hydrophobic interactions with Glu444 side chain.
4	Glu	Side chain polar interactions with Tyr195 and Arg233 side chains.
5	Ile	Side chain hydrophobic interactions with Phe288, Leu292, Ile367 side chains. States 1 and 2: Additional hydrophobic interaction with Ile363.
6	Gln	Side chain $–NH_2$ H-bonds with Thr430 –NH, Trp437 and Gln440 side chains.
7	Leu	Side chain hydrophobic interactions with Phe184, Leu187, Tyr191, Trp437, Met441, Met445 side chains.
8	Met	Side chain hydrophobic interactions with Val285, Phe288, and Leu289 side chains.
9	His	States 1 and 2: Side chain N H-bond with Ser355 –NH. State 3: Side chain N H-bond with Tyr429 –OH side chain.
10	Gln	Side chain H-bond with Thr430 –CO.
11	Arg	Side chain hydrophobic interactions with Phe184 side chain. Polar interactions with Phe184 –CO and Asp185 side chain.
12	Ala	Side chain hydrophobic interactions with Asp353 and Leu354 side chains.
13	Lys	State 1: Side chain polar interaction with Ser355 side chain. States 2 and 3: No direct interactions.
14	Trp	State 1: Side chain polar interactions with Glu177 –CO, Glu180 side chain. Side chain hydrophobic interactions with Arg181, Phe184, Val432. State 2: Side chain polar interactions with Glu180 side chain. Side chain hydrophobic interactions with Arg181, Phe184. State 3: Side chain polar interactions with Glu177 –CO. Side chain hydrophobic interactions with Arg181.
15	Ile	Side chain hydrophobic interaction with Leu244 side chain.
16	Gln	Side chain hydrophobic interaction with Leu354 side chain.
17	Asp	Long-range repulsive interactions with Asp137 and Glu177. State 2: Side chain hydrophobic interaction with Val31 side chain.

Appendix Table 3 continued.

18	Ala	No direct interactions.
19	Arg	State 1: –CO H-bond with Lys34 side chain. States 2 and 3: No direct interactions.
20	Arg	State 1: Side chain polar interactions with Met32 –NH and –CO; Asp137 side chain. State 2: Side chain polar interactions with Asp137 side chain. State 3: Possible polar interaction with Gln37 side chain, Tyr134 –CO, Tyr136 –NH.
21	Arg	State 1: Side chain polar interaction with Asp137 side chain. State 2: No direct interactions. State 3: Side chain polar interaction with Glu177 side chain. Side chain hydrophobic interaction with Leu174 side chain.
22	Ala	No direct interactions.
23	Phe	State 1: Side chain hydrophobic interactions with Lys34, Gln37, and Ile38 side chains. State 2: Side chain hydrophobic interactions with Lys34, Gln37, and Leu41 side chains. State 3: Side chain hydrophobic interactions Leu41 and Ile115 side chains.
24	Leu	States 1 and 2: Side chain hydrophobic interactions with Ile135, Asp137, and Phe138 side chains. State 3: Side chain hydrophobic interactions with Phe138 and Val171 side chains.
25	His	State 1: No direct interactions. State 2: Side chain hydrophobic interaction with Leu174 side chain. State 3: Side chain H-bond with Tyr167 –OH.
26	Lys	No direct interactions.
27	Leu	States 1 and 2: Side chain hydrophobic interactions with His114 and Ile115 side chains. State 3: No direct interactions.
28	Ile	State 1: Side chain hydrophobic interactions with Phe138 and Val171 side chains. State 2: Side chain hydrophobic interactions with Phe138, Tyr167, and Val171 side chains. State 3: No direct interactions.
29	Ala	No direct interactions.
30	Glu	States 1 and 2: Side chain polar interactions with Arg162 side chain. State 1: –CO polar interaction with Arg162 side chain. State 3: No direct interactions.
31	Ile	States 1 and 2: Side chain hydrophobic interactions with His114, Ile115, and Tyr167 side chains. State 2: Side chain hydrophobic interaction with Ala165 side chain. –CO polar interaction with Ala165 –NH. State 3: No electron density in structure.
32	His	States 1 and 2: Side chain hydrophobic interactions with Tyr167 side chain. Side chain polar interactions with Ala165 –CO. State 1: Side chain polar interactions with Asn166 –CO, and Tyr167 –NH. State 2: Side chain polar interactions with Ser168 –NH.

Appendix Table 3 continued.

32	His	State 3: No electron density in structure.
33	Thr	States 1 and 3: No electron density in structures. State 2: Side chain hydrophobic interaction with Val157 side chain. Side chain polar interactions with Trp164 side chain –NH and Ala165 –NH. –NH polar interaction with Ala165 –CO.
34	Ala	States 1 and 3: No electron density in structures. State 2: No direct interactions.

Appendix Table 4. Polar contacts between PTH Arg25 and PTHR in last 100 ns of triplicate MD simulations.

Residues are side chains unless otherwise indicated.

#1		#2		#3	
Residue	**Occupancy**	**Residue**	**Occupancy**	**Residue**	**Occupancy**
L174 Main	6.79%	L174 Main	1.00%	L174 Main	15.77%
E177	1.80%	T175	1.20%	E177	15.97%
E259	7.39%	N176	0.20%		
E260	1.60%	E177	1.80%		

Appendix Table 5. Alpha hydrogen chemical shifts of PTH.

Chemical shifts (δHα) were obtained from 3D NOESY spectra. Chemical shift indices (CSI) were determined by comparing experimental chemical shifts with random coil values (see Section 2.2.5.2). Chemical shifts and CSIs are plotted in Figure 2.10. Peaks for PTH residues 1 and 2 were not visible in the spectra. Residues 35–44 constitute the glycine linker and Strep-tag at the C-terminus of ^{15}N-PTH.

Residue		pH = 7.2		pH = 5.9		Random
		δHα	CSI	δHα	CSI	coil value
1	**Ser**					
2	**Val**					
3	**Ser**	4.45	0	4.42	0	4.50
4	**Glu**	4.18	-1	4.17	-1	4.29
5	**Ile**	3.97	0	3.97	0	3.95
6	**Gln**	4.24	-1	4.20	-1	4.37
7	**Leu**	4.21	0	4.20	0	4.17
8	**Met**	4.24	-1	4.25	-1	4.52
9	**His**	4.24	-1	4.30	-1	4.63
10	**Asn**	4.52	-1	4.60	-1	4.75
11	**Leu**	4.27	0	4.27	0	4.17
12	**Gly**	3.75	-1	3.79	-1	3.97
13	**Lys**	4.14	-1	4.20	-1	4.36
14	**His**	4.62	0	4.60	0	4.63
15	**Leu**	4.34	1	4.30	1	4.17
16	**Asn**	4.76	0	4.72	0	4.75
17	**Ser**	4.22	-1	4.26	-1	4.50
18	**Met**	4.37	-1	4.36	-1	4.52
19	**Glu**	4.14	-1	4.14	-1	4.29
20	**Arg**	4.16	-1	4.17	-1	4.38
21	**Val**	3.84	-1	3.86	0	3.95
22	**Glu**	4.15	-1	4.17	-1	4.29
23	**Trp**	4.36	-1	4.27	-1	4.70
24	**Leu**	3.83	-1	3.87	-1	4.17
25	**Arg**	3.92	-1	3.87	-1	4.38
26	**Lys**	4.03	-1	4.00	-1	4.36
27	**Lys**	3.96	-1	3.96	-1	4.36
28	**Leu**	3.98	-1	4.00	-1	4.17
29	**Gln**	4.16	-1	4.15	-1	4.37
30	**Asp**	4.60	-1	4.58	-1	4.76
31	**Val**	3.94	0	3.94	0	3.95
32	**His**	4.56	0	4.55	0	4.63
33	**Asn**	4.63	-1	4.58	-1	4.75
34	**Phe**	4.58	0	4.60	0	4.66
35	**Gly**	3.81	-1	3.81	-1	3.97
36	**Gly**	3.82	-1	3.82	-1	3.97
37	**Trp**	4.60	0	4.65	0	4.70
38	**Ser**	4.91	1	4.93	1	4.50
39	**His**	4.32	-1	4.34	-1	4.63
40	**Pro**	4.32	-1	4.34	-1	4.44
41	**Gln**	4.23	-1	4.19	-1	4.37
42	**Phe**	4.67	0	4.66	0	4.66
43	**Glu**	4.23	0	4.24	0	4.29
44	**Lys**					4.36

Appendix Table 6. Interactions between first 14 peptide residues and receptor in MD simulations.

Interactions were determined using the final snapshot of 100 ns LA-PTH–PTHR–G_s simulation. All other systems were analyzed after 200 ns simulation. For each residue, the number of polar (*P*) and nonpolar (*N*) interactions are listed, along with totals for all 14 residues. Polar interactions involved distances < 4.0 Å; nonpolar interactions involved distances < 5.0 Å.

	LA-PTH–PTHR		**LA-PTH–PTHR–G_s**		**PTH–PTHR–G_s**		**PTH–PTHR**					
							Run 1		**Run 2**		**Run 3**	
	P	***N***	***P***	***N***	***P***	***N***	***P***	***N***	***P***	***N***	***P***	***N***
1	4	4	3	2	6	1	1	1	4	0	4	1
2	1	4	1	4	3	2	0	4	0	4	0	3
3	1	3	1	3	2	2	2	1	2	2	3	3
4	4	4	2	5	2	1	3	3	2	4	2	3
5	0	5	0	3	0	3	0	3	0	4	0	5
6	1	2	2	0	1	2	0	1	2	2	1	2
7	0	6	0	6	0	5	0	6	0	3	0	5
8	0	3	0	2	0	2	0	1	0	2	0	4
9	3	1	3	2	3	1	1	1	2	2	2	1
10	1	3	0	3	1	2	1	3	0	1	2	2
11	0	1	3	0	0	2	0	1	0	1	0	3
12	0	2	0	2	0	0	0	0	0	0	0	0
13	2	1	2	3	4	1	0	1	3	2	3	2
14	1	5	1	4	0	4	1	3	0	1	0	4
Total	18	44	18	39	22	28	9	29	15	28	17	38
Total (*P* + *N*)	**62**		**57**		**50**		**38**		**43**		**55**	
									45			

Appendix C Supporting Information for Chapter 3

Appendix C.1 Chapter 3 Supporting Figures

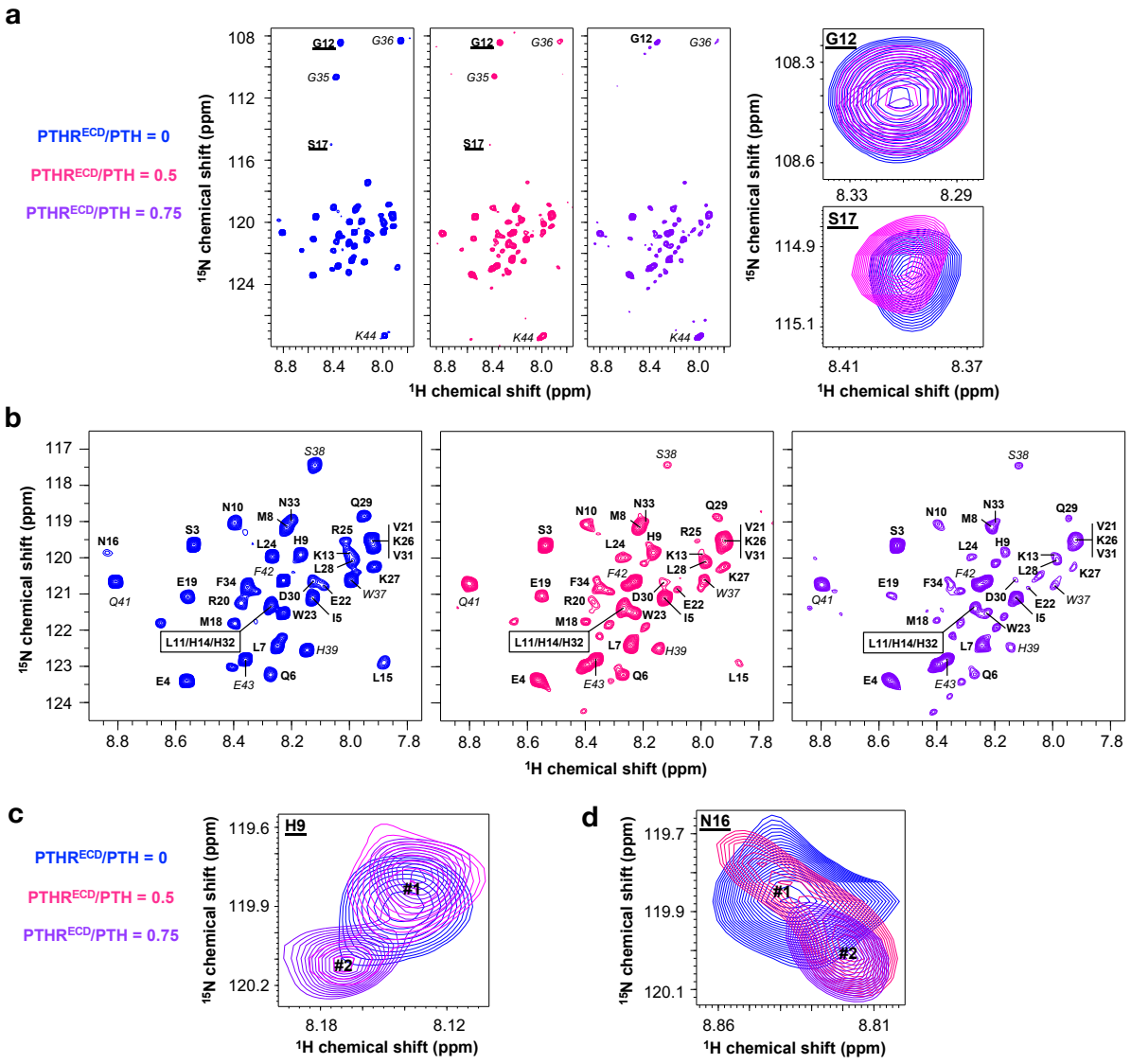

Appendix Figure 12. Two-dimensional ^{1}H-^{15}N transverse relaxation optimized spectroscopy (TROSY) spectra of ^{15}N-PTH.

Spectra were obtained in the absence (blue) or presence of $PTHR^{ECD}$, 0.5 (pink) or 0.75 (purple) molar ratio. **a,** On the *left panel*, full spectra showing all peaks of PTH. On the *right panel*, spectra of Gly12 and Ser17. Ser17 peak was too weak to be seen at 0.75 molar ratio. **b,** Zoomed-in spectra showing most peaks of PTH. PTH peaks are labeled with bold text, and peaks corresponding to attached Strep-tag are labeled with italicized text. **c,** Zoomed-in spectral region of PTH His9. The conformation of His9 in free PTH is marked by Peak #1. Peak #2 represents the new conformation of His9 that occurred in the presence of 0.5 molar ratio $PTHR^{ECD}$ and becomes stronger at 0.75 molar ratio $PTHR^{ECD}$. **d,** Zoomed-in spectral region of PTH Asn16, showing PTH conformational changes in the presence of $PTHR^{ECD}$. Peak #1 represents the conformation of Asn16 in the free PTH. Peak #2 represents the new conformation of Asn16 when PTH is bound to $PTHR^{ECD}$.

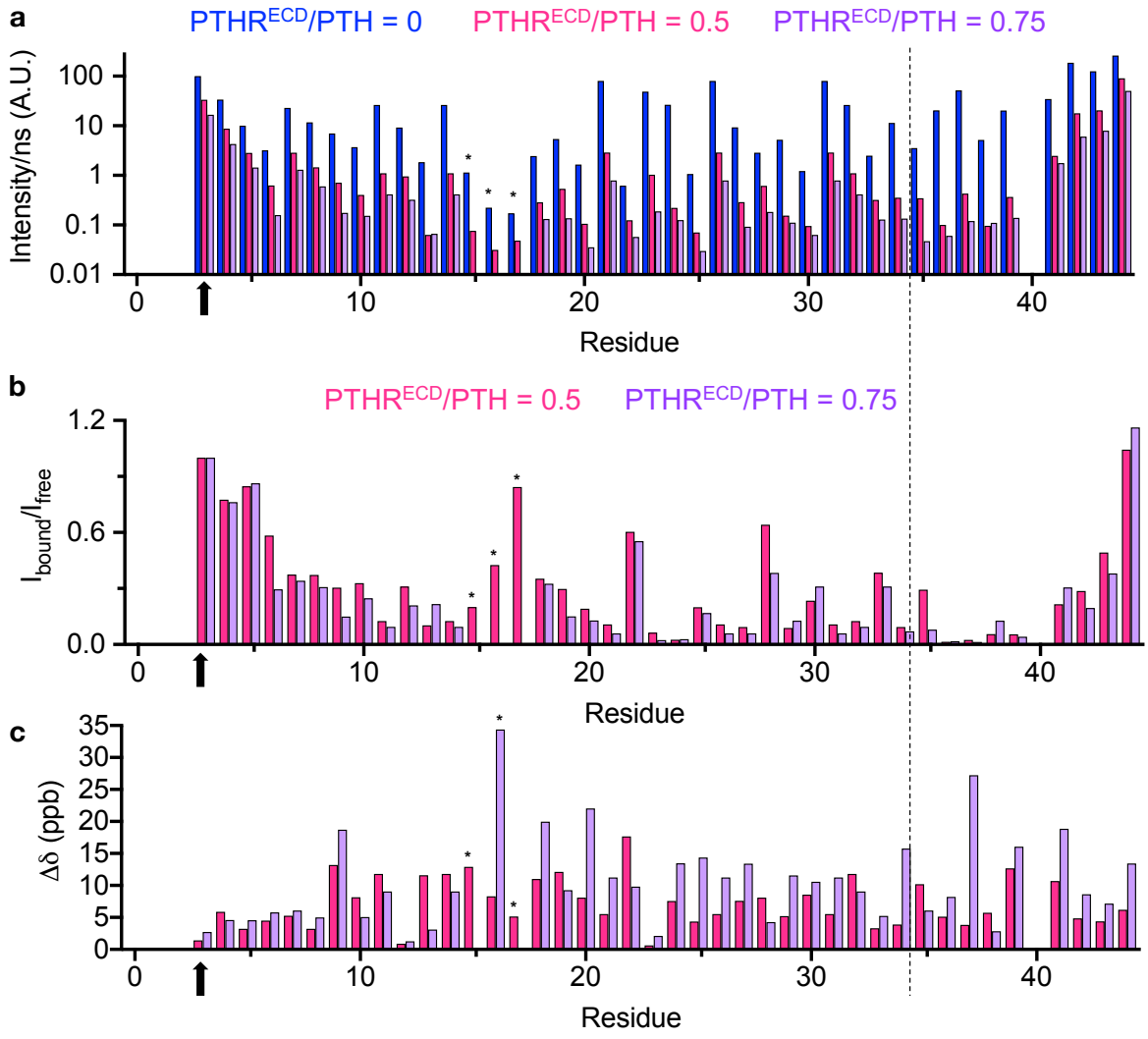

Appendix Figure 13. TROSY peak intensity (height), peak intensity ratio (I_{bound}/I_{free}), and chemical shift perturbation (Δδ).

a, Peak intensities (normalized with respect to the number of scans in TROSY experiments) varied along the PTH sequence, and the variations increased upon binding to 0.5 and 0.75 molar ratios of $PTHR^{ECD}$ due to reduced PTH flexibility. **b,** Peak intensity ratio (I_{bound}/I_{free}) and **c,** chemical shift perturbation (Δδ) of individual residues upon binding to 0.5 or 0.75 molar ratios of $PTHR^{ECD}$. Residue intensities from the same experiment were normalized with respect to the intensity of Ser3 (indicated by an arrow) prior to calculations in **b**. Residues 15–17, indicated by asterisks, do not have visible peaks in the presence of 0.75 molar ratio $PTHR^{ECD}$. The new peak at Asn16 in the

presence of 0.75 molar ratio $PTHR^{ECD}$ was not used for I_{bound}/I_{free} analyses but is displayed in the chemical shift perturbation plot. PTH is separated from residues in the linker and Strep-tag by a thin dashed line.

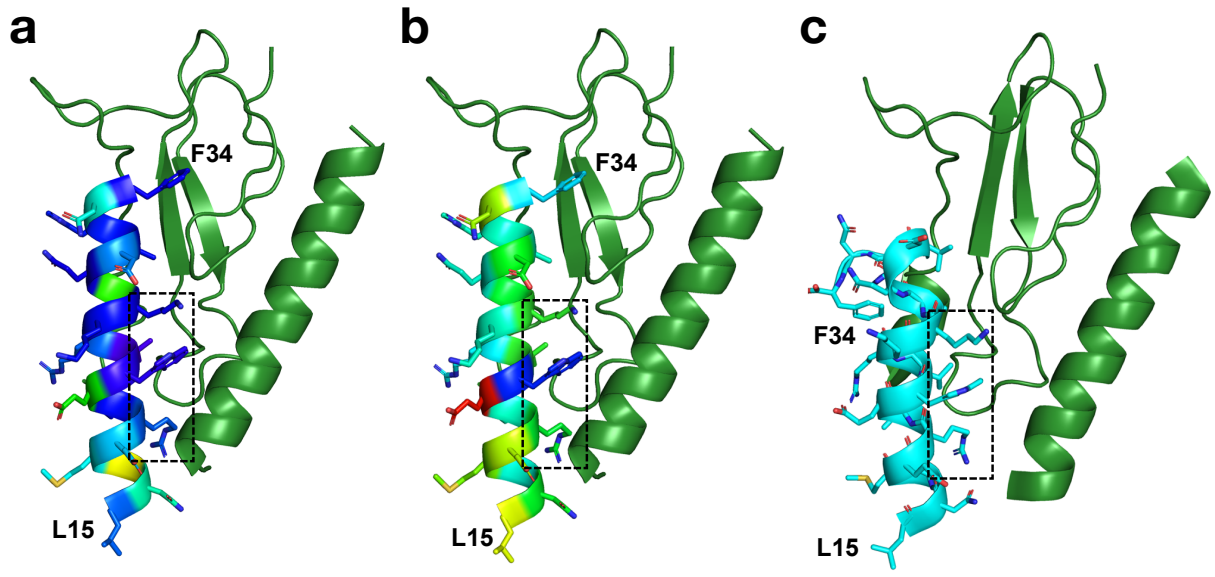

Appendix Figure 14. Comparison of PTH(15–34) interactions with $PTHR^{ECD}$ in PTH(15–34)–$PTHR^{ECD}$ crystal structure and PTH^{WT}–PTHR MD simulation.

a, PTH(15–34)–$PTHR^{ECD}$ crystal structure (PDB 3C4M)[42], with PTH colored according to I_{bound}/I_{free} values. **b,** PTH(15–34)–$PTHR^{ECD}$ crystal structure, with PTH colored according to chemical shift perturbation. **c,** MD snapshot of PTH^{WT}–PTHR at 200 ns, showing similar interactions between PTH and $PTHR^{ECD}$ as seen in the crystal structure. PTH residues Arg20, Trp23, Leu24, and Lys27, which are positioned near or within the $PTHR^{ECD}$ binding interface, are indicated by a dashed box.

Appendix C.2 Chapter 3 Supporting Tables

Appendix Table 7. TROSY chemical shifts of ^{15}N-PTH residues.

Residues 35–44 refer to the C-terminal Strep-tag plus glycine linker (GGWSHPQFEK).

		Chemical Shift (ppm)					
		Free PTH		PTHR^{ECD}/PTH = 0.5		PTHR^{ECD}/PTH = 0.75	
Residue		HN	N	HN	N	HN	N
Ser	1	--	--	--	--	--	--
Val	2	--	--	--	--	--	--
Ser	3	8.538	119.641	8.537	119.648	8.537	119.654
Glu	4	8.562	123.401	8.563	123.372	8.561	123.379
Ile	5	8.127	121.119	8.124	121.107	8.125	121.097
Gln	6	8.272	123.235	8.268	123.226	8.269	123.211
Leu	7	8.248	122.429	8.244	122.411	8.244	122.405
Met	8	8.217	119.147	8.214	119.137	8.212	119.142
His	9	8.168	119.918	8.165	119.855	8.163	119.828
Asn	10	8.397	119.035	8.397	119.076	8.396	119.059
Leu	11	8.270	121.343	8.268	121.401	8.268	121.388
Gly	12	8.339	108.430	8.339	108.426	8.340	108.435
Lys	13	7.999	119.897	7.999	119.839	7.998	119.882
His	14	8.270	121.343	8.268	121.401	8.268	121.388
Leu	15	7.881	122.897	7.868	122.902	--	--
Asn	16	8.837	119.864	8.838	119.823	8.820	120.014
Ser	17	8.415	114.994	8.419	115.011	--	--
Met	18	8.395	121.820	8.397	121.766	8.400	121.724
Glu	19	8.558	121.081	8.550	121.038	8.556	121.036
Arg	20	8.374	121.255	8.370	121.220	8.352	121.273
Val	21	7.924	119.539	7.920	119.518	7.922	119.483
Glu	22	8.087	120.787	8.081	120.869	8.083	120.832
Trp	23	8.228	121.522	8.228	121.522	8.227	121.513
Leu	24	8.267	119.967	8.271	119.997	8.280	119.970
Arg	25	8.011	119.547	8.013	119.528	8.007	119.478
Lys	26	7.924	119.539	7.920	119.518	7.922	119.483
Lys	27	7.914	120.254	7.921	120.240	7.928	120.255
Leu	28	7.988	120.077	7.983	120.111	7.984	120.076
Gln	29	7.948	118.850	7.944	118.867	7.944	118.904
Asp	30	8.126	120.642	8.129	120.681	8.128	120.591
Val	31	7.924	119.539	7.920	119.518	7.922	119.483
His	32	8.270	121.343	8.268	121.401	8.268	121.388
Asn	33	8.198	118.983	8.196	118.993	8.194	118.997
Phe	34	8.353	120.814	8.349	120.825	8.351	120.736
Gly	35	8.376	110.641	8.383	110.602	8.382	110.653
Gly	36	7.854	108.305	7.849	108.309	7.854	108.346
Trp	37	7.993	120.617	7.989	120.617	7.994	120.753
Ser	38	8.119	117.448	8.116	117.424	8.116	117.444
His	39	8.146	122.554	8.146	122.490	8.145	122.473
Pro	40	--	--	--	--	--	--
Gln	41	8.808	120.660	8.801	120.702	8.798	120.739
Phe	42	8.228	120.628	8.229	120.651	8.233	120.663
Glu	43	8.359	122.814	8.364	122.812	8.366	122.817
Lys	44	7.985	127.304	7.990	127.322	7.996	127.346

Appendix D Supporting Information for Chapter 4

Appendix D.1 Chapter 4 Supporting Figures

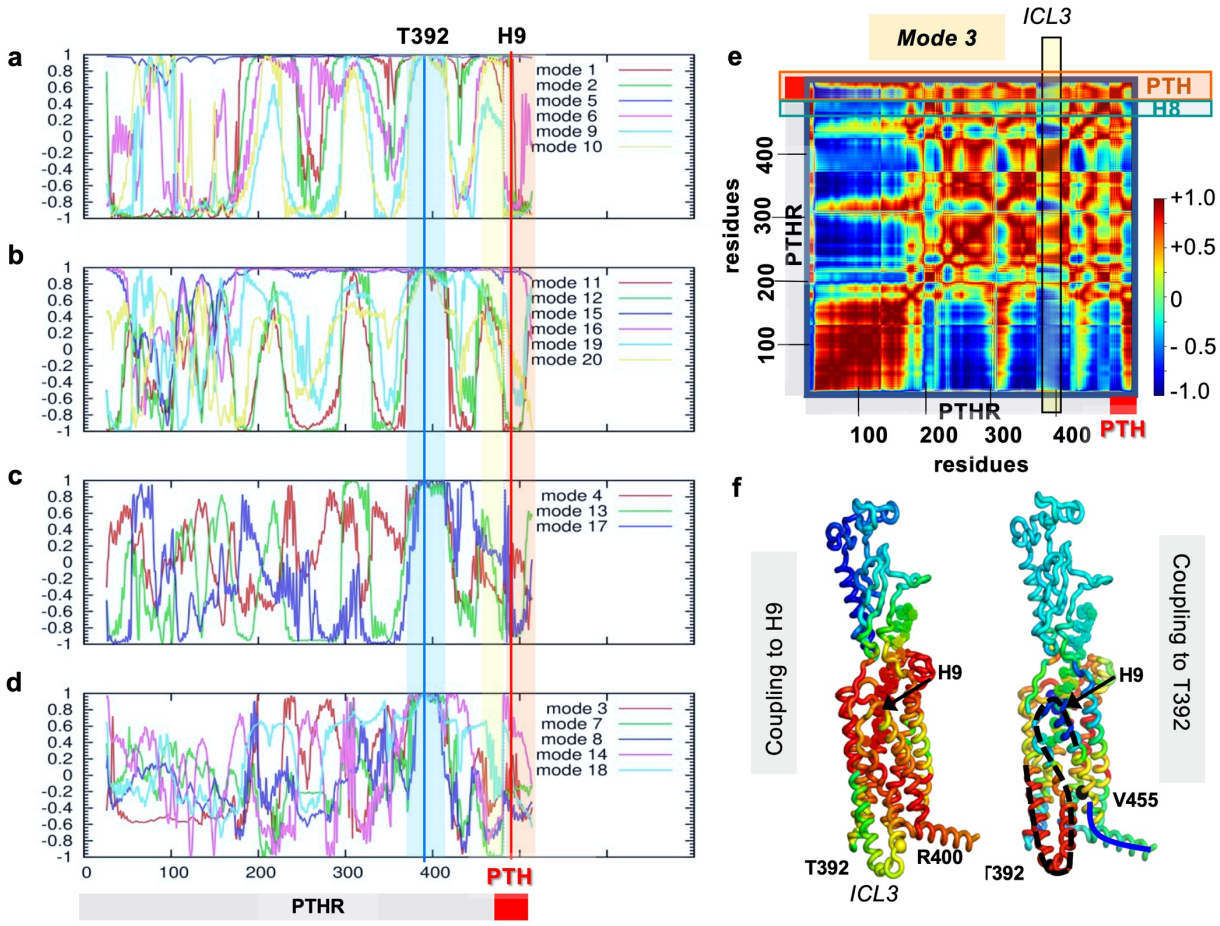

Appendix Figure 15. Cross-correlations between the spatial movements of Thr392 and all other residues in PTH-bound-PTHR.

Results are shown for the slowest 20 modes accessible to the complex in the presence of the lipid bilayer, organized in panels **a–d**. Each curve represents the correlations in a given ANM mode (as labeled). The region near Thr392 (mainly the cytoplasmic ends of TM5 and TM6, and the connecting loop ICL3; residues Asn374–Pro415) is indicated by the blue vertical shade across all panels, the C-tail helix (Ala455–Leu481) is highlighted by the yellow shade, and

the PTHR, by the orange shade. The position of PTH His9 is indicated by the red vertical line and that of Thr392 by the blue line. **a–b**, ANM modes where $PTHR^{TMD}$ is almost rigid and the other structural elements, including $PTHR^{ECD}$ or membrane, undergo global motions with respect to $PTHR^{TMD}$. The modes involve bending (modes 1, 2, 10) or twisting (modes 6, 7, 19) of $PTHR^{ECD}$ with respect to $PTHR^{TMD}$; the rigid-body movements of $PTHR^{TMD}$ with respect to the membrane (mode 5); or mixed (bending+ twisting) of $PTHR^{ECD}$ (modes 11, 12, 15). **c**, ANM modes driving the movements of $PTHR^{TMD}$ but showing no strong correlation between blue and yellow regions. **d**, ANM modes where the internal movements of $PTHR^{TMD}$ are coupled to those of the PTH (moving in the opposite direction). In particular, modes 3, 14, and 18 induce an opening at the cytoplasmic end of the PTHR (anticorrelated movements between the blue and yellow regions), while the TM5/6 cytoplasmic ends and ICL3 move in concert with $PTHR^{ECD}$ and PTH. Panels **e–f** display the cross-correlations in mode 3 and the associated ribbon diagram. *ANM calculations were performed by Ji Young Lee, and the figure was prepared by Ivet Bahar and Ji Young Lee.*

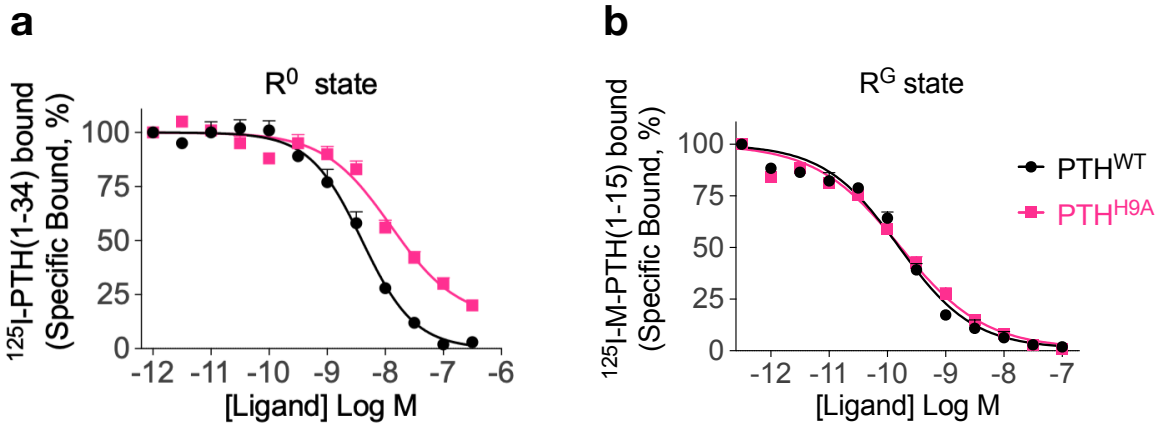

Appendix Figure 16. Binding properties of PTH^{WT} and PTH^{H9A}.

a, Radioligand competition assays of PTH^{WT} and PTH^{H9A} binding to PTHR R^0 (G protein-free) conformation. **b,** Radioligand competition assays of PTH^{WT} and PTH^{H9A} binding to PTHR R^G conformation. For **a** and **b**, data are averaged from $n = 4$ and $n = 5$ independent experiments, respectively. *Data were acquired and analyzed by the Thomas Gardella laboratory (Harvard).*

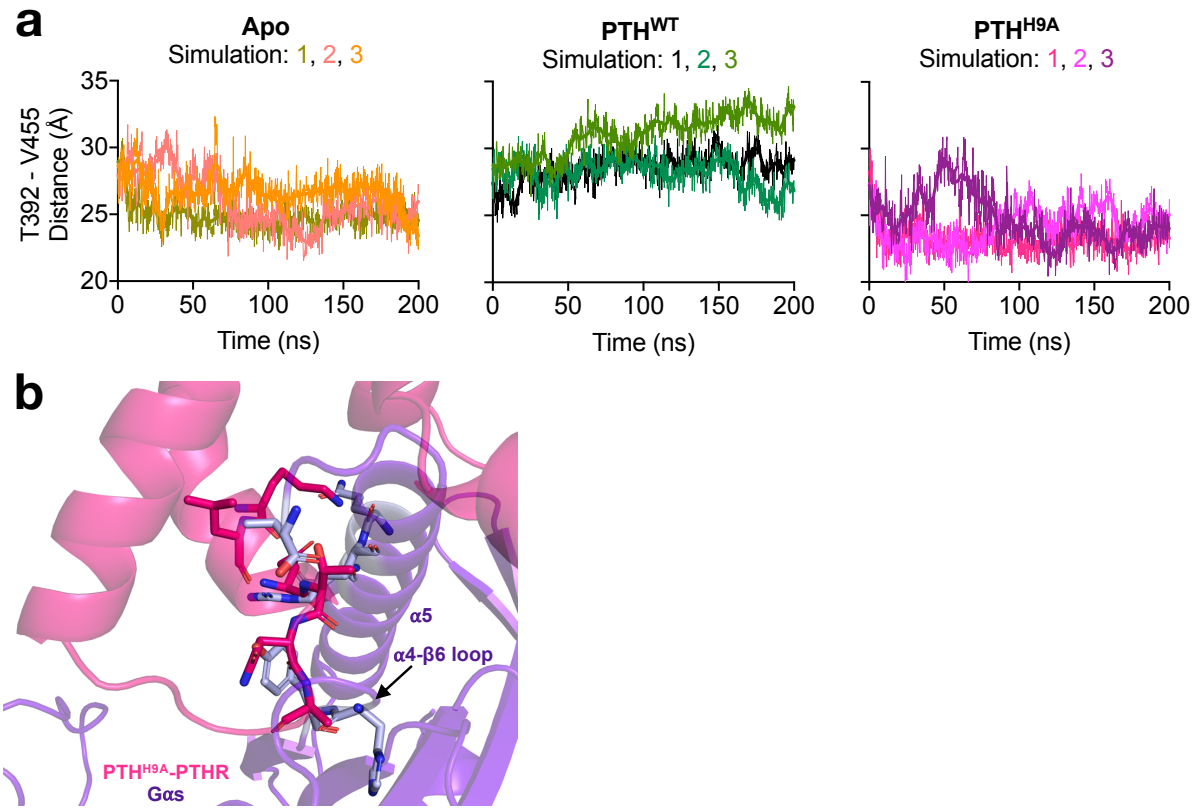

Appendix Figure 17. PTH^{H9A}-stabilized kink 5 and its consequences.

a, Thr392-Val455 distance distributions over triplicate 200 ns simulations of apo, PTH^{WT}-bound, and PTH^{H9A}-bound receptor. Raw data are shown as thin lines. Second-order smoothed data (over 30 neighbors) are shown as thick lines. **b,** Alignment of PTH^{H9A}-bound receptor (hot pink) TMD with the TMD of the PTHR–G_s cryo-EM structure. Gα_s is colored purple. Clashing residues are shown as sticks.

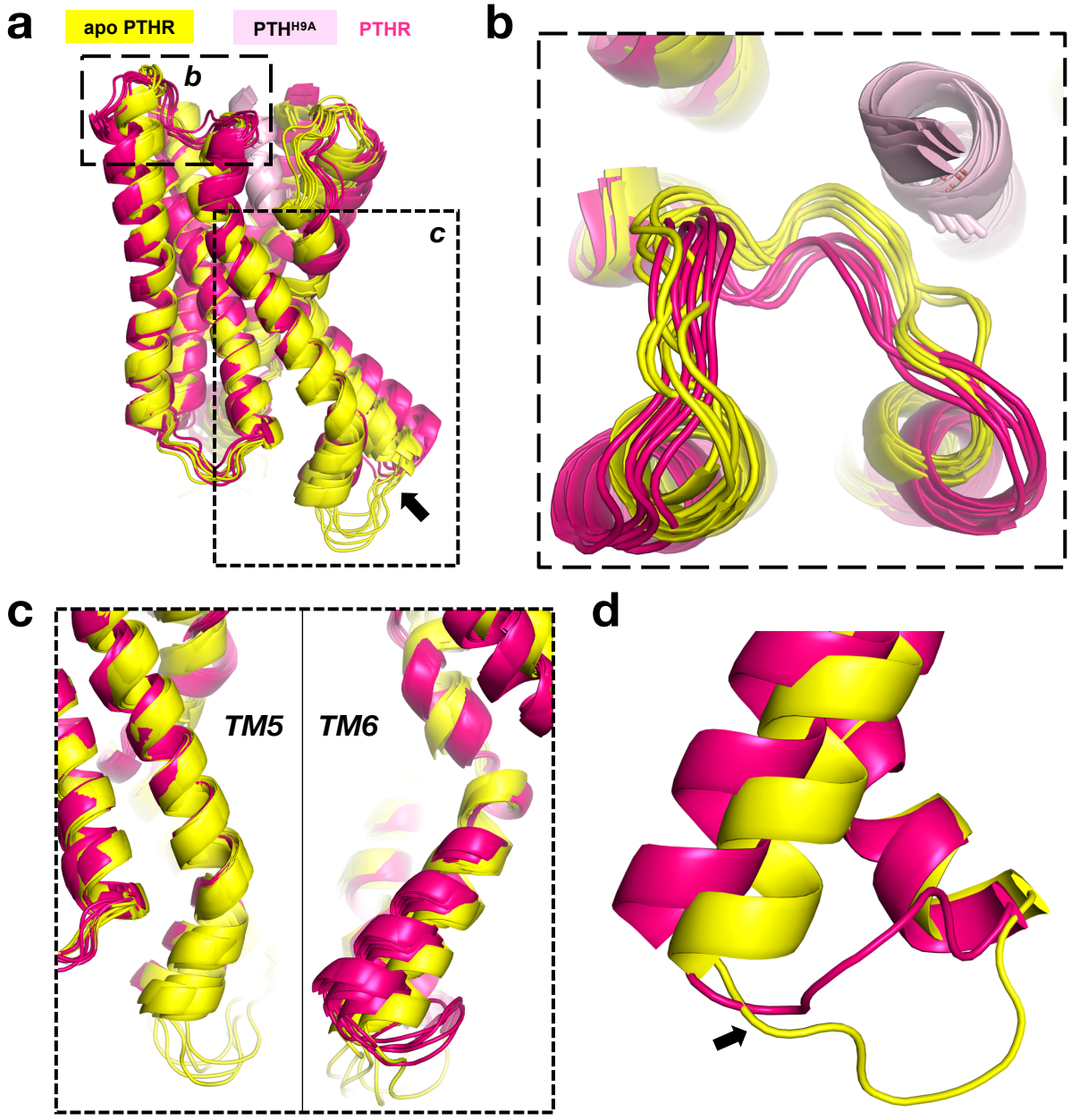

Appendix Figure 18. Conformations of apo and PTH^{H9A}-bound PTHR.

Snapshots of apo PTH^{H9A}-bound receptor collected during the last 50 ns of triplicate simulations (10 ns intervals), aligned by PTHR TM helices. **a,** Aligned receptor structures, with dashed boxes indicating areas shown in **b** and **c**. The arrow points to ICL3. PTHR^{ECD} (residues 27–179), ECL1 (residues 247–275), TM3 residues 276–280, and peptide residues 14–34 are hidden for clarity. **b,** ECL2 conformations. **c,** *Left*, TM5. *Right,* TM6. **d,** ICL3 conformations in apo and PTH^{H9A}-bound receptor snapshots after one 200 ns simulation. The ICL3 is indicated by an arrow.

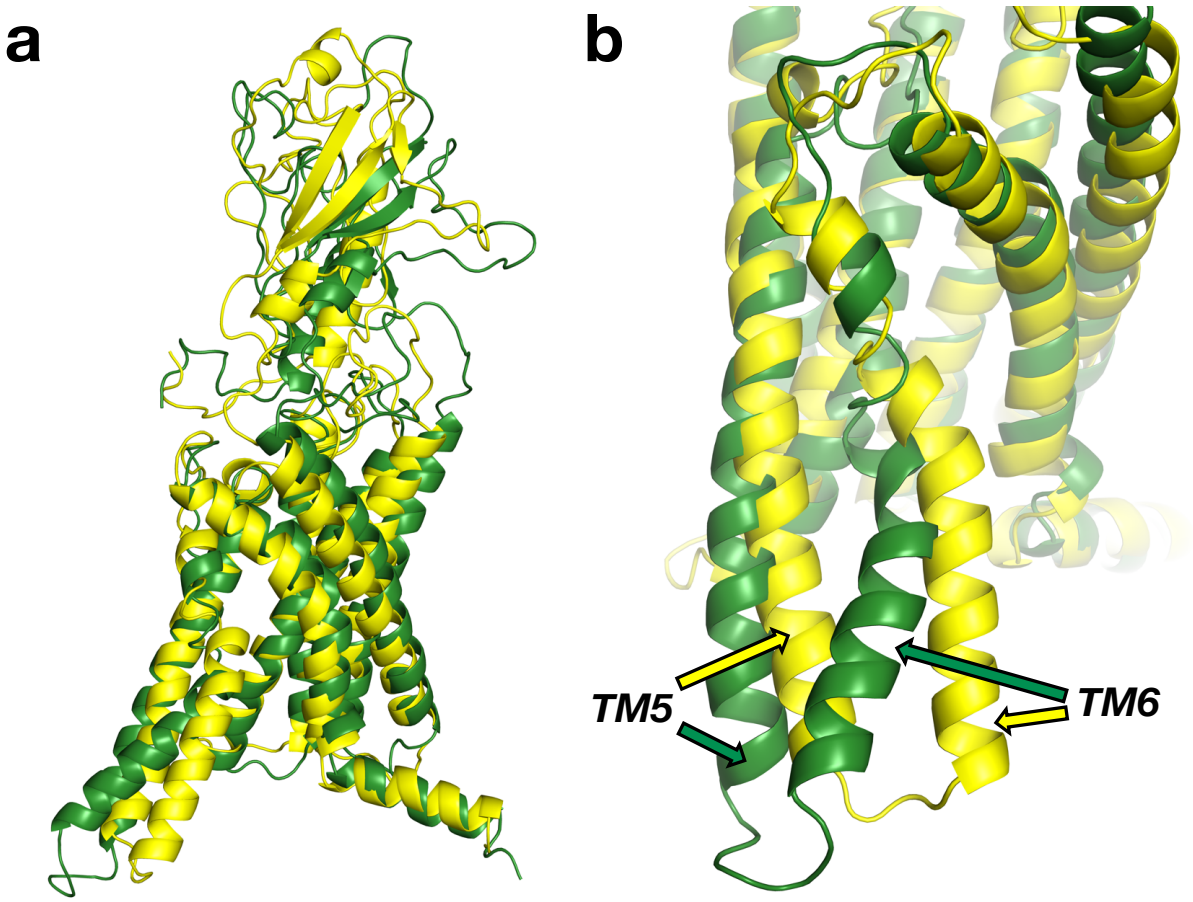

Appendix Figure 19. Accelerated MD (aMD) of apo PTHR.

Two snapshots from 100 ns aMD simulation of apo PTHR were aligned by their TM helices. The snapshot exhibiting the largest TM6 movement is colored dark green. The snapshot with the smallest TM6 displacement is colored yellow. **a,** Full receptor structures. **b,** Zoomed-in structures, with TM5 and TM6 of each receptor indicated by colored arrows.

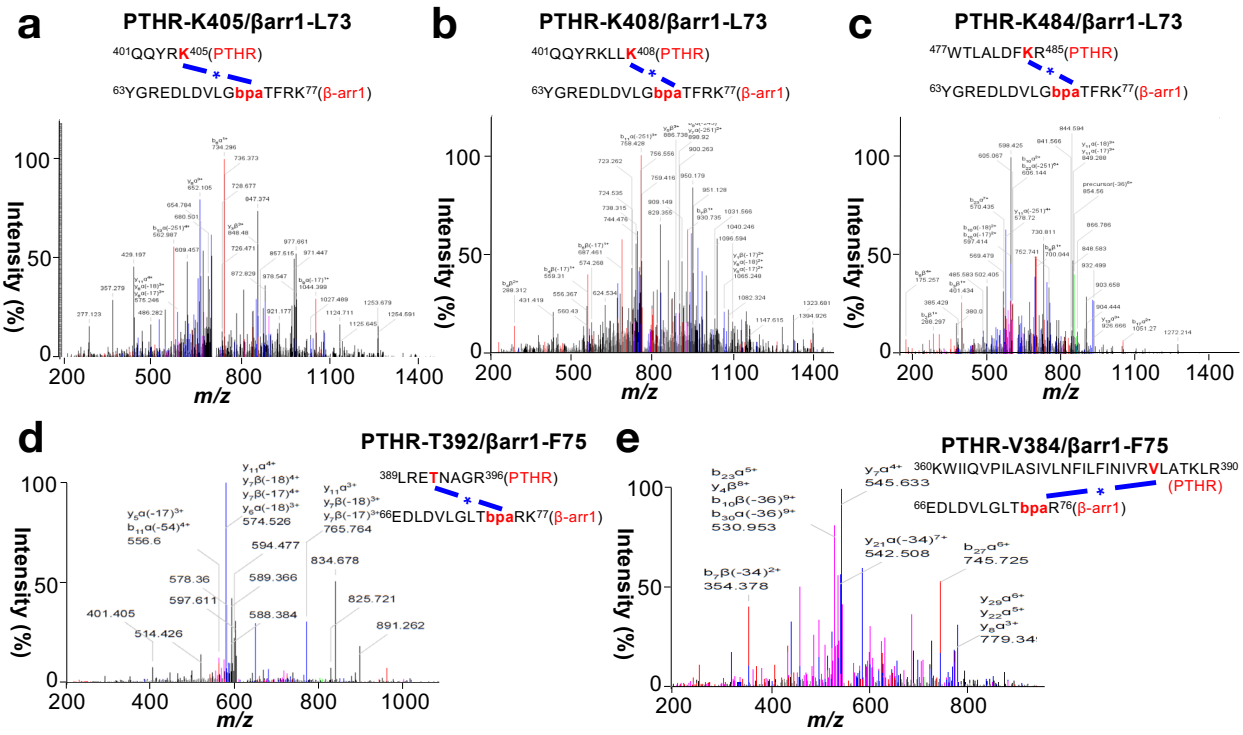

Appendix Figure 20. LC-MS/MS data identifying photo-crosslinking between PTHR and β-arrestin-1 Bpa in PTH-stimulated cells.

a, PTHR Lys405 and β-arrestin-1 Leu73Bpa. **b,** PTHR Lys408 and β-arrestin-1 Leu73Bpa. **c,** PTHR Lys484 and β-arrestin-1 Leu73Bpa. **d,** PTHR Thr392 and β-arrestin-1 Phe75Bpa. **e,** PTHR Val384 and β-arrestin-1 Phe75Bpa. *Photo-crosslinking mass spectrometry data acquisition and analysis were performed by Kunhong Xiao and Fei Fang.*

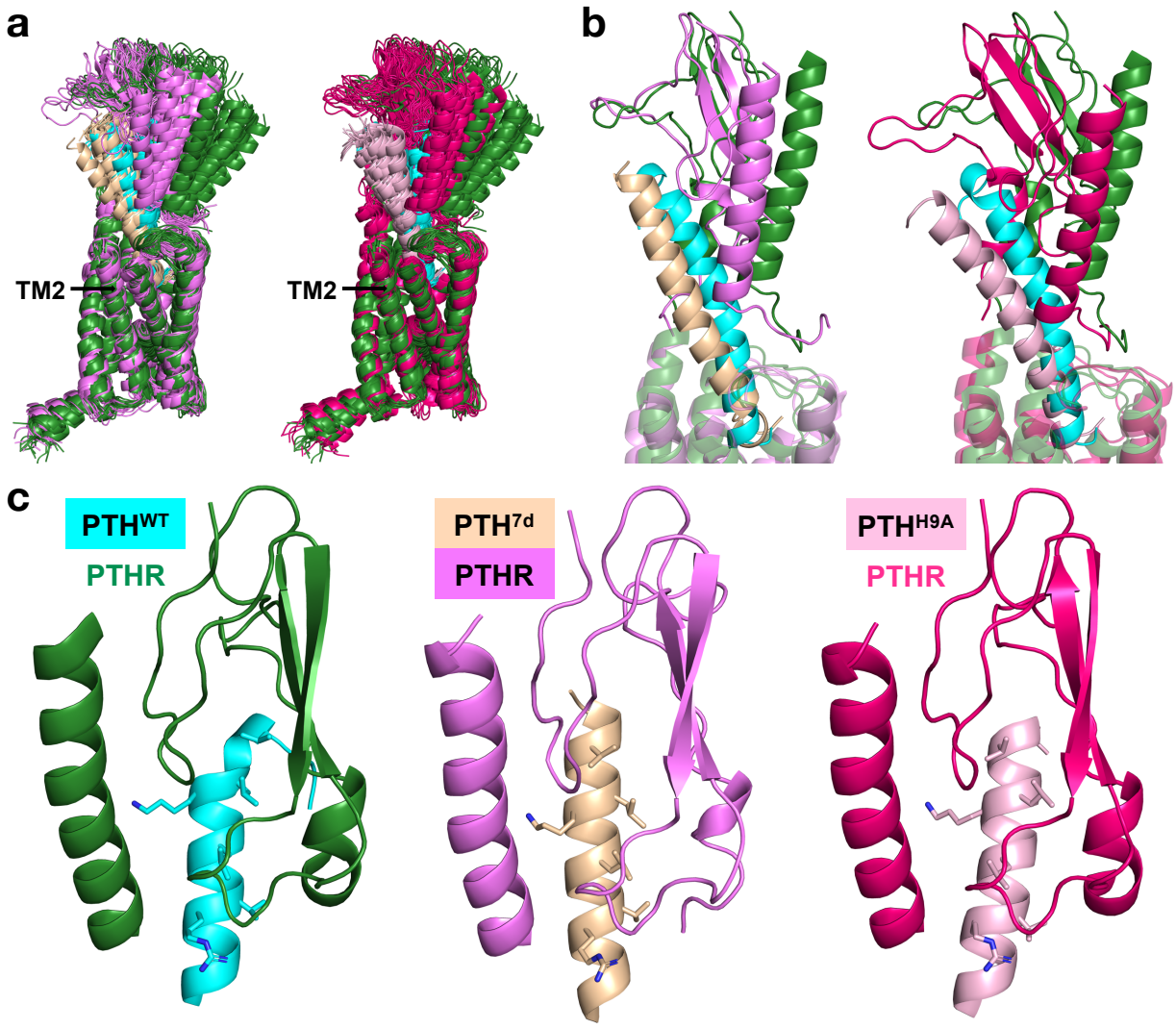

Appendix Figure 21. Position of receptor extracellular domain in the presence of PTH^{WT}, PTH^{7d}, PTH^{H9A}. PTH^{WT}, PTH^{7d}, and PTH^{H9A} are colored cyan, wheat, and light pink, respectively. PTH^{WT}, PTH^{7d}, and PTH^{H9A}-bound receptors are colored dark green, violet, and hot pink, respectively. **a,** MD snapshots acquired every 10 ns during the last 50 ns of simulations were aligned by receptor TM helices. $PTHR^{ECD}$ residues 56–105 and ECL1 (247–278) are hidden for clarity. TM2 is indicated by arrows. **b,** Aligned snapshots after 200 ns, highlighting the altered $PTHR^{ECD}$ positions triggered by each ligand. **c,** Ligand residues participating in the $PTHR^{ECD}$ binding interface.

A

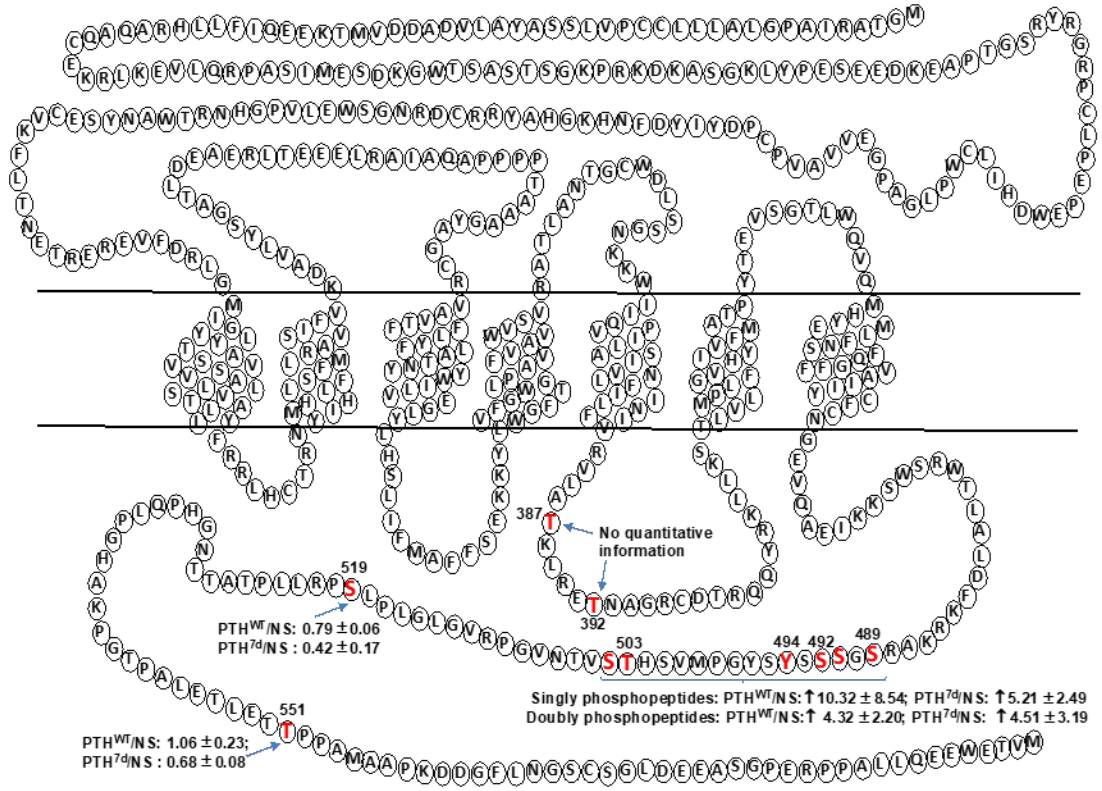

B

Phosphopeptides	PTH	PTH^{7d}
^{540}PGTPALETLET**pT**PPAM*AAPK^{559}	1.06 ± 0.23	0.68 ± 0.08
^{489}**pS**GSSSYSYGPM*VSHTSVTNVGPR^{511}	10.32 ± 8.54	5.21 ± 2.49
^{489}SG**pS**SSYSYGPM*VSHTSVTNVGPR^{511}		
^{489}SGS**pS**SYSYGPM*VSHTSVTNVGPR^{511}		
^{489}SGSSS**pY**SYGPM*VSHTSVTNVGPR^{511}		
^{489}SGSSSYSYGPM*VSH**pT**SVTNVGPR^{511}		
^{489}SGSSSYSYGPM*VSHT**pS**VTNVGPR^{511}		
^{489}SGS**pS**SYSYGPM*VSHT**pS**VTNVGPR^{511}	4.32 ± 2.20	4.51 ± 3.17
^{512}VGLGLPL**pS**PR^{521}	0.79 ± 0.06	0.42 ± 0.17
^{384}VLA**pT**KLRETNAGRCDTRQQYRK^{405}	No quantitative information	
^{384}VLATKLRE**pT**NAGR^{396}		

C

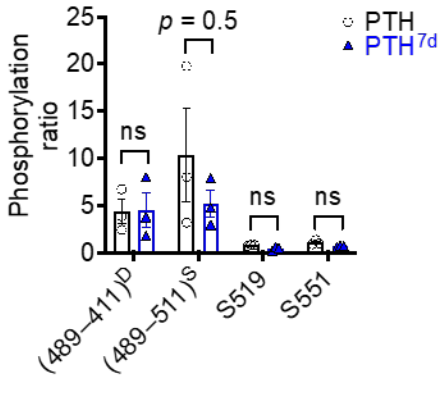

Appendix Figure 22. SILAC-based quantitative phosphorylation analysis of PTHR.

a, Summary of intracellular phosphorylation sites in PTHR and corresponding changes in response to 30 nM PTH^{WT} or PTH^{7d} stimulation. Phosphorylation sites were determined by LC-MS/MS and indicated in red in the snake view map of PTHR. The fold changes corresponding to the extents of phosphorylation were determined by SILAC-based quantitative LC-MS/MS analysis. **b, c,** List of phosphopeptide sequences identified (**b**) and fold changes (**b, c**)

determined by SILAC-based quantitative LC-MS/MS analysis. Since isomeric singly phosphorylated peptides (^{489}SGSSSYSYGPM*VSHTSVTNVGPR^{511}) with phosphorylation at distinct positions co-eluted from LC column during chromatographic separation, the quantitative analysis reflects a summary of a mixture of these co-eluted singly phosphorylated peptides. Mean ± s.d. of $N = 3$ separated experiments; NS (non-significant) by two-way ANOVA. *Data were acquired and figure was prepared by Fei Fang and Kunhong Xiao.*

TM5	CTR	CALCRL	CRF_1R	CRF_2R	GHRHR	GIPR	GLP-1R	GLP-2R	GCGR	SCTR	PTH1R	PTH2R	PAC_1R	$VPAC_1R$	$VPAC_2R$
5.58	V320	V313	V291	V287	I304	L318	I328	L362	V326	L317	V382	V337	I328	I316	I303
5.59	R321	R314	R292	R288	R305	G319	C329	K363	Q327	R318	R383	R338	V329	R317	R304
5.60	V322	V315	I293	I289	I306	I320	I330	L364	L328	I319	V384	V339	I330	I318	I305
5.61	L323	L316	L294	L290	L307	L321	V331	L365	L329	L320	L385	L340	L331	L319	L306
5.62	V324	I317	M295	M291	V308	L322	V332	I366	V330	M321	A386	A341	V332	L320	L307
5.63	T325	T318	T296	T292	R309	S323	S333	S367	A331	R322	T387	T342	Q333	Q321	Q308
5.64	K326	K319	K297	K293	K310	K324	K334	K368	K332	K323	K388	K343	K334	K322	K309
5.65	M327	L320	L298	L294	L311	L325	L335	L369	L333	L324	L389	I344	L335	L323	L310

Residue Property: Nonpolar Polar Basic Glycine Cysteine

Appendix Figure 23. Chemical properties of PTHR kink 5 are highly conserved amongst class B GPCRs.

Sequence alignment of class B GPCR residues 5.58–5.65 (Wooten numbering) from GPCRdb[7]. Residues are colored by their chemical properties.

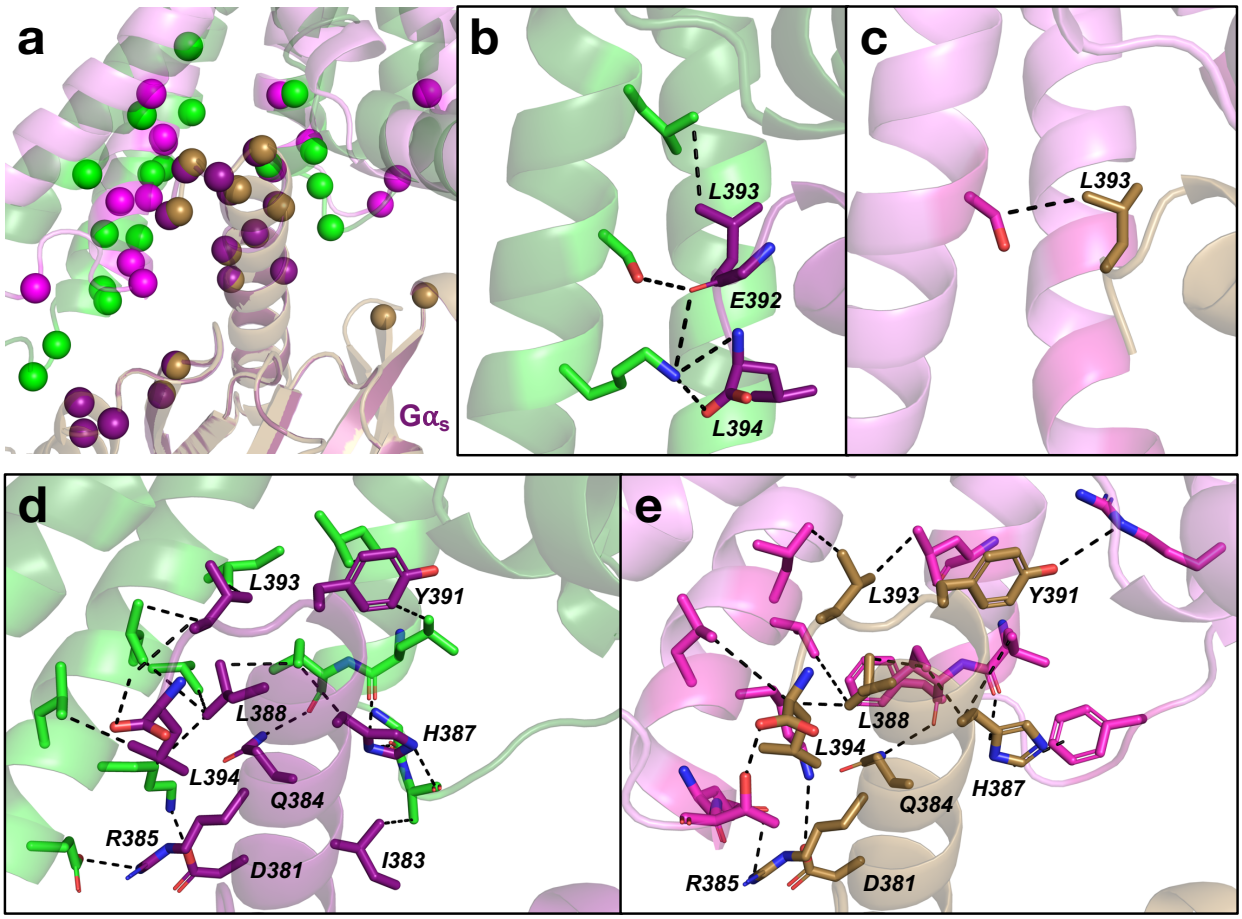

Appendix Figure 24. PTHR–G_s models.

PTH^{WT}-stabilized receptor is green, and PTH^{7d}-stabilized receptor is pink. $G\alpha_s$ residues interacting with PTH^{WT}–PTHR and PTH^{7d}–PTHR are purple and tan, respectively. **a,** All interacting residues, with Cα atoms as spheres. **b–e,** Interacting residues shown as sticks. **b,** PTH^{WT}–PTHR TM6. **c,** PTH^{7d}–PTHR TM6. **d,** All additional interactions between $G\alpha_s$ α5 and PTH^{WT}–PTHR. **e,** All additional interactions between $G\alpha_s$ α5 and PTH^{7d}–PTHR.

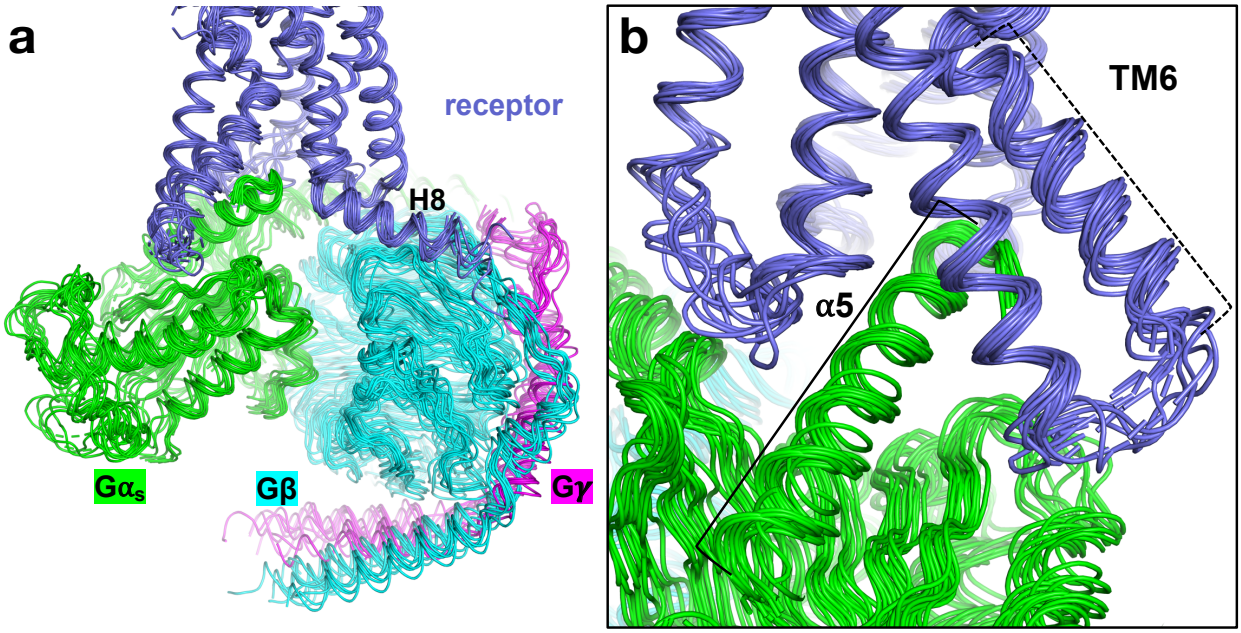

Appendix Figure 25. Flexibility of class B GPCR TM6 and G_s.

Cryo-EM structures of class B GPCRs in complex with G_s, aligned structurally by their TM helices in PyMOL. **a,** Alignment showing flexible positioning of G_s within the receptor core, along with GPCR TM6 and H8. **b,** Zoomed-in image highlighting flexible $G\alpha_s$ α5 helix and GPCR TM6. Receptors shown: CTR (PDB 6NIY[59]), AM1R (PDB 6UUN[225]), AM2R (PDB 6UUS, 6UVA[225]), CGRPR (PDB 6E3Y[60]), CRF1R (PDB 6P9X[229]), CRFR2R (PDB 6PB1[226]), GCGR (PDB 6LMK[227]), GLP1R (PDB 6B3J[61], 5VAI[62]), PTHR (PDB 6NBF[63]), PACR (PDB 6LPB[228], 6P9Y[229]).

	CTR	CALCRL	CRF_1R	CRF_2R	GHRHR	GIPR	GLP-1R	GLP-2R	GCGR	SCTR	PTH1R	PTH2R	PAC_1R	$VPAC_1R$	$VPAC_2R$
6.35	Y338	Y331	Y309	Y305	Y324	R336	K346	K380	K344	Y337	Y403	Y358	Y348	Y336	Y323
6.36	L339	M332	R310	R306	W325	L337	C347	Y381	F345	K338	R404	R359	L349	S337	K324
6.37	K340	K333	K311	K307	R326	R338	R348	R382	R346	R339	K405	K360	R350	R338	R325
6.38	A341	A334	A312	A308	L327	L339	L349	L383	L347	L340	L406	L361	L351	L339	L326
6.39	V342	V335	V313	V309	S328	A340	A350	A384	A348	A341	L407	A362	A352	A340	A327
6.40	K343	R336	K314	K310	K329	R341	K351	K385	K349	R342	K408	K363	R353	R341	K328
6.41	A344	A337	A315	A311	S330	S342	S352	S386	S350	S343	S409	S364	S354	S342	S329
6.42	T345	T338	T316	T312	T331	T343	T353	T387	T351	T344	T410	T365	T355	T343	T330
6.43	M346	L339	L317	L313	L332	L344	L354	L388	L352	L345	L411	L366	L356	L344	L331
6.44	I347	I340	V318	V314	F333	T345	T355	V389	T353	L346	V412	V367	L357	L345	L332
6.45	L348	L341	L319	L315	L334	L346	L356	L390	L354	L347	L413	L368	L358	L346	L333
6.46	V349	V342	L320	L316	I335	V347	I357	I391	I355	I348	M414	V369	I359	I347	I334
6.47	P350	P343	P321	P317	P336	P348	P358	P392	P356	P349	P415	L370	P360	P348	P335
6.48	L351	L344	L322	L318	L337	L349	L359	L393	L357	L350	L416	V371	L361	L349	L336
6.49	L352	L345	L323	L319	F338	L350	L360	L394	L358	F351	F417	F372	F362	F350	F337
6.50	G353	G346	G324	G320	G339	G351	G361	G395	G359	G352	G418	G373	G363	G351	G338
6.51	I354	I347	I325	I321	I340	V352	T362	V396	V360	I353	V419	V374	I364	V352	V339
6.52	Q355	E348	T326	T322	H341	H353	H363	H397	H361	H354	H420	H375	H365	H353	H340
6.53	F356	F349	Y327	Y323	Y342	E354	E364	E398	E362	Y355	Y421	Y376	Y366	Y354	Y341
6.54	V357	V350	M328	M324	I343	V355	V365	I399	V363	I356	I422	I377	T367	I355	M342
6.55	V358	L351	L329	L325	I344	V356	I366	L400	V364	V357	V423	V378	V368	M356	V343
6.56	F359	I352	F330	F326	F345	F357	F367	F401	F365	F358	F424	F379	F369	F357	F344
6.57	P360	P353	F331	F327	N346	A358	A368	S402	A366	A359	M425	V380	A370	A358	A345
6.58	W361	W354	V332	V328	F347	P359	F369	F403	F367	F360	A426	C381	F371	F359	V346

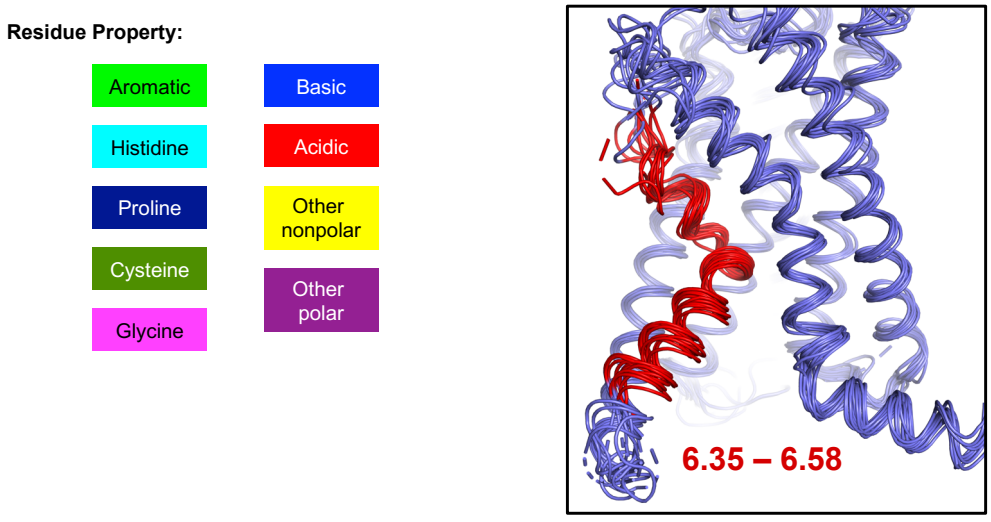

Appendix Figure 26. Chemical properties of TM6 are highly conserved amongst class B GPCRs.

Sequence alignment of class B GPCR residues 6.35–6.58 (Wooten numbering) from GPCRdb[7]. Residues are colored by their chemical properties. Insert displays active class B GPCR structures (same as Appendix Figure 25), with the conserved TM6 region highlighted in red.

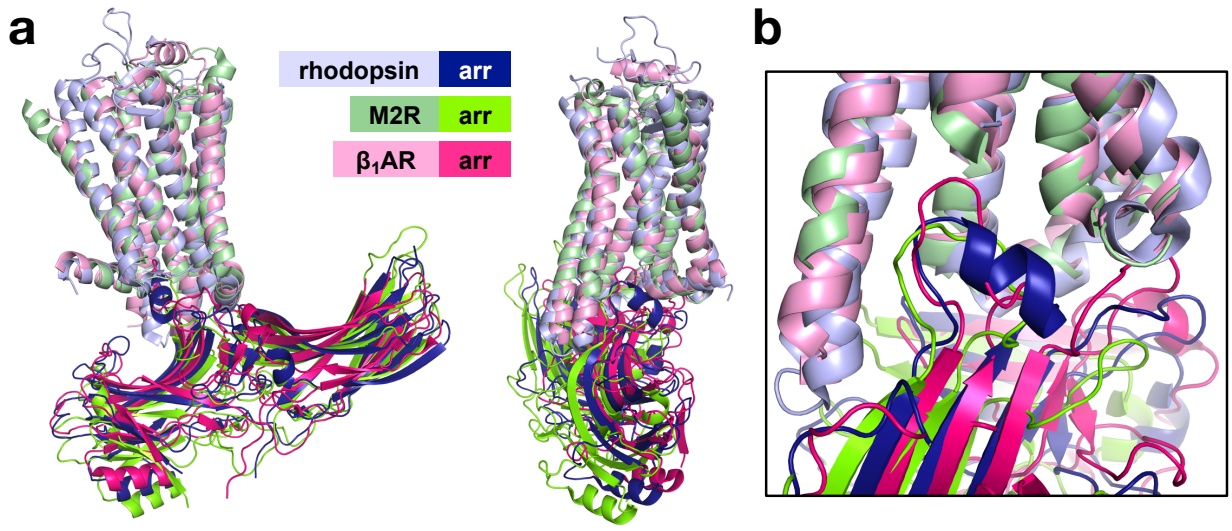

Appendix Figure 27. Comparison of GPCR–arrestin structures.

Structures of rhodopsin–visual arrestin and M2R–β-arrestin-1 (PDB 5W0P[77], 6U1N[187]), used for PTHR–arrestin models 1 and 2, respectively, were compared with recently published structure of β_1AR–β-arrestin-1 complex (PDB 6TKO)[230]. Structures were aligned by receptor TMDs.

Appendix D.2 Chapter 4 Supporting Tables

Appendix Table 8. Binding to the R^0 and R^G states of the PTHR.

Reported are ligand concentrations that inhibited binding of radioligand by 50% (IC_{50}). Data are the mean value ± s.e.m. of $n = 4$ (R^0 state), and $n = 5$ (R^G state), each in duplicate. *P* values are pairwise comparison (Student's t-test) to PTH^{WT}. *Data were acquired and analyzed by the Thomas Gardella laboratory (Harvard).*

	R^0 State ($n = 4$)		R^G State ($n = 5$)	
	IC_{50}, nM	*P*	IC_{50}, nM	*P*
PTH^{WT}	3.84 ± 0.91	1.00	0.16 ± 0.02	1.00
PTH^{H9A}	13.70 ± 2.24	0.02	0.19 ± 0.06	0.60

Appendix Table 9. Hydrogen bonds involving ligand residue Glu4 in PTH^{WT}–PTHR and PTH^{7d}–PTHR triplicate 200 ns MD simulations.

Donor and acceptor groups are side chains unless otherwise indicated.

PTH^{WT}

#1			#2			#3		
Donor	**Acceptor**	**Occupancy**	**Donor**	**Acceptor**	**Occupancy**	**Donor**	**Acceptor**	**Occupancy**
R233	E4	60.94%	R233	E4	102.40%	R233	E4	94.01%
Y195	E4	58.04%	Y195	E4	69.13%	Y195	E4	79.62%
Y296	E4	0.50%	Y191	E4	6.39%			
			N448	E4	5.00%			
			Y296	E4	0.30%			
			S449	E4	0.20%			

PTH^{7d}

#1			#2			#3		
Donor	**Acceptor**	**Occupancy**	**Donor**	**Acceptor**	**Occupancy**	**Donor**	**Acceptor**	**Occupancy**
Y421	E4	91.71%	Y296	E4	64.94%	R233	E4	104.60%
R233	E4	83.32%	R233	E4	63.44%	Y421	E4	98.10%
Y296	E4	73.83%	N448	E4	61.64%	Y296	E4	67.03%
E4 Main	E444	6.59%	E4 Main	E444	42.46%	N448	E4	25.07%
N448	E4	5.99%	Y195	E4	14.39%	Y195	E4	11.49%
Y195	E4	2.00%				Y191	E4	5.09%
S449	E4	0.10%				E4 Main	E444	0.10%
						Q451	E4	0.10%

Appendix D.3 PTHR–β-arrestin-1 models: C-terminal tail

All starting PTHR structures for MD simulations terminated after H8 residue 481, reflecting the lack of strong electron density for the receptor C-terminal tail in the PTHR/G_s cryo-EM structures[24]. During triplicate 200 ns MD simulations, a portion of H8 experienced unraveling into a more flexible strand. In some cases, this strand moved PTHR Leu481$^{8.65}$ away from the receptor core. For PTHR–β-arrestin-1 Models 1, 2, and 3, the distances between β-arrestin-1 Leu73 and PTHR Leu481$^{8.65}$ were 38.6, 40.7, and 29.3 Å, respectively (Appendix Table 10). Given the approximate maximum length of 3.5 Å per residue (i.e., 10.5 Å maximum distance between PTHR Leu481$^{8.65}$ and Lys484$^{8.68}$) and the flexibility of the unraveled C-terminus in the MD

models, Lys484$^{8.68}$ could be 10–30 Å away from Leu73, satisfying the Bpa photo-crosslinking distance restraints.

In the GPCR–arrestin structures used to generate the PTHR–β-arrestin-1 models, β-arrestin-1 Lys11 interacts with the most N-terminal phosphorylated residue in the receptor C-tail, and the Cα-Cα distances between Lys11 and Leu73 are 30.7–33.8 Å[219-221] (Appendix Table 10, Appendix Figure 28). Our group has performed phosphorylation analysis of PTHR via mass spectrometry (unpublished), revealing a patch of phosphorylated serines at residues 489 and 491–493. The maximal distance between Lys484 and Ser489 is 17.5 Å. Assuming that PTHR residue 489 is in close proximity to β-arrestin-1 Lys11, the distances between Lys484 and Ser489 are compatible with Lys484 photo-crosslinking with β-arrestin-1 Leu73Bpa and Ser489 interacting with β-arrestin-1 Lys11 (Appendix Table 10).

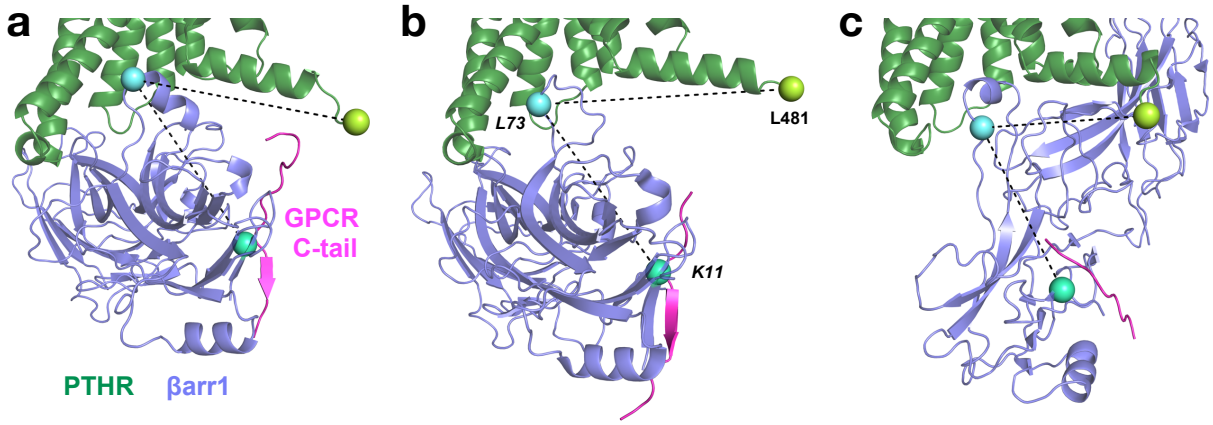

Appendix Figure 28. Restraints of the PTHR C-terminal tail on the PTHR–β-arrestin-1 models.

PTHR and β-arrestin-1 are dark green and slate blue, respectively. The C-terminal tails from each published structure are magenta. PTHR Leu481 is a limon sphere. β-arrestin-1 Lys11 and Leu73 are green cyan and aquamarine spheres, respectively. Distances between these residues are listed in Appendix Table 10. **a,** Model 1. **b,** Model 2. **c,** Model 3.

Appendix Table 10. Distances in PTHR–β-arrestin-1 models.

The asterisk (*) measurement is the theoretical minimum distance between PTHR Lys484 and β-arrestin-1 Leu73, calculated by subtracting 17.5 Å from the distance between β-arrestin-1 Leu73 and Lys11.

	Distance (Å)		
	Model 1	**Model 2**	**Model 3**
PTHR Leu481 – β-arrestin-1 Leu73	38.6	40.7	29.3
β-arrestin-1 Leu73 – β-arrestin-1 Lys11	32.7	33.8	30.7
***PTHR Lys484 – β-arrestin-1 Leu73**	15.2	16.3	13.2

Appendix E Mechanism of PTHR constitutive activation by Jansen's metaphyseal chondrodysplasia mutant H223R

The parathyroid hormone (PTH), the key regulator of blood calcium homeostasis and bone remodeling, acts via the PTH receptor (PTHR)[92]. PTHR is a G protein-coupled receptor (GPCR), which contains seven transmembrane (TM) helices. As with all GPCRs, PTHR activation is characterized by outward kinking of the cytosolic portion of TM6, which permits engagement with G proteins and arrestins[24]. For wild-type receptors, agonist (e.g., PTH) binding is necessary for receptor activation. Single mutations in PTHR that lead to constitutively active receptors (H223R, T410P, T410R, and I458R) cause Jansen's metaphyseal chondrodysplasia (JMC), a rare disorder characterized by short-limbed short stature and hypercalcemia[99]. Here, we present molecular dynamics (MD) data that give insight into the molecular basis of the most common JMC mutation: H223R.

We performed 100 ns MD simulation of apo wild-type PTHR, H223R PTHR, and PTH-bound PTHR. Simulation inputs were generated using CHARMM-GUI Membrane Builder[160]; simulations were run in NAMD using the CHARMM36m force field[166,167]. PTH residues in the N-terminal part of the peptide, especially Glu4, coordinate an extensive polar network that stabilizes outward TM6 kink (Appendix Figure 29a, d; also discussed in Section 2.1.3.2). The polar network is less extensive in apo wild-type PTHR and H223R PTHR simulations (Appendix Figure 29b–c). In wild-type PTHR simulations, Tyr459 on TM7 forms aromatic-aromatic interactions with His223 (TM2) and polar interactions with Glu302 (TM3) (Appendix Figure 30a, b). The larger arginine side chain of H223R PTHR pushes Tyr459 toward TM6, where its side chain forms polar interactions with Val412 and Leu416 main chains, thus stabilizing the outward TM6 kink

and rendering the receptor constitutively active (Appendix Figure 30c). In the inactive state of PTHR, the inward TM6 conformation renders Val412 and Leu416 away from the receptor core[55]. Instead, Tyr459 interacts with Thr410 on TM6 as well as with Glu302 and His223 (Appendix Figure 30d). The polar core of the inactive receptor conformation was previously discovered in the GCGR, and the core residues are conserved amongst class B GPCRs[234]. The tight interaction network as seen in the inactive state would not be possible in the H223R receptor given the large arginine side chain. Our results provide a foundation for drug development targeting JMC mutants.

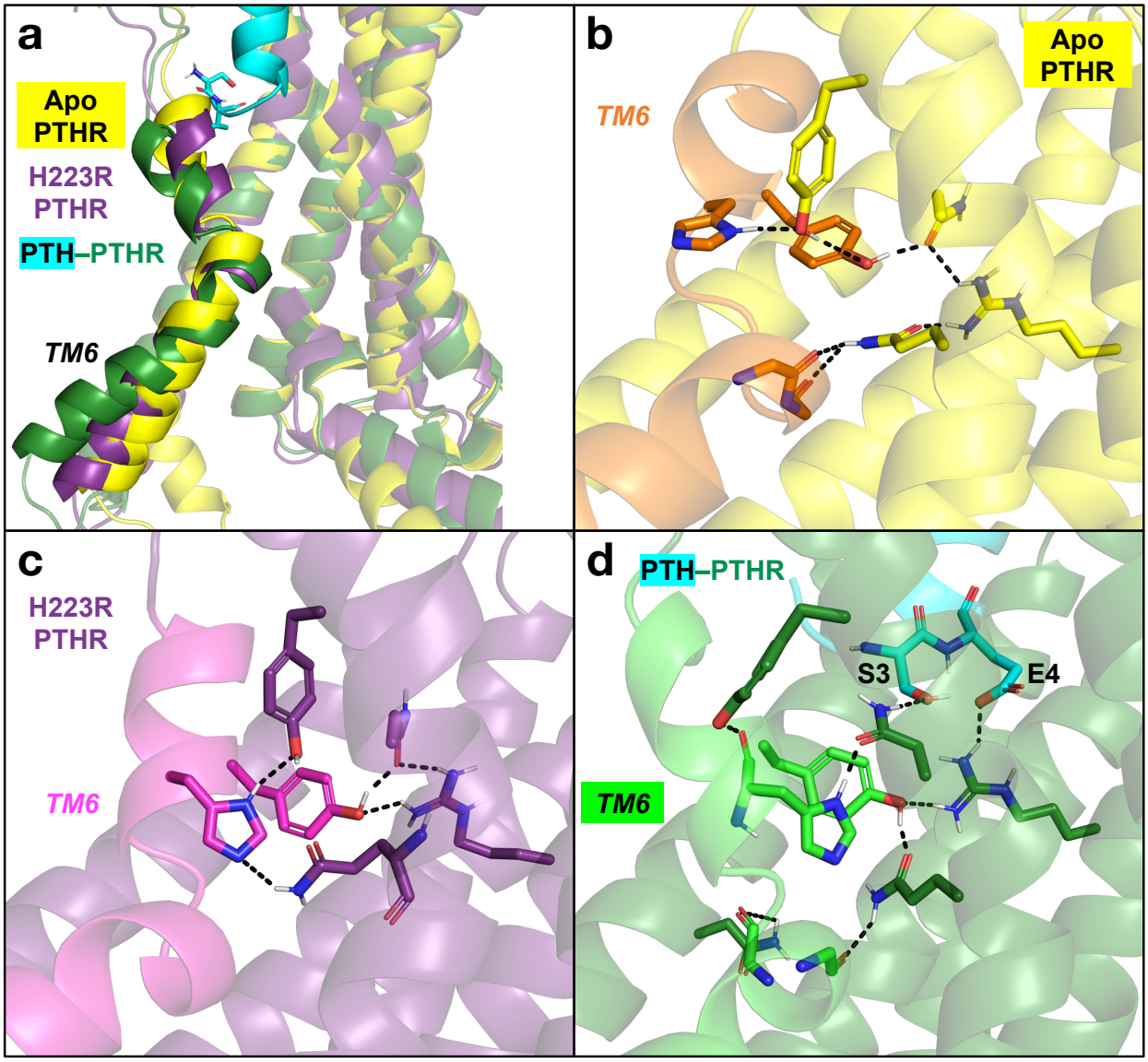

Appendix Figure 29. PTH promotes outward movement of TM6.

MD snapshots of apo wild-type PTHR (yellow), H223R PTHR (violet), and PTH-bound PTHR (cyan ligand, dark green receptor) after 100 ns. Residues 179–191 and 435–456 are hidden for clarity. **a,** PTH residues 1 and 2 (sticks) push on the C-terminal part of TM6, promoting outward kink in the N-terminal (cytosolic) part of TM6. Note the slightly outward kink of H223R PTHR relative to apo PTHR. **b–d,** Polar contacts stabilizing TM6 in apo, H223R, and PTH-bound receptors (black dashes). PTH Glu4 coordinates an extensive polar network to stabilize TM6.

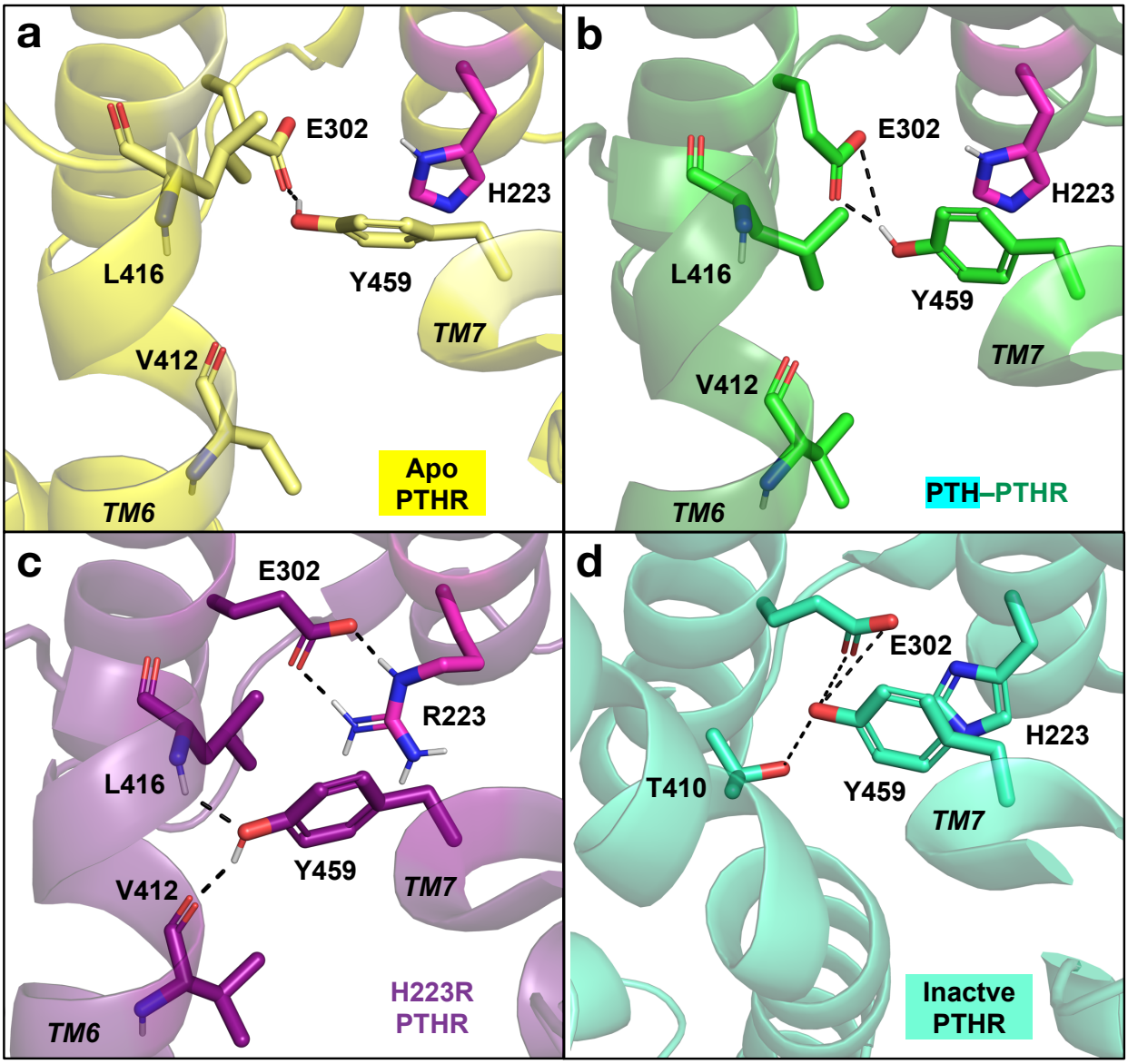

Appendix Figure 30. JMC mutant H223R induces Y459 polar interactions with TM6 to stabilize outward kink.

MD snapshots of apo wild-type PTHR (yellow, **a**), PTH-bound PTHR (dark green, **b**), and H223R PTHR (violet, **c**) after 100 ns. **d,** Inactive state crystal structure of PTHR (PDB 6FJ3[55]), where Tyr459 also interacts with Thr410 on TM6. Tyr459 polar interactions are shown as black dashes. Residues 179–191 and 435–456 are hidden for clarity.

Bibliography

1 Hauser, A. S., Attwood, M. M., Rask-Andersen, M., Schioth, H. B. & Gloriam, D. E. Trends in GPCR drug discovery: new agents, targets and indications. *Nat Rev Drug Discov* **16**, 829-842, doi:10.1038/nrd.2017.178 (2017).

2 Alana, I. *et al.* NMR and alanine scan studies of glucose-dependent insulinotropic polypeptide in water. *J Biol Chem* **281**, 16370-16376, doi:10.1074/jbc.M510414200 (2006).

3 Lambright, D. G. *et al.* The 2.0 A crystal structure of a heterotrimeric G protein. *Nature* **379**, 311-319, doi:10.1038/379311a0 (1996).

4 Han, M., Gurevich, V. V., Vishnivetskiy, S. A., Sigler, P. B. & Schubert, C. Crystal structure of beta-arrestin at 1.9 A: possible mechanism of receptor binding and membrane Translocation. *Structure* **9**, 869-880, doi:10.1016/s0969-2126(01)00644-x (2001).

5 Schiöth, H. B. & Fredriksson, R. The GRAFS classification system of G-protein coupled receptors in comparative perspective. *Gen Comp Endocrinol* **142**, 94-101, doi:10.1016/j.ygcen.2004.12.018 (2005).

6 Alexander, S. P. *et al.* The Concise Guide to PHARMACOLOGY 2015/16: G protein-coupled receptors. *Br J Pharmacol* **172**, 5744-5869, doi:10.1111/bph.13348 (2015).

7 Pándy-Szekeres, G. *et al.* GPCRdb in 2018: adding GPCR structure models and ligands. *Nucleic Acids Research* **46**, D440-D446, doi:10.1093/nar/gkx1109 (2017).

8 Congreve, M., de Graaf, C., Swain, N. A. & Tate, C. G. Impact of GPCR Structures on Drug Discovery. *Cell* **181**, 81-91, doi:10.1016/j.cell.2020.03.003 (2020).

9 de Graaf, C. *et al.* Extending the Structural View of Class B GPCRs. *Trends Biochem Sci* **42**, 946-960, doi:10.1016/j.tibs.2017.10.003 (2017).

10 Leon, K. *et al.* Structural basis for adhesion G protein-coupled receptor Gpr126 function. *Nat Commun* **11**, 194, doi:10.1038/s41467-019-14040-1 (2020).

11 Arac, D. *et al.* A novel evolutionarily conserved domain of cell-adhesion GPCRs mediates autoproteolysis. *EMBO J* **31**, 1364-1378, doi:10.1038/emboj.2012.26 (2012).

12 Koehl, A. *et al.* Structural insights into the activation of metabotropic glutamate receptors. *Nature* **566**, 79-84, doi:10.1038/s41586-019-0881-4 (2019).

13 Park, J. *et al.* Structure of human GABAB receptor in an inactive state. *Nature*, doi:10.1038/s41586-020-2452-0 (2020).

14 Zhang, X., Dong, S. & Xu, F. Structural and Druggability Landscape of Frizzled G Protein-Coupled Receptors. *Trends Biochem Sci* **43**, 1033-1046, doi:10.1016/j.tibs.2018.09.002 (2018).

15 Ellis, C. & The Nature Reviews Drug Discovery, G. Q. P. The state of GPCR research in 2004. *Nature Reviews Drug Discovery* **3**, 577-626, doi:10.1038/nrd1458 (2004).

16 Sutkeviciute, I. & Vilardaga, J. P. Structural insights into emergent signaling modes of G protein-coupled receptors. *J Biol Chem*, doi:10.1074/jbc.REV120.009348 (2020).

17 Sprang, S. R. Invited review: Activation of G proteins by GTP and the mechanism of Gα-catalyzed GTP hydrolysis. *Biopolymers* **105**, 449-462, doi:10.1002/bip.22836 (2016).

18 Dupré, D. J., Robitaille, M., Rebois, R. V. & Hébert, T. E. The Role of Gβγ Subunits in the Organization, Assembly, and Function of GPCR Signaling Complexes. *Annual Review of Pharmacology and Toxicology* **49**, 31-56, doi:10.1146/annurev-pharmtox-061008-103038 (2009).

19 Vadas, O. *et al.* Molecular determinants of PI3Kgamma-mediated activation downstream of G-protein-coupled receptors (GPCRs). *Proc Natl Acad Sci U S A* **110**, 18862-18867, doi:10.1073/pnas.1304801110 (2013).

20 Lohse, M. J. *et al.* Receptor-specific desensitization with purified proteins. Kinase dependence and receptor specificity of beta-arrestin and arrestin in the beta 2-adrenergic receptor and rhodopsin systems. *J Biol Chem* **267**, 8558-8564 (1992).

21 Drake, M. T., Shenoy, S. K. & Lefkowitz, R. J. Trafficking of G protein-coupled receptors. *Circ Res* **99**, 570-582, doi:10.1161/01.RES.0000242563.47507.ce (2006).

22 Gardella, T. J. & Vilardaga, J. P. International Union of Basic and Clinical Pharmacology. XCIII. The parathyroid hormone receptors--family B G protein-coupled receptors. *Pharmacol Rev* **67**, 310-337, doi:10.1124/pr.114.009464 (2015).

23 Ferrandon, S. *et al.* Sustained cyclic AMP production by parathyroid hormone receptor endocytosis. *Nat Chem Biol* **5**, 734-742, doi:10.1038/nchembio.206 (2009).

24 Zhao, L. H. *et al.* Structure and dynamics of the active human parathyroid hormone receptor-1. *Science* **364**, 148-153, doi:10.1126/science.aav7942 (2019).

25 Johansson, E. *et al.* Type II Turn of Receptor-bound Salmon Calcitonin Revealed by X-ray Crystallography. *J Biol Chem* **291**, 13689-13698, doi:10.1074/jbc.M116.726034 (2016).

26 ter Haar, E. *et al.* Crystal structure of the ectodomain complex of the CGRP receptor, a class-B GPCR, reveals the site of drug antagonism. *Structure* **18**, 1083-1093, doi:10.1016/j.str.2010.05.014 (2010).

27 Booe, J. M., Warner, M. L., Roehrkasse, A. M., Hay, D. L. & Pioszak, A. A. Probing the Mechanism of Receptor Activity-Modifying Protein Modulation of GPCR Ligand Selectivity through Rational Design of Potent Adrenomedullin and Calcitonin Gene-Related Peptide Antagonists. *Mol Pharmacol* **93**, 355-367, doi:10.1124/mol.117.110916 (2018).

28 Roehrkasse, A. M., Booe, J. M., Lee, S. M., Warner, M. L. & Pioszak, A. A. Structure-function analyses reveal a triple beta-turn receptor-bound conformation of adrenomedullin 2/intermedin and enable peptide antagonist design. *J Biol Chem* **293**, 15840-15854, doi:10.1074/jbc.RA118.005062 (2018).

29 Booe, J. M. *et al.* Structural Basis for Receptor Activity-Modifying Protein-Dependent Selective Peptide Recognition by a G Protein-Coupled Receptor. *Mol Cell* **58**, 1040-1052, doi:10.1016/j.molcel.2015.04.018 (2015).

30 Kusano, S. *et al.* Structural basis for extracellular interactions between calcitonin receptor-like receptor and receptor activity-modifying protein 2 for adrenomedullin-specific binding. *Protein Sci* **21**, 199-210, doi:10.1002/pro.2003 (2012).

31 Pioszak, A. A., Parker, N. R., Suino-Powell, K. & Xu, H. E. Molecular recognition of corticotropin-releasing factor by its G-protein-coupled receptor CRFR1. *J Biol Chem* **283**, 32900-32912, doi:10.1074/jbc.M805749200 (2008).

32 Pal, K., Swaminathan, K., Xu, H. E. & Pioszak, A. A. Structural basis for hormone recognition by the Human CRFR2{alpha} G protein-coupled receptor. *J Biol Chem* **285**, 40351-40361, doi:10.1074/jbc.M110.186072 (2010).

33 Koth, C. M. *et al.* Molecular basis for negative regulation of the glucagon receptor. *Proc Natl Acad Sci U S A* **109**, 14393-14398, doi:10.1073/pnas.1206734109 (2012).

34 Pike, A. C. W. *et al.* Crystal structure of the extracellular domain of human growth hormone releasing hormone receptor. doi:10.2210/pdb2XDG/pdb (2010).

35 Parthier, C. *et al.* Crystal structure of the incretin-bound extracellular domain of a G protein-coupled receptor. *Proc Natl Acad Sci U S A* **104**, 13942-13947, doi:10.1073/pnas.0706404104 (2007).

36 Ravn, P. *et al.* Structural and pharmacological characterization of novel potent and selective monoclonal antibody antagonists of glucose-dependent insulinotropic polypeptide receptor. *J Biol Chem* **288**, 19760-19772, doi:10.1074/jbc.M112.426288 (2013).

37 Underwood, C. R. *et al.* Crystal structure of glucagon-like peptide-1 in complex with the extracellular domain of the glucagon-like peptide-1 receptor. *J Biol Chem* **285**, 723-730, doi:10.1074/jbc.M109.033829 (2010).

38 Lau, J. *et al.* Discovery of the Once-Weekly Glucagon-Like Peptide-1 (GLP-1) Analogue Semaglutide. *J Med Chem* **58**, 7370-7380, doi:10.1021/acs.jmedchem.5b00726 (2015).

39 Runge, S., Thogersen, H., Madsen, K., Lau, J. & Rudolph, R. Crystal structure of the ligand-bound glucagon-like peptide-1 receptor extracellular domain. *J Biol Chem* **283**, 11340-11347, doi:10.1074/jbc.M708740200 (2008).

40 Hennen, S. *et al.* Structural insight into antibody-mediated antagonism of the Glucagon-like peptide-1 Receptor. *Sci Rep* **6**, 26236, doi:10.1038/srep26236 (2016).

41 Pioszak, A. A., Harikumar, K. G., Parker, N. R., Miller, L. J. & Xu, H. E. Dimeric arrangement of the parathyroid hormone receptor and a structural mechanism for ligand-induced dissociation. *J Biol Chem* **285**, 12435-12444, doi:10.1074/jbc.M109.093138 (2010).

42 Pioszak, A. A. & Xu, H. E. Molecular recognition of parathyroid hormone by its G protein-coupled receptor. *Proc Natl Acad Sci U S A* **105**, 5034-5039, doi:10.1073/pnas.0801027105 (2008).

43 Pioszak, A. A., Parker, N. R., Gardella, T. J. & Xu, H. E. Structural basis for parathyroid hormone-related protein binding to the parathyroid hormone receptor and design of conformation-selective peptides. *J Biol Chem* **284**, 28382-28391, doi:10.1074/jbc.M109.022905 (2009).

44 Kumar, S., Pioszak, A., Zhang, C., Swaminathan, K. & Xu, H. E. Crystal structure of the PAC1R extracellular domain unifies a consensus fold for hormone recognition by class B G-protein coupled receptors. *PLoS One* **6**, e19682, doi:10.1371/journal.pone.0019682 (2011).

45 Pike, A. C. W. *et al.* Crystal structure of the extracellular domain of human Vasoactive intestinal polypeptide receptor 2. doi:10.2210/pdb2X57/pdb (2010).

46 Grace, C. R. *et al.* NMR structure of the first extracellular domain of corticotropin-releasing factor receptor 1 (ECD1-CRF-R1) complexed with a high affinity agonist. *J Biol Chem* **285**, 38580-38589, doi:10.1074/jbc.M110.121897 (2010).

47 Grace, C. R. *et al.* NMR structure and peptide hormone binding site of the first extracellular domain of a type B1 G protein-coupled receptor. *Proc Natl Acad Sci U S A* **101**, 12836-12841, doi:10.1073/pnas.0404702101 (2004).

48 Grace, C. R. *et al.* Structure of the N-terminal domain of a type B1 G protein-coupled receptor in complex with a peptide ligand. *Proc Natl Acad Sci U S A* **104**, 4858-4863, doi:10.1073/pnas.0700682104 (2007).

49 Sun, C. *et al.* Solution structure and mutational analysis of pituitary adenylate cyclase-activating polypeptide binding to the extracellular domain of PAC1-RS. *Proc Natl Acad Sci U S A* **104**, 7875-7880, doi:10.1073/pnas.0611397104 (2007).

50 Hollenstein, K. *et al.* Structure of class B GPCR corticotropin-releasing factor receptor 1. *Nature* **499**, 438-443, doi:10.1038/nature12357 (2013).

51 Siu, F. Y. *et al.* Structure of the human glucagon class B G-protein-coupled receptor. *Nature* **499**, 444-449, doi:10.1038/nature12393 (2013).

52 Zhang, H. *et al.* Structure of the full-length glucagon class B G-protein-coupled receptor. *Nature* **546**, 259-264, doi:10.1038/nature22363 (2017).

53 Jazayeri, A. *et al.* Extra-helical binding site of a glucagon receptor antagonist. *Nature* **533**, 274-277, doi:10.1038/nature17414 (2016).

54 Song, G. *et al.* Human GLP-1 receptor transmembrane domain structure in complex with allosteric modulators. *Nature* **546**, 312-315, doi:10.1038/nature22378 (2017).

55 Ehrenmann, J. *et al.* High-resolution crystal structure of parathyroid hormone 1 receptor in complex with a peptide agonist. *Nat Struct Mol Biol* **25**, 1086-1092, doi:10.1038/s41594-018-0151-4 (2018).

56 Zhang, H. *et al.* Structure of the glucagon receptor in complex with a glucagon analogue. *Nature* **553**, 106-110, doi:10.1038/nature25153 (2018).

57 Jazayeri, A. *et al.* Crystal structure of the GLP-1 receptor bound to a peptide agonist. *Nature* **546**, 254-258, doi:10.1038/nature22800 (2017).

58 Kühlbrandt, W. The Resolution Revolution. *Science* **343**, 1443-1444, doi:10.1126/science.1251652 (2014).

59 dal Maso, E. *et al.* The Molecular Control of Calcitonin Receptor Signaling. *ACS Pharmacology & Translational Science* **2**, 31-51, doi:10.1021/acsptsci.8b00056 (2019).

60 Liang, Y. L. *et al.* Cryo-EM structure of the active, Gs-protein complexed, human CGRP receptor. *Nature* **561**, 492-497, doi:10.1038/s41586-018-0535-y (2018).

61 Liang, Y. L. *et al.* Phase-plate cryo-EM structure of a biased agonist-bound human GLP-1 receptor-Gs complex. *Nature* **555**, 121-125, doi:10.1038/nature25773 (2018).

62 Zhang, Y. *et al.* Cryo-EM structure of the activated GLP-1 receptor in complex with a G protein. *Nature* **546**, 248-253, doi:10.1038/nature22394 (2017).

63 Hilger, D. *et al.* Structural insights into differences in G protein activation by family A and family B GPCRs. *Science* **369**, doi:10.1126/science.aba3373 (2020).

64 Oldham, W. M. & Hamm, H. E. Structural basis of function in heterotrimeric G proteins. *Q Rev Biophys* **39**, 117-166, doi:10.1017/S0033583506004306 (2006).

65 Sunahara, R. K., Tesmer, J. J., Gilman, A. G. & Sprang, S. R. Crystal structure of the adenylyl cyclase activator Gsalpha. *Science* **278**, 1943-1947, doi:10.1126/science.278.5345.1943 (1997).

66 Oldham, W. M. & Hamm, H. E. Heterotrimeric G protein activation by G-protein-coupled receptors. *Nature Reviews Molecular Cell Biology* **9**, 60-71, doi:10.1038/nrm2299 (2008).

67 Rasmussen, S. G. *et al.* Crystal structure of the beta2 adrenergic receptor-Gs protein complex. *Nature* **477**, 549-555, doi:10.1038/nature10361 (2011).

68 Liu, X. *et al.* Structural Insights into the Process of GPCR-G Protein Complex Formation. *Cell* **177**, 1243-1251 e1212, doi:10.1016/j.cell.2019.04.021 (2019).

69 Goricanec, D. *et al.* Conformational dynamics of a G-protein alpha subunit is tightly regulated by nucleotide binding. *Proc Natl Acad Sci U S A* **113**, E3629-3638, doi:10.1073/pnas.1604125113 (2016).

70 Qi, C., Sorrentino, S., Medalia, O. & Korkhov, V. M. The structure of a membrane adenylyl cyclase bound to an activated stimulatory G protein. *Science* **364**, 389-394, doi:10.1126/science.aav0778 (2019).

71 Tesmer, J. J. *et al.* Molecular basis for P-site inhibition of adenylyl cyclase. *Biochemistry* **39**, 14464-14471, doi:10.1021/bi0015562 (2000).

72 Tesmer, V. M., Kawano, T., Shankaranarayanan, A., Kozasa, T. & Tesmer, J. J. Snapshot of activated G proteins at the membrane: the Galphaq-GRK2-Gbetagamma complex. *Science* **310**, 1686-1690, doi:10.1126/science.1118890 (2005).

73 Slep, K. C. *et al.* Structural determinants for regulation of phosphodiesterase by a G protein at 2.0 A. *Nature* **409**, 1071-1077, doi:10.1038/35059138 (2001).

74 Soundararajan, M. *et al.* Structural diversity in the RGS domain and its interaction with heterotrimeric G protein alpha-subunits. *Proc Natl Acad Sci U S A* **105**, 6457-6462, doi:10.1073/pnas.0801508105 (2008).

75 Shukla, A. K. *et al.* Structure of active beta-arrestin-1 bound to a G-protein-coupled receptor phosphopeptide. *Nature* **497**, 137-141, doi:10.1038/nature12120 (2013).

76 Chen, Q., Iverson, T. M. & Gurevich, V. V. Structural Basis of Arrestin-Dependent Signal Transduction. *Trends Biochem Sci* **43**, 412-423, doi:10.1016/j.tibs.2018.03.005 (2018).

77 Zhou, X. E. *et al.* Identification of Phosphorylation Codes for Arrestin Recruitment by G Protein-Coupled Receptors. *Cell* **170**, 457-469 e413, doi:10.1016/j.cell.2017.07.002 (2017).

78 Eichel, K. *et al.* Catalytic activation of beta-arrestin by GPCRs. *Nature* **557**, 381-386, doi:10.1038/s41586-018-0079-1 (2018).

79 Latorraca, N. R. *et al.* Molecular mechanism of GPCR-mediated arrestin activation. *Nature* **557**, 452-456, doi:10.1038/s41586-018-0077-3 (2018).

80 Goodman, O. B., Jr. *et al.* Beta-arrestin acts as a clathrin adaptor in endocytosis of the beta2-adrenergic receptor. *Nature* **383**, 447-450, doi:10.1038/383447a0 (1996).

81 Laporte, S. A., Miller, W. E., Kim, K. M. & Caron, M. G. beta-Arrestin/AP-2 interaction in G protein-coupled receptor internalization: identification of a beta-arrestin binging site in beta 2-adaptin. *J Biol Chem* **277**, 9247-9254, doi:10.1074/jbc.M108490200 (2002).

82 Urena, P. *et al.* Parathyroid hormone (PTH)/PTH-related peptide receptor messenger ribonucleic acids are widely distributed in rat tissues. *Endocrinology* **133**, 617-623, doi:10.1210/endo.133.2.8393771 (1993).

83 McCauley, L. K. & Martin, T. J. Twenty-five years of PTHrP progress: from cancer hormone to multifunctional cytokine. *J Bone Miner Res* **27**, 1231-1239, doi:10.1002/jbmr.1617 (2012).

84 Vilardaga, J. P., Romero, G., Friedman, P. A. & Gardella, T. J. Molecular basis of parathyroid hormone receptor signaling and trafficking: a family B GPCR paradigm. *Cell Mol Life Sci* **68**, 1-13, doi:10.1007/s00018-010-0465-9 (2011).

85 Horwitz, M. J. *et al.* Continuous PTH and PTHrP infusion causes suppression of bone formation and discordant effects on 1,25(OH)2 vitamin D. *J Bone Miner Res* **20**, 1792-1803, doi:10.1359/JBMR.050602 (2005).

86 Miao, D. *et al.* Skeletal abnormalities in Pth-null mice are influenced by dietary calcium. *Endocrinology* **145**, 2046-2053, doi:10.1210/en.2003-1097 (2004).

87 Philbrick, W. M. *et al.* Defining the roles of parathyroid hormone-related protein in normal physiology. *Physiol Rev* **76**, 127-173, doi:10.1152/physrev.1996.76.1.127 (1996).

88 Dean, T., Vilardaga, J. P., Potts, J. T., Jr. & Gardella, T. J. Altered selectivity of parathyroid hormone (PTH) and PTH-related protein (PTHrP) for distinct conformations of the PTH/PTHrP receptor. *Mol Endocrinol* **22**, 156-166, doi:10.1210/me.2007-0274 (2008).

89 White, A. D. *et al.* Ca(2+) allostery in PTH-receptor signaling. *Proc Natl Acad Sci U S A* **116**, 3294-3299, doi:10.1073/pnas.1814670116 (2019).

90 Nissenson, R. A., Diep, D. & Strewler, G. J. Synthetic peptides comprising the amino-terminal sequence of a parathyroid hormone-like protein from human malignancies. Binding to parathyroid hormone receptors and activation of adenylate cyclase in bone cells and kidney. *J Biol Chem* **263**, 12866-12871 (1988).

91 Potts, J. T., Jr. *et al.* Synthesis of a biologically active N-terminal tetratriacontapeptide of parathyroid hormone. *Proc Natl Acad Sci U S A* **68**, 63-67, doi:10.1073/pnas.68.1.63 (1971).

92 Cheloha, R. W., Gellman, S. H., Vilardaga, J. P. & Gardella, T. J. PTH receptor-1 signalling-mechanistic insights and therapeutic prospects. *Nat Rev Endocrinol* **11**, 712-724, doi:10.1038/nrendo.2015.139 (2015).

93 Jobert, A. S. *et al.* Absence of functional receptors for parathyroid hormone and parathyroid hormone-related peptide in Blomstrand chondrodysplasia. *J Clin Invest* **102**, 34-40, doi:10.1172/JCI2918 (1998).

94 Hoogendam, J. *et al.* Novel mutations in the parathyroid hormone (PTH)/PTH-related peptide receptor type 1 causing Blomstrand osteochondrodysplasia types I and II. *J Clin Endocrinol Metab* **92**, 1088-1095, doi:10.1210/jc.2006-0300 (2007).

95 Pansuriya, T. C., Kroon, H. M. & Bovee, J. V. Enchondromatosis: insights on the different subtypes. *Int J Clin Exp Pathol* **3**, 557-569 (2010).

96 Hanisch, M., Hanisch, L., Kleinheinz, J. & Jung, S. Primary failure of eruption (PFE): a systematic review. *Head Face Med* **14**, 5, doi:10.1186/s13005-018-0163-7 (2018).

97 Tokavanich, N. *et al.* A three-dimensional analysis of primary failure of eruption in humans and mice. *Oral Dis* **26**, 391-400, doi:10.1111/odi.13249 (2020).

98 Schipani, E., Kruse, K. & Juppner, H. A constitutively active mutant PTH-PTHrP receptor in Jansen-type metaphyseal chondrodysplasia. *Science* **268**, 98-100, doi:10.1126/science.7701349 (1995).

99 Schipani, E. *et al.* A novel parathyroid hormone (PTH)/PTH-related peptide receptor mutation in Jansen's metaphyseal chondrodysplasia. *J Clin Endocrinol Metab* **84**, 3052-3057, doi:10.1210/jcem.84.9.6000 (1999).

100 Schipani, E. *et al.* Constitutively activated receptors for parathyroid hormone and parathyroid hormone-related peptide in Jansen's metaphyseal chondrodysplasia. *N Engl J Med* **335**, 708-714, doi:10.1056/NEJM199609053351004 (1996).

101 Giovanella, L., Bacigalupo, L., Treglia, G. & Piccardo, A. Will 18F-fluorocholine PET/CT replace other methods of preoperative parathyroid imaging? *Endocrine*, doi:10.1007/s12020-020-02487-y (2020).

102 Rubin, M. R. Recent advances in understanding and managing hypoparathyroidism. *F1000Res* **9**, doi:10.12688/f1000research.22717.1 (2020).

103 Feldenzer, K. L. & Sarno, J. Hypercalcemia of Malignancy. *J Adv Pract Oncol* **9**, 496-504 (2018).

104 Canalis, E., Giustina, A. & Bilezikian, J. P. Mechanisms of anabolic therapies for osteoporosis. *N Engl J Med* **357**, 905-916, doi:10.1056/NEJMra067395 (2007).

105 Cohen, A. *et al.* Effect of Teriparatide on Bone Remodeling and Density in Premenopausal Idiopathic Osteoporosis: A Phase II Trial. *J Clin Endocrinol Metab* **105**, doi:10.1210/clinem/dgaa489 (2020).

106 Ono, K. *et al.* Evaluations of daily teriparatide using finite-element analysis over 12 months in rheumatoid arthritis patients. *J Bone Miner Metab*, doi:10.1007/s00774-020-01146-6 (2020).

107 Leder, B. Z. *et al.* Effects of abaloparatide, a human parathyroid hormone-related peptide analog, on bone mineral density in postmenopausal women with osteoporosis. *J Clin Endocrinol Metab* **100**, 697-706, doi:10.1210/jc.2014-3718 (2015).

108 Sleeman, A. & Clements, J. N. Abaloparatide: A new pharmacological option for osteoporosis. *American Journal of Health-System Pharmacy* **76**, 130-135, doi:10.1093/ajhp/zxy022 (2019).

109 Miller, P. D. *et al.* Bone mineral density response rates are greater in patients treated with abaloparatide compared with those treated with placebo or teriparatide: Results from the ACTIVE phase 3 trial. *Bone* **120**, 137-140, doi:10.1016/j.bone.2018.10.015 (2019).

110 Arlt, H. *et al.* Effects of abaloparatide and teriparatide on bone resorption and bone formation in female mice. *Bone Reports* **13**, 100291, doi:https://doi.org/10.1016/j.bonr.2020.100291 (2020).

111 Vilardaga, J. P., Jean-Alphonse, F. G. & Gardella, T. J. Endosomal generation of cAMP in GPCR signaling. *Nat Chem Biol* **10**, 700-706, doi:10.1038/nchembio.1611 (2014).

112 Wehbi, V. L. *et al.* Noncanonical GPCR signaling arising from a PTH receptor-arrestin-Gbetagamma complex. *Proc Natl Acad Sci U S A* **110**, 1530-1535, doi:10.1073/pnas.1205756110 (2013).

113 White, A. D. *et al.* Gq/11-dependent regulation of endosomal cAMP generation by parathyroid hormone class B GPCR. *Proc Natl Acad Sci U S A* **117**, 7455-7460, doi:10.1073/pnas.1918158117 (2020).

114 Gidon, A. *et al.* Endosomal GPCR signaling turned off by negative feedback actions of PKA and v-ATPase. *Nat Chem Biol* **10**, 707-709, doi:10.1038/nchembio.1589 (2014).

115 Feinstein, T. N. *et al.* Retromer terminates the generation of cAMP by internalized PTH receptors. *Nat Chem Biol* **7**, 278-284, doi:10.1038/nchembio.545 (2011).

116 Okazaki, M. *et al.* Prolonged signaling at the parathyroid hormone receptor by peptide ligands targeted to a specific receptor conformation. *Proc Natl Acad Sci U S A* **105**, 16525-16530, doi:10.1073/pnas.0808750105 (2008).

117 Shimizu, M. *et al.* Pharmacodynamic Actions of a Long-Acting PTH Analog (LA-PTH) in Thyroparathyroidectomized (TPTX) Rats and Normal Monkeys. *J Bone Miner Res* **31**, 1405-1412, doi:10.1002/jbmr.2811 (2016).

118 Sutkeviciute, I., Clark, L. J., White, A. D., Gardella, T. J. & Vilardaga, J. P. PTH/PTHrP Receptor Signaling, Allostery, and Structures. *Trends Endocrinol Metab* **30**, 860-874, doi:10.1016/j.tem.2019.07.011 (2019).

119 Hattersley, G., Dean, T., Corbin, B. A., Bahar, H. & Gardella, T. J. Binding Selectivity of Abaloparatide for PTH-Type-1-Receptor Conformations and Effects on Downstream Signaling. *Endocrinology* **157**, 141-149, doi:10.1210/en.2015-1726 (2016).

120 Goltzman, D., Peytremann, A., Callahan, E., Tregear, G. W. & Potts, J. T., Jr. Analysis of the requirements for parathyroid hormone action in renal membranes with the use of inhibiting analogues. *J Biol Chem* **250**, 3199-3203 (1975).

121 Horiuchi, N., Holick, M. F., Potts, J. T., Jr. & Rosenblatt, M. A parathyroid hormone inhibitor in vivo: design and biological evaluation of a hormone analog. *Science* **220**, 1053-1055, doi:10.1126/science.6302844 (1983).

122 Shimizu, M., Carter, P. H. & Gardella, T. J. Autoactivation of type-1 parathyroid hormone receptors containing a tethered ligand. *J Biol Chem* **275**, 19456-19460, doi:10.1074/jbc.M001596200 (2000).

123 Maeda, A. *et al.* Critical role of parathyroid hormone (PTH) receptor-1 phosphorylation in regulating acute responses to PTH. *Proc Natl Acad Sci U S A* **110**, 5864-5869, doi:10.1073/pnas.1301674110 (2013).

124 Iiri, T., Bell, S. M., Baranski, T. J., Fujita, T. & Bourne, H. R. A Gsalpha mutant designed to inhibit receptor signaling through Gs. *Proc Natl Acad Sci U S A* **96**, 499-504, doi:10.1073/pnas.96.2.499 (1999).

125 Zheng, S. Q. *et al.* MotionCor2: anisotropic correction of beam-induced motion for improved cryo-electron microscopy. *Nat Methods* **14**, 331-332, doi:10.1038/nmeth.4193 (2017).

126 Zhang, K. Gctf: Real-time CTF determination and correction. *J Struct Biol* **193**, 1-12, doi:10.1016/j.jsb.2015.11.003 (2016).

127 Scheres, S. H. RELION: implementation of a Bayesian approach to cryo-EM structure determination. *J Struct Biol* **180**, 519-530, doi:10.1016/j.jsb.2012.09.006 (2012).

128 Punjani, A., Rubinstein, J. L., Fleet, D. J. & Brubaker, M. A. cryoSPARC: algorithms for rapid unsupervised cryo-EM structure determination. *Nat Methods* **14**, 290-296, doi:10.1038/nmeth.4169 (2017).

129 Heymann, J. B. Guidelines for using Bsoft for high resolution reconstruction and validation of biomolecular structures from electron micrographs. *Protein Sci* **27**, 159-171, doi:10.1002/pro.3293 (2018).

130 Pettersen, E. F. *et al.* UCSF Chimera--a visualization system for exploratory research and analysis. *J Comput Chem* **25**, 1605-1612, doi:10.1002/jcc.20084 (2004).

131 Emsley, P. & Cowtan, K. Coot: model-building tools for molecular graphics. *Acta Crystallogr D Biol Crystallogr* **60**, 2126-2132, doi:10.1107/S0907444904019158 (2004).

132 Adams, P. D. *et al.* PHENIX: a comprehensive Python-based system for macromolecular structure solution. *Acta Crystallogr D Biol Crystallogr* **66**, 213-221, doi:10.1107/S0907444909052925 (2010).

133 Chen, V. B. *et al.* MolProbity: all-atom structure validation for macromolecular crystallography. *Acta Crystallogr D Biol Crystallogr* **66**, 12-21, doi:10.1107/S0907444909042073 (2010).

134 Liang, Y. L. *et al.* Phase-plate cryo-EM structure of a class B GPCR-G-protein complex. *Nature* **546**, 118-123, doi:10.1038/nature22327 (2017).

135 Cao, C., Zhang, H., Yang, Z. & Wu, B. Peptide recognition, signaling and modulation of class B G protein-coupled receptors. *Curr Opin Struct Biol* **51**, 53-60, doi:10.1016/j.sbi.2018.03.008 (2018).

136 Farrens, D. L., Altenbach, C., Yang, K., Hubbell, W. L. & Khorana, H. G. Requirement of rigid-body motion of transmembrane helices for light activation of rhodopsin. *Science* **274**, 768-770, doi:10.1126/science.274.5288.768 (1996).

137 Sheikh, S. P. *et al.* Similar structures and shared switch mechanisms of the beta2-adrenoceptor and the parathyroid hormone receptor. Zn(II) bridges between helices III and VI block activation. *J Biol Chem* **274**, 17033-17041, doi:10.1074/jbc.274.24.17033 (1999).

138 Gether, U. *et al.* Agonists induce conformational changes in transmembrane domains III and VI of the beta2 adrenoceptor. *EMBO J* **16**, 6737-6747, doi:10.1093/emboj/16.22.6737 (1997).

139 Vilardaga, J. P. *et al.* Differential conformational requirements for activation of G proteins and the regulatory proteins arrestin and G protein-coupled receptor kinase in the G protein-coupled receptor for parathyroid hormone (PTH)/PTH-related protein. *J Biol Chem* **276**, 33435-33443, doi:10.1074/jbc.M011495200 (2001).

140 Gardella, T. J. *et al.* Parathyroid hormone (PTH)-PTH-related peptide hybrid peptides reveal functional interactions between the 1-14 and 15-34 domains of the ligand. *J Biol Chem* **270**, 6584-6588, doi:10.1074/jbc.270.12.6584 (1995).

141 Gardella, T. J. & Juppner, H. Molecular properties of the PTH/PTHrP receptor. *Trends Endocrinol Metab* **12**, 210-217, doi:10.1016/s1043-2760(01)00409-x (2001).

142 Takahashi, A. *et al.* Autocrine regulation of mesenchymal progenitor cell fates orchestrates tooth eruption. *Proc Natl Acad Sci U S A* **116**, 575-580, doi:10.1073/pnas.1810200115 (2019).

143 Ono, W., Sakagami, N., Nishimori, S., Ono, N. & Kronenberg, H. M. Parathyroid hormone receptor signalling in osterix-expressing mesenchymal progenitors is essential for tooth root formation. *Nat Commun* **7**, 11277, doi:10.1038/ncomms11277 (2016).

144 Roth, H. *et al.* Expanding the spectrum of PTH1R mutations in patients with primary failure of tooth eruption. *Clin Oral Investig* **18**, 377-384, doi:10.1007/s00784-013-1014-3 (2014).

145 Lee, S. *et al.* A Homozygous [Cys25]PTH(1-84) Mutation That Impairs PTH/PTHrP Receptor Activation Defines a Novel Form of Hypoparathyroidism. *J Bone Miner Res* **30**, 1803-1813, doi:10.1002/jbmr.2532 (2015).

146 Biebermann, H. *et al.* A New Multisystem Disorder Caused by the Galphas Mutation p.F376V. *J Clin Endocrinol Metab* **104**, 1079-1089, doi:10.1210/jc.2018-01250 (2019).

147 Wishart, D. S., Sykes, B. D. & Richards, F. M. The chemical shift index: a fast and simple method for the assignment of protein secondary structure through NMR spectroscopy. *Biochemistry* **31**, 1647-1651, doi:10.1021/bi00121a010 (1992).

148 Pahari, S., Sun, L. & Alexov, E. PKAD: a database of experimentally measured pKa values of ionizable groups in proteins. *Database (Oxford)* **2019**, doi:10.1093/database/baz024 (2019).

149 Radak, B. K. *et al.* Constant-pH Molecular Dynamics Simulations for Large Biomolecular Systems. *J Chem Theory Comput* **13**, 5933-5944, doi:10.1021/acs.jctc.7b00875 (2017).

150 Marx, U. C., Adermann, K., Bayer, P., Forssmann, W. G. & Rosch, P. Solution structures of human parathyroid hormone fragments hPTH(1-34) and hPTH(1-39) and bovine parathyroid hormone fragment bPTH(1-37). *Biochem Biophys Res Commun* **267**, 213-220, doi:10.1006/bbrc.1999.1958 (2000).

151 Skinner, S. P. *et al.* CcpNmr AnalysisAssign: a flexible platform for integrated NMR analysis. *J Biomol NMR* **66**, 111-124, doi:10.1007/s10858-016-0060-y (2016).

152 GraphPad Prism version 8 for Mac, GraphPad Software, La Jolla California USA, www.graphpad.com".

153 Nikolaev, V. O., Bunemann, M., Hein, L., Hannawacker, A. & Lohse, M. J. Novel single chain cAMP sensors for receptor-induced signal propagation. *J Biol Chem* **279**, 37215-37218, doi:10.1074/jbc.C400302200 (2004).

154 Yang, J. *et al.* The I-TASSER Suite: protein structure and function prediction. *Nat Methods* **12**, 7-8, doi:10.1038/nmeth.3213 (2015).

155 Roy, A., Kucukural, A. & Zhang, Y. I-TASSER: a unified platform for automated protein structure and function prediction. *Nat Protoc* **5**, 725-738, doi:10.1038/nprot.2010.5 (2010).

156 Zhang, Y. I-TASSER server for protein 3D structure prediction. *BMC Bioinformatics* **9**, 40, doi:10.1186/1471-2105-9-40 (2008).

157 The PyMOL Molecular Graphics System, Version 2.1 Schrödinger, LLC.

158 Lee, J. *et al.* CHARMM-GUI Input Generator for NAMD, GROMACS, AMBER, OpenMM, and CHARMM/OpenMM Simulations Using the CHARMM36 Additive Force Field. *J Chem Theory Comput* **12**, 405-413, doi:10.1021/acs.jctc.5b00935 (2016).

159 Lomize, M. A., Pogozheva, I. D., Joo, H., Mosberg, H. I. & Lomize, A. L. OPM database and PPM web server: resources for positioning of proteins in membranes. *Nucleic Acids Res* **40**, D370-376, doi:10.1093/nar/gkr703 (2012).

160 Lee, J. *et al.* CHARMM-GUI Membrane Builder for Complex Biological Membrane Simulations with Glycolipids and Lipoglycans. *J Chem Theory Comput* **15**, 775-786, doi:10.1021/acs.jctc.8b01066 (2019).

161 Wu, E. L. *et al.* CHARMM-GUI Membrane Builder toward realistic biological membrane simulations. *J Comput Chem* **35**, 1997-2004, doi:10.1002/jcc.23702 (2014).

162 Brooks, B. R. *et al.* CHARMM: the biomolecular simulation program. *J Comput Chem* **30**, 1545-1614, doi:10.1002/jcc.21287 (2009).

163 Jo, S., Kim, T., Iyer, V. G. & Im, W. CHARMM-GUI: a web-based graphical user interface for CHARMM. *J Comput Chem* **29**, 1859-1865, doi:10.1002/jcc.20945 (2008).

164 Jo, S., Kim, T. & Im, W. Automated builder and database of protein/membrane complexes for molecular dynamics simulations. *PLoS One* **2**, e880, doi:10.1371/journal.pone.0000880 (2007).

165 Jo, S., Lim, J. B., Klauda, J. B. & Im, W. CHARMM-GUI Membrane Builder for mixed bilayers and its application to yeast membranes. *Biophys J* **97**, 50-58, doi:10.1016/j.bpj.2009.04.013 (2009).

166 Phillips, J. C. *et al.* Scalable molecular dynamics with NAMD. *J Comput Chem* **26**, 1781-1802, doi:10.1002/jcc.20289 (2005).

167 Huang, J. *et al.* CHARMM36m: an improved force field for folded and intrinsically disordered proteins. *Nat Methods* **14**, 71-73, doi:10.1038/nmeth.4067 (2017).

168 Humphrey, W., Dalke, A. & Schulten, K. VMD: visual molecular dynamics. *J Mol Graph* **14**, 33-38, 27-38, doi:10.1016/0263-7855(96)00018-5 (1996).

169 Karageorgos, V. *et al.* Current understanding of the structure and function of family B GPCRs to design novel drugs. *Hormones (Athens)* **17**, 45-59, doi:10.1007/s42000-018-0009-5 (2018).

170 Castro, M., Nikolaev, V. O., Palm, D., Lohse, M. J. & Vilardaga, J. P. Turn-on switch in parathyroid hormone receptor by a two-step parathyroid hormone binding mechanism. *Proc Natl Acad Sci U S A* **102**, 16084-16089, doi:10.1073/pnas.0503942102 (2005).

171 Kawai, M., Modder, U. I., Khosla, S. & Rosen, C. J. Emerging therapeutic opportunities for skeletal restoration. *Nat Rev Drug Discov* **10**, 141-156, doi:10.1038/nrd3299 (2011).

172 Neer, R. M. *et al.* Effect of parathyroid hormone (1-34) on fractures and bone mineral density in postmenopausal women with osteoporosis. *N Engl J Med* **344**, 1434-1441, doi:10.1056/NEJM200105103441904 (2001).

173 Parthier, C., Reedtz-Runge, S., Rudolph, R. & Stubbs, M. T. Passing the baton in class B GPCRs: peptide hormone activation via helix induction? *Trends Biochem Sci* **34**, 303-310, doi:10.1016/j.tibs.2009.02.004 (2009).

174 Miao, Y., Bhattarai, A., Nguyen, A. T. N., Christopoulos, A. & May, L. T. Structural Basis for Binding of Allosteric Drug Leads in the Adenosine A1 Receptor. *Sci Rep* **8**, 16836, doi:10.1038/s41598-018-35266-x (2018).

175 Rana, S. & Sahoo, A. R. Model structures of inactive and peptide agonist bound C5aR: Insights into agonist binding, selectivity and activation. *Biochem Biophys Rep* **1**, 85-96, doi:10.1016/j.bbrep.2015.03.002 (2015).

176 Zhang, C. *et al.* High-resolution crystal structure of human protease-activated receptor 1. *Nature* **492**, 387-392, doi:10.1038/nature11701 (2012).

177 Song, W., Yen, H. Y., Robinson, C. V. & Sansom, M. S. P. State-dependent Lipid Interactions with the A2a Receptor Revealed by MD Simulations Using In Vivo-Mimetic Membranes. *Structure* **27**, 392-403 e393, doi:10.1016/j.str.2018.10.024 (2019).

178 Mouritsen, O. G. & Zuckermann, M. J. What's so special about cholesterol? *Lipids* **39**, 1101-1113, doi:10.1007/s11745-004-1336-x (2004).

179 Jin, L. *et al.* Crystal structure of human parathyroid hormone 1-34 at 0.9-A resolution. *J Biol Chem* **275**, 27238-27244, doi:10.1074/jbc.M001134200 (2000).

180 Wu, F. *et al.* Full-length human GLP-1 receptor structure without orthosteric ligands. *Nat Commun* **11**, 1272, doi:10.1038/s41467-020-14934-5 (2020).

181 Cheloha, R. W., Watanabe, T., Dean, T., Gellman, S. H. & Gardella, T. J. Backbone Modification of a Parathyroid Hormone Receptor-1 Antagonist/Inverse Agonist. *ACS Chem Biol* **11**, 2752-2762, doi:10.1021/acschembio.6b00404 (2016).

182 Liu, S., Cheloha, R. W., Watanabe, T., Gardella, T. J. & Gellman, S. H. Receptor selectivity from minimal backbone modification of a polypeptide agonist. *Proc Natl Acad Sci U S A* **115**, 12383-12388, doi:10.1073/pnas.1815294115 (2018).

183 Liu, S. *et al.* Use of Backbone Modification To Enlarge the Spatiotemporal Diversity of Parathyroid Hormone Receptor-1 Signaling via Biased Agonism. *J Am Chem Soc* **141**, 14486-14490, doi:10.1021/jacs.9b04179 (2019).

184 Cupp, M. E. *et al.* Investigating hydrophobic ligand-receptor interactions in parathyroid hormone receptor using peptide probes. *J Pept Sci* **19**, 337-344, doi:10.1002/psc.2502 (2013).

185 Wang, Y., Harrison, C. B., Schulten, K. & McCammon, J. A. Implementation of Accelerated Molecular Dynamics in NAMD. *Comput Sci Discov* **4**, doi:10.1088/1749-4699/4/1/015002 (2011).

186 Hamelberg, D., Mongan, J. & McCammon, J. A. Accelerated molecular dynamics: a promising and efficient simulation method for biomolecules. *J Chem Phys* **120**, 11919-11929, doi:10.1063/1.1755656 (2004).

187 Staus, D. P. *et al.* Structure of the M2 muscarinic receptor-beta-arrestin complex in a lipid nanodisc. *Nature*, doi:10.1038/s41586-020-1954-0 (2020).

188 Huang, W. *et al.* Structure of the neurotensin receptor 1 in complex with beta-arrestin 1. *Nature*, doi:10.1038/s41586-020-1953-1 (2020).

189 Kang, Y. *et al.* Crystal structure of rhodopsin bound to arrestin by femtosecond X-ray laser. *Nature* **523**, 561-567, doi:10.1038/nature14656 (2015).

190 Waterhouse, A. *et al.* SWISS-MODEL: homology modelling of protein structures and complexes. *Nucleic Acids Res* **46**, W296-W303, doi:10.1093/nar/gky427 (2018).

191 Bakan, A. *et al.* Evol and ProDy for bridging protein sequence evolution and structural dynamics. *Bioinformatics* **30**, 2681-2683, doi:10.1093/bioinformatics/btu336 (2014).

192 Bakan, A., Meireles, L. M. & Bahar, I. ProDy: protein dynamics inferred from theory and experiments. *Bioinformatics* **27**, 1575-1577, doi:10.1093/bioinformatics/btr168 (2011).

193 McGarvey, J. C. *et al.* Actin-Sorting Nexin 27 (SNX27)-Retromer Complex Mediates Rapid Parathyroid Hormone Receptor Recycling. *J Biol Chem* **291**, 10986-11002, doi:10.1074/jbc.M115.697045 (2016).

194 Liu, C. C. & Schultz, P. G. Adding new chemistries to the genetic code. *Annu Rev Biochem* **79**, 413-444, doi:10.1146/annurev.biochem.052308.105824 (2010).

195 Chin, J. W. *et al.* An expanded eukaryotic genetic code. *Science* **301**, 964-967, doi:10.1126/science.1084772 (2003).

196 Serfling, R. & Coin, I. Incorporation of Unnatural Amino Acids into Proteins Expressed in Mammalian Cells. *Methods Enzymol* **580**, 89-107, doi:10.1016/bs.mie.2016.05.003 (2016).

197 Coin, I. *et al.* Genetically encoded chemical probes in cells reveal the binding path of urocortin-I to CRF class B GPCR. *Cell* **155**, 1258-1269, doi:10.1016/j.cell.2013.11.008 (2013).

198 Gotze, M. *et al.* StavroX--a software for analyzing crosslinked products in protein interaction studies. *J Am Soc Mass Spectrom* **23**, 76-87, doi:10.1007/s13361-011-0261-2 (2012).

199 Nobles, K. N. *et al.* Distinct phosphorylation sites on the beta(2)-adrenergic receptor establish a barcode that encodes differential functions of beta-arrestin. *Science signaling* **4**, ra51, doi:10.1126/scisignal.2001707 (2011).

200 Xiao, K. & Shenoy, S. K. Beta2-adrenergic receptor lysosomal trafficking is regulated by ubiquitination of lysyl residues in two distinct receptor domains. *The Journal of biological chemistry* **286**, 12785-12795, doi:10.1074/jbc.M110.203091 (2011).

201 Kahsai, A. W., Rajagopal, S., Sun, J. & Xiao, K. Monitoring protein conformational changes and dynamics using stable-isotope labeling and mass spectrometry. *Nat Protoc* **9**, 1301-1319, doi:10.1038/nprot.2014.075 (2014).

202 Xiao, K. *et al.* Revealing the architecture of protein complexes by an orthogonal approach combining HDXMS, CXMS, and disulfide trapping. *Nat Protoc* **13**, 1403-1428, doi:10.1038/nprot.2018.037 (2018).

203 Haas, W. *et al.* Optimization and use of peptide mass measurement accuracy in shotgun proteomics. *Molecular & cellular proteomics : MCP* **5**, 1326-1337, doi:10.1074/mcp.M500339-MCP200 (2006).

204 Bakalarski, C. E. *et al.* The impact of peptide abundance and dynamic range on stable-isotope-based quantitative proteomic analyses. *Journal of proteome research* **7**, 4756-4765, doi:10.1021/pr800333e (2008).

205 Eyal, E., Lum, G. & Bahar, I. The anisotropic network model web server at 2015 (ANM 2.0). *Bioinformatics* **31**, 1487-1489, doi:10.1093/bioinformatics/btu847 (2015).

206 Lezon, T. R. & Bahar, I. Constraints imposed by the membrane selectively guide the alternating access dynamics of the glutamate transporter GltPh. *Biophys J* **102**, 1331-1340, doi:10.1016/j.bpj.2012.02.028 (2012).

207 Doruker, P., Atilgan, A. R. & Bahar, I. Dynamics of proteins predicted by molecular dynamics simulations and analytical approaches: application to alpha-amylase inhibitor. *Proteins* **40**, 512-524 (2000).

208 Bahar, I., Lezon, T. R., Bakan, A. & Shrivastava, I. H. Normal mode analysis of biomolecular structures: functional mechanisms of membrane proteins. *Chem Rev* **110**, 1463-1497, doi:10.1021/cr900095e (2010).

209 Atilgan, A. R. *et al.* Anisotropy of fluctuation dynamics of proteins with an elastic network model. *Biophys J* **80**, 505-515, doi:10.1016/S0006-3495(01)76033-X (2001).

210 Dror, R. O. *et al.* Activation mechanism of the beta2-adrenergic receptor. *Proc Natl Acad Sci U S A* **108**, 18684-18689, doi:10.1073/pnas.1110499108 (2011).

211 Fleetwood, O., Matricon, P., Carlsson, J. & Delemotte, L. Energy Landscapes Reveal Agonist Control of G Protein-Coupled Receptor Activation via Microswitches. *Biochemistry*, doi:10.1021/acs.biochem.9b00842 (2020).

212 Lovera, S., Cuzzolin, A., Kelm, S., De Fabritiis, G. & Sands, Z. A. Reconstruction of apo A2A receptor activation pathways reveal ligand-competent intermediates and state-dependent cholesterol hotspots. *Sci Rep* **9**, 14199, doi:10.1038/s41598-019-50752-6 (2019).

213 Isin, B., Schulten, K., Tajkhorshid, E. & Bahar, I. Mechanism of signal propagation upon retinal isomerization: insights from molecular dynamics simulations of rhodopsin restrained by normal modes. *Biophys J* **95**, 789-803, doi:10.1529/biophysj.107.120691 (2008).

214 Vilardaga, J. P., Bunemann, M., Krasel, C., Castro, M. & Lohse, M. J. Measurement of the millisecond activation switch of G protein-coupled receptors in living cells. *Nat Biotechnol* **21**, 807-812, doi:10.1038/nbt838 (2003).

215 Oakley, R. H., Laporte, S. A., Holt, J. A., Caron, M. G. & Barak, L. S. Differential affinities of visual arrestin, beta arrestin1, and beta arrestin2 for G protein-coupled receptors delineate two major classes of receptors. *J Biol Chem* **275**, 17201-17210, doi:10.1074/jbc.M910348199 (2000).

216 Farrell, I. S., Toroney, R., Hazen, J. L., Mehl, R. A. & Chin, J. W. Photo-cross-linking interacting proteins with a genetically encoded benzophenone. *Nat Methods* **2**, 377-384, doi:10.1038/nmeth0505-377 (2005).

217 Yin, W. *et al.* A complex structure of arrestin-2 bound to a G protein-coupled receptor. *Cell Res* **29**, 971-983, doi:10.1038/s41422-019-0256-2 (2019).

218 Shiraishi, Y. *et al.* Phosphorylation-induced conformation of β(2)-adrenoceptor related to arrestin recruitment revealed by NMR. *Nature communications* **9**, 194-194, doi:10.1038/s41467-017-02632-8 (2018).

219 Mayer, D. *et al.* Distinct G protein-coupled receptor phosphorylation motifs modulate arrestin affinity and activation and global conformation. *Nature communications* **10**, 1261, doi:10.1038/s41467-019-09204-y (2019).

220 Liggett, S. B. Phosphorylation Barcoding as a Mechanism of Directing GPCR Signaling. *Science signaling* **4**, pe36, doi:10.1126/scisignal.2002331 (2011).

221 Staus, D. P. *et al.* Sortase ligation enables homogeneous GPCR phosphorylation to reveal diversity in beta-arrestin coupling. *Proc Natl Acad Sci U S A* **115**, 3834-3839, doi:10.1073/pnas.1722336115 (2018).

222 Dore, A. S. *et al.* Decoding Corticotropin-Releasing Factor Receptor Type 1 Crystal Structures. *Curr Mol Pharmacol* **10**, 334-344, doi:10.2174/1874467210666170110114727 (2017).

223 Woolley, M. J. & Conner, A. C. Understanding the common themes and diverse roles of the second extracellular loop (ECL2) of the GPCR super-family. *Mol Cell Endocrinol* **449**, 3-11, doi:10.1016/j.mce.2016.11.023 (2017).

224 Wootten, D. *et al.* The Extracellular Surface of the GLP-1 Receptor Is a Molecular Trigger for Biased Agonism. *Cell* **165**, 1632-1643, doi:https://doi.org/10.1016/j.cell.2016.05.023 (2016).

225 Liang, Y. L. *et al.* Structure and Dynamics of Adrenomedullin Receptors AM1 and AM2 Reveal Key Mechanisms in the Control of Receptor Phenotype by Receptor Activity-Modifying Proteins. *ACS Pharmacol Transl Sci* **3**, 263-284, doi:10.1021/acsptsci.9b00080 (2020).

226 Ma, S. *et al.* Molecular Basis for Hormone Recognition and Activation of Corticotropin-Releasing Factor Receptors. *Mol Cell* **77**, 669-680.e664, doi:10.1016/j.molcel.2020.01.013 (2020).

227 Qiao, A. *et al.* Structural basis of Gs and Gi recognition by the human glucagon receptor. *Science* **367**, 1346-1352, doi:10.1126/science.aaz5346 (2020).

228 Kobayashi, K. *et al.* Cryo-EM structure of the human PAC1 receptor coupled to an engineered heterotrimeric G protein. *Nat Struct Mol Biol* **27**, 274-280, doi:10.1038/s41594-020-0386-8 (2020).

229 Liang, Y. L. *et al.* Toward a Structural Understanding of Class B GPCR Peptide Binding and Activation. *Mol Cell* **77**, 656-668.e655, doi:10.1016/j.molcel.2020.01.012 (2020).

230 Lee, Y. *et al.* Molecular basis of beta-arrestin coupling to formoterol-bound beta1-adrenoceptor. *Nature* **583**, 862-866, doi:10.1038/s41586-020-2419-1 (2020).

231 Munk, C. *et al.* An online resource for GPCR structure determination and analysis. *Nat Methods* **16**, 151-162, doi:10.1038/s41592-018-0302-x (2019).

232 Berman, H. M. *et al.* The Protein Data Bank. *Nucleic Acids Res* **28**, 235-242, doi:10.1093/nar/28.1.235 (2000).

233 Zhang, J., Yang, J., Jang, R. & Zhang, Y. GPCR-I-TASSER: A Hybrid Approach to G Protein-Coupled Receptor Structure Modeling and the Application to the Human Genome. *Structure* **23**, 1538-1549, doi:10.1016/j.str.2015.06.007 (2015).

234 Yin, Y. *et al.* Rearrangement of a polar core provides a conserved mechanism for constitutive activation of class B G protein-coupled receptors. *J Biol Chem* **292**, 9865-9881, doi:10.1074/jbc.M117.782987 (2017).